Zero-energy states in Majorana nanowire devices

Bommer, J.D.S.

DOI
10.4233/uuid:bf8250f8-6377-4dd2-bb6a-dfd9e41451fc

Publication date
2020

Document Version
Final published version

Citation (APA)
Bommer, J. D. S. (2020). *Zero-energy states in Majorana nanowire devices*. [Dissertation (TU Delft), Delft University of Technology]. https://doi.org/10.4233/uuid:bf8250f8-6377-4dd2-bb6a-dfd9e41451fc

ZERO-ENERGY STATES IN MAJORANA NANOWIRE DEVICES

JOURI BOMMER

ZERO-ENERGY STATES IN MAJORANA NANOWIRE DEVICES

Proefschrift

ter verkrijging van de graad van doctor
aan de Technische Universiteit Delft,
op gezag van de Rector Magnificus prof. dr. ir. T.H.J.J. van der Hagen,
voorzitter van het College voor Promoties,
in het openbaar te verdedigen op woensdag 6 januari 2021 om 15:00 uur

door

Jurriaan Daniël Siegfried BOMMER

Natuurkundig ingenieur, Universiteit Twente, Nederland,
geboren te Vinkeveen, Nederland.

This dissertation has been approved by the promotors.

Composition of the doctoral committee:

Rector Magnificus	chairperson
Prof. dr. ir. L. P. Kouwenhoven	Delft University of Technology, promotor
Dr. M. T. Wimmer	Delft University of Technology, copromotor
Independent members:	
Prof. dr. S. Das Sarma	University of Maryland
Prof. dr. C. W. J. Beenakkker	Leiden University
Prof. dr. ir. A. F. Otte	Delft University of Technology
Dr. A. Kou	University of Illinois Urbana-Champaign
Prof. dr. Y. M. Blanter	Delft University of Technology, reserve member

Printed by: Gildeprint

Cover art: Design by Anouk Bommer, www.LookNouk.nl

Casimir PhD Series, Delft-Leiden 2020-35

ISBN 978-90-8593-460-8

CONTENTS

SUMMARY

In the voyage towards solving increasingly challenging computations of physical systems, quantum computation has arisen as a contender for conventional computational approaches. To address the issue of keeping the required quantum mechanical states sufficiently stable against environmental disturbances, novel proposals suggested to employ topological quantum states, where information can be stored nonlocally, essentially by sharing the information over physically different locations. Because suitable topological states are elusive in existing materials, an approach of great interest is to engineer the required topological Majorana modes by combining a spin-orbit coupled semiconductor nanowire exposed to a magnetic field with a superconducting material: a Majorana nanowire. After the first experimental signs of Majorana modes were observed in 2012, it also became clear that the experiments showed deviations from the theoretical expectations and alternative interpretations were suggested.

This dissertation explores the intricate physics that emerges in Majorana nanowires, with the aim to find improved Majorana signatures in transport experiments. By addressing disorder at the interface between the nanowire and the superconductor, we find Majorana signatures through the electrical transport through a ballistic tunnel junction, which allows us to exclude certain alternative explanations based on disorder. We also look into two key elements required to obtain Majorana modes: spin-orbit interaction and induced superconductivity. First, through measurements of the effect of a magnetic field and its direction on the size of the induced superconducting gap, we show that spin-orbit interaction counteracts the closing of the superconducting gap. This protection of the superconducting gap is ultimately responsible for the possibility of a topological nontrivial phase in nanowires. Second, we investigate the influence of an electric field in the nanowire on the coupling between electronic states in the nanowire and the superconductor and find that the electric field modifies the strength of the effective nanowire parameters essential to Majorana physics. Returning to the study of transport signatures of Majorana modes, we explore plateaus in the zero-bias conductance near the quantization value predicted for topological Majorana modes. Instabilities of the observed quantized plateaus on tunnel-barrier details indicate instead the presence of topologically trivial zero-energy states, which can be described as local Majorana modes and may offer an alternative route towards the demonstration of non-Abelian exchange statistics. Finally, we address the nonlocal distribution of Majorana nanowire zero-energy states through the modulation of the energy splitting due to a remote electrostatic gate decoupled from the tunneling barrier region. We identify states consistent with overlapping Majorana modes in a short nanowire. The dissertation is concluded by discussing interesting future avenues to solidify the understanding of Majorana nanowires and we indicating a possible alternative approach to demonstrate non-Abelian properties by deliberately stabilizing local Majorana modes.

SAMENVATTING

In de zoektocht naar methodes om steeds complexere berekeningen van fysieke systemen op te lossen, hebben kwantum berekeningen hun intrede gemaakt als een uitdager voor conventionele berekeningstechnieken. Om het probleem van het voldoende stabiel houden van de benodigde kwantumtoestanden tegen verstoringen uit de omgeving aan te pakken, opperden nieuwe voorstellen om topologische kwantumtoestanden te gebruiken, waarin informatie op niet-lokale wijze opgeslagen kan worden, in essentie door de informatie over verschillende fysieke locaties te verspreiden. Omdat geschikte topologische toestanden in bestaande materialen een zeldzaamheid lijken te zijn, is een zeer interessante aanpak om de benodigde topologische Majorana toestanden te creëren, om een halfgeleider nanodraad die spin-baan koppeling vertoont, blootgesteld aan een magneetveld, te combineren met een supergeleider: een Majorana nanodraad. Nadat de eerste experimentelen tekenen van Majorana toestanden in 2012 werden waargenomen, tekenden zich ook afwijkingen van de theoretische verwachtingen af en kwamen alternatieve interpretaties naar voren.

Dit proefschrift verkent de fijnmazige natuurkunde die opduikt in Majorana nanodraden, met als doel om verbeterde Majorana tekenen in transport experimenten te vinden. Door wanorde op het grensvlak van de nanodraad en de supergeleider aan te pakken, vinden we Majorana tekenen in het elektrische transport door een ballistische tunnel junctie, wat bepaalde alternatieve interpretaties op basis van wanorde uitsluit. We werpen ook een nadere blik op twee vitale elementen benodigd om Majorana toestanden te verkrijgen: spin-baan koppeling en geïnduceerde supergeleiding. Ten eerste, door metingen van het effect van een magneetveld en zijn richting op de omvang van de geïnduceerde supergeleidende bandkloof, tonen we aan dat spin-baan koppeling het sluiten van de supergeleidende bandkloof tegengaat. Deze bescherming van de supergeleidende bandkloof is uiteindelijk verantwoordelijk voor de mogelijkheid van een topologisch niet-triviale toestand in nanodraden. Ten tweede, onderzoeken we de invloed van een elektrisch veld in de nanodraad op de koppeling tussen de elektronische toestanden in de nanodraad en de supergeleider, waaruit we concluderen dat het elektrische veld de omvang van de effectieve nanodraad parameters, die essentieel zijn voor Majorana verschijnselen, aanpast. Terugkerend naar de studie van transporttekenen van Majorana toestanden, bekijken we plateaus in de hoogte van de geleidingspiek op nul spanning nabij de verwachte kwantizatiewaarde voor topologische Majorana toestanden. Instabiliteiten van de kwantizatieplateaus ten opzichte van details van de tunnel barrière wijzen echter op de aanwezigheid van topologisch triviale toestanden op nul energie, die beschreven kunnen worden als lokale Majorana toestanden en mogelijk een alternatieve route bieden voor de demonstratie van niet-Abelse uitwisselingsstatistiek. Ten slotte, onderzoeken we de niet-lokale verdeling van Majorana nanodraad toestanden nabij nul energie door middel van de modulatie van de energiesplitsing veroorzaakt door elektrostatische beïnvloeding met een gate ver verwijderd en ontkoppeld van de

tunnel barrière. We identificeren toestanden die consistent zijn met overlappende Majorana toestanden in een korte nanodraad. Het proefschrift wordt afgesloten met een discussie van interessante toekomstige onderzoeksrichtingen om het begrip van Majorana nanodraden te verstevigen en we duiden een potentiële alternatieve aanpak aan om niet-Abelse eigenschappen aan te tonen door doelbewust lokale Majorana toestanden te stabilizeren.

1

INTRODUCTION

1.1. QUANTUM COMPUTING

With the arrival of the 20th century came a tremendous change in how we describe the microscopic world around us due to the inception of quantum mechanics. Despite the often unintuitive interpretations of quantum mechanics, which remains a matter of debate to this day, the success of this new paradigm is undoubted. Right now, the macroscopic world we live in is getting ready to implement quantum mechanics in the state of the art technologies. Beside applications in quantum communication and cryptography [1], one of the appealing technological aims is the construction of a quantum computer. Quantum computers hold promise to solve particular problems with a significant speed-up over classical computers and may effectively simulate natural phenomena, as quantum computers follow the same laws as nature does at small scales [2].

In classical computers the elementary unit of information is a bit, which can only assume two values (0 and 1, or no and yes). Instead, in a quantum computer, the basic element of information is a quantum bit, or qubit, which can be in a mixture of the 0 and 1 states, an inherently quantum mechanical property called superposition. When the state of the qubit is measured, either 0 or 1 is found with a probability determined by the degree of the superposition. The true power of a quantum computer emerges when the number of qubits is increased, and quantum entanglement (where a quantum state is shared between multiple particles) and parallelism (exploring multiple paths at once) can be employed to provide the opportunities of a quantum speed-up.

The physical realization of a qubit requires a system consisting of two quantum states between which transitions can be induced through an external excitation. Most approaches currently being pursued, use two levels of an (artificial) atom as the basis states of the qubit. A prime challenge within the field is to maintain the quantum information stored in the qubit over sufficiently long timescales to be able to use it. Inadvertent interaction of the qubit with the environment, results in the loss of the useful quantum information in a process called decoherence, which leads to errors in quantum computations [3]. By using multiple physical qubits to encode a single logical qubit, such errors can be dealt with in error correction schemes if the decoherence is sufficiently low [4, 5].

An alternative approach is to use a qubit which is intrinsically protected from errors. By splitting the storage of information contained by the qubit over multiple locations (storing it nonlocally), local interactions with the environment cannot harm the quantum information [6]. This is the approach pursued in topological quantum computation. Instead of atom-like levels, a topological qubit uses exotic quasiparticles, called Majorana zero-modes. Below, we will discuss the basics of topology in condensed matter, how Majorana zero-modes emerge, and their special properties in relation to quantum computation.

1.2. TOPOLOGY IN CONDENSED MATTER

Historically, phase transitions between states of matter have long been characterized by a change in the symmetries underlying the physical system, following Landau theory. However, after the observation of the quantum Hall effect, it turned out that a phase transition can instead be associated with a change in the topology of the system [8]. Within mathematics, topology classifies objects based on properties that do not change

Figure 1.1: Illustration of the Möbius strip. Due to the twist, a Möbius strip cannot be smoothly deformed into a ring without cutting the strip and is thus topologically distinct. Adapted from [7].

under continuous deformations. For example, a normal strip and a Möbius strip are topologically different, since they cannot be transformed into each other without cutting the strip (see Fig. 1.1). The topology of the two objects is different in the number of half twists. Topological classification can also be applied in momentum space to electronic band structures in physics. Two topologically distinct phases with a bandgap (e.g. an insulator, semiconductor or superconductor) cannot be transformed into each other under smooth deformations of the Hamiltonian without closing the bandgap.

The quantum Hall effect occurs in low density two dimensional semiconductors in a magnetic field and causes an extremely precise quantization of the Hall conductance in integer multiples of the quantum of conductance, e^2/h, with e the elementary electron charge and h the Planck constant [9]. Remarkably, the quantization occurs independent of details of the sample, like its geometry or the presence of disorder. The reason behind the precise quantization, is that each quantization plateau results from a discrete number of edge states, each allowing a conductance of e^2/h. The number of edge states is determined by the topological invariant called the Chern number [10]. Only when the topological invariant changes, can the number of edge states and the associated quantized conductance change by an integer multiple of the conductance quantum.

Novel topological states have recently been discovered, including states that are useful in topological quantum computation, such as the 5/2 fractional quantum Hall state, and topological superconductors [11]. In these systems peculiar quasiparticles called Majorana zero-modes emerge at the edges of the topological phase. In a simplified picture, the presence of a zero-energy mode at the edge of a topological superconductor can be intuitively understood as follows. Since the edge of the topological superconductor constitutes the border between two systems with distinct topology, and because a transition between systems with different topology is only possible when the gap is closed, at the edge a local state emerges in the middle of the gap, as illustrated in Fig. 1.2a. For a topological superconductor, the edge state is called a Majorana mode, and since for superconductors the middle of the superconducting gap is commonly defined as zero-energy, the Majorana mode lives at zero-energy.

The two Majorana modes at the opposite ends of a topological superconductor together form a state which can host an electron at zero energy cost. A topological qubit can be created based on the state in which Majorana modes remains empty, and the state in which the Majorana modes carry an electron [12]. Fascinatingly, the electron can be

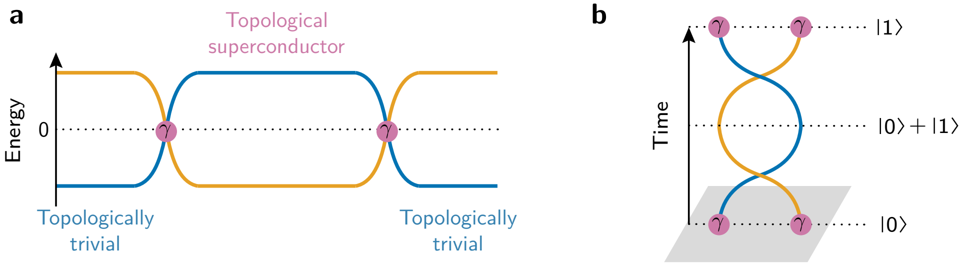

Figure 1.2: **(a)** At the edges of a one-dimensional topological superconductor, where the topology of the system changes and the band gap goes to zero, zero-energy Majorana bound states emerge (indicated by γ). The lines indicate the band gap, which is inverted in the topologically nontrivial part of the superconductor. **(b)** Two Majorana zero-modes are rotated, or braided, around each other twice. The grey plane indicates two-dimensional surface over which the Majorana modes can move. Through vertical axis the movement over time is tracked. If the Majorana zero-modes initially encode the logical $|0\rangle$, where the electron state composed by the Majorana modes is empty, after the first exchange of the Majorana zero-modes, the system is turned into an equal superposition of being occupied and unoccupied by an electron. After the second exchange, the system transitions into the logical $|1\rangle$ state, with the Majorana modes occupied by an electron. Only a fourfold exchange returns the system back to the $|0\rangle$ in which it started (not shown).

regarded as being split into two Majorana modes that are located far away from each other, which means that local noise will not influence the qubit. More technically, the half-electron characteristic of Majorana zero-modes reflects that they are non-Abelian anyons, which means that they obey exotic exchange statistics. In ordinary fermionic or bosonic exchange statistics, a double exchange of two particles leads to the same state as before the exchange. For Majorana zero-modes, on the other hand, a double exchange, or braid, induces a transition in the electron occupancy of the Majorana modes, as illustrated in Fig. 1.2b. And since the qubit state is encoded in the electron occupancy, exchanging Majorana modes is equal to a qubit rotation, which can be used to construct logical operations. Because the exchange procedure leads to exact qubit rotations, the logical operations are protected from errors by the topology of the exchange procedure, which is expected to give topological quantum computation a powerful competitive edge over competing approaches.

Although topological superconductivity appears to be an extremely rare phenomenon in nature, it can be realized in an engineering approach by combining multiple more accessible materials. Fu and Kane [13] first realized that topological superconductivity may be created by combining a topological insulator with an ordinary *s*-wave superconductor. Since then, many different proposals to create systems that can host Majorana zero-modes have emerged, including atomic chains [14], two-dimensional electron gases [15, 16], graphene [17], and semiconductor nanowires coupled to an ordinary superconductor [18, 19]. In this dissertation we focus on the hybrid semiconductor-superconducting nanowire approach and we will refer to nanowires with the relevant material requirements as Majorana nanowires.

Soon after the theoretical proposals, the first experimental indications of Majorana zero-modes were found in 2012 [20]. Following the first experimental results it soon became clear that the physics of Majorana nanowires is subtle. In real experimental systems the required physical phenomena such as spin-orbit interaction and superconductivity often behave in more complex ways than assumed in the foundational models. Additionally, the experimental signatures of Majorana modes are often not unique, requiring increasingly advanced experiments to rule out alternative explanations. The aim of this thesis is to improve the understanding of the subtleties of physical phenomena in Majorana nanowires and to explore novel aspects of experimental Majorana signatures.

1.3. THESIS OUTLINE

Chapter 2 provides the theoretical aspects of Majorana zero-modes to provide a basis to interpret the experimental results in the following chapters.

In chapter 3 we find experimental signatures of Majorana zero-modes coexisting with ballistic transport, which rules out alternative explanations based on disorder in the tunneling barrier region.

Chapter 4 explores spin-orbit interaction in the presence of superconductivity. Through the anisotropy of the magnetic field resilience of superconductivity, we find that spin-orbit interaction acts to protect the superconducting gap from closing. Our approach indicates the strength and orientation of the spin-orbit interaction.

Chapter 5 investigates the effect of electric fields in Majorana nanowires on the strength of the coupling between the semiconducting nanowire and the superconductor, which has consequences on the size of the superconducting gap in the nanowire, and other essential nanowire parameters including the Landé g-factor and the spin-orbit strength.

In Chapter 6 we return to the study of Majorana signatures and demonstrate plateaus in the zero-bias peak height near the predicted quantized value of $2e^2/h$ upon variation of the tunneling strength. Through analysis of the response to various electrostatic gates and the interaction with localized states in the tunneling region of the device, we attribute the nearly quantized zero-bias peaks to topologically trivial zero-energy states. The topologically trivial zero-energy states can be interpreted as local Majorana modes induced by a smooth electrostatic tunneling barrier profile.

Chapter 7 employs a remote electrostatic gate far removed from the barrier region of the Majorana nanowire to investigate the nonlocality of Majorana signatures through the modulation of the energy splitting. We identify zero-energy states which are consistent with overlapping Majorana modes in a short nanowire.

Chapter 8 concludes the findings of this thesis and explores avenues for future investigation. We suggest experiments for improved understanding of disorder in Majorana nanowires and indicate detection techniques capable of providing a stronger distinction between topological Majorana modes and topologically trivial alternative interpretations. In addition, we propose an experimental setup to purposefully create stable local Majorana modes, which may provide an alternative route towards the demonstration of non-Abelian braiding statistics.

REFERENCES

[1] S. Wehner, D. Elkouss, and R. Hanson, *Quantum internet: A vision for the road ahead,* Science **362**, eaam9288 (2018).

[2] T. D. Ladd, F. Jelezko, R. Laflamme, Y. Nakamura, C. Monroe, and J. L. O'Brien, *Quantum computers,* Nature **464**, 45 (2010).

[3] W. H. Zurek, *Quantum Darwinism,* Nat. Phys. **5**, 181 (2009).

[4] A. G. Fowler, M. Mariantoni, J. M. Martinis, and A. N. Cleland, *Surface codes: Towards practical large-scale quantum computation,* Phys. Rev. A **86**, 032324 (2012).

[5] S. J. Devitt, W. J. Munro, and K. Nemoto, *Quantum error correction for beginners,* Rep. Prog. Phys. **76**, 076001 (2013).

[6] S. Das Sarma, M. Freedman, and C. Nayak, *Topological quantum computation,* Phys. Today **59**, 32 (2006).

[7] BojanV03, *3d rendering of a Mobius strip,* (2015), availble under license CC BY-SA.

[8] *Topological phase transitions and topological phases of matter,* (2016), Scientific Background on the Nobel Prize in Physics 2016, compiled by the Class for Physics of the Royal Swedish Academy of Sciences.

[9] K. von Klitzing, G. Dorda, and M. Pepper, *New method for high-accuracy determination of the fine-structure constant based on quantized Hall resistance,* Phys. Rev. Lett. **45**, 494 (1980).

[10] J. E. Avron, D. Osadchy, and R. Seiler, *A topological look at the quantum Hall effect,* Physics Today **56**, 38 (2003).

[11] A. Stern, *Non-Abelian states of matter,* Nature **464**, 187 (2010).

[12] C. Nayak, S. H. Simon, A. Stern, M. Freedman, and S. Das Sarma, *Non-Abelian anyons and topological quantum computation,* Rev. Mod. Phys. **80**, 1083 (2008).

[13] L. Fu and C. L. Kane, *Superconducting proximity effect and Majorana fermions at the surface of a topological insulator,* Phys. Rev. Lett. **100**, 096407 (2008).

[14] S. Nadj-Perge, I. K. Drozdov, J. Li, H. Chen, S. Jeon, J. Seo, A. H. MacDonald, B. A. Bernevig, and A. Yazdani, *Observation of Majorana fermions in ferromagnetic atomic chains on a superconductor,* Science **346**, 602 (2014).

[15] M. Hell, M. Leijnse, and K. Flensberg, *Two-dimensional platform for networks of Majorana bound states,* Phys. Rev. Lett. **118**, 107701 (2017).

[16] F. Pientka, A. Keselman, E. Berg, A. Yacoby, A. Stern, and B. I. Halperin, *Topological superconductivity in a planar Josephson junction,* Phys. Rev. X **7**, 021032 (2017).

[17] P. San-Jose, J. L. Lado, R. Aguado, F. Guinea, and J. Fernández-Rossier, *Majorana zero modes in graphene,* Phys. Rev. X **5**, 041042 (2015).

[18] R. M. Lutchyn, J. D. Sau, and S. Das Sarma, *Majorana fermions and a topological phase transition in semiconductor-superconductor heterostructures,* Phys. Rev. Lett. **105**, 077001 (2010).

[19] Y. Oreg, G. Refael, and F. von Oppen, *Helical liquids and Majorana bound states in quantum wires,* Phys. Rev. Lett. **105**, 177002 (2010).

[20] V. Mourik, K. Zuo, S. M. Frolov, S. R. Plissard, E. P. A. M. Bakkers, and L. P. Kouwenhoven, *Signatures of Majorana fermions in hybrid superconductor-semiconductor nanowire devices,* Science **336**, 1003 (2012).

2

THEORY

2.1. SUPERCONDUCTIVITY

Superconductivity is a state in which materials are able to conduct current without dissipation. Some materials transition into this special state as their temperature is lowered below a critical temperature, as first discovered by Kamerlingh Onnes [1]. Superconductors also expel magnetic fields up to a critical magnetic field (the Meissner effect), after which the superconducting state is broken [2]. Remarkably, superconductivity is associated with the pairing of two electrons into Cooper pairs, which condense into a collective coherent many-body state, as described by the microscopic theory of superconductivity introduced by Bardeen *et al.* [3], now known as BCS theory. Since the BCS formalism is used in the theory of Majorana modes in topological superconductors, we will first provide a succinct overview of the core elements of BCS theory.

2.1.1. BCS SUPERCONDUCTIVITY

The ground state of a superconductor is described by Cooper pairs, which are composed of two electrons with opposite momentum and spin that experience an attractive binding interaction V_{kl}. The pairing Hamiltonian describing the superconductor is [4]:

$$H=\sum_{k\sigma}\epsilon_k c^\dagger_{k\sigma}c_{k\sigma}+\sum_{kl}V_{kl}c^\dagger_{k\uparrow}c^\dagger_{-k\downarrow}c_{-l\downarrow}c_{l\uparrow},\tag{2.1}$$

where $c^\dagger_{k\sigma}$ and $c_{k\sigma}$ respectively create and annihilate an electron with a momentum k and a spin σ. The first term accounts for the kinetic energy $\epsilon_k=\hbar^2k^2/2m^*-\mu$ of an electron with momentum k and an effective mass m^* relative to the Fermi energy μ. The second term describes the attractive interaction between two electrons, where $V_{kl}<0$ for values of k,l close to the Fermi wavevector and $V=0$ otherwise[1]. To simplify eq. 2.1, the mean-field approximation can be applied, in which the variations of the operators $c^\dagger_{k\uparrow}c^\dagger_{-k\downarrow}$ and $c_{-l\downarrow}c_{l\uparrow}$ around their expectation values $b^*_k=\langle c^\dagger_{k\uparrow}c^\dagger_{-k\downarrow}\rangle$ and $b_l=\langle c^\dagger_{-l\downarrow}c^\dagger_{l\uparrow}\rangle$ are assumed to be small. By substituting $c^\dagger_{k\uparrow}c^\dagger_{-k\downarrow}=b^*_k+(c_{-k\downarrow}c_{k\uparrow}-b^*_k)$ (and similar for $c_{-l\downarrow}c_{l\uparrow}$) and neglecting the term that is bilinear in the small variations we arrive at the mean-field Hamiltonian:

$$H=\sum_{k\sigma}\epsilon_k c^\dagger_{k\sigma}c_{k\sigma}-\sum_k\left(\Delta_k c^\dagger_{k\uparrow}c^\dagger_{-k\downarrow}+\Delta^*_k c_{k\uparrow}c_{-k\downarrow}-\Delta_k b^*_k\right),\tag{2.2}$$

where we defined $\Delta_k=\sum_l V_{kl}b_l$, which is termed the superconducting gap, as it corresponds to a gap in the spectrum of the excitations of the superconducting ground state, as we will see below. Note that as a result of the mean-field approximation, the number of particles is no longer conserved. Instead, only the *parity*, i.e. the even- or oddness of the number of particles is conserved. To diagonalize the Hamiltonian, we have to perform the Bogoliubov transformation [5, 6]:

$$c_{k\uparrow}=u^*_k a_{k\uparrow}+v_k a^\dagger_{k\downarrow}\tag{2.3}$$

$$c^\dagger_{-k\downarrow}=-v^*_k a_{k\uparrow}+u_k a^\dagger_{k\downarrow}\tag{2.4}$$

---

[1] Since the second term describes a scattering process of a pair of electrons with opposite spin from momentum l to momentum k, the l-state has to be occupied and the k-state has to be unoccupied. This is only possible near the Fermi level.

where $a_{k\uparrow}$ and $a_{k\downarrow}$ are new fermionic quasiparticle operators, sometimes called Bogoliubons, which are superpositions of the electron operator $c^\dagger_{k\sigma}$ and the hole operator $c_{-k-\sigma}$, as becomes clear when we invert eqs. (2.3) and (2.4):

$$a_{k\uparrow} = u_k c_{k\uparrow} - v_k c^\dagger_{-k\downarrow} \tag{2.5}$$

$$a_{k\downarrow} = v_k c^\dagger_{k\uparrow} + u_k c_{-k\downarrow} \tag{2.6}$$

With the normalization condition $|u_k|^2 + |v_k|^2 = 1$, the appropriate coherence factors that render the Hamiltonian diagonal are [4]:

$$|v_k|^2 = 1 - |u_k|^2 = \frac{1}{2}\left(1 - \frac{\epsilon_k}{E_k}\right), \tag{2.7}$$

with $E_k = \sqrt{\epsilon_k^2 + |\Delta_k|^2}$. After implementing this transformation, the Hamiltonian in eq. 2.2 can be written as:

$$H = \sum_k \left(\epsilon_k - E_k + \Delta_k b_k^\dagger\right) + \sum_k E_k \left(a^\dagger_{k\uparrow} a_{k\uparrow} + a^\dagger_{k\downarrow} a_{k\downarrow}\right). \tag{2.8}$$

The first term only contains constants and gives the ground state energy of the superconducting state. The second term describes the excitations above the ground state with an energy E_k, which has its minimal value at $E_k = \Delta$ for $\epsilon_k = 0$. A superconductor therefore features an *energy gap* Δ below which quasiparticle excitations are not allowed.

Quasiparticle density of states

As the Bogoliubov quasiparticle operator $a_k^\dagger$ creates a fermionic state analogous to how the operator $c^\dagger$ creates an electron, we can obtain the quasiparticle density of states by correspondence to the normal density of states $N_n(\epsilon)$ in the normal metal state: $N_n(\epsilon)\mathrm{d}\epsilon = N_s(E)\mathrm{d}E$. Assuming a constant density of states at energies near the Fermi level in the normal metal, $N_n(\epsilon) = N$, and after using $E_k = \sqrt{\epsilon_k^2 + |\Delta_k|^2}$, we get:

$$N_s(E) = N\frac{E}{\sqrt{E^2 - \Delta^2}}. \tag{2.9}$$

The density of states exhibits a peak when the energy equals the superconducting gap, which is known as the coherence peak. At high energy, the density of states approaches the density of states obtained in the normal state. The density of states is illustrated in Fig. 2.1a.

Bogoliubov-de Gennes formalism

The Bogoliubov transformation described by eqs. 2.5 can be conveniently applied to more general Hamiltonians by using the Bogoliubov-de Gennes formalism. As this method is used in the description of Majorana zero-modes, we give a short overview of the approach [5, 7, 8]. In real space the Hamiltonian of a superconductor can be described as:

$$\mathcal{H} = \int \mathrm{d}r \sum_{\sigma,\sigma'} H_0^{\sigma,\sigma'}(r) c^\dagger_{\sigma r} c_{\sigma' r} + \Delta(r) c^\dagger_{\uparrow r} c^\dagger_{\downarrow r} + \Delta^*(r) c_{\uparrow r} c_{\downarrow r}, \tag{2.10}$$

where the summation is over the spin indices $\sigma, \sigma' = \uparrow, \downarrow$. $H_0^{\sigma,\sigma'}(r)$ describes all single particle terms, which do not have to be restricted to the kinetic energy and Fermi energy, as we had assumed in eq. 2.1. By introducing the Nambu spinor[2] $\Psi(r) = \left(c_{\uparrow r}, c_{\downarrow r}, c^\dagger_{\downarrow r}, -c^\dagger_{\uparrow r}\right)^T$, the Hamiltonian can be written in the Bogoliubov-de Gennes (BdG) form:

$$\mathcal{H} = \frac{1}{2}\int \mathrm{d}r \Psi^\dagger(r) H_{\mathrm{BdG}} \Psi(r) \tag{2.11}$$

$$H_{\mathrm{BdG}} = \begin{bmatrix} H_0(r) & \Delta(r) \\ \Delta^*(r) & -\sigma_y H_0^*(r)\sigma_y \end{bmatrix}, \tag{2.12}$$

where -$\sigma_y H_0^*(r)\sigma_y$ is the time-reversed version of $H_0(r)$, describing holes. The eigenenergies can then be found from:

$$H_{\mathrm{BdG}}\Phi_n(r) = E_n \Phi_n(r), \tag{2.13}$$

with $\Phi_n = \left(u_{n\uparrow}(r), u_{n\downarrow}(r), v_{n\downarrow}(r), v_{n\uparrow}(r)\right)^T$, resulting in the diagonalized Hamiltonian

$$\mathcal{H} = \frac{1}{2}\sum_n E_n a_n^\dagger a_n \tag{2.14}$$

in terms of the Bogoliubov quasiparticle operators

$$a_n = \int \mathrm{d}r \Phi_n(r)^\dagger \Psi(r) = \int \mathrm{d}r \left(u^*_{n\uparrow}(r) c_{r\uparrow} + u^*_{n\downarrow}(r) c_{r\downarrow} + v_{n\downarrow}(r) c^\dagger_{r\downarrow} - v_{n\uparrow}(r) c^\dagger_{r,\uparrow}\right). \tag{2.15}$$

Note that the explicit introduction of the hole operators $c^\dagger_{\sigma r}$ in the Nambu spinor leads to an artificial doubling of the number of states. For every electron-like state with energy E there is a hole-like partner at energy $-E$. This symmetry of states, resulting from the Bogoliubov-de Gennes formalism, is called particle-hole symmetry.

2.2. ANDREEV REFLECTION

In the previous section we found that the minimum energy for a quasiparticle excitation in a superconductor is $E_k = \Delta$. At lower energies, the quasiparticle spectrum is gapped, or in other words, a superconductor cannot host quasiparticles at $E < \Delta$. This has consequences for the electronic transport between a normal metal and a superconductor. Let us consider a system where a normal metal is connected to a superconductor. Electrons in the normal metal at energies $E > \Delta$ incident on the superconductor can be converted into a Bogoliubov quasiparticle and are therefore transmitted, contributing a charge transfer of e. However, at energies below the superconducting gap, this process is forbidden. Instead, the electron is reflected back into the normal metal as a hole of equal energy. As the hole of positive charge moves in the opposite direction of the electron, the net charge transported is $2e$, which is compensated for in the superconductor by the injection of a Cooper pair. This process is called Andreev reflection [9], and is associated with the doubling of the conductance compared to the normal state, in which only a charge of e is transferred.

---

[2] Other variations of the Nambu spinor are sometimes used in literature. Note that these variations come with a slightly different definition of H_{BdG}.

A single mode, one-dimensional model describing the charge transport at the interface between a normal metal (N) and a superconductor (S) was developed by Blonder, Tinkham, and Klapwijk, now know as the BTK model [10]. The model includes a delta shaped electrostatic potential barrier at the NS-interface, which is characterized by a transmission T in the normal state. The introduction of this barrier allows for the possibility of an electron to be normally reflected at the interface, contributing no charge transfer. At zero temperature, the differential conductance of the NS junction is given by

$$\frac{\mathrm{d}I}{\mathrm{d}V} = \frac{2e^2}{h}\left(1 + |r_\mathrm{A}|^2 - |r_\mathrm{N}|^2\right), \tag{2.16}$$

where the amplitudes for Andreev and normal reflection, $|r_\mathrm{A}|^2$ and $|r_\mathrm{N}|^2$, can be obtained from the continuity of plane waves in the normal metal and the superconductor. The result is: [3]

$$|r_\mathrm{A}|^2 = \begin{cases} \dfrac{\Delta^2}{E^2 + \left(\Delta^2 - E^2\right)(2/T - 1)^2} \\ \dfrac{u_0^2 v_0^2}{\gamma^2} \end{cases}, \qquad |r_\mathrm{N}|^2 = \begin{cases} 1 - |r_\mathrm{A}|^2 & \text{if } E < \Delta \\ \dfrac{(1-T)\left(u_0^2 - v_0^2\right)^2}{T^2\gamma^2} & \text{if } E > \Delta \end{cases} \tag{2.17}$$

with u_0 and v_0 given by eq. 2.7 and $\gamma = \left(u_0^2 - v_0^2\right)/T + v_0^2$. At bias voltages much larger than the superconducting gap, $E \gg \Delta$, the conductance is the same as for a quantum point contact in the normal state:

$$\frac{\mathrm{d}I}{\mathrm{d}V} = \frac{2e^2}{h}T \tag{2.18}$$

In the experimental chapters of this thesis, we will refer to this situation as the above-gap conductance. In a single band model, the above-gap conductance is a measure of the transmission of the barrier. The limiting case of the zero-bias voltage, results in the equation also known as the Beenakker formula [12]:

$$\frac{\mathrm{d}I}{\mathrm{d}V} = \frac{2e^2}{h}\frac{2T^2}{(2-T)^2} \tag{2.19}$$

As transmission of electrons is not allowed within the superconducting gap, the conductance is entirely determined by Andreev reflection. In the limit of low transmission, the conductance is suppressed quadratically in T, since both the electron and the hole need to tunnel through the barrier. The bias dependence of the conductance obtained from eqs. (2.16) and (2.17) shows that at low transmission (in the tunneling regime), the conductance reflects the quasiparticle density of states, as shown in Fig. 2.1a,b. On the other hand, at complete transmission, the subgap conductance is doubled to $4e^2/h$, a situation we refer to as Andreev enhancement (see Fig. 2.1a,b).

---

[3] The derivation of the reflection amplitudes involves the approximation that the group velocity of the electrons and holes in the normal metal and in superconductor are equal to the Fermi velocity. This approximation holds for a large Fermi energy $\mu \gg E, \Delta$, which is not necessarily valid in a semiconducting nanowire, where the Fermi level may be close to the band bottom. Andreev reflection in Majorana nanowires, at low Fermi energy and including Zeeman and spin-orbit effects, is discussed by Liu *et al.* [11].

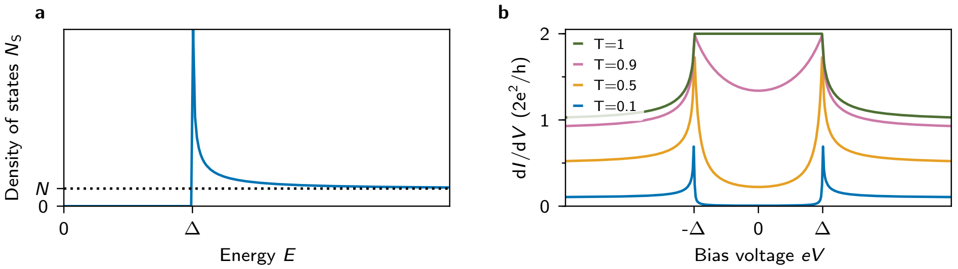

Figure 2.1: **(a)** The quasiparticle density of states in a superconductor (eq. 2.9) is zero within the superconducting gap, and peaks at the superconducting gap edge. At energies far above the superconducting gap, the density of states approaches the value obtained in the normal state. **(b)** The differential conductance $\mathrm{d}I/\mathrm{d}V$ for a normal-superconductor junction obtained from the BTK model (eqs. (2.16) and (2.17)), shown for four different values of the transmission. At low transmission Andreev reflection is strongly suppressed, and the conductance reflects the density of states (see **a**). At high transmission the subgap conductance is enhanced above $2e^2/h$ due to Andreev reflection. Note that at high bias voltage the conductance in units of $2e^2/h$ approaches the transmission T.

2.3. KITAEV CHAIN

Widespread attention to Majorana zero-modes was raised by the toy model devised by Kitaev [13], which describes an chain of atoms which can host Majorana quasiparticles at its ends. In this toy model only a single spin band is considered (the model is often called spinless). The chain consists of N lattice sites, of which the onsite energy is characterized by a chemical potential μ. Additionally, the neighboring sites are coupled by a hopping term t and an unconventional (p-type) superconducting pairing of adjacent

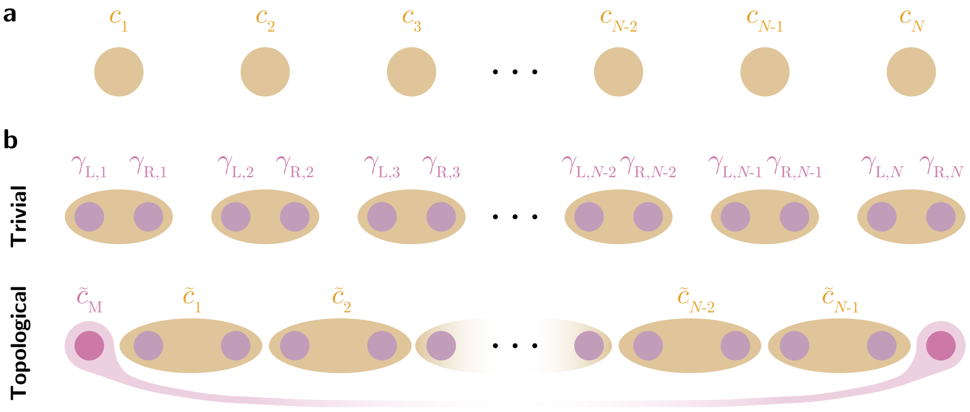

Figure 2.2: **Kitaev chain** **(a)** The Kitaev chain illustrated by the fermionic lattice sites, where each site is represented by c_i. **(b)** In the Majorana decomposition, every lattice site is split into two Majorana quasiparticles $\gamma_{\mathrm{L},i}$ and $\gamma_{\mathrm{R},i}$. Depending on the choice of the system parameters t and Δ, either the two Majorana quasiparticles on the same site couple, forming a topologically trivial system (top), or the two Majorana quasiparticles on adjacent sites couple, forming a topologically nontrivial system (bottom). In the nontrivial case, the two Majorana quasiparticles at the end of the chain remain uncoupled and together form a nonlocal zero-energy fermionic state $\tilde{c}_\mathrm{M}$.

sites of equal spin parameterized by a strength Δ. Putting these elements together, the Hamiltonian of the system can be expressed as

$$H = -\mu \sum_{j=1}^{N} \left(c_j^\dagger c_j - \tfrac{1}{2} \right) - t \sum_{j=1}^{N-1} \left(c_j^\dagger c_{j+1} + c_{j+1}^\dagger c_j \right) + \sum_{j=1}^{N-1} \left(\Delta c_j c_{j+1} + \Delta^* c_{j+1}^\dagger c_j^\dagger \right), \tag{2.20}$$

where a_j and $a_j^\dagger$ are the electron annihilation and creation operators on site j (see Fig. 2.2a). In general, the electronic lattice sites on the atomic chain can be formally decomposed into two Majorana quasiparticles, denoted as the left and right Majorana quasiparticle, γ_L and γ_R:

$$c_j = \tfrac{1}{2}(\gamma_{\mathrm{L},j} + i\gamma_{\mathrm{R},j}) \tag{2.21}$$

$$c_j^\dagger = \tfrac{1}{2}(\gamma_{\mathrm{L},j} - i\gamma_{\mathrm{R},j}). \tag{2.22}$$

At first sight, this decomposition into Majorana operators may seem like a trivial exercise, since when two of these Majorana operators are coupled, they form a fermionic state at finite energy. For example, if we consider $\Delta = t = 0$ and $\mu < 0$, we can rewrite the Hamiltonian as:

$$H = -\mu \sum_{j=1}^{N} \left(c_j^\dagger c_j - \tfrac{1}{2} \right) = -\mu \sum_{j=1}^{N} \tfrac{i}{2} \left(\gamma_{\mathrm{L},j} \gamma_{\mathrm{R},j} \right). \tag{2.23}$$

In this case the two Majorana operators *on each site* are coupled to each other, forming a conventional chain of electronic states (see upper part of Fig. 2.2b). However, the situation changes if we choose the model parameters as $|\Delta| = t > 0$ and $\mu = 0$, which yields:

$$H = it \sum_{j=1}^{N-1} \gamma_{\mathrm{R},j} \gamma_{\mathrm{L},j+1}. \tag{2.24}$$

Now, the right and left Majorana operators on *adjacent* sites are coupled and we can regard each set as forming an electronic state $\tilde{c}_j = \frac{1}{2}\left(\gamma_{\mathrm{R},j} + i\gamma_{\mathrm{L},j+1}\right)$ (see lower part of Fig. 2.2b). Interestingly, careful examination of eq. 2.24 shows that two Majorana quasiparticles are missing in the Hamiltonian: $\gamma_{\mathrm{L},1}$ and $\gamma_{\mathrm{R},N}$. In other words, the first and last Majorana operators on the chain are uncoupled and since they do not appear in the Hamiltonian, they do not contribute any energy. So, together, they form a zero energy electronic mode expressed by $\tilde{c}_\mathrm{M} = \frac{1}{2}\left(\gamma_{\mathrm{L},1} + i\gamma_{\mathrm{R},N}\right)$. Due to the zero-energy property of $\tilde{c}_\mathrm{M}$, we call the Majorana quasiparticles that compose this state Majorana zero-modes (MZMs). Since the electronic state $\tilde{c}_\mathrm{M}$ can be occupied free of an energy cost, the ground state of the system is twofold degenerate, with the two ground states differing in the parity (whether an even or an odd number of electrons are present). The two ground states can be used as the basis states of a qubit with the even parity state $\tilde{c}_\mathrm{M}^\dagger \tilde{c}_\mathrm{M} |0\rangle = 0$ and the odd parity state $\tilde{c}_\mathrm{M}^\dagger \tilde{c}_\mathrm{M} |1\rangle = 1$. Since the qubit states are derived from MZMs located at the opposite ends of the chain, the states are spatially *nonlocal*, which is how a Majorana quantum bit is predicted to derive its coveted resilience to noise.

To demonstrate how MZMs appear in the Kitaev chain model, rather specific choices of parameters were used above. However, more generally, it can be shown that MZMs appear provided that $2t > |\mu|$ and $\Delta \neq 0$ (the topologically nontrivial phase), while otherwise the Majorana operators are paired on the same site (the topologically trivial phase).

The point $2t = |\mu|$ separates a topologically trivial from a topologically nontrivial phase with MZMs at its ends.

Strictly speaking, the above discussion is valid for a chain of infinite length. For a finite size chain, a correction term describing the interaction between the MZM at the ends enters the Hamiltonian:

$$\delta H = \frac{i t_{\mathrm{M}}}{2} \gamma_{\mathrm{L},1} \gamma_{\mathrm{R},N}. \tag{2.25}$$

This interaction splits the ground state degeneracy by an energy t_{M} which decays exponentially with the length of the chain. So for a sufficiently long chain, MZMs appear with an energy splitting virtually indistinguishable from zero.

2.4. MAJORANA NANOWIRES

The Kitaev chain model provides an excellent basis to understand how MZMs and their properties arise, however, the model is not very realistic experimentally. At its basis lie two important ad hoc assumptions: the occupation of a single spinless band and unconventional superconducting pairing of aligned spins (triplet p-wave superconductivity). However, real electronic systems exhibit two spin orientations, up and down, and the existence of materials that have p-wave superconducting pairing has not been established[4]. However, Lutchyn *et al.* [15] and Oreg *et al.* [16] proposed an idealized model building on a hybrid of conventional materials to induce an effectively spinless system with p-wave superconducting pairing. The proposal considers a one-dimensional semiconductor nanowire with strong spin-orbit interaction and strong spin-splitting of the semiconductor states by the Zeeman effect in a magnetic field. This nanowire is covered by a conventional s-wave superconductor, which induces superconducting correlations through the proximity effect [17]. The combination of these ingredients can lead to a system that effectively satisfies the key assumptions in the Kitaev chain model.

To understand how a spinless, p-wave superconducting state can be achieved in nanowires, we go through the ingredients of the proposal step by step. First, the system needs to be one-dimensional, which can be achieved in a nanowire of a small diameter. Due to strong lateral confinement, electron movement is restricted to only be allowed along the nanowire axis (x-direction). As as a result, the energy spectrum is split into

---

[4] Sr_2RuO_4 is a notable candidate material that may exhibit p-wave pairing [14].

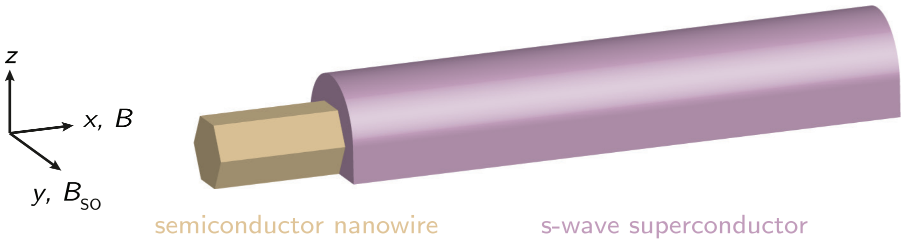

Figure 2.3: Majorana nanowire A semiconductor nanowire with strong spin-orbit coupling and a large g-factor is covered by a conventional s-wave superconductor. The choice of axes is shown on the left.

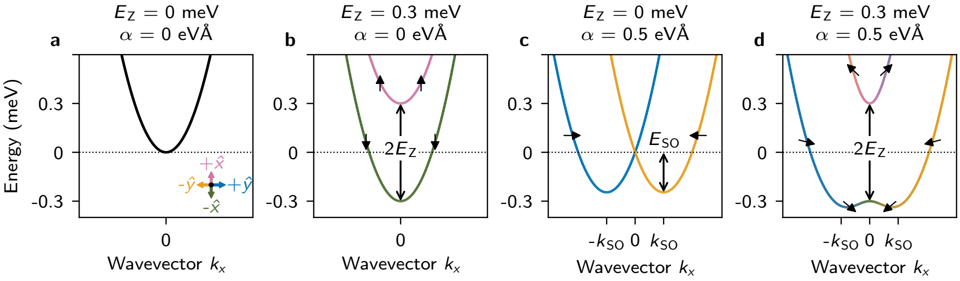

Figure 2.4: Energy spectrum of the nanowire (a) The band spectrum of a single subband nanowire has spin-degenerate bands. **(b)** Upon applying a magnetic field the two subbands are spin-split by the Zeeman field by and energy $2E_Z$. The spin-orientation of the bands is shown by the arrows and encoded in the line color (see legend in the inset of **a**). **(c)** Rashba spin-orbit interaction, in the absence of a magnetic field, splits the subbands along the wavevector axis by $\pm k_{SO}$ and down in energy by E_{SO}. Note that at each energy there are always two bands: spin-degeneracy is not lifted. **(d)** The combined effect of a magnetic field and Rashba spin-orbit interaction opens up a gap at $k_x = 0$. The expectation value of the spin polarization is tilted towards the x-axis by the magnetic field. The chemical potential μ is set to 0 in all panels. The expectation value of the spin operators $\langle\Psi|\sigma_i|\Psi\rangle$ is color coded in the lines, according to the legend in the inset of **a**, with $\pm\hat{i}$ indicating $\langle\Psi|\sigma_i|\Psi\rangle = \pm 1$.

subbands, so that at a low chemical potential only a single spin-degenerate subband is occupied. Next, to transform this system into an effectively spinless system, we need to ensure that only one of the spin bands is occupied. This means that the subbands need to be spin-split, which is exactly what the Zeeman effect due to a magnetic field achieves.[5] The effect of the Zeeman field becomes clear if we consider the band spectrum defined by the Hamiltonian of the nanowire

$$H_{\mathrm{NW}} = \left(\frac{\hbar^2 k_x^2}{2m^*} - \mu\right)\sigma_0 + \alpha_{\mathrm{R}} k_x \sigma_y + E_Z \sigma_x, \tag{2.26}$$

which describes a single one-dimensional semiconductor conduction band with an effective mass m^*, and where k_x is the wavevector along the nanowire. The second term accounts for a Rashba spin-orbit interaction with a strength α_{R}, which we will return to below. The third term expresses a Zeeman spin-splitting $E_Z = \frac{1}{2} g\mu_{\mathrm{B}} B$ of which the strength is characterized by the Landé g-factor, induced by a magnetic field B, which we assume to be orientated along the nanowire axis[6], and μ_{B} is the Bohr magneton. σ_{i} denotes the ith-Pauli matrix acting in spin space, with σ_0 equal to the two dimensional identity operator. The energy spectrum is defined by $H_{\mathrm{NW}}\Psi = E\Psi$, using the basis $\Psi = (c_\uparrow, c_\downarrow)^T$.

The effect of the Zeeman field is illustrated in Fig. 2.4a,b, where the two spin bands are shifted from each other by an energy E_Z. We see that only a single spin band is occupied whenever $|\mu| < E_Z$.

---

[5] Formally, the Kramers degeneracy theorem dictates that in the presence of time-reversal symmetric every state with a spin of $\hbar/2$ is at least twofold degenerate [18]. Since the spin degeneracy needs to be lifted, we need to break time-reversal symmetry, which is achieved by applying an external magnetic field.

[6] The magnetic does not necessarily need to be along the nanowire axis. In this model, any direction perpendicular to the spin-orbit field, i.e. any direction in the xz-plane, leads to equivalent results.

Although the Zeeman field can induce an effectively spinless state in the nanowire, this does not induce p-wave superconducting pairing. To achieve that, there needs to be pairing of electrons and holes which have both an antiparallel and a parallel component, which can be achieved by spin mixing through a Rashba spin-orbit interaction. Rashba spin-orbit interaction results from structural inversion asymmetry, i.e. asymmetry in the device geometry, which is associated with an electric field in the nanowire E [19]. Its strength $\alpha_\mathrm{R} \approx \alpha_0 \langle E\rangle$ depends on both the average electric field $\langle E\rangle$ and the material properties through the material dependent prefactor α_0. By rewriting the Rashba Hamiltonian, we can understand the effect of the Rashba spin-orbit interaction effect as a momentum dependent magnetic field pointing perpendicular to both the electron momentum and the electric field:

$$H_\mathrm{R} = \alpha_\mathrm{R} k_x \sigma_y = \frac{1}{2}\hbar\sigma\cdot B_\mathrm{SO} \tag{2.27}$$

where the spin-orbit field $B_\mathrm{SO} = \frac{2\alpha_\mathrm{R}}{\hbar} k \times \hat{E}$ points along the y-direction when E points along the z-axis, as is expected for the nanowire device geometry. In the absence of an external magnetic field, the effect of the spin-orbit interaction is to shift the two spin bands horizontally by $k_\mathrm{SO} = m^* \alpha_\mathrm{R}/\hbar^2$ and down by an energy $E_\mathrm{SO} = \hbar^2 k_\mathrm{SO}^2/2m^*$ (Fig. 2.4c). The spin orientation of each band is along $\pm\sigma_y$. When an external Zeeman field is applied, a Zeeman gap is opened up at $k = 0$, where the spin-orbit strength is zero (Fig. 2.4d). Again, the system is effectively spinless when $|\mu| < E_\mathrm{Z}$, but now the spin orientation at opposite k also has both parallel and antiparallel components (see arrows in Fig. 2.4d). The Zeeman induced gap in the spectrum at $k = 0$ in the presence of spin-orbit interaction is also often called the *helical* gap, as the electron spin is locked to its momentum.

To be able to see the effective p-wave pairing more directly, we turn to the Bogoliubov-de Gennes form of the Hamiltonian, where induced superconductivity is implemented

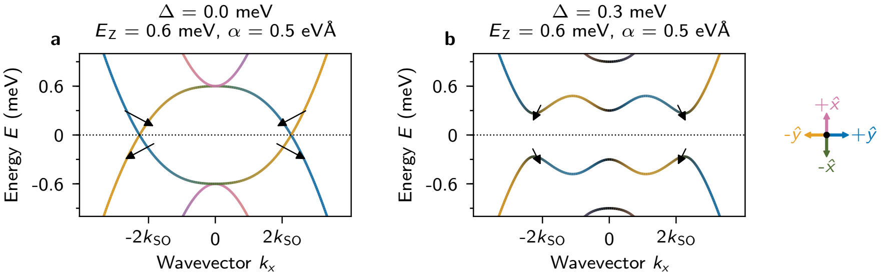

Figure 2.5: Energy spectrum of the nanowire in BdG basis (a) The band spectrum without superconductivity (Δ=0). At the crossing of the particle and hole bands the spin polarization (indicated by the black arrows) have both parallel and antiparallel components. **(b)** Upon inclusion of the superconducting pairing, the particle and holes bands are coupled, leading to an energy gap around the crossings in **a**. The chemical potential μ is set to 0 in all panels. Again, the lines are color coded to express the spin expectation value $\langle\Psi|\tau_z \otimes \sigma_i|\Psi\rangle$ according to the legend shown on the right.

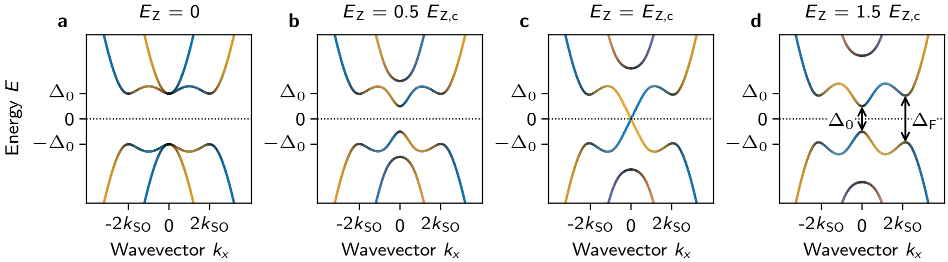

Figure 2.6: Energy spectrum of the Majorana nanowire upon increasing Zeeman energy. **(a)** At $E_Z = 0$ the spectrum is gapped for all k_x. **(b)** Increasing E_Z decreases the gap size, in particular at $k_x = 0$. **(c)** When E_Z equals the critical field of the topological phase transition, states cross at zero energy and at zero k_x. **(d)** Upon further increase of the Zeeman field the gap reopens and is inverted at $k = 0$. In all panels: $\mu = 0$, $\alpha = 0.5\,\text{eV}\text{Å}$, $\Delta = 0.3\,\text{meV}$. The line color shows the spin polarization, using the same color coding as in Fig. 2.4 and 2.5.

as an s-wave pairing gap Δ in the nanowire:

$$H_{\text{BdG}} = \left(\frac{\hbar^2 k_x^2}{2m^*} - \mu\right)(\tau_z \otimes \sigma_0) + \alpha_{\text{R}} k_x \left(\tau_z \otimes \sigma_y\right) + E_{\text{Z}}(\tau_0 \otimes \sigma_x) + \Delta(\tau_x \otimes \sigma_0), \tag{2.28}$$

with τ_{i} denoting the identity matrix and Pauli matrices acting on the particle-hole space, and using the Nambu basis $\Psi = \left(c_\uparrow, c_\downarrow, c_\downarrow^\dagger, -c_\uparrow^\dagger\right)^T$. Fig. 2.5a shows the nanowire spectrum in the helical state at finite Zeeman energy and with spin-orbit interaction in the Bogoliubov-de Gennes basis, without induced superconductivity. In this particle-hole symmetric basis, the spectrum is doubled: for every electron state, a hole state is introduced at negative energy and momentum ($E_{\text{hole}}(k) = -E_{\text{electron}}(-k)$) [20]. At the Fermi momentum (near $2k_{\text{SO}}$) the electron and hole states cross, which is where the states are coupled when superconductivity is introduced (see Fig. 2.5b). Since the spin orientation of the electron and hole states at the crossing has both antiparallel and parallel components (see the black arrows in Fig. 2.5a), a mix of s-wave and p-wave superconductivity is induced in the nanowire.[7]

Now, we arrived at a nanowire model that satisfies the key assumptions of the Kitaev chain. The final requirement needed to induce MZMs, is inversion of the bulk gap, i.e. closing and reopening of the superconducting gap at the topological phase transition. To see how the topological phase transition can be observed in the spectrum, we start with a nanowire with spin-orbit coupling and induced superconductivity at zero Zeeman field (see Fig. 2.6a). A topologically trivial superconducting gap of size Δ appears at $k_x = 0$ and $k_x = k_{\text{F}}$, the Fermi wavevector. When the Zeeman energy is increased, the gap starts to close significantly at $k_x = 0$ (Fig. 2.6b), until the spectrum becomes gapless with states crossing zero-energy (Fig. 2.6c), signifying the topological phase transition. Increasing the Zeeman energy further, the gap at $k_x = 0$ reopens and is now inverted: the bulk spectrum becomes topologically nontrivial and MZMs appear at the ends of the

---

[7] To explicitly retrieve the mixed s-wave and p-wave superconducting pairing mathematically, the s-wave pairing term in eq. 2.28 can be transformed into the helical basis, which results in two terms, one that couples opposite spins in the new basis (s-wave), and one that couples equal spin in the new basis (p-wave). See e.g. Aguado [8] for a pedagogical explanation.

nanowire. We can identify two gaps in the spectrum, Δ_0 at $k_x = 0$ and Δ_F at the Fermi wavevector. At $k_x = 0$ the Rashba spin-orbit interaction is zero (recall eq. 2.27), which implies that the spins are fully polarized along the direction of the Zeeman field. As a result the states at $k_x = 0$ linearly disperse with E_Z. For general values of μ the gap at $k_x = 0$ is:

$$\Delta_0 = \left| \sqrt{\Delta^2 + \mu^2} - E_Z \right|. \tag{2.29}$$

The critical Zeeman field for the topological phase transition is given by the field where $\Delta_0 = 0$:

$$E_{Z,c} = \sqrt{\Delta^2 + \mu^2}. \tag{2.30}$$

The gap at k_F, on the other hand, has a weak dependence on the Zeeman field, since the spin-orbit field B_{SO} tilts the spin orientation towards $\pm\hat{y}$, perpendicular to the Zeeman field, which slows down the closing of Δ_F. This spin-orbit protection of Δ_F is however lifted if the magnetic field is orientated parallel to B_{SO}, in which case the spin orientation is always along the Zeeman field and the gap closes linearly with the Zeeman field [20–22]. The superconducting gap closes at $E_{Z,y} = \Delta$ for any $\mu > -E_{SO}$ (the chemical potential at which the charge density in the nanowire is depleted at zero Zeeman field), and does not reopen at higher Zeeman energy, as illustrated in Fig. 2.7.

Up to this point we have discussed Majorana nanowires of infinite length, described by the bulk energy spectrum. To introduce the MZMs in the energy spectrum we need to include the ends of the nanowire. Fig. 2.8a shows the energy spectrum of a long nanowire of 10 µm as a function of the Zeeman energy. Indeed, now we observe the emergence of a zero-energy state after the topological phase transition stated in eq. 2.30. The wavefunctions of the two MZMs are localized at the ends of the nanowire and have an oscillating character with an exponential decay into the middle of the nanowire (see Fig. 2.8c), with a localization length $\xi = \hbar v_F / \Delta_{top}$, where Δ_{top} is the topological gap and v_F is the Fermi velocity. This spatial distribution has consequences for the properties of the MZMs as the nanowire length is decreased and the wavefunctions of the MZMs at the opposite ends start to overlap when the nanowire length becomes comparable to the MZM localization length. The wavefunction overlap corresponds to a coupling of the MZMs, which

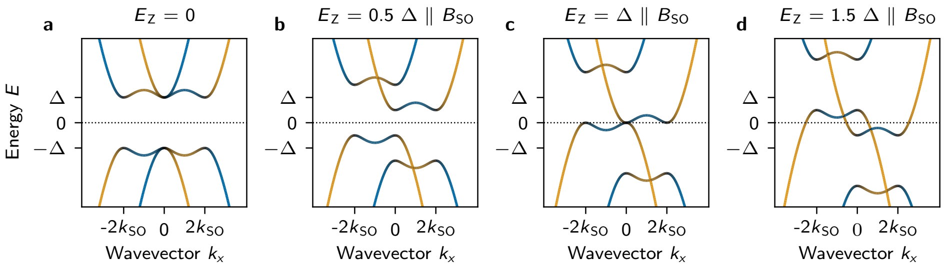

Figure 2.7: Energy spectrum of the Majorana nanowire upon increasing Zeeman energy directed along the spin-orbit field. As the Zeeman field is increased along the direction of B_{SO}, the energy bands are shifted linearly with E_Z, resulting in a tilted band structure. The gap closes when the Zeeman field along the spin-orbit direction is equal to gap, and does not reopen at higher fields. $\mu = 0$ in all panels.

induces an energy splitting ΔE away from zero energy. Due to the oscillating character of the wavefunctions, and the decrease of the topological gap with an increasing Zeeman field, the energy splitting is oscillatory, with an amplitude that increases with the Zeeman field [23], as shown in Fig. 2.8b, with the overlap of the wavefunctions illustrated in Fig. 2.8d. Also note that, for a short nanowire, the superconducting gap no longer closes completely upon the topological phase transition as a result of finite size effects [24, 25]. If instead of changing the Zeeman energy, we vary the chemical potential at constant Zeeman field, we find similar behavior: a ZBP appears at the topological phase transition and splits away as the chemical is increased beyond $\mu > \sqrt{E_Z^2 - \Delta^2}$, at which point the wire transitions into the topologically trivial phase (Fig. 2.8e). In a short nanowire, energy splitting oscillations with increasing amplitude also appear as the chemical potential is increased, which is predominantly caused by the increase in the Fermi velocity, increasing the localization length.

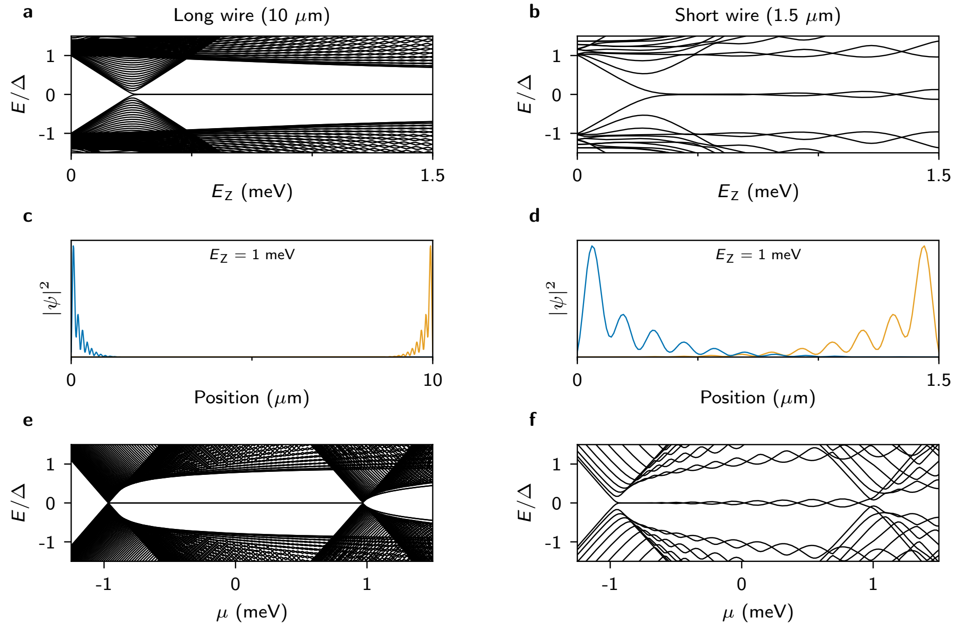

Figure 2.8: Energy spectrum as a function of Zeeman energy, chemical potential, and nanowire length (a) The spectrum of a long nanowire as a function of the Zeeman field at $\mu = 0$ shows the closing of the superconducting gap at the topological phase transition $E_{Z,c} = \sqrt{\Delta^2 + \mu^2} = 0.25\,\text{meV}$, after which the topological gap opens and a zero-energy MZM appears. **(b)** Same as **a**, but for a short nanowire. The gap no longer completely closes at the phase transition and peak splitting oscillations of the MZM appear at higher Zeeman energies. **(c)** The Majorana wavefunctions of the lowest energy mode in **a** at $E_Z = 1\,\text{meV}$ show that the MZMs appear at the two ends of the nanowire, with an exponential decaying wavefunction towards the middle of the nanowire. **(d)** In a short nanowire the wavefunctions of the MZMs at the opposite ends of the nanowire overlap, which leads to a finite energy splitting. **(e)** The energy spectrum as a function of the chemical potential in the nanowire shows a transition into and out of the topologically nontrivial phase at $\mu \approx -1\,\text{meV}$. As the chemical potential is increased beyond $\mu \approx 1\,\text{meV}$, the nanowire transitions into the topologically trivial phase, in which both spin bands are occupied. **(f)** Analogous to the Zeeman energy dependence, in a short nanowire peak splitting oscillations appear as a function of the chemical potential.

2.5. EXPERIMENTAL DETECTION OF MZMS

Tunneling spectroscopy

In this section we will discuss how MZMs can be detected by using tunneling spectroscopy. To perform tunneling spectroscopy a voltage bias V is applied over an electrostatic tunneling barrier created in between a normal metal contact and the Majorana nanowire, while measuring the resulting current I. The measured differential conductance $\mathrm{d}I/\mathrm{d}V$ is proportional to the density of states in the nanowire. In the experiment we therefore observe a peak in the differential conductance whenever the applied bias voltage equals an energy state within the spectrum. When a MZM is present at the end of the nanowire, a zero-energy state is present within the superconducting gap in the energy spectrum, which is reflected as a zero-bias peak (ZBP) in the tunneling experiment.

Quantized zero-bias peak

The zero-bias peak (ZBP) due to a MZM has a special property: the peak height is quantized at the conductance quantum $2e^2/h$ due to resonant Andreev reflection with unity probability [26–28]. Intuitively, the resonant reflection can be understood from the perspective of conventional resonant tunneling, where an incoming wave is incident on a double tunneling barrier. If the transmission through each of the two barriers is equal, the incident wave is transmitted with unity probability. Analogously, the Andreev reflection process can also be considered as transmission through a double barrier, where the incident electron and the reflected hole are transmitted through the same barrier. Because the MZM is at zero-energy, the electron and hole traverse the barrier at the same energy, providing equal transmission of the electon and hole, leading to resonant Andreev reflection.

To arrive at the same conclusion more formally, we can use the scattering matrix formalism to describe Andreev reflection. The scattering matrix r relates the electon (e) and hole (h) components of reflected wave (r) to those of an incident wave (i):

$$\begin{bmatrix} \psi_{\mathrm{e}}^{r} \\ \psi_{\mathrm{h}}^{\mathrm{r}} \end{bmatrix} = r \begin{bmatrix} \psi_{\mathrm{e}}^{i} \\ \psi_{\mathrm{h}}^{\mathrm{i}} \end{bmatrix} \quad \text{with} \quad r = \begin{bmatrix} r_{\mathrm{ee}} & r_{\mathrm{eh}} \\ r_{\mathrm{he}} & r_{\mathrm{hh}} \end{bmatrix}. \tag{2.31}$$

Each $\psi_{\mathrm{e/h}}^{i/r}$ can have N modes, counting spin and possibly subband degrees of freedom, yielding an $N \times N$ matrix for each $r_{\alpha\beta}$ block. Since the quasiparticle spectrum is gapped, an incident wave cannot be transmitted into the superconductor, so instead the wave must be either normally reflected or Andreev reflected, which requires r to be unitary. Because Andreev reflection leads to the transmission of a Cooper pair into the superconductor, it contributes a current, whereas normal reflection does not. The differential conductance is therefore only determined by Andreev reflection[8]:

$$\frac{\mathrm{d}I}{\mathrm{d}V} = \frac{2e^2}{h}\mathrm{Tr}\left(r_{\mathrm{he}}^{\dagger} r_{\mathrm{he}}\right). \tag{2.32}$$

For a single mode, as is the case for the simplest case of the spinless Majorana nanowire, $N = 1$, so $\mathrm{d}I/\mathrm{d}V = 2e^2/h \cdot r_{\mathrm{he}}^{\dagger} r_{\mathrm{he}}$. In addition, the scattering matrix should be particle-

---

[8] The factor of 2 results from the charge doubling associated with Andreev reflection resulting from the transmission of a Cooper pair of charge 2e upon incidence of an electron of charge e.

hole symmetric [28, 29], which at zero-energy imposes $r_{\mathrm{ee}} = r^*_{\mathrm{hh}}$ and $r_{\mathrm{eh}} = r^*_{\mathrm{he}}$.[9] Combined with the unitarity of the scattering matrix this gives:

$$r^*_{\mathrm{ee}} r_{\mathrm{eh}} + r^*_{\mathrm{he}} r_{\mathrm{hh}} = r_{\mathrm{ee}} r_{\mathrm{he}} + r_{\mathrm{hh}} r_{\mathrm{eh}} = 0, \tag{2.33}$$

which is satisfied by $r_{\mathrm{eh}} = r_{\mathrm{he}} = 0$ or by $r_{\mathrm{ee}} = r_{\mathrm{hh}} = 0$, giving two possible solutions for the scattering matrix and the resulting conductance [28–30]:

$$r_{\mathrm{trivial}} = \pm \begin{bmatrix} e^{i\phi} & 0 \\ 0 & e^{-i\phi} \end{bmatrix} \quad \text{or} \quad r_{\mathrm{topological}} = \pm \begin{bmatrix} 0 & e^{i\phi} \\ e^{-i\phi} & 0 \end{bmatrix} \tag{2.34}$$

$$\frac{\mathrm{d}I}{\mathrm{d}V} = 0 \ \text{(trivial)} \quad \text{or} \quad \frac{\mathrm{d}I}{\mathrm{d}V} = \frac{2e^2}{h} \ \text{(topological)} \tag{2.35}$$

In fact, the scattering matrix provides a topological quantum number $Q = \det(r) = \pm 1$ [28, 31]. For a topological superconductor, $Q = -1$, which ensures a quantized conductance at zero-bias voltage.

A very interesting property of the quantized zero-bias conductance due to MZMs is that it persists regardless of the transmission of the tunneling barrier.[10] When the tunneling barrier is replaced by a ballistic quantum point contact, which allows for the transmission of multiple modes through the nanowire junction, the zero-bias conductance is given by [29]:

$$\frac{\mathrm{d}I}{\mathrm{d}V} = \frac{2e^2}{h} \times 2n \qquad \text{if } Q = 1 \ \text{(trivial)} \tag{2.36}$$

$$\frac{\mathrm{d}I}{\mathrm{d}V} = \frac{2e^2}{h} \times (1 + 2n) \qquad \text{if } Q = -1 \ \text{(topological)} \tag{2.37}$$

where the integer n counts the number of open orbital subbands (not counting spin subbands) in the quantum point contact. In the topological phase, the zero-bias conductance is quantized at $2e^2/h$, until the second mode is opened (blue line in Fig. 2.9a). This starkly contrasts the trivial phase, where the conductance is quantized in steps of $4e^2/h$ due to Andreev enhancement (orange line in Fig. 2.9a). Although the zero-bias conductance is quantized at $2e^2/h$ in the topological phase for $n < 2$, at finite bias voltage, Andreev reflection still increases the subgap conductance above $2e^2/h$ when the transmission of the first subband approaches unity, as illustrated in Fig. 2.9b. Due to the finite bias Andreev enhancement, the quantized zero-bias *peak* develops into a quantized zero-bias conductance *dip*. The remarkable topological nature of the quantized conductance is furthermore reflected by the insensitivity of the conductance plateau to random electrostatic disorder in the nanowire. In Fig. 2.9c the disorder disturbs all trivial conductance plateaus, whereas the plateau due to MZMs remains unperturbed, due to the topological protection of the Hamiltonian to perturbations that do not close the topological gap.

---

[9] The particle-hole symmetry relation is given by $\tau_x r(-E)^* \tau_x = r(E)$, with τ_x the Pauli matrix acting in particle-hole space.

[10] The insensitivity of the ZBP height on the tunneling transmission relies on the assumption of zero temperature. We discuss the effect of a finite temperature below.

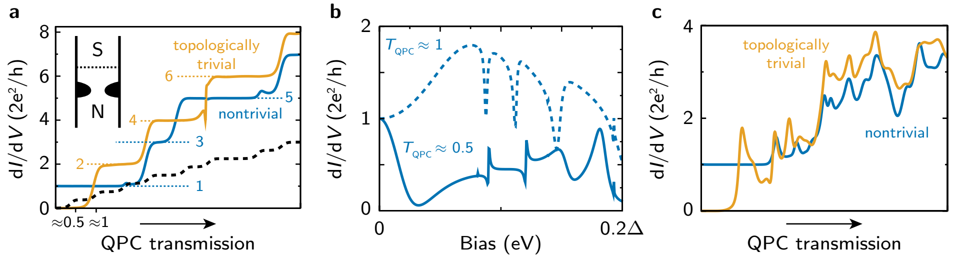

Figure 2.9: Conductance quantization in a quantum point contact to a Majorana nanowire. **(a)** The zero bias conductance through a quantum point contact for a Majorana nanowire in the topogically nontrivial state (blue) remains quantized at $2e^2/h$ until the second mode opens up. In the topologically trivial state (orange) the conductance is quantized in steps of $4e^2/h$. The black dashed line shows the conductance in the normal state, where the quantized conductance plateaus arise at e^2/h due spin splitting of the bands. The inset shows an illustrations of the system, where N (normal) indicates the part of the nanowire without superconductivity, which contains a gate-tunable restriction to adjust the transmission through the junction. S indicates the part of the nanowire where superconductivity is induced and where a MZM is formed at the end in the topological phase. **(b)** Dependence of the conductance on the bias voltage in the topological phase in the tunneling regime, with a transmission of $T \approx 0.5$, (solid line) and when the first subband is nearly completely transmitted (dashed line), so Andreev reflection enhances the finite bias conductance above $2e^2/h$, turning the zero-bias peak into a zero-bias dip. **(c)** When random potential disorder is introduced in the nanowire, the plateau due to MZMs remains well quantized, whereas all trivial plateaus are strongly disturbed. Figure adapted from Wimmer *et al.* [29].

Thermal broadening

So far we have considered the zero-bias conductance at zero-temperature, which is an ideal case in which the ZBP height due to a MZM is always exactly quantized. However, at finite temperature, thermal broadening can lower the peak height if the ZBP is narrow. The bias dependence of the ZBP at zero-temperature is given by [27]:

$$\frac{\mathrm{d}I}{\mathrm{d}V}(T=0) = g_0(V) = \frac{2e^2}{h}\frac{4\Gamma^2}{(eV)^2+4\Gamma^2}, \tag{2.38}$$

which describes a Lorentzian peak of height $2e^2/h$ with a width proportional to the tunnel coupling at the MZM to the lead Γ. The thermal broadening of the peak can be accounted for by convolution of the zero-temperature conductance with the derivative of the Fermi-Dirac distribution $f(E)$:

$$\frac{\mathrm{d}I}{\mathrm{d}V}(T) = \int_{-\infty}^{\infty} g_0(V)\left(-\frac{\partial f(E-eV)}{\partial E}\right)\mathrm{d}E. \tag{2.39}$$

The derivative of the Fermi-Dirac distribution is a peaked function with unity area and a full width at half maximum of $\sim 3.5 k_\mathrm{B} T$, with k_B the Boltzmann constant, which amounts to a broadening of $\sim 15\,\mu\mathrm{eV}$ at a temperature of $50\,\mathrm{mK}$. As a result, temperature broadening reduces the height of narrow peaks resulting from a small coupling to the lead, like is the case in the strong tunneling regime, where Γ is small.

When a single subband is occupied in the Majorana nanowire, the above gap conductance can be used as an estimate of tunnel coupling to the MZM. However, under experimental conditions, multiple subbands may be occupied in the nanowire, in which

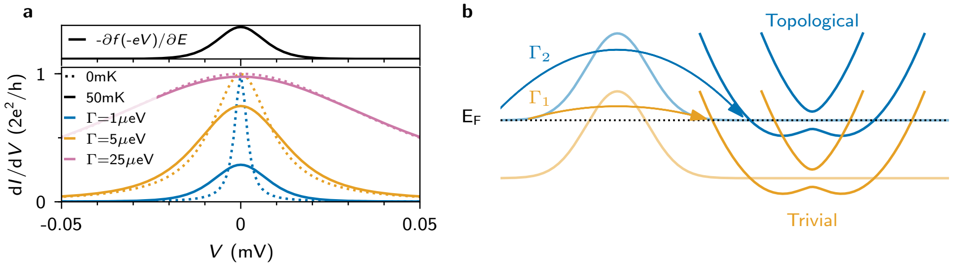

Figure 2.10: Thermal broadening of a zero-bias peak (a) Top panel: The derivative of the Fermi-Dirac distribution as a function of the bias voltage at $T = 50\,\mathrm{mK}$ and $E = 0$. Bottom panel: The bias dependence of a zero-bias peak at three different values of the tunnel broadening at zero temperature (dotted lines, from eq. 2.38) and at 50 mK (solid lines, broadened using eq. 2.39). At zero temperature the ZBP is always quantized to $2e^2/h$. At low Γ, narrow ZBPs are broadened to $\sim 3.5k_BT$, resulting in a reduced peak height. **(b)** Illustration of the tunnel coupling to a MZM when multiple orbital subbands are occupied. On the right the spectrum of two occupied subbands in the nanowire is shown (without superconductivity), with the Fermi level in the helical gap of the upper band, making the upper subband topologically nontrivial (blue lines) and the lower subband trivial (orange lines) in the presence of superconductivity. An electrostatic tunneling barrier (shown by the lighter lines) raises the upper band higher above the Fermi level than the lower band, which leads to smaller tunneling coupling to the topological band (Γ_2) than to the lower lying trivial band (Γ_1).

case the tunneling coupling to the MZM can be much lower than expected from the above-gap conductance. The situation is sketched in Fig. 2.10b, where on the right the energy spectrum is sketched for a nanowire where two orbital subbands are occupied, with the Fermi level within the helical gap of the upper subband, so that the top band will host MZMs at the ends of the nanowire. The lighter lines indicate the potential energy of each band in the presence of a tunneling barrier, indicating that the upper subband experiences a higher tunneling barrier than the lower subband, $\Gamma_1 \gg \Gamma_2$[11]. This leads to a small tunnel coupling to the MZM, and a narrow ZBP, with reduced height at finite temperature, while the above-gap conductance, which is dominated by Γ_2, remains significant. The above argument has been proposed as an explanation of a low ZBP height in spectroscopy experiments on Majorana nanowires [32–34].

Dissipation broadening

A different mechanism that leads to peak broadening and lowering of the ZBP height, is dissipation, where quasiparticle states in the nanowire can leak into the superconductor due to a finite quasiparticle density of states in the parent superconductor [35, 36]. This quasiparticle density can have various origins, such as disorder in the presence of interaction, the formation of vortices in the parent superconductor, or an inverse proximity effect when a normal lead is attached to the end of the parent superconductor [37]. These effects can be phenomenologically accounted for by introducing an imaginary term on the diagonal of the Hamiltonian [35, 36]:

$$H_{\mathrm{dissipation}} = i\Gamma\,(\tau_0 \otimes \sigma_0)\,, \tag{2.40}$$

---

[11] We assume that the tunneling barrier has a finite width and height, which is expected under realistic experimental conditions. For a sharp and high tunneling barrier, the tunneling coupling to each subband can be of comparable strength.

where Γ is the strength of the dissipation broadening. The effect of this term is to broaden and lower conductance peaks, similar to temperature broadening. In addition, dissipation broadening also induces particle-hole asymmetry in the conductance spectrum. Importantly, as dissipation results from a finite subgap quasiparticle density of states, it is closely related to the problem of a soft gap induced in the nanowire [38]. This broadening mechanism is therefore mitigated by a hard induced superconducting gap.

2.6. QUASI MAJORANA ZERO-MODES

In the previous section we discussed that the emergence of a zero-energy MZM at the end of a topological nontrivial nanowire leads to the appearance of a characteristic zero-bias peak in tunneling spectroscopy. In particular, the ZBP height is predicted to be quantized at $2e^2/h$. Unfortunately though, the observation of a ZBP is not unique to the appearance of MZMs. Notable examples include ZBPs formed due to disorder in the nanowire [39–42], or due to the Kondo effect [43], or Andreev levels [44] in a quantum dot[12] preceding the Majorana nanowire. While these scenarios are less likely to occur in the state-of-the art devices, in the presence of smooth electrostatic confinement, ZBPs can appear due to Andreev bound states in the topologically trivial phase [32, 45, 47–52]. As the tunneling experiments involve a gate-defined tunneling barrier, a smooth spatial electrostatic profile along the nanowire is likely an experimental reality. Within the smooth potential scenario, ZBPs can be remarkably stably pinned near zero-energy as a function of magnetic field, similar to the behavior expected in the topological regime. In addition, recent theoretical studies found that the ZBP height can also assume the quantized value of $2e^2/h$ over significant ranges of the tunnel coupling to the lead [49, 50]. The origin of the stability of an ABS in the topologically trivial phase and the possible zero-bias conductance quantization can be well understood by decomposing the ABS into two MZMs, which become decoupled in the presence of a smooth potential profile. We refer to these MZMs as quasi-MZMs [50].

To understand why quasi-MZMs apppear, we follow the framework introduced by Kells *et al.* [47]. We consider the Majorana nanowire Hamiltonian (eq. 2.28) in the regime where both spin bands are occupied, $\mu \gg E_Z \gg \Delta$, which is necessarily in the topologically trivial phase. As both spin bands exhibit p-wave superconductivity (see Fig. 2.11a), each band contributes a set of MZMs near the ends of the nanowire, at the point where the spin bands are depleted (classical turning point), leading to *two* quasi-MZMs at a single end of the nanowire, as indicated in Fig. 2.11b. At a sharp boundary at the end of the nanowire, these two MZMs are coupled, together forming an ABS with an energy near the superconducting gap edge.[13] However, when the electrostatic boundary at the end of the nanowire is smooth, the coupling between the MZMs becomes weak, resulting in an energy splitting which becomes essentially zero for sufficiently smooth confine-

---

[12] Here, the term quantum dot is used in the conventional sense, i.e. describing a highly confined system with a charging energy. Often in Majorana literature, the term is used in a more general sense, for example, to describe an (unconfined) section of the nanowire that is not covered by a superconductor, without charging energy physics [45, 46].

[13] The ABSs formed at the nanowire ends due to a hard wall potential boundary are sometimes referred to as intrinsic ABSs [53]. Due to their distribution near the nanowire ends, these states lead to conductance peaks that follow the gap closing as a function of magnetic field and are much more prominent than the other states at the gap edge, which are bulk states distributed throughout the nanowire.

ment. To understand why this is the case, we first notice that since the two quasi-MZMs at a single end stem from bands with opposite spin, the quasi-MZMs themselves have opposite spin orientation (see Fig. 2.11d). On the other hand, MZMs at opposite ends of the nanowire in the topological phase originate from the same spin band and have equal spin orientation (see Fig. 2.11e). The coupling of the quasi-MZMs therefore requires effects that couple opposite spins, which is achieved by the spin-orbit interaction term $\alpha_{\mathrm{R}} k_x$ and the remaining s-wave superconducting coupling. For a sharp, hard wall potential barrier at the end, the momentum k_x stays finite up to the classical turning point, resulting in a finite spin-orbit interaction of the MZMs and a significant associated energy splitting. For a smooth potential barrier, on the other hand, the momentum smoothly goes to zero at the classical turning point, leading to a negligible spin-orbit in-

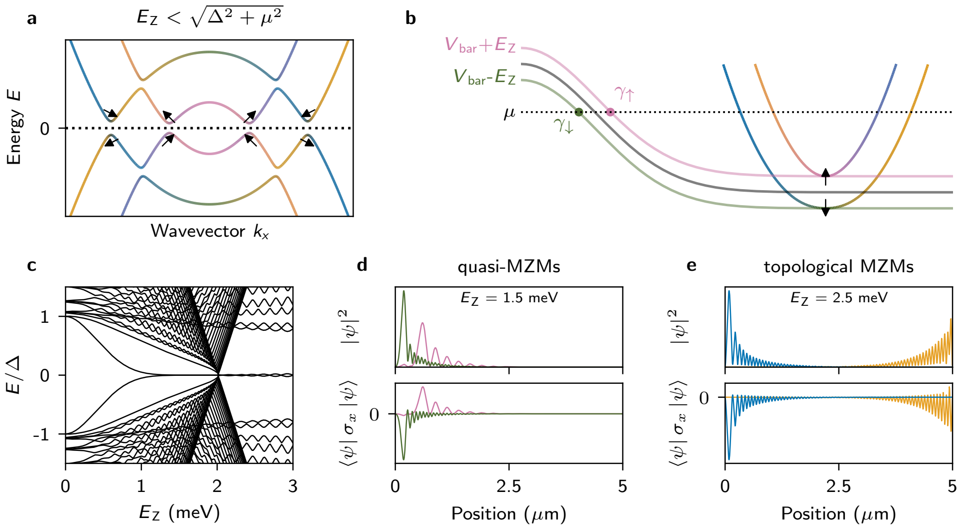

Figure 2.11: Quasi-MZMs (a) In the BdG band spectrum for $\mu > E_Z$, within the topologically trivial phase, we see that both spin bands cross zero-energy at finite momentum, resulting in p-wave superconducting components in both spin bands (compare with Fig. 2.5 in the topological phase, where only one spin band is occupied). **(b)** Quasi-MZMs appear in the presence of a smooth potential at the nanowire ends. The potential as a function of the position from the end of the wire is indicated by the black line and shifted by $\pm E_Z$, as shown in green and pink. On the right side the band spectrum is sketched for the scenario $\mu \gg E_Z \gg \Delta$ (for the purpose of illustration without superconductivity). Two classical turning points, one for each spin band, form within the smooth potential (where $\mu \pm E_Z = V_{\mathrm{bar}}(x)$, i.e. the band is depleted). At these points, two quasi-MZMs of opposite spin are formed, stemming from the two p-wave spin bands within the bulk of the wire. **(c)** In the energy spectrum as a function of the Zeeman field in the presence of a smooth potential of the type shown in **b**, the conventional topological phase transition coinciding with the closing of the gap and the emergence of a zero-energy MZM occurs at $E_Z \gtrsim 2\,\mathrm{meV}$. Before this transition, in the topologically trivial phase, there is an additional zero-energy state, due to the quasi-MZMs induced by the smooth potential barrier. **(d,e)** The wavefunctions (top) and spin-density projected along the nanowire axis (bottom) of the lowest energy mode, decomposed into its Majorana components, at $E_Z = 1.5\,\mathrm{meV}$ (trivial, **d**) and $E_Z = 2.5\,\mathrm{meV}$ (topological, **e**). The two quasi-MZMs are both located near the same end of the nanowire, whereas the topological MZMs are located at the opposite ends of the wire. The spindensity of each of the quasi-MZMs is opposite, whereas the spindensity of both the topological MZMs is negative. The spectrum shown in **c** is obtained for $\mu = 2\,\mathrm{meV}$, $\alpha = 0.5\,\mathrm{eV\AA}$, $m^* = 0.015 m_e$ and $V_{\mathrm{bar}} = V_0 \exp\left(-x^2/2\sigma^2\right)$ with $V_0 = 4\,\mathrm{meV}$ and $\sigma = 250\,\mathrm{nm}$, in a wire of $5\,\mu\mathrm{m}$.

teraction in the region where the two MZMs are located, with a (nearly) zero-energy ABS as a result, as illustrated in Fig. 2.11c. The zero-energy stability of quasi-MZMs has an opposite dependence on the size of the superconducting gap and the spin-orbit strength compared to topological MZMs. The energy splitting of topological MZMs is reduced for a large topological gap, which relies on a sizable bulk superconducting gap and spin-orbit strength, whereas the energy splitting of quasi-MZMs is reduced at smaller superconducting gaps and spin-orbit strength, as those are the two effects that are responsible for the coupling of the opposite spin quasi-MZMs [54].

As the two spin bands are split by the Zeeman energy, the classical turning points of the two bands will typically occur at a different position along the smooth potential (see Fig. 2.11b).[14] The two quasi-MZMs will therefore be separated by a distance determined by the smoothness of the barrier and the applied Zeeman field, as illustrated in Fig. 2.11d. For potential profiles in which this spatial separation between quasi-MZMs is quite prominent, the quasi-MZMs are sometimes also referred to as partially separated Andreev bound states in literature [48, 49]. Note, however, that the lack of coupling between the quasi-MZMs predominantly stems from the opposite spin character, combined with the smoothness of the barrier, instead of from the spatial separation of the quasi-MZMs [54]. The spatial separation can, however, play a role in the transport characteristics of quasi-MZMs, as we will discuss below.

As we saw that quasi-MZMs can produce a zero-energy state very similar to the one expected for MZMs in the topologically nontrivial phase, it is natural to wonder if the transport characteristic in a tunneling spectroscopy experiment are also similar, and in particular if a quantized conductance peak is also expected for quasi-MZMs. To find a general expression for the conductance due to quasi-MZMs, we consider a state described by two wavefunctions ψ_1 and ψ_2 in the Majorana basis, which exhibit a coupling described by the energy splitting E_M, described by the Hamiltonian:

$$H_\mathrm{M} = \begin{bmatrix} 0 & iE_\mathrm{M} \\ -iE_\mathrm{M} & 0 \end{bmatrix} \tag{2.41}$$

Using the Mahaux-Weidenmüller formula for the scattering matrix in terms of H_M, the conductance due to Andreev processes can be expressed as [50, 55]:

$$G(E) = \frac{2e^2}{h} \mathrm{Tr}\left(S_\mathrm{eh}^\dagger S_\mathrm{eh}\right) \tag{2.42}$$

$$S_\mathrm{eh} = \frac{1}{Z} \begin{bmatrix} i\Gamma_1 (E + i\Gamma_2) & -E_\mathrm{M}\sqrt{\Gamma_1\Gamma_2} \\ E_\mathrm{M}\sqrt{\Gamma_1\Gamma_2} & i\Gamma_2 (E + i\Gamma_1) \end{bmatrix} \tag{2.43}$$

$$Z = \left(E_\mathrm{M}^2 - (E + i\Gamma_1)(E + i\Gamma_2)\right) \tag{2.44}$$

where Γ_1 and Γ_2 are the coupling energies of each quasi-MZM to the lead. More intuition can be gained by approximating eqs. (2.42) to (2.44) in the limit $\Gamma_1 \gg E_\mathrm{M}, \Gamma_2, E$ as [50]:

$$G(E) \approx \frac{2e^2}{h} \left(\frac{\Gamma_1^2}{\Gamma_1^2 + E^2} + \frac{\Gamma_2^2 - 2E_\mathrm{M}^2\Gamma_2/\Gamma_1}{\Gamma_2^2 + 2E_\mathrm{M}^2\Gamma_2/\Gamma_1 + E^2} \right). \tag{2.45}$$

---

[14] Note that in the limit of very high chemical potential the two classical turning points are nearly overlapping, leading to highly overlapping quasi-MZMs, which can nevertheless still result in a near zero-energy state [47, 50].

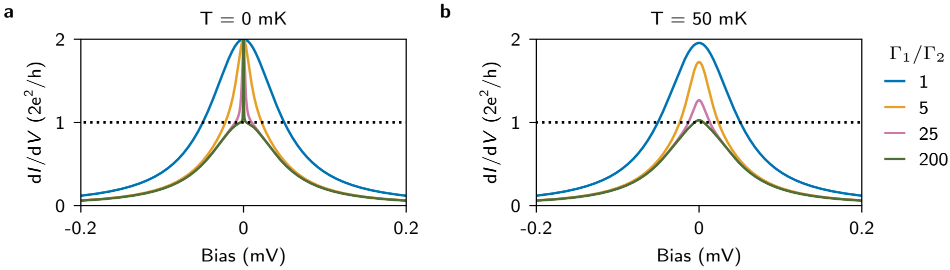

Figure 2.12: ZBPs due to quasi-MZMs (a) The conductance due to quasi-MZMs as a function of bias voltage obtained from eqs. (2.42) to (2.44) for varying tunnel coupling to the second quasi-MZM Γ_2 at zero temperature. At low Γ_2 we find a ZBP quantized at $2e^2/h$ due to tunneling to the first quasi-MZM, superimposed with a very sharp additional peak with raises the conductance to $4e^2/h$. Upon increase of Γ_2 the peak associated with tunneling to the second quasi-MZM broadens. **(b)** At a finite temperature of 50 mK the narrow conductance peaks are broadened and are no longer visible, leading to a quantized ZBP for $\Gamma_2 \ll 3.5k_BT \ll \Gamma_1$. The curves are obtained by convolution of the zero-temperature with the derivative of the Fermi-Dirac distribution, eq. 2.39. In both panels, $E_M = 0$ and $\Gamma_1 = 50\,\mu\text{eV}$.

The conductance peak can therefore be described by two (semi-)Lorentzians. The first term describes the conductance due to the first quasi-MZM (note that this term is equal to the conductance expected of a MZM at the end of a topological nontrivial superconductor, eq. 2.38). The second term expresses the conduction due to tunneling to the second quasi-MZM, which contributes a zero-bias conductance of $\pm 2e^2/h$, with a peak width proportional to Γ_2 (see Fig. 2.12a). When the coupling to the second quasi-MZM is smaller than the temperature broadening, this second peak will no longer be noticeable in a transport experiment, and a ZBP of height $2e^2/h$ is recovered (see Fig. 2.12b). This strong suppression of Γ_2, with the associated appearance of a quantized zero-bias conductance, has been theoretically predicted to be caused by the spin-splitting of the tunneling barrier due to the Zeeman effect, which results in different effective tunnel barrier heights for the two quasi-MZMs of opposite spin [50] (notice the different tunnel barrier heights for the two spin orientations in Fig. 2.11b, analogous to the argument illustrated in Fig. 2.10b). In addition, coupling to the second MZM may be suppressed due to its spatial separation away from the barrier [49]. An interesting difference with the quantized ZBP due to well separated MZMs at the ends of a topological phase, is that for quasi-MZMs, upon lowering the tunneling barrier height, the coupling to the second quasi-MZM should eventually exceed the thermal broadening, which will result in an increase of the zero-bias conductance to $4e^2/h$ (see Fig. 2.12b).

So far, we have discussed the case of a particularly smooth potential, which is paradigmatic for the formation of highly stable ZBPs and quantized zero-bias peaks in the topologically trivial phase. In the case of sharper potential profiles, or more complicated profiles, which for example include a potential dip after the peak [45], the difference in the coupling of the two quasi-MZMs to the lead may be less drastic, leading to $\Gamma_1 \approx \Gamma_2$. If the state is nevertheless close to zero-energy, $E_M \ll \Gamma_2$, we retrieve the conductance of a zero-energy *trivial Andreev bound state*:

$$G(E) \approx \frac{4e^2}{h} \frac{\Gamma^2}{\Gamma^2 + E^2} \tag{2.46}$$

with $\Gamma = \Gamma_1 \approx \Gamma_2$. For these trivial Andreev bound states a peak height in between 0 and $4e^2/h$ is expected at finite temperature [45], depending on the tunnel broadening Γ compared to the thermal broadening $3.5k_\mathrm{B}T$. Note, however, that there is no strict boundary between trivial ABSs and quasi-MZMs: as the smoothness of the barrier increases, trivial ABSs transition into quasi-MZMs. Similarly, as the ratio Γ_2/Γ_1 decreases, there is a smooth transition from a $4e^2/h$ peak height to a peak height quantized at $2e^2/h$.

REFERENCES

[1] H. Kamerlingh Onnes, *Investigations into the properties of substances at low temperatures, which have led, amongst other things, to the preparation of liquid helium,* Nobel lecture **4** (1913).

[2] W. Meissner and R. Ochsenfeld, *Ein neuer Effekt bei Eintritt der Supraleitfähigkeit,* Naturwissenschaften **21**, 787 (1933).

[3] J. Bardeen, L. N. Cooper, and J. R. Schrieffer, *Theory of superconductivity,* Phys. Rev. **108**, 1175 (1957).

[4] M. Tinkham, *Introduction to Superconductivity* (Dover Publications, 2004).

[5] N. N. Bogoliubov, *On a new method in the theory of superconductivity,* Nuovo Cimento **7**, 794 (1958).

[6] J. G. Valatin, *Comments on the theory of superconductivity,* Nuovo Cimento **7**, 843 (1958).

[7] P. De Gennes, *Superconductivity Of Metals And Alloys* (Boca Raton: CRC Press, 1999).

[8] R. Aguado, *Majorana quasiparticles in condensed matter,* Riv. Nuovo Cimento **40**, 523 (2017).

[9] A. Andreev, *The thermal conductivity of the intermediate state in superconductors,* Sov. Phys. JETP **19**, 1228 (1964).

[10] G. E. Blonder, M. Tinkham, and T. M. Klapwijk, *Transition from metallic to tunneling regimes in superconducting microconstrictions: Excess current, charge imbalance, and supercurrent conversion,* Phys. Rev. B **25**, 4515 (1982).

[11] C.-X. Liu, F. Setiawan, J. D. Sau, and S. Das Sarma, *Phenomenology of the soft gap, zero-bias peak, and zero-mode splitting in ideal Majorana nanowires,* Phys. Rev. B **96**, 054520 (2017).

[12] C. W. J. Beenakker, *Quantum transport in semiconductor-superconductor microjunctions,* Phys. Rev. B **46**, 12841 (1992).

[13] A. Y. Kitaev, *Unpaired Majorana fermions in quantum wires,* Phys. Usp. **44**, 131 (2001).

[14] A. P. Mackenzie and Y. Maeno, *The superconductivity of* Sr_2RuO_4 *and the physics of spin-triplet pairing,* Rev. Mod. Phys. **75**, 657 (2003).

[15] R. M. Lutchyn, J. D. Sau, and S. Das Sarma, *Majorana fermions and a topological phase transition in semiconductor-superconductor heterostructures,* Phys. Rev. Lett. **105**, 077001 (2010).

[16] Y. Oreg, G. Refael, and F. von Oppen, *Helical liquids and Majorana bound states in quantum wires,* Phys. Rev. Lett. **105**, 177002 (2010).

[17] T. M. Klapwijk, *Proximity effect from an Andreev perspective,* J. Supercond. **17**, 593 (2004).

[18] H. A. Kramers, *Théorie générale de la rotation paramagnétique dans les cristaux,* Proc. Acad. Amst **33**, 959 (1930).

[19] R. Winkler, S. J. Papadakis, E. P. De Poortere, and M. Shayegan, *Spin-orbit coupling effects in two-dimensional electron and hole systems*, Vol. 41 (Springer, 2003).

[20] B. Nijholt and A. R. Akhmerov, *Orbital effect of magnetic field on the Majorana phase diagram,* Phys. Rev. B **93**, 235434 (2016).

[21] J. Osca, D. Ruiz, and L. Serra, *Effects of tilting the magnetic field in one-dimensional Majorana nanowires,* Phys. Rev. B **89**, 245405 (2014).

[22] S. Rex and A. Sudbø, *Tilting of the magnetic field in Majorana nanowires: Critical angle and zero-energy differential conductance,* Phys. Rev. B **90**, 115429 (2014).

[23] S. Das Sarma, J. D. Sau, and T. D. Stanescu, *Splitting of the zero-bias conductance peak as smoking gun evidence for the existence of the Majorana mode in a superconductor-semiconductor nanowire,* Phys. Rev. B **86**, 220506 (2012).

[24] T. D. Stanescu, S. Tewari, J. D. Sau, and S. Das Sarma, *To close or not to close: The fate of the superconducting gap across the topological quantum phase transition in Majorana-carrying semiconductor nanowires,* Phys. Rev. Lett. **109**, 266402 (2012).

[25] R. V. Mishmash, D. Aasen, A. P. Higginbotham, and J. Alicea, *Approaching a topological phase transition in Majorana nanowires,* Phys. Rev. B **93**, 245404 (2016).

[26] K. T. Law, P. A. Lee, and T. K. Ng, *Majorana fermion induced resonant Andreev reflection,* Phys. Rev. Lett. **103**, 237001 (2009).

[27] K. Flensberg, *Tunneling characteristics of a chain of Majorana bound states,* Phys. Rev. B **82**, 180516 (2010).

[28] C. W. J. Beenakker, J. P. Dahlhaus, M. Wimmer, and A. R. Akhmerov, *Random-matrix theory of Andreev reflection from a topological superconductor,* Phys. Rev. B **83**, 085413 (2011).

[29] M. Wimmer, A. R. Akhmerov, J. P. Dahlhaus, and C. W. J. Beenakker, *Quantum point contact as a probe of a topological superconductor,* New J. of Phys. **13**, 053016 (2011).

[30] B. Béri, *Dephasing-enabled triplet Andreev conductance,* Phys. Rev. B **79**, 245315 (2009).

[31] A. R. Akhmerov, J. P. Dahlhaus, F. Hassler, M. Wimmer, and C. W. J. Beenakker, *Quantized conductance at the Majorana phase transition in a disordered superconducting wire,* Phys. Rev. Lett. **106**, 057001 (2011).

[32] E. Prada, P. San-Jose, and R. Aguado, *Transport spectroscopy of NS nanowire junctions with Majorana fermions,* Phys. Rev. B **86**, 180503 (2012).

[33] F. Pientka, G. Kells, A. Romito, P. W. Brouwer, and F. von Oppen, *Enhanced zero-bias Majorana peak in the differential tunneling conductance of disordered multisubband quantum-wire/superconductor junctions,* Phys. Rev. Lett. **109**, 227006 (2012).

[34] D. Rainis, L. Trifunovic, J. Klinovaja, and D. Loss, *Towards a realistic transport modeling in a superconducting nanowire with Majorana fermions,* Phys. Rev. B **87**, 024515 (2013).

[35] S. Das Sarma, A. Nag, and J. D. Sau, *How to infer non-Abelian statistics and topological visibility from tunneling conductance properties of realistic Majorana nanowires,* Phys. Rev. B **94**, 035143 (2016).

[36] C.-X. Liu, J. D. Sau, and S. Das Sarma, *Role of dissipation in realistic Majorana nanowires,* Phys. Rev. B **95**, 054502 (2017).

[37] J. Danon, E. B. Hansen, and K. Flensberg, *Conductance spectroscopy on Majorana wires and the inverse proximity effect,* Phys. Rev. B **96**, 125420 (2017).

[38] S. Takei, B. M. Fregoso, H.-Y. Hui, A. M. Lobos, and S. Das Sarma, *Soft superconducting gap in semiconductor Majorana nanowires,* Phys. Rev. Lett. **110**, 186803 (2013).

[39] D. Bagrets and A. Altland, *Class D spectral peak in Majorana quantum wires,* Phys. Rev. Lett. **109**, 227005 (2012).

[40] D. I. Pikulin, J. P. Dahlhaus, M. Wimmer, H. Schomerus, and C. W. J. Beenakker, *A zero-voltage conductance peak from weak antilocalization in a Majorana nanowire,* New J. of Phys. **14**, 125011 (2012).

[41] J. Liu, A. C. Potter, K. T. Law, and P. A. Lee, *Zero-bias peaks in the tunneling conductance of spin-orbit-coupled superconducting wires with and without Majorana end-states,* Phys. Rev. Lett. **109**, 267002 (2012).

[42] D. E. Liu, E. Rossi, and R. M. Lutchyn, *Impurity-induced states in superconducting heterostructures,* Phys. Rev. B **97**, 161408 (2018).

[43] E. J. H. Lee, X. Jiang, R. Aguado, G. Katsaros, C. M. Lieber, and S. De Franceschi, *Zero-bias anomaly in a nanowire quantum dot coupled to superconductors,* Phys. Rev. Lett. **109**, 186802 (2012).

[44] E. J. Lee, X. Jiang, M. Houzet, R. Aguado, C. M. Lieber, and S. De Franceschi, *Spin-resolved Andreev levels and parity crossings in hybrid superconductor–semiconductor nanostructures,* Nat. Nanotech. **9**, 79 (2014).

[45] C.-X. Liu, J. D. Sau, T. D. Stanescu, and S. Das Sarma, *Andreev bound states versus Majorana bound states in quantum dot-nanowire-superconductor hybrid structures: Trivial versus topological zero-bias conductance peaks,* Phys. Rev. B **96**, 075161 (2017).

[46] C. Reeg, O. Dmytruk, D. Chevallier, D. Loss, and J. Klinovaja, *Zero-energy Andreev bound states from quantum dots in proximitized Rashba nanowires,* Phys. Rev. B **98**, 245407 (2018).

[47] G. Kells, D. Meidan, and P. W. Brouwer, *Near-zero-energy end states in topologically trivial spin-orbit coupled superconducting nanowires with a smooth confinement,* Phys. Rev. B **86**, 100503 (2012).

[48] C. Moore, T. D. Stanescu, and S. Tewari, *Two-terminal charge tunneling: Disentangling Majorana zero modes from partially separated Andreev bound states in semiconductor-superconductor heterostructures,* Phys. Rev. B **97**, 165302 (2018).

[49] C. Moore, C. Zeng, T. D. Stanescu, and S. Tewari, *Quantized zero-bias conductance plateau in semiconductor-superconductor heterostructures without topological Majorana zero modes,* Phys. Rev. B **98**, 155314 (2018).

[50] A. Vuik, B. Nijholt, A. R. Akhmerov, and M. Wimmer, *Reproducing topological properties with quasi-Majorana states,* SciPost Phys. **7**, 061 (2019).

[51] B. D. Woods, J. Chen, S. M. Frolov, and T. D. Stanescu, *Zero-energy pinning of topologically trivial bound states in multiband semiconductor-superconductor nanowires,* Phys. Rev. B **100**, 125407 (2019).

[52] T. D. Stanescu and S. Tewari, *Robust low-energy Andreev bound states in semiconductor-superconductor structures: Importance of partial separation of component Majorana bound states,* Phys. Rev. B **100**, 155429 (2019).

[53] Y. Huang, H. Pan, C.-X. Liu, J. D. Sau, T. D. Stanescu, and S. Das Sarma, *Metamorphosis of Andreev bound states into Majorana bound states in pristine nanowires,* Phys. Rev. B **98**, 144511 (2018).

[54] M. W. A. de Moor, *Quantum transport in nanowire networks,* Ph.D. thesis, Delft University of Technology (2019), chapter 8: Bound states in 1D Majorana nanowires.

[55] J. Nilsson, A. R. Akhmerov, and C. W. J. Beenakker, *Splitting of a Cooper pair by a pair of Majorana bound states,* Phys. Rev. Lett. **101**, 120403 (2008).

3

BALLISTIC MAJORANA NANOWIRE DEVICES

Önder Gül*, Hao Zhang*, Jouri D.S. Bommer*, Michiel W.A. de Moor, Diana Car, Sébastien R. Plissard, Erik P.A.M. Bakkers, Attila Geresdi, KenjiWatanabe, Takashi Taniguchi, Leo P. Kouwenhoven

Majorana modes are zero-energy excitations of a topological superconductor that exhibit non-Abelian statistics [1–3]. Following proposals for their detection in a semiconductor nanowire coupled to an s-wave superconductor [4, 5], several tunneling experiments reported characteristic Majorana signatures [6–11]. Reducing disorder has been a prime challenge for these experiments because disorder can mimic the zero-energy signatures of Majoranas [12–16], and renders the topological properties inaccessible [17–20]. Here, we show characteristic Majorana signatures in InSb nanowire devices exhibiting clear ballistic transport properties. Application of a magnetic field and spatial control of carrier density using local gates generates a zero-bias peak that is rigid over a large region in the parameter space of chemical potential, Zeeman energy, and tunnel barrier potential. The reduction of disorder allows us to resolve separate regions in the parameter space with and without a zero-bias peak, indicating topologically distinct phases. These observations are consistent with the Majorana theory in a ballistic system [21], and exclude for the first time the known alternative explanations that invoke disorder [12–16] or a nonuniform chemical potential [22, 23] in the tunneling region of the nanowire.

This chapter has been published in Nature Nanotechnology **13**, 192-197 (2018). Minor corrections have been made in the preparation of this chapter.

*These authors contributed equally to this work.

3.1. INTRODUCTION

Semiconductor nanowires are the primary contender for realizing a topological quantum bit (qubit) based on Majorana modes. Their confined geometry together with the highly tunable electronic properties readily allow for localizing Majoranas, engineering the coupling between Majoranas, and finally controlling the coupling between the topological superconductor and the external circuity. These requirements for the implementation of a Majorana qubit are challenging to achieve in other Majorana systems such as 2D and 3D topological insulators. Moreover, various basic networks [24] and high-quality interfaces to different superconductors [18–20] have already been realized in semiconductor nanowires, fulfilling the further requirements for Majorana qubits. However, despite these advances in materials, alternative explanations have been proposed for the characteristic Majorana signatures. Most alternative explanations invoke bulk or interface disorder [12–16] or a nonuniform chemical potential along the wire [22, 23]. Notable examples are weak antilocalization [14], Kondo effect [15], and Andreev levels [16, 22], all shown to result in transport signatures mimicking those attributed to Majoranas. Here, we show characteristic Majorana signatures in nanowire devices that exhibit ballistic transport, ruling out known disorder- or nonuniformity-based explanations involving the tunneling region of the nanowire for the first time.

3.2. EXPERIMENTAL SETUP

Figure 3.1a shows the measured device consisting of an InSb nanowire (green) contacted with a grounded NbTiN superconductor (purple), and normal metal leads (yellow). The local bottom gate electrodes are separated from the nanowire by a boron nitride flake and are operated individually to allow for spatial control of the carrier density in the nanowire. We have realized our devices following our recently developed nanofabrication recipe which results in a high-quality InSb–NbTiN interface, an induced hard superconducting gap, and ballistic transport in the proximitized nanowire (see Ref. [19] and [20]). All measurements are performed in a dilution refrigerator with an electron temperature of $\sim 50\,\mathrm{mK}$. The data is taken by applying a bias voltage V between the normal metal lead and the superconductor indicated by N and S, respectively, and monitoring the current flow. The other normal lead is kept floating.

3.3. BALLISTIC SUPERCONDUCTING QUANTUM POINT CONTACT

Figure 3.1b shows the differential conductance $\mathrm{d}I/\mathrm{d}V$ while varying V, and stepping the voltage applied to the barrier gate. Importantly, we find no signs of formation of quantum dots or any other localization effects. Vertical line cuts at the gate voltages indicated with colored bars are shown in Figure 3.1c. Figure 3.1c (bottom) is from the tunneling regime of the device where a sufficiently negative voltage on barrier gate locally depletes the noncovered nanowire section, and creates a tunnel barrier between the normal lead and the superconductor. In this regime we find an induced superconducting gap with a strong conductance suppression for subgap bias. The extracted gap value is $\Delta^* = 0.65\,\mathrm{meV}$. Increasing the voltage on barrier gate first lowers the tunnel barrier and then removes it completely. Figure 3.1c (top) is from the regime in which the noncovered nanowire section admits a single fully-transmitting transport channel. In this regime the subgap conductance is strongly enhanced due to Andreev reflection compared to the large-bias (above-gap) conductance of $2e^2/h$, the conductance quantum, with e the elementary charge and h the Planck constant. The extracted enhancement factor > 1.5 implies a contact interface transparency > 0.93 [20]. Figure 3.1d shows the horizontal line cuts from Figure 3.1b at the bias voltages indicated with colored bars. For a bias $V > \Delta^*$ we find a quantized conductance plateau at $2e^2/h$, a clear signature of a ballistic device. For zero bias voltage the strong Andreev enhancement is evident in the plateau

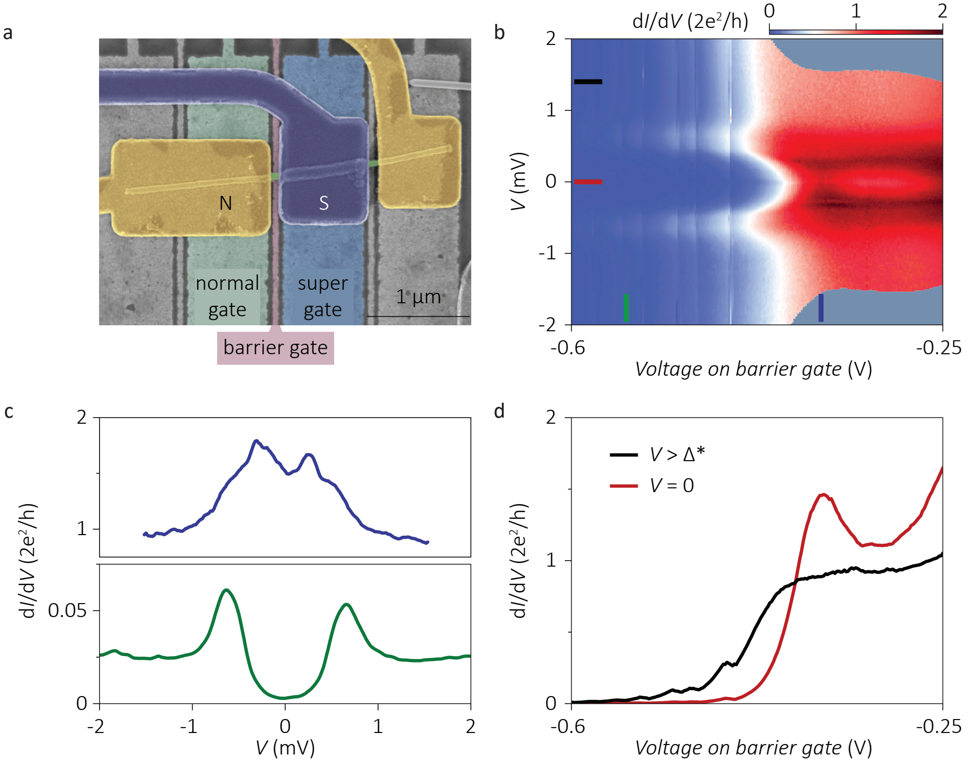

Figure 3.1: Hybrid device and ballistic transport properties. **(a)** False-color electron micrograph of the measured device. The InSb nanowire (green) is contacted by a grounded NbTiN superconductor (purple) and two Au normal metal leads (yellow). The nanowire has a diameter of ~ 80 nm. The local bottom gates (normal, barrier, and super gate) are separated from the nanowire by a boron nitride flake (~ 30 nm) and are operated individually. Two-terminal measurements are performed between N and S, while the other normal lead is floating. **(b)** Differential conductance dI/dV as a function of bias voltage V, and voltage on barrier gate (the other gate electrodes are grounded). Vertical lines at certain gate voltages are due to slow fluctuations in the electrostatic environment. **(c)** Vertical line cuts from **b** at the gate voltages marked with colored bars. Top panel shows the dI/dV from the transport regime in which the current is carried by a single fully-transmitting channel. We find an enhancement of conductance at small bias by more than a factor of 1.5 compared to the large-bias conductance of $2e^2/h$. Bottom panel is from the tunneling regime in which the current is carried by a single channel with low transmission. We extract an induced superconducting gap $\Delta^* = 0.65$ meV. **(d)** Horizontal line cuts from **b** at the bias voltages marked with colored bars. Subgap conductance ($V = 0$) shows an enhancement reaching $1.5 \times 2e^2/h$ when the large-bias conductance ($V = 1.4\,\mathrm{mV} > \Delta^*$) has a quantized value of $2e^2/h$.

region followed by a dip in conductance due to channel mixing [20]. From the absence of quantum dots, the observed induced gap with a strongly reduced subgap density of states, high interface transparency, and quantized conductance, we conclude a very low disorder strength for our device, consistent with our recent findings [20].

3.4. ZERO-BIAS PEAKS AS MAJORANA SIGNATURES

We now turn to the tunneling regime of the device where Majorana modes are characterized by a zero-bias peak. To drive the nanowire device into the topological phase, we apply a magnetic field B along the wire axis and tune the voltage applied to the super gate ($V_{\mathrm{s-gate}}$) which controls μ, the chemical potential in the nanowire section underneath the superconductor. Figure 3.2a shows that an increasing B closes the induced gap at 0.55 T and generates a zero-bias peak rigidly bound to $V = 0$ up to 1.2 T (line cuts in Fig. 3.S1a). The gap closure is expected to occur for a Zeeman energy $E_z \gtrsim \Delta^*$. From linear interpolation we find $g \gtrsim 40$ which matches our independent measurements [25, 26]. Converting the B axis into a Zeeman energy E_z scale (right vertical axis), we find that the zero-bias peak is bound to zero over 0.75 meV, a range in Zeeman energy that is 30 times larger than the peak width (the full width at half maximum, FWHM ~ 20μeV, see Fig. 3.S1c and Fig. 3.S4). This excludes a level crossing as the origin for our zero-bias peak [15]. We note that all our devices show a significant increase of subgap density of states for the magnetic fields required for topological phase transition. This behavior is likely due to vortex formation or a short mean free path [27, 28] in our NbTiN film. The formation of vortices is speculated to create a dissipation channel [21], the leading hypothetical mechanism that limits our zero-bias peak height from reaching the quantized value of $2e^2/h$.

The origin of zero-bias peak can be spatially resolved by varying the voltages applied to individual gates. Figure 3.2b shows that the presence of the zero-bias peak is not affected when gating the wire section underneath the normal contact which changes the conductance by more than a factor of 5 (see also Fig. 3.S1d). Extending the same analysis to the noncovered wire section yields the same result (Figure 3.2c), i.e., changing the tunnel barrier conductance by nearly an order of magnitude does not split the zero-bias peak, nor makes it disappear (see also Fig. 3.S1e). In contrast, Figure 3.2d shows that the zero-bias peak is present over a finite range in voltage applied to the super gate (line cuts in Fig. 3.S1f). This indicates that proper tuning of μ is essential for the appearance of the zero-bias peak. The observation of a zero-bias peak that does not split when changing the tunnel barrier conductance (Figure 3.2c) excludes Kondo effect [15] and crossing of Andreev levels [16] as the origin of our zero-bias peak. Most importantly, it rules out an explanation provided by recent theory work [22] demonstrating trivial Andreev levels localized near the noncovered wire section that are bound to zero energy for varying E_z and μ, but quickly split to finite energies for varying tunnel barrier strength. Here we demonstrate for the first time a zero-bias peak rigidly bound to $V = 0$ over a changing tunnel barrier conductance—a behavior observed in all devices (Fig. 3.S5 to 3.S7). From the combined analysis (Figure 3.2b-d) we conclude that the zero-bias peak originates in the wire section underneath the superconductor, consistent with a Majorana interpretation.

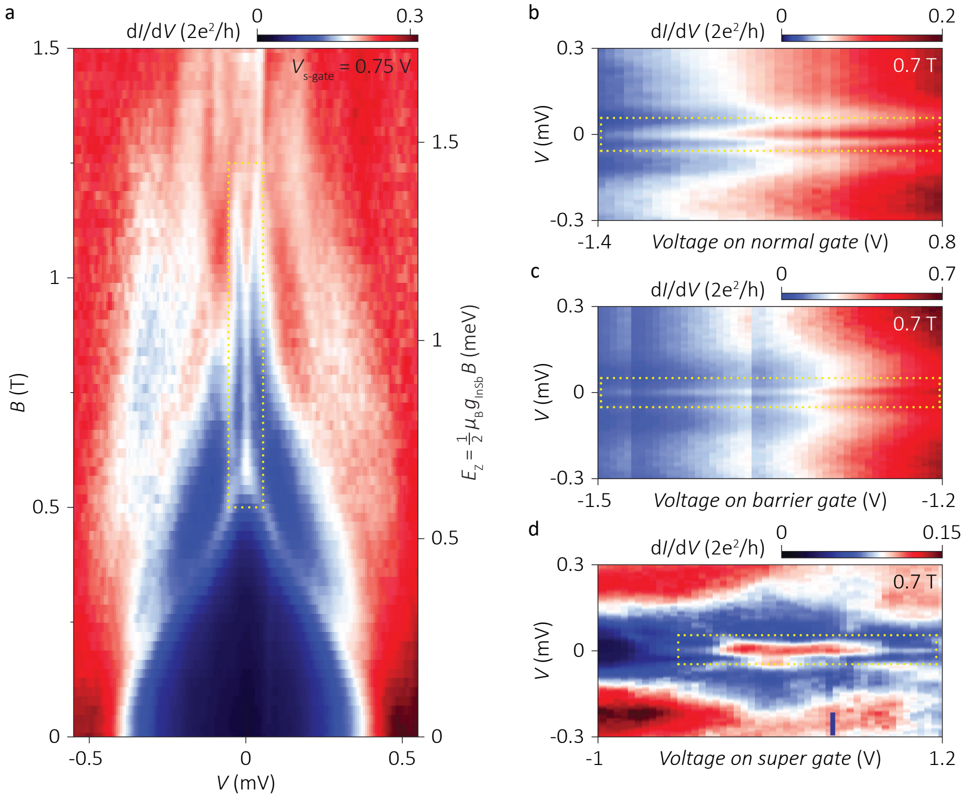

Figure 3.2: Zero-bias peak and its dependence on magnetic field and local gate voltages. **(a)** Differential conductance dI/dV as a function of bias voltage V, and an external magnetic field B along the nanowire axis for $V_{\mathrm{s-gate}} = 0.75$ V. The magnetic field closes the induced gap at 0.55 T and generates a zero-bias peak which persists up to 1.2 T. The right axis scales with Zeeman energy E_z assuming a g factor of 40 obtained independently [25, 26]. (Voltage on normal and barrier gate: 0 V and −1.4 V) **(b)** dI/dV as a function of V and voltage on normal gate. The voltage on normal gate changes the conductance by more than a factor of 5 but does not affect the presence of the zero-bias peak. **(c)** dI/dV as a function of V and voltage on barrier gate. The voltage on barrier gate changes the conductance by nearly an order of magnitude but does not affect the presence of zero-bias peak. **(d)** dI/dV as a function of V and voltage on super gate. The zero-bias peak persists for a finite gate voltage range. The blue bar indicates the voltage on super gate in **a**, **b** and **c**. The voltage on the barrier gate is adjusted to keep the overall conductance the same when sweeping the voltage on super gate.

In a Majorana nanowire [4, 5], the existence of a topological phase strictly requires an external magnetic field with a finite component perpendicular to the spin–orbit field B_{so}, see Figure 3.3a. An external field along the wire fulfills this requirement, shown in Figure 3.2a. In contrast, Figure 3.3b shows that an external magnetic field parallel to B_{so} does not generate a zero-bias peak for the same gate settings in Figure 3.2a. Figure 3.3c shows the dependence of the zero-bias peak on the direction of the external field. The zero-bias peak is limited to an angle range where the external field is mostly aligned with the wire, perpendicular to B_{so} (see Fig. 3.S2 for a measurement in a larger angle range). We observe a low conductance region around the zero-bias peak, indicating the

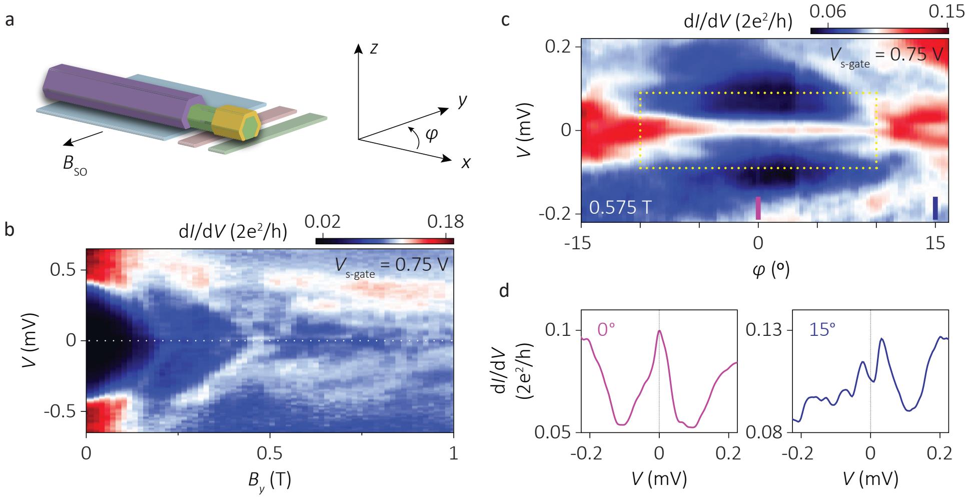

Figure 3.3: Dependence of zero-bias peak on magnetic field orientation. **(a)** Orientation of the nanowire device. The wire is along x and the spin–orbit field B_{SO} is along y. The substrate plane is spanned by x and y. φ is the angle between the x axis and the orientation of the external magnetic field in the plane of the substrate. **(b)** Differential conductance $\mathrm{d}I/\mathrm{d}V$ as a function of bias voltage V, and an external magnetic field along the y axis. Application of a magnetic field along B_{SO} closes the induced gap but does not generate a zero-bias peak. **(c)** $\mathrm{d}I/\mathrm{d}V$ as a function of V, and in-plane rotation of the magnetic field with a magnitude of 0.575 T. The zero-bias peak appears in an angle range in which the external magnetic field is mostly aligned with the wire. We attribute the low conductance region around the zero-bias peak to the induced gap. Orienting the magnetic field away from the wire axis and more towards B_{SO} closes the induced gap and splits the zero-bias peak (see line cuts in **d**). **(d)** Vertical line cuts from **c** at the angles indicated with colored bars. For $\varphi = 0°$ the zero-bias peak is present, which is split for $\varphi = 15°$.

induced gap. Orienting the magnetic field away from the wire axis and more towards B_{SO} closes the induced gap and splits the zero-bias peak. This is indicated by the vertical line cuts from Figure 3.3c at marked angles, shown in Figure 3.3d. A gap closing is expected for the critical angle φ_c given by the projection rule [29, 30] $E_z \sin(\varphi_c) = \Delta^*$. From the observed zero-field gap $\Delta^* = 650\,\mu\mathrm{eV}$ and an effective orbital effect enhanced g-factor along B_{SO} [31] of 110 (estimated from the gap closing along B_{SO} in Fig. 3.3b), we obtain $\varphi_c \approx 20°$, in agreement with the observed value of $\varphi_c \sim 10°$ (a reduction in φ_c is expected due to orbital effect of the external magnetic field [32]). Finally, in Fig. 3.S2 we show that increasing B decreases φ_c, a behavior consistent with the projection rule.

We now turn our attention to an identical device but with a longer proximitized wire section (1.2 µm, see Fig. 3.S3a). Figure 3.4a-c show an induced gap $\Delta^* = 0.9\,\mathrm{meV}$ at zero magnetic field, significantly larger than the device in Figure 3.1-3.3. As a result, the induced gap closes at a higher magnetic field ($\sim 1\,\mathrm{T}$). The zero-bias peak is visible and unsplit over a range of at least 1.3 T, corresponding to a Zeeman energy scale $> 1.5\,\mathrm{meV}$. The FWHM is around 0.07 meV yielding a ratio ZBP-range/FWHM $\gtrsim 20$ (Fig. 3.S4). A disorder-free Majorana theory model with parameters extracted from this device (geometry, induced gap, spin–orbit coupling, temperature) finds perfect agreement between simulation [21] and our data (Figure 3.4a). Fig. 3.S3b,c shows that the zero-bias peak position is robust against a change in conductance when varying the voltage applied to the

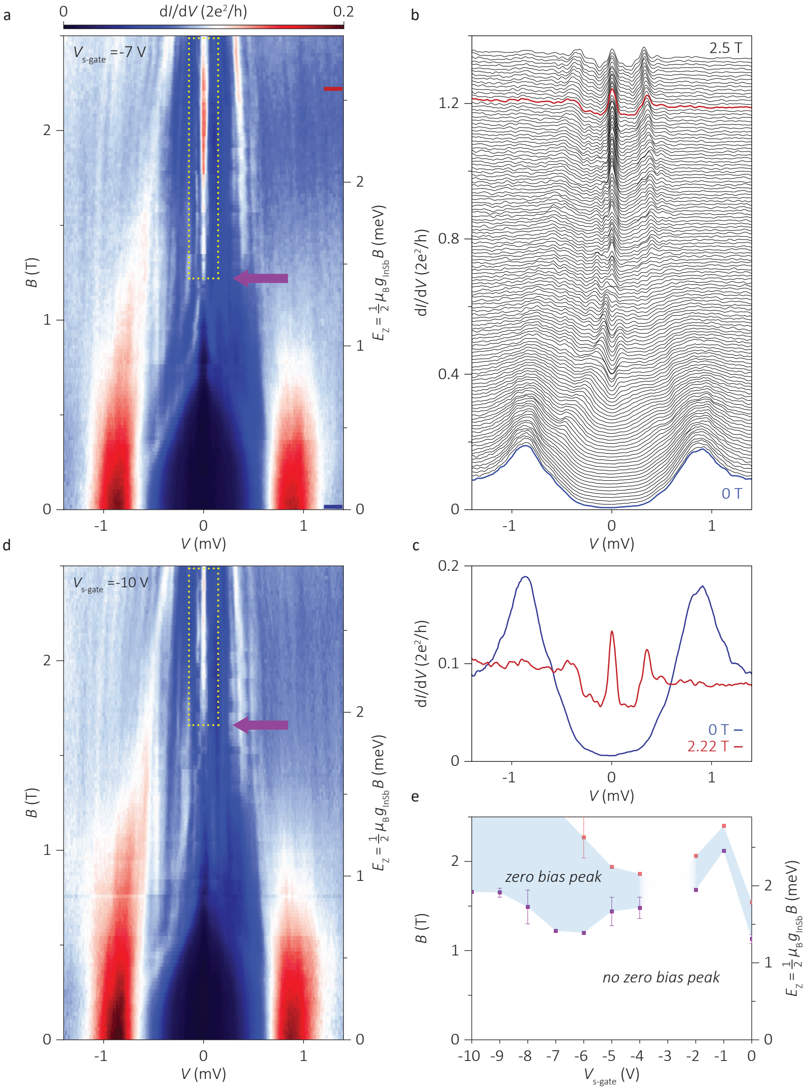

Figure 3.4: Zero-bias peak and phase diagram. **(a)** Differential conductance dI/dV of another device measured as a function of bias voltage V, and an external magnetic field B along the nanowire axis. We find an induced gap $\Delta^* = 0.9$ meV at zero magnetic field. Increasing the magnetic field closes the induced gap at ~1 T and generates a zero-bias peak that persists up to at least 2.5 T. The right axis scales with Zeeman energy E_Z assuming $g_{\text{InSb}} = 40$ obtained independently [25, 26]. The purple arrow at 1.22 T indicates the onset of the zero-bias peak. **(b)** Line cuts from **a** with $0.01 \times 2e^2/h$ offset. **(c)** Line cuts from **a** and **b** at 0 and 2.22 T. **(d)** Same as **a** but with a different super gate voltage $V_{\text{s-gate}} = -10$ V. For this super gate voltage, the onset of the zero-bias peak is at a larger magnetic field of 1.66 T, as marked by a purple arrow. **(e)** Phase diagram constructed by the onset and the end of the zero-bias peak in magnetic field for different super gate voltages. The purple squares denote the onset, pink the end. For $V_{\text{s-gate}} = -3$ V no zero-bias peak is observed.

normal and the barrier gate, ruling out the trivial Andreev-level explanation [22] consistent with our earlier discussion (Figure 3.2b,c). In contrast to normal and barrier gate, the voltage applied to the super gate changes the onset and the end of the zero-bias peak in magnetic field. Figure 3.4d shows that for $V_{\text{s-gate}} = -10\,\text{V}$ the zero-bias peak appears at a higher magnetic field compared to Figure 3.4a where $V_{\text{s-gate}} = -7\,\text{V}$ (1.66 T vs. 1.22 T). We have extended this analysis for $-10\,\text{V} \leq V_{\text{s-gate}} \leq 0\,\text{V}$ and marked the magnetic field values at which the zero-bias peak starts and ends (Fig. 3.S3d). The resulting phase diagram is shown in Figure 3.4e. For large negative voltages applied to the super gate, we find a region in which the zero-bias peak persists for large ranges of magnetic field and $V_{\text{s-gate}}$, indicating the topological phase. We attribute the appearance of a trivial phase at large magnetic fields above the topological phase to multi-channel occupation in the proximitized wire section [21, 22]. A precise knowledge of the phase boundaries requires theory including finite-size effects [33], the orbital effect of the magnetic field [32], and an accurate electrostatic modeling of the device [34], and will be addressed in future studies.

3.5. CONCLUSION

In conclusion, the presented experiments demonstrate zero-bias peaks over an extended range in Zeeman energy and gate voltage in devices that show clear ballistic transport properties, and reveal the distinct phases in the topology of Majorana wires. These observations exclude known alternative explanations involving disorder in the tunneling region of the nanowire for our zero-bias peaks.

AUTHOR CONTRIBUTIONS

Ö.G., H.Z., and J.D.S.B fabricated the devices, performed the measurements, and analyzed the data. M.W.A.d.M. contributed to the device fabrication. D.C., S.R.P. and E.P.A.M.B. grew the InSb nanowires. A.G. contributed to the experiments. K.W. and T.T. synthesized the hBN crystals. L.P.K. supervised the project. Ö.G., H.Z., and J.D.S.B. co-wrote the paper. All authors commented on the manuscript.

DATA AVAILABILITY

The data shown in the figures are available at Ref. [35].

3.S. SUPPLEMENTAL MATERIAL

3.S.1. NANOWIRE GROWTH AND DEVICE FABRICATION

InSb nanowires have been grown by Au-catalyzed Vapor-Liquid-Solid mechanism in a Metal Organic Vapor Phase Epitaxy reactor. The InSb nanowires are zinc blende, along [111] crystal direction, and are free of stacking faults and dislocations [36]. As-grown nanowires are deposited one-by-one using a micro-manipulator [37] on a substrate patterned with local gates covered by a $\sim 30\,\mathrm{nm}$ thick hBN dielectric. The contact deposition process starts with resist development followed by oxygen plasma cleaning. Then, the chip is immersed in a sulfur-rich ammonium sulfide solution diluted by water (with a ratio of 1:200) at 60°C for half an hour [38]. At all stages care is taken to expose the solution to air as little as possible. For normal metal contacts [25, 26], the chip is placed into an evaporator. A 30 second helium ion milling is performed in situ before evaporation of Cr/Au (10 nm/125 nm) at a base pressure $< 10^{-7}$ mbar. For superconducting contacts [19, 20], the chip is mounted in a sputtering system. After 5 seconds of in situ argon plasma etching at a power of 25 Watts and a pressure of 10 mTorr, 5 nm NbTi is sputtered followed by 85 nm NbTiN.

3.S.2. SUPPLEMENTAL FIGURES

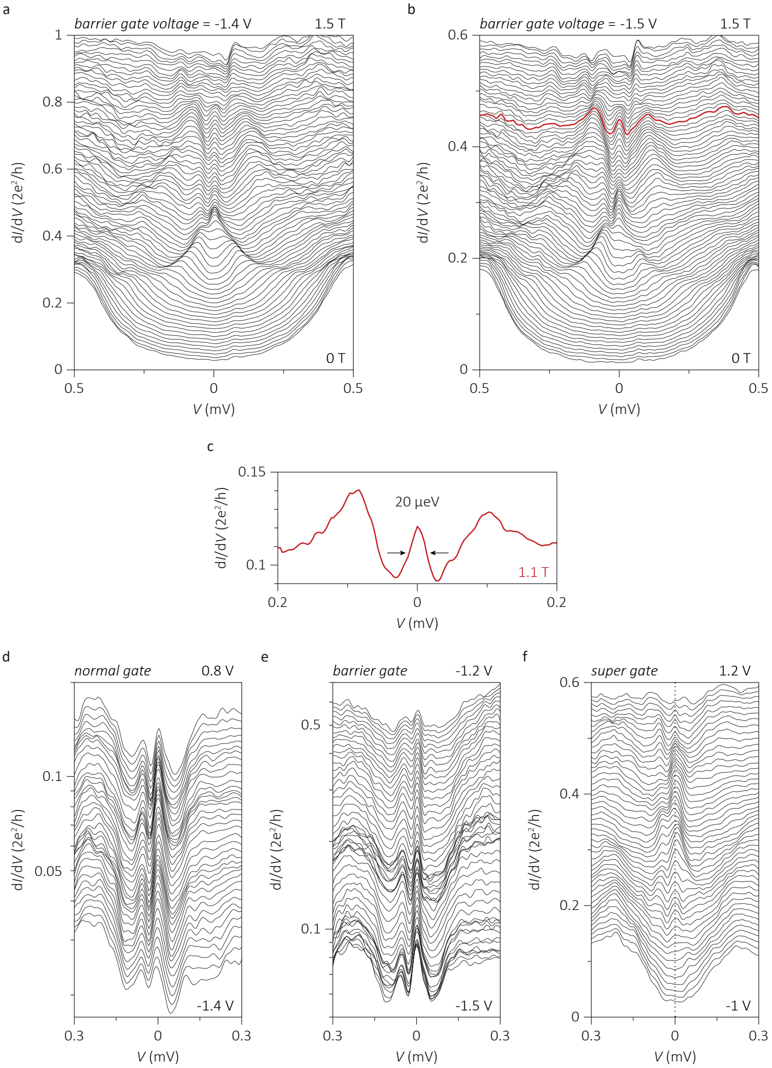

Figure 3.S1: Line cuts from main text Figure 2. **(a)** Line cuts from main text Figure 3.2a with $0.01 \times 2e^2/h$ offset. An increasing magnetic field closes the induced gap at 0.55 T and generates a zero-bias peak up to 1.2 T. **(b)** Same as **a** but for a larger tunnel barrier strength. Offset: $0.006 \times 2e^2/h$. **(c)** Line cut from 1.1 T. We find the full width at half maximum of the zero-bias peak to be 20 μeV. **(d)** Line cuts from main text Figure 3.2b in logarithmic scale (without offset). A variation in voltage on the normal gate ($-1.4\,\mathrm{V} \leq V_{\mathrm{n-gate}} \leq 0.8\,\mathrm{V}$) changes the conductance by more than a factor of 5, but does not remove the zero-bias peak. **(e)** Line cuts from main text Figure 3.2c in logarithmic scale (without offset). A variation in voltage on the barrier gate ($-1.5\,\mathrm{V} \leq V_{\mathrm{b-gate}} \leq -1.2\,\mathrm{V}$) changes the conductance by nearly an order of magnitude, but does not remove the zero-bias peak. **(f)** Line cuts from main text Figure 3.2d with $0.006 \times 2e^2/h$ offset. A variation in voltage on the super gate ($-1\,\mathrm{V} \leq V_{\mathrm{s-gate}} \leq 1.2\,\mathrm{V}$) affects the presence of the zero-bias peak, which is stable for a finite gate voltage range.

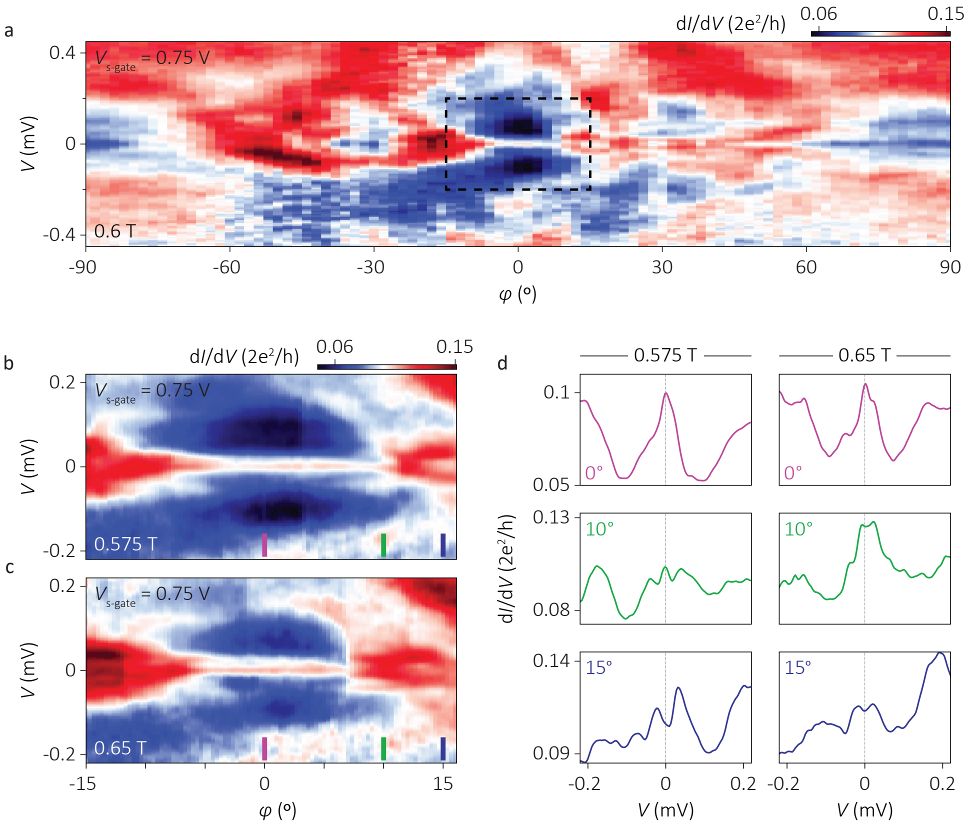

Figure 3.S2: Dependence of the zero-bias peak on the orientation of an in-plane magnetic field. **(a)** Differential conductance $\mathrm{d}I/\mathrm{d}V$ as a function of bias voltage V, and in-plane rotation of the magnetic field with a magnitude of 0.6 T. $\varphi = 0°$ corresponds to an external field along the wire, $\varphi = \pm 90°$ to an external field parallel to the spin–orbit field B_{SO}. The zero-bias peak is present in an angle range ($|\varphi| < 10°$) when the external magnetic field is mostly aligned with the wire. We observe a low conductance region around the zero-bias peak, indicating the induced gap. Orienting the magnetic field away from the wire axis and more towards B_{SO} closes the induced gap and splits the zero-bias peak. We do not observe a stable zero-bias peak for $|\varphi| > 10°$ in the entire angle range. The dashed square indicates the angle range shown in main text Figure 3.3c. **(b)** **(c)** $\mathrm{d}I/\mathrm{d}V$ as a function of V, and in-plane rotation of the magnetic field with two different magnitudes. Increasing the magnetic field decreases the angle range of the zero-bias peak (compare **b** and **c**). **(d)** Vertical line cuts from **b** and **c** at the angles indicated with colored bars. Top panels: For $\varphi = 0°$ the zero-bias peak is present for both magnetic field magnitudes. Bottom panels: For $\varphi = 15°$ no zero-bias peak is present for both magnitudes. Middle panels: For $\varphi = 10°$ the zero-bias peak is present only for 0.575 T, while is split for 0.65 T.

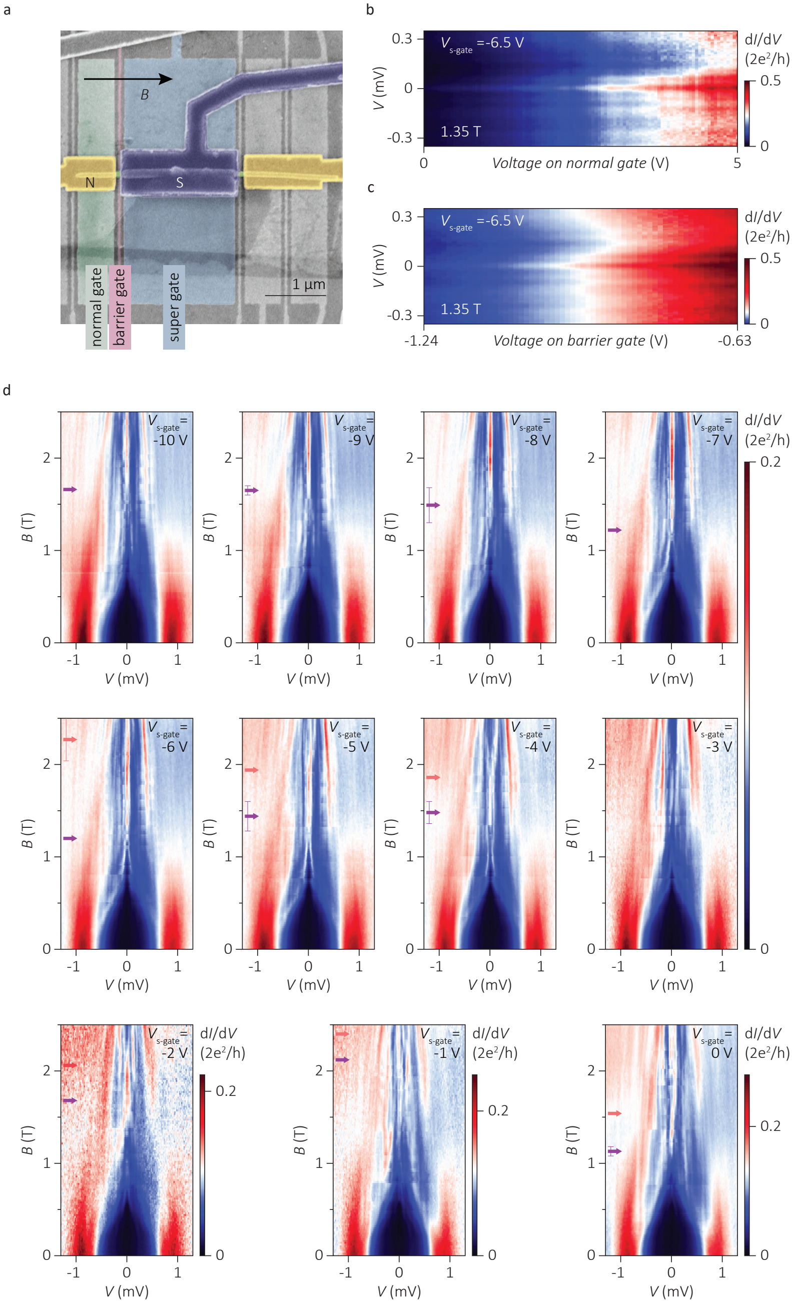

Figure 3.S3: Zero-bias peak in a large range of magnetic field and local gate voltages. (a) False-color electron micrograph of the measured device. **(b) (c)** Differential conductance dI/dV as a function of bias voltage V, and voltages on normal and barrier gate, respectively. A variation in each gate voltage changes the conductance by an order of magnitude, but does not affect the presence of the zero-bias peak. **(d)** dI/dV as a function of V and an external magnetic field B along the nanowire axis, measured at different voltages on super gate ($-10\,\mathrm{V} \leq V_{\mathrm{S-gate}} \leq 0\,\mathrm{V}$). A variation in $V_{\mathrm{S-gate}}$ changes the magnetic field range in which the zero-bias peak appears. The purple (pink) arrows indicate the onset (end) of the zero-bias peak in external magnetic field. When changing the super gate voltage, we adjust the tunnel gate voltage to keep the overall conductance the same.

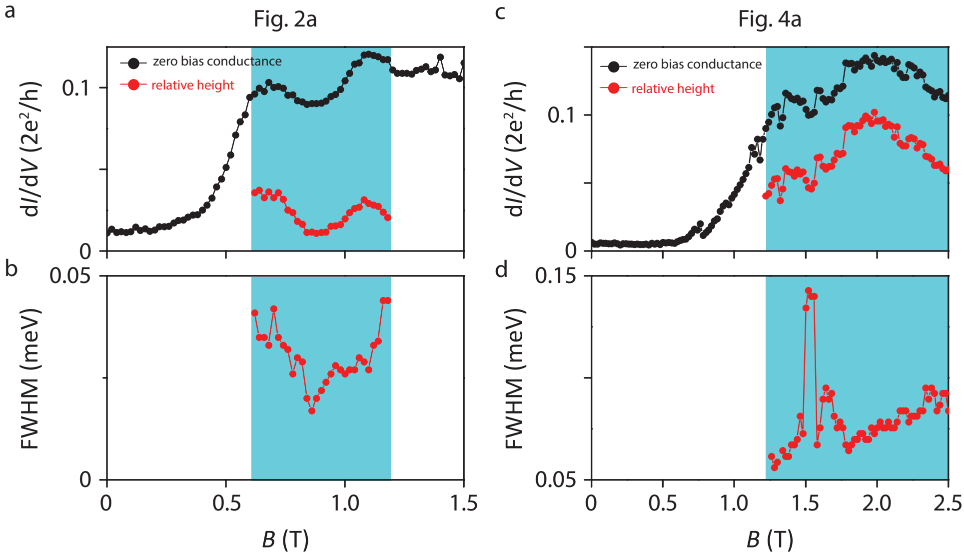

Figure 3.S4: Zero-bias peak height and width. **(a)** The absolute and the relative height of the zero-bias peak extracted from main text Figure 3.2a. The difference between the absolute and the relative height is the subgap conductance around zero bias for each magnetic field. **(b)** The full width at half maximum (FWHM) of the zero-bias peak extracted from main text Figure 3.2a. **(c,d)** Same as **a** and **b** but for the zero-bias peak from main text Figure 3.4a.

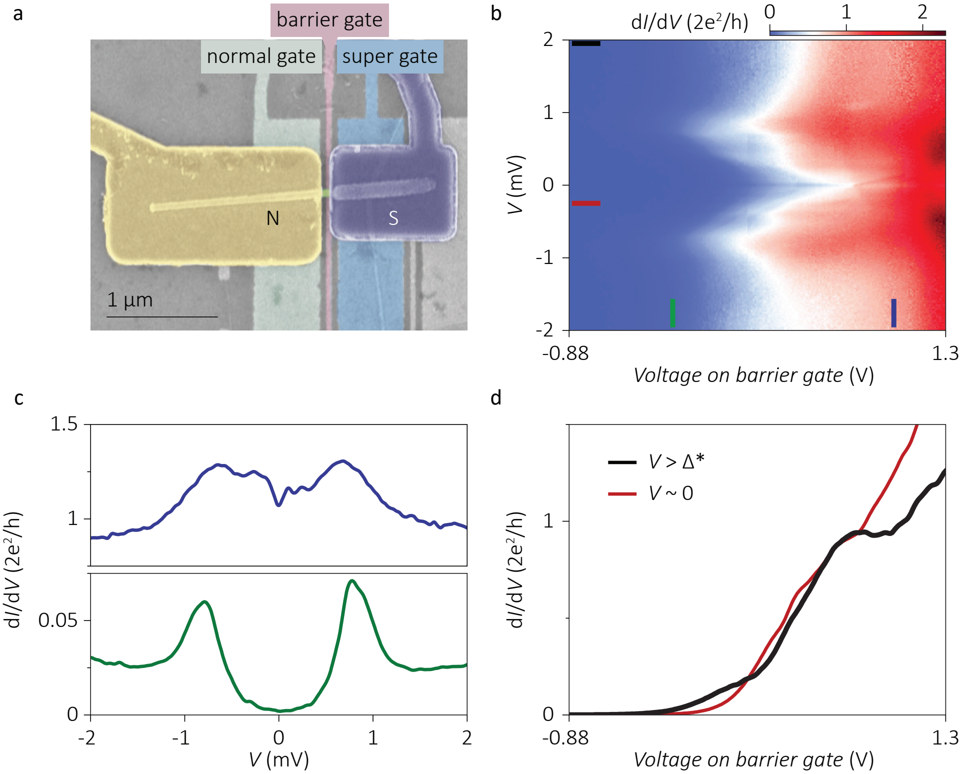

Figure 3.S5: Additional device 1 - ballistic transport properties. **(a)** False-color electron micrograph of the measured device. **(b)** Differential conductance dI/dV as a function of bias voltage V, and voltage on barrier gate. **(c)** Vertical line cuts from **b** at the gate voltages marked with colored bars. Top panel shows the dI/dV from the transport regime in which the current is carried by a single fully-transmitting channel. We find an enhancement of conductance at small bias by a factor of 1.25 compared to the large-bias conductance of $2e^2/h$. Bottom panel is from the tunneling regime. We extract an induced superconducting gap $\Delta^* = 0.75$ meV. **(d)** Horizontal line cuts from **b** at the bias voltages marked with colored bars. Large-bias conductance ($V = 2\,\text{mV} > \Delta^*$) shows a quantized plateau of $2e^2/h$. The subgap conductance ($V = -0.25\,\text{mV}$) is enhanced within the gate voltage range in which the large-bias conductance is quantized. We excluded a series resistance of 0.5 kΩ, solely to account for the contact resistance of the normal lead [20, 25].

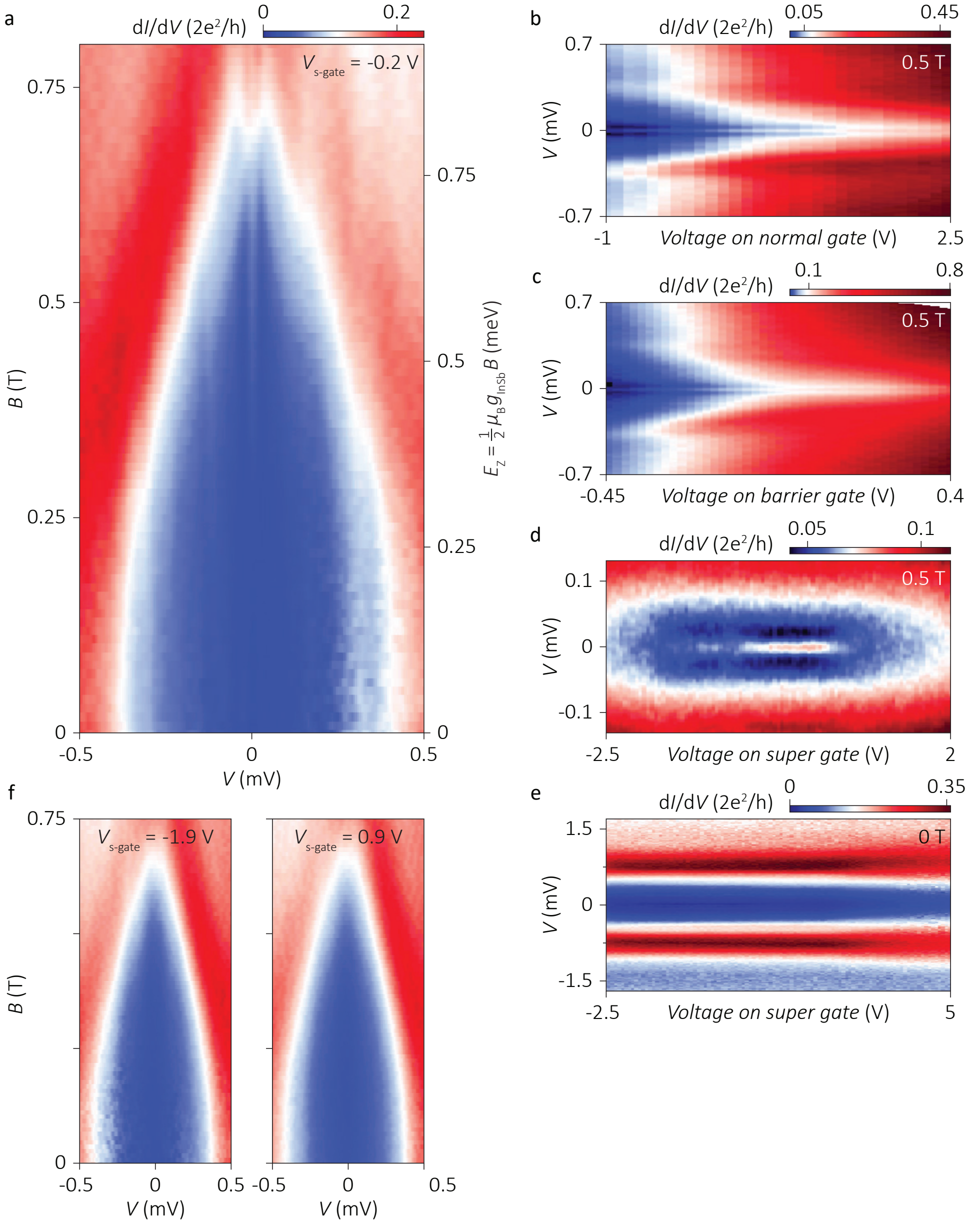

Figure 3.S6: Additional device 1 - zero-bias peak in a large range of magnetic field and local gate voltages. **(a)** Differential conductance dI/dV as a function of bias voltage V, and an external magnetic field B along the nanowire axis. Application of a magnetic field generates a zero-bias peak at 0.3 T. The zero-bias peak persists up to 0.7 T and splits for larger magnetic fields. The right axis scales with Zeeman energy E_Z assuming a g factor of 40. **(b)** dI/dV as a function of V and voltage on the normal gate. The voltage on the normal gate changes the conductance by a factor of 10 but does not affect the presence of the zero-bias peak. **(c)** dI/dV as a function of V and voltage on the barrier gate. The voltage on the barrier gate changes the conductance by a factor of 20 but does not affect the presence of the zero-bias peak. **(d)** dI/dV as a function of V and voltage on the super gate. The zero-bias peak is stable for a finite range of voltages on the super gate. **(e)** Same as **d** but at zero magnetic field. No zero-bias peak is present. **(f)** Same as **a** but for different voltages on the super gate ($V_{\text{s-gate}}$). No zero-bias peak is present for the measured magnetic field range for $V_{\text{s-gate}} = -1.9$ V and $V_{\text{s-gate}} = 0.9$ V, consistent with **d**.

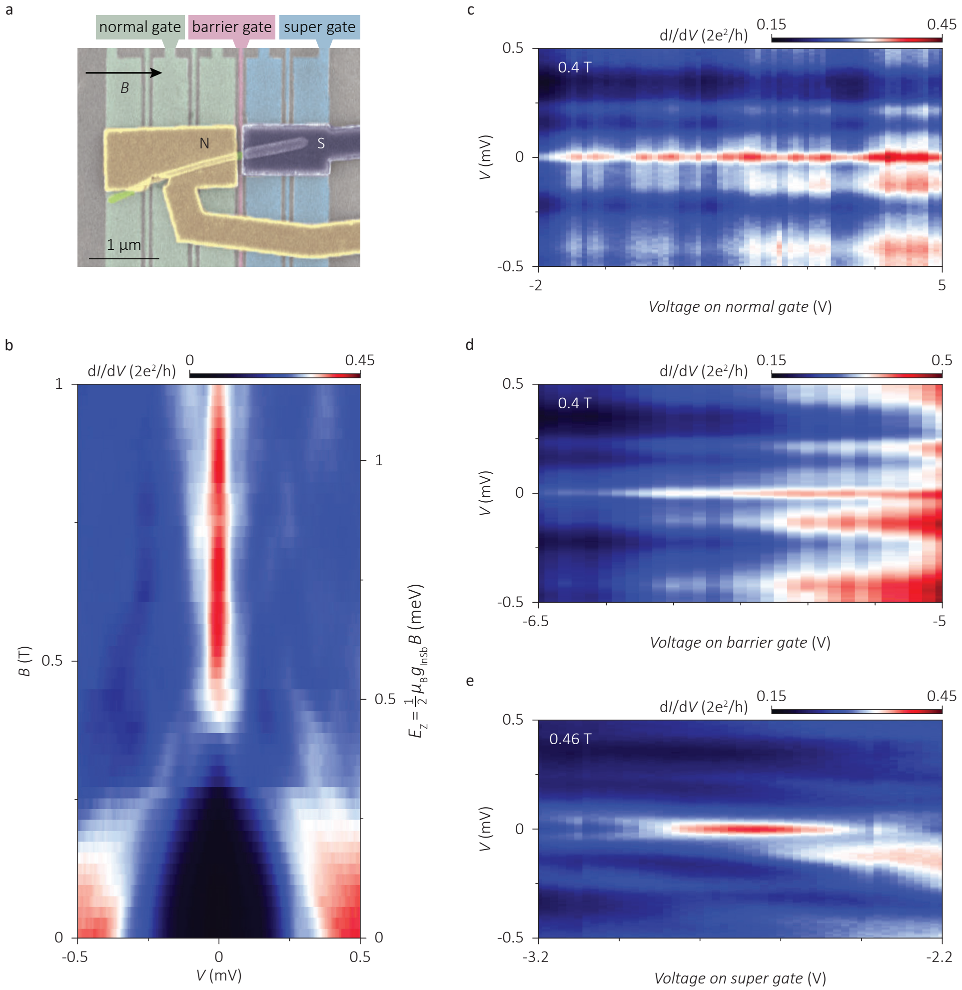

Figure 3.S7: Additional device 2 - zero-bias peak in a large range of magnetic field and local gate voltages. **(a)** False-color electron micrograph of the measured device. **(b)** Differential conductance $\mathrm{d}I/\mathrm{d}V$ as a function of bias voltage V and magnetic field B. Increasing the magnetic field closes the gap and generates a zero-bias peak which persists up to at least 1 T. The right axis scales with Zeeman energy assuming $g_{\mathrm{InSb}} = 40$. Gate voltages are fixed at $V_{\mathrm{n-gate}} = 1\,\mathrm{V}$, $V_{\mathrm{b-gate}} = -5.5\,\mathrm{V}$, and $V_{\mathrm{s-gate}} = -2.8\,\mathrm{V}$ for normal, barrier, and super gate, respectively. **(c)** $\mathrm{d}I/\mathrm{d}V$ as a function of V, and normal gate voltage $V_{\mathrm{n-gate}}$. A large variation in $V_{\mathrm{n-gate}}$ can modulate the overall conductance but it does not remove the zero-bias peak. Taken at $B = 0.4\,\mathrm{T}$, $V_{\mathrm{b-gate}} = -5.5\,\mathrm{V}$, and $V_{\mathrm{s-gate}} = -2.85\,\mathrm{V}$. **(d)** $\mathrm{d}I/\mathrm{d}V$ as a function of V, and barrier gate voltage. Changing the tunnel barrier conductance by more than a factor of 3 does not split the zero-bias peak, nor makes it disappear. Taken at $V_{\mathrm{n-gate}} = 2.5\,\mathrm{V}$ and $V_{\mathrm{s-gate}} = -2.85\,\mathrm{V}$. **(e)** $\mathrm{d}I/\mathrm{d}V$ as a function of V, and super gate voltage $V_{\mathrm{s-gate}}$. The zero-bias peak is stable over a finite range in $V_{\mathrm{s-gate}}$. Taken at $V_{\mathrm{n-gate}} = 1\,\mathrm{V}$ and $V_{\mathrm{b-gate}} = -5.5\,\mathrm{V}$.

REFERENCES

[1] N. Read and D. Green, *Paired states of fermions in two dimensions with breaking of parity and time-reversal symmetries and the fractional quantum Hall effect,* Phys. Rev. B **61**, 10267 (2000).

[2] A. Y. Kitaev, *Unpaired Majorana fermions in quantum wires,* Phys. Usp. **44**, 131 (2001).

[3] L. Fu and C. L. Kane, *Superconducting proximity effect and Majorana fermions at the surface of a topological insulator,* Phys. Rev. Lett. **100**, 096407 (2008).

[4] R. M. Lutchyn, J. D. Sau, and S. Das Sarma, *Majorana fermions and a topological phase transition in semiconductor-superconductor heterostructures,* Phys. Rev. Lett. **105**, 077001 (2010).

[5] Y. Oreg, G. Refael, and F. von Oppen, *Helical liquids and Majorana bound states in quantum wires,* Phys. Rev. Lett. **105**, 177002 (2010).

[6] V. Mourik, K. Zuo, S. M. Frolov, S. R. Plissard, E. P. A. M. Bakkers, and L. P. Kouwenhoven, *Signatures of Majorana fermions in hybrid superconductor-semiconductor nanowire devices,* Science **336**, 1003 (2012).

[7] A. Das, Y. Ronen, Y. Most, Y. Oreg, M. Heiblum, and H. Shtrikman, *Zero-bias peaks and splitting in an Al–InAs nanowire topological superconductor as a signature of Majorana fermions,* Nat. Phys. **8**, 887 (2012).

[8] M. T. Deng, C. L. Yu, G. Y. Huang, M. Larsson, P. Caroff, and H. Q. Xu, *Anomalous zero-bias conductance peak in a Nb–InSb nanowire–Nb hybrid device,* Nano Lett. **12**, 6414 (2012).

[9] S. M. Albrecht, A. P. Higginbotham, M. Madsen, F. Kuemmeth, T. S. Jespersen, J. Nygård, P. Krogstrup, and C. M. Marcus, *Exponential protection of zero modes in Majorana islands,* Nature **531**, 206 (2016).

[10] M. T. Deng, S. Vaitiekėnas, E. B. Hansen, J. Danon, M. Leijnse, K. Flensberg, J. Nygård, P. Krogstrup, and C. M. Marcus, *Majorana bound state in a coupled quantum-dot hybrid-nanowire system,* Science **354**, 1557 (2016).

[11] J. Chen, P. Yu, J. Stenger, M. Hocevar, D. Car, S. R. Plissard, E. P. A. M. Bakkers, T. D. Stanescu, and S. M. Frolov, *Experimental phase diagram of zero-bias conductance peaks in superconductor/semiconductor nanowire devices,* Sci. Adv. **3**, e1701476 (2017).

[12] J. Liu, A. C. Potter, K. T. Law, and P. A. Lee, *Zero-bias peaks in the tunneling conductance of spin-orbit-coupled superconducting wires with and without Majorana end-states,* Phys. Rev. Lett. **109**, 267002 (2012).

[13] D. Bagrets and A. Altland, *Class D spectral peak in Majorana quantum wires,* Phys. Rev. Lett. **109**, 227005 (2012).

[14] D. I. Pikulin, J. P. Dahlhaus, M. Wimmer, H. Schomerus, and C. W. J. Beenakker, *A zero-voltage conductance peak from weak antilocalization in a Majorana nanowire,* New J. of Phys. **14**, 125011 (2012).

[15] E. J. H. Lee, X. Jiang, R. Aguado, G. Katsaros, C. M. Lieber, and S. De Franceschi, *Zero-bias anomaly in a nanowire quantum dot coupled to superconductors,* Phys. Rev. Lett. **109**, 186802 (2012).

[16] E. J. Lee, X. Jiang, M. Houzet, R. Aguado, C. M. Lieber, and S. De Franceschi, *Spin-resolved Andreev levels and parity crossings in hybrid superconductor–semiconductor nanostructures,* Nat. Nanotech. **9**, 79 (2014).

[17] S. Takei, B. M. Fregoso, H.-Y. Hui, A. M. Lobos, and S. Das Sarma, *Soft superconducting gap in semiconductor Majorana nanowires,* Phys. Rev. Lett. **110**, 186803 (2013).

[18] W. Chang, S. M. Albrecht, T. S. Jespersen, F. Kuemmeth, P. Krogstrup, J. Nygård, and C. M. Marcus, *Hard gap in epitaxial semiconductor-superconductor nanowires,* Nat. Nanotech. **10**, 232 (2015).

[19] O. Gül, H. Zhang, F. K. de Vries, J. van Veen, K. Zuo, V. Mourik, S. Conesa-Boj, M. P. Nowak, D. J. van Woerkom, M. Quintero-Pérez, M. C. Cassidy, A. Geresdi, S. Koelling, D. Car, S. R. Plissard, E. P. A. M. Bakkers, and L. P. Kouwenhoven, *Hard superconducting gap in InSb nanowires,* Nano Lett. **17**, 2690 (2017).

[20] H. Zhang, O. Gül, S. Conesa-Boj, M. P. Nowak, M. Wimmer, K. Zuo, V. Mourik, F. K. de Vries, J. van Veen, M. W. A. de Moor, J. D. S. Bommer, D. J. van Woerkom, D. Car, S. R. Plissard, E. P. A. M. Bakkers, M. Quintero-Pérez, M. C. Cassidy, S. Koelling, S. Goswami, K. Watanabe, T. Taniguchi, and L. P. Kouwenhoven, *Ballistic superconductivity in semiconductor nanowires,* Nat. Commun. **8**, 16025 (2017).

[21] C.-X. Liu, J. D. Sau, and S. Das Sarma, *Role of dissipation in realistic Majorana nanowires,* Phys. Rev. B **95**, 054502 (2017).

[22] C.-X. Liu, J. D. Sau, T. D. Stanescu, and S. Das Sarma, *Andreev bound states versus Majorana bound states in quantum dot-nanowire-superconductor hybrid structures: Trivial versus topological zero-bias conductance peaks,* Phys. Rev. B **96**, 075161 (2017).

[23] E. Prada, P. San-Jose, and R. Aguado, *Transport spectroscopy of NS nanowire junctions with Majorana fermions,* Phys. Rev. B **86**, 180503 (2012).

[24] S. Gazibegovic, D. Car, H. Zhang, S. C. Balk, J. A. Logan, M. W. A. de Moor, M. C. Cassidy, R. Schmits, D. Xu, G. Wang, P. Krogstrup, R. L. M. Op het Veld, K. Zuo, Y. Vos, J. Shen, D. Bouman, B. Shojaei, D. Pennachio, J. S. Lee, P. J. van Veldhoven, S. Koelling, M. A. Verheijen, L. P. Kouwenhoven, C. J. Palmstrøm, and E. P. A. M. Bakkers, *Epitaxy of advanced nanowire quantum devices,* Nature **548**, 434 (2017).

[25] J. Kammhuber, M. C. Cassidy, H. Zhang, O. Gül, F. Pei, M. W. A. de Moor, B. Nijholt, K. Watanabe, T. Taniguchi, D. Car, S. R. Plissard, E. P. A. M. Bakkers, and L. P.

Kouwenhoven, *Conductance quantization at zero magnetic field in InSb nanowires,* Nano Lett. **16**, 3482 (2016).

[26] J. Kammhuber, M. C. Cassidy, F. Pei, M. P. Nowak, A. Vuik, O. Gül, D. Car, S. R. Plissard, E. P. A. M. Bakkers, M. Wimmer, and L. P. Kouwenhoven, *Conductance through a helical state in an indium antimonide nanowire,* Nat. Commun. **8**, 478 (2017).

[27] W. S. Cole, J. D. Sau, and S. Das Sarma, *Proximity effect and Majorana bound states in clean semiconductor nanowires coupled to disordered superconductors,* Phys. Rev. B **94**, 140505 (2016).

[28] T. D. Stanescu and S. Das Sarma, *Proximity-induced low-energy renormalization in hybrid semiconductor-superconductor Majorana structures,* Phys. Rev. B **96**, 014510 (2017).

[29] J. Osca, D. Ruiz, and L. Serra, *Effects of tilting the magnetic field in one-dimensional Majorana nanowires,* Phys. Rev. B **89**, 245405 (2014).

[30] S. Rex and A. Sudbø, *Tilting of the magnetic field in Majorana nanowires: Critical angle and zero-energy differential conductance,* Phys. Rev. B **90**, 115429 (2014).

[31] J. D. S. Bommer, H. Zhang, O. Gül, B. Nijholt, M. Wimmer, F. N. Rybakov, J. Garaud, D. Rodic, E. Babaev, M. Troyer, D. Car, S. R. Plissard, E. P. A. M. Bakkers, K. Watanabe, T. Taniguchi, and L. P. Kouwenhoven, *Spin-orbit protection of induced superconductivity in Majorana nanowires,* Phys. Rev. Lett. **122**, 187702 (2019).

[32] B. Nijholt and A. R. Akhmerov, *Orbital effect of magnetic field on the Majorana phase diagram,* Phys. Rev. B **93**, 235434 (2016).

[33] R. V. Mishmash, D. Aasen, A. P. Higginbotham, and J. Alicea, *Approaching a topological phase transition in Majorana nanowires,* Phys. Rev. B **93**, 245404 (2016).

[34] A. Vuik, D. Eeltink, A. R. Akhmerov, and M. Wimmer, *Effects of the electrostatic environment on the Majorana nanowire devices,* New J. Phys. **18**, 033013 (2016).

[35] Ö. Gül, H. Zhang, J. D. S. Bommer, M. W. A. de Moor, D. Car, S. R. Plissard, E. Bakkers, A. Geresdi, K. Watanabe, T. Taniguchi, and L. P. Kouwenhoven, *Ballistic Majorana nanowire devices,* 4TU.ResearchData (2017).

[36] D. Car, J. Wang, M. A. Verheijen, E. P. A. M. Bakkers, and S. R. Plissard, *Rationally designed single-crystalline nanowire networks,* Adv. Mater. **26**, 4875 (2014).

[37] K. Flöhr, M. Liebmann, K. Sladek, H. Y. Günel, R. Frielinghaus, F. Haas, C. Meyer, H. Hardtdegen, T. Schäpers, D. Grützmacher, and M. Morgenstern, *Manipulating InAs nanowires with submicrometer precision,* Rev. Sci. Instrum. **82**, 113705 (2011).

[38] D. B. Suyatin, C. Thelander, M. T. Björk, I. Maximov, and L. Samuelson, *Sulfur passivation for ohmic contact formation to InAs nanowires,* Nanotechnology **18**, 105307 (2007).

4

SPIN-ORBIT PROTECTION OF INDUCED SUPERCONDUCTIVITY IN MAJORANA NANOWIRES

Jouri D.S. Bommer*, Hao Zhang*, Önder Gül*, Bas Nijholt, Michael Wimmer, Filipp N. Rybakov, Julien Garaud, Donjan Rodic, Egor Babaev, Matthias Troyer, Diana Car, Sébastien R. Plissard, Erik P.A.M. Bakkers, Kenji Watanabe, Takashi Taniguchi, and Leo P. Kouwenhoven

Spin-orbit interaction (SOI) plays a key role in creating Majorana zero modes in semiconductor nanowires proximity coupled to a superconductor. We track the evolution of the induced superconducting gap in InSb nanowires coupled to a NbTiN superconductor in a large range of magnetic field strengths and orientations. Based on realistic simulations of our devices, we reveal SOI with a strength of 0.15–0.35 eVÅ. Our approach identifies the direction of the spin-orbit field, which is strongly affected by the superconductor geometry and electrostatic gates.

This chapter has been published in Physical Review Letters **122**, 187702 (2019)

*These authors contributed equally to this work.

4.1. INTRODUCTION

Spin-orbit interaction (SOI) is a relativistic effect that results from electrons moving (orbit) in an electric field (E) experiencing a magnetic field (B_{SO}) in their moving reference frame that couples to the electron's magnetic moment (spin). SOI is an essential ingredient of various realizations of topological superconductors, which host Majorana zero modes, the building blocks of topological quantum computation [1–3]. The prime platform for topological quantum computation is based on a semiconductor nanowire coupled to a superconductor, where the proximity effect opens a superconducting energy gap in the density of states of the nanowire[4, 5]. In general, a magnetic field suppresses superconductivity by closing the superconducting gap due to Zeeman and orbital effects [6]. If the nanowire has strong SOI, suppression of the superconducting gap is counteracted and a sufficiently large Zeeman energy drives the system into a topological superconducting phase, with Majorana zero modes localized at the wire ends [4, 5]. The main experimental effort in the last few years has focused on detecting these Majorana zero modes as a zero-bias peak in the tunneling conductance [7–13]. However, SOI, the mechanism providing the topological protection, has been challenging to detect directly in Majorana nanowires.

The electric field that gives rise to SOI in our system mainly results from structural inversion asymmetry of the confinement potential (Rashba SOI), which depends on the work function difference at the interface between the nanowire and the superconductor and on voltages applied to nearby electrostatic gates [14–17]. The Rashba SOI in nanowires has been investigated extensively by measuring spin-orbit related quantum effects: level repulsion of quantum dot levels [18, 19], and of Andreev states [9, 20], weak antilocalization in long diffusive wires [21, 22], and a helical liquid signature in short quasiballistic wires [23]. However, the SOI strength relevant to the topological protection is affected by the presence of the superconductor, necessitating direct observation of SOI in Majorana nanowires. Here, we reveal SOI in an InSb nanowire coupled to a NbTiN superconductor through the dependence of the superconducting gap on the magnetic field, both strength and orientation. We find that the geometry of the superconductor on the nanowire strongly modifies the direction of the spin-orbit field, which is further tunable by electrostatic gating, in line with the expected modifications of the electric field due to work function difference and electrostatic screening at the nanowire-superconductor interface.

4.2. RESULTS

Device characterization

Figure 4.1(a) shows the device image. An InSb nanowire (blue) is covered by a NbTi/NbTiN superconducting contact (purple) and a Cr/Au normal metal contact (yellow). The barrier gate underneath the uncovered wire (red) can deplete the nanowire, locally creating a tunnel barrier. The tunneling differential conductance (dI/dV) resolves the induced superconducting gap, by sweeping the bias voltage (V) across the tunnel barrier (see Fig. 4.1(b)). The dashed arrow indicates the induced gap of 0.65 meV. In this device, we have recently shown ballistic transport and Majorana signatures [10].

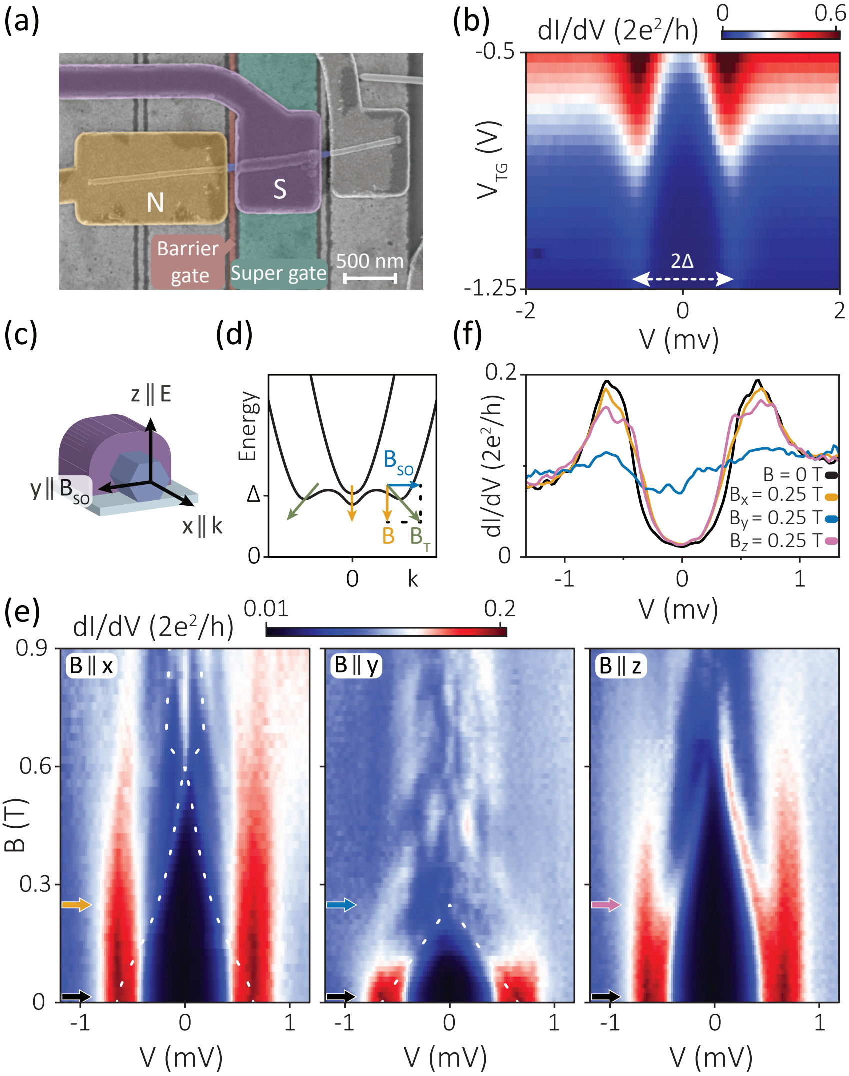

Figure 4.1: **(a)** False-color scanning electron micrograph of Majorana nanowire device *A*. An InSb nanowire (blue) is contacted by a normal metal contact (*N*, yellow) and a NbTiN superconducting contact (*S*, purple). The additional contact (gray) is kept floating. The nanowire is isolated from the barrier gate (red) and the super gate (green) by ~ 30 nm thick boron nitride. **(b)** Differential conductance dI/dV as a function of bias voltage V and barrier gate voltage V_{barrier} at $B = 0$ T. **(c)** Schematic of the nanowire device and definition of the axes. **(d)** Band diagram of a Majorana nanowire at an externally applied magnetic field B perpendicular to the spin-orbit field B_{SO}. The arrows indicate the total magnetic field $B_T = B + B_{\text{SO}}$ along which the spin eigenstates are directed. At $k = 0$ the spin always aligns with B. At increasing k, B_{SO} increases, tilting the spin more towards B_{SO}. **(e)** dI/dV as a function of V at B along x, y, z (left, middle, right) for super gate voltage $V_{\text{SG}} = 0$ V. The white dashed lines indicate a fit to the gap closing corresponding to $\alpha = 0.15 \pm 0.05$ eVÅ. **(f)** Horizontal line cuts of (e) at B indicated by the colored arrows in (e).

Spin-orbit protection of induced superconductivity

The magnetic field (B) dependence of the induced gap of device A, with B along three different directions, is shown in Fig. 4.1(e). The coordinate system is illustrated in Fig. 4.1(c). The x-axis is along the nanowire, parallel to the electron momentum (k). The z axis is perpendicular to the substrate and coincides with the electric field (E) direction due to the spatial symmetry of the device and the bottom gate. Since the Rashba spin-orbit field ($B_{SO} \propto E \times k$) is perpendicular to both k and E, it points along the y axis. When B is aligned with x or z [left and right panels in Fig. 4.1(e)], both perpendicular to B_{SO}, the gap closes slowly (at around 0.6 T), followed by the emergence of a zero-bias peak possibly characteristic of a Majorana zero mode when B is along the nanowire, although we emphasize that a conjecture of Majorana zero modes is not essential for the purposes of this Letter. On the contrary, when B is aligned with the y axis (middle panel), parallel to B_{SO}, the gap closes much faster (at around 0.25 T). Figure 1f shows the line cuts at $|B| = 0.25$ T along the three axes: for $B \perp B_{SO}$, the gap is almost the same as when $B = 0$ T, while the gap is closed for $B \parallel B_{SO}$. This observation matches the predictions of the Majorana nanowire model, as illustrated in Fig. 4.1(d): when $B \perp B_{SO}$, SOI counteracts the Zeeman-induced gap closing by rotating the spin eigenstate towards B_{SO}, which reduces the component of the Zeeman field along the direction of the spin eigenstate. In contrast, when $B \parallel B_{SO}$, the spin eigenstate is always parallel to B, which prevents spin-orbit protection and results in a fast gap closing [24, 25]. This pronounced anisotropy of the gap closing with respect to different B directions is universally observed in over ten devices (four shown in this Letter) for all gate settings [1], which is a direct consequence of SOI in Majorana nanowires.

Before we discuss the SOI in more detail, we rule out alternative mechanisms for the anisotropy which can originate in the bulk superconductor, or the InSb nanowire. First, an anisotropic magnetic field-induced closing of the bulk superconducting gap is excluded for the fields we apply, which are far below the critical field of NbTiN (>9 T) [38]. We note that this is different from aluminium films [9, 11, 39, 40], where a small magnetic field (<0.3 T) perpendicular to the film completely suppresses superconductivity, making them unsuitable to reveal SOI from an anisotropic gap closing. Next, we consider Meissner screening currents in NbTiN that can cause deviations in the magnetic field in the nanowire. Our Ginzburg-Landau simulations show that the field corrections due to Meissner screening are negligible, since the dimensions of the NbTiN film (<1 μm) are comparable to the penetration depth (~290 nm). The simulations also show that vortex formation is most favorable along the z axis, which implies that the observed anisotropic gap closing is not caused by gap suppression due to vortices near the nanowire [41], since we do not observe the fastest gap closing along z (see Fig. 4.1(f)). Finally, in the InSb nanowire, the Zeeman g factor can become anisotropic due to quantum confinement [19, 42, 43]. However, our nanowire geometry leads to confinement in both the y and z directions, implying similar gap closing along y and z, inconsistent with our observations (see Fig. 4.1(e)).

Having excluded the above mechanisms, we are now left with three effects: spin splitting of the electron states in magnetic fields with the Landé g factor (Zeeman effect),

---

[1] See Supplemental Material, which includes Refs. [26–37], for experimental details, theoretical details, and additional experimental data

the orbital effect of the magnetic field representing the Lorentz force acting on traveling electrons, and SOI. To investigate the role of these effects, we use a theoretical three-dimensional Majorana nanowire model defined by the Hamiltonian [4–6]:

$$\begin{aligned} H = & \left(\frac{\mathbf{p}^2}{2m^*} - \mu + V(y,z)\right)\tau_z + \frac{\alpha}{\hbar}\boldsymbol{\sigma}\cdot(\hat{\mathbf{E}}\times\mathbf{p})\tau_z \\ & + \frac{1}{2}g\mu_B\mathbf{B}\cdot\boldsymbol{\sigma} + \Delta_0\tau_x \end{aligned}$$

Here, the first term represents the kinetic and potential energy, with μ the chemical potential measured from the middle of the helical gap and $V(y,z) = \frac{\Delta V_G}{R}[0,y,z]\cdot\hat{\mathbf{E}}$ is the electrostatic potential in the wire, whose magnitude is parametrized by ΔV_G, with $\hat{\mathbf{E}}$ the direction of the electric field and R the wire radius. The orbital effect enters the Hamiltonian via the vector potential $\mathbf{A}$ in the canonical momentum: $\mathbf{p} = -i\hbar\nabla + e\mathbf{A}$. Here, e is the electron charge, $\hbar$ is Plank's constant, and $m^* = 0.015\ m_e$ is the effective mass with m_e the electron mass. The second term represents Rashba SOI characterized by a SOI strength α, which we set to 0.2 eVÅ to find qualitative agreement with the measurements. The third term is the Zeeman term, with an isotropic g factor set to 50 and μ_B is the Bohr magneton. The last term accounts for the superconducting proximity effect, which we implement in the weak coupling approximation [6]. The Pauli matrices τ and σ act in the particle-hole and spin space respectively. We perform numerical simulations of this Hamiltonian on a 3D lattice in a realistic nanowire geometry using the KWANT code [44]. We note that recent theory work shows that the anisotropy is unaffected by additional factors such as the wire length, temperature, and strong coupling to the superconductor [45]. Additional details are provided in the Supplemental Material.

We identify which effects explain the observed anisotropic gap closing behavior by including them separately in our simulations. Figure 4.2(a) shows the magnetic field dependence of the gap without SOI (setting $\alpha = 0$ in the Hamiltonian). In contrast to Fig. 4.1(e) the gap closes around 0.3 T for all three directions, reflecting the dominant contribution of the Zeeman effect. In Fig. 4.2(b), we turn on the SOI, and turn off the orbital effect by setting the magnetic vector potential $\mathbf{A} = 0$, which qualitatively reproduces the anisotropic behavior between the y axis and the x and z-axes. We have explored other combinations of parameters and find that the experimental results of Fig. 4.1(e) can only be reproduced by including SOI. We note that adding the orbital effect in Fig. 4.2(c) shifts the gap closing to a field almost twice as small for $B \parallel y$, which explains why we observe a gap closing for $B \parallel y$ at around 0.25 T, far below 0.45 T, the critical field expected when only the Zeeman effect with $g = 50$ suppresses the gap. By fitting the curvature of the gap closing [46, 47] along x [white dashed line in Fig. 4.1(e)] we estimate a range of the SOI strength α of 0.15 – 0.35 eVÅ from devices A-D (for fitting details and fits to additional devices, see Supplemental Material). This SOI strength is in agreement with the values extracted from level repulsion of Andreev states [20, 48] in an additional device E. Since α depends on the electric field in the wire, we expect the observed variation in the SOI strength of devices to be caused by differences in the applied gate voltages and wire diameter. Recently, the level repulsion of Andreev states in InSb nanowires covered with epitaxial aluminium has shown a SOI strength of approximately 0.1 eVÅ [20], slightly lower than we find for NbTiN covered nanowires, most likely due to

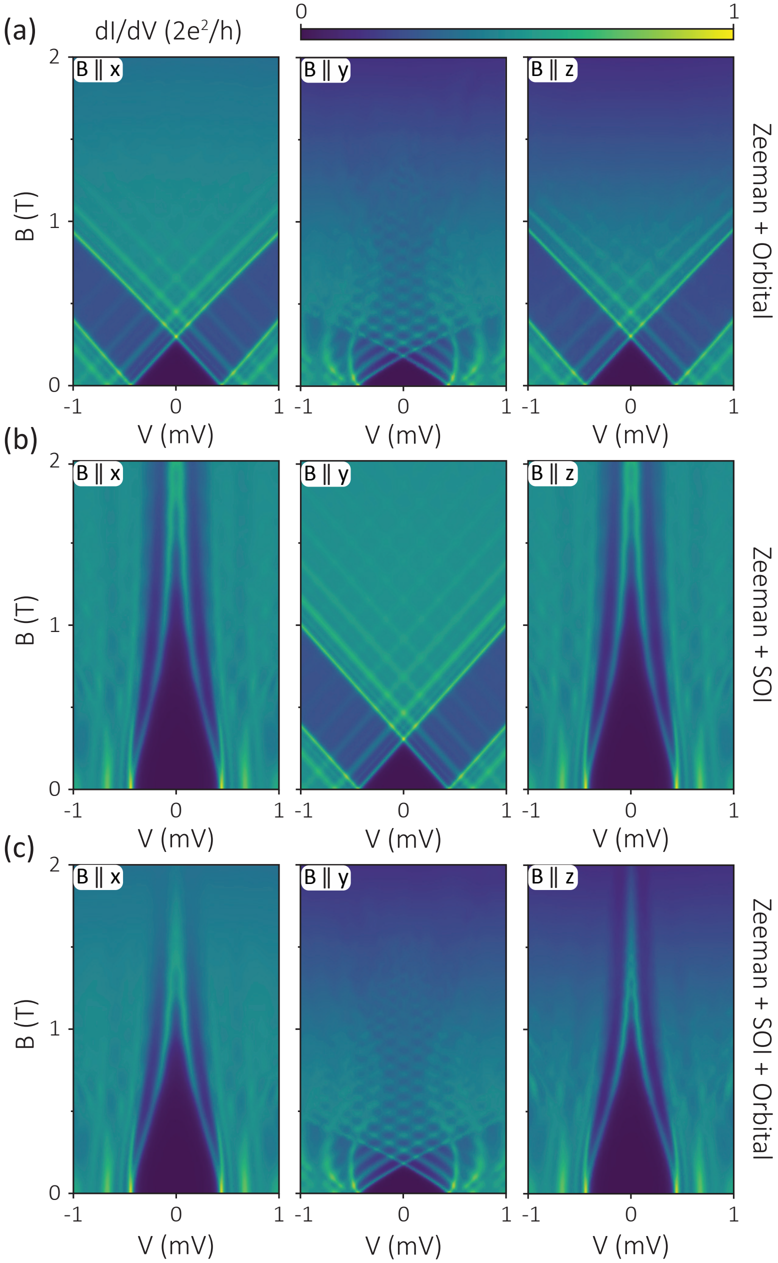

Figure 4.2: **(a)** Numerical simulations of dI/dV as a function of V and B, including the Zeeman and the orbital (Lorentz) effect of the magnetic field. **(b)** Same as (a), but including Zeeman and SOI instead of the orbital effect, reproducing the anisotropy in Fig. 4.1(e). **(c)** Same as (b), but including the Zeeman, SOI and orbital effect. The parameters used in (a)-(c) are $\mu = 5.6$ meV and $\Delta V_G = -8$ meV.

strong coupling to the aluminium superconductor, leading to stronger renormalization of the InSb material parameters [15–17, 49–51].

Orientation of the spin-orbit field

To resolve the direction of the spin-orbit field, we fix the B amplitude and continuously rotate the B direction, parametrized by the angle Θ in the zy plane [inset Fig. 4.3(a)]. Figure 4.3(a) shows the dependence of the gap on Θ, where we adjust the electric field strength in the nanowire with a voltage V_{SG} on the super gate (SG) underneath the superconductor [green in Fig. 4.1(a)]. We define the angle at which the gap is hardest as $\Theta_{\max}$ and find $\Theta_{\max} = 3 \pm 2°$ (z axis) for all V_{SG} and in multiple devices (Fig. 3 and Fig. S5) (error due to uncertainty in the extraction procedure). This is illustrated in Fig. 4.3(c), which shows horizontal line cuts for subgap bias. The largest gap for a given B amplitude is expected for $B \perp B_{\mathrm{SO}}$, indicating that $B_{\mathrm{SO}} \parallel y$, in agreement with the E-field direction

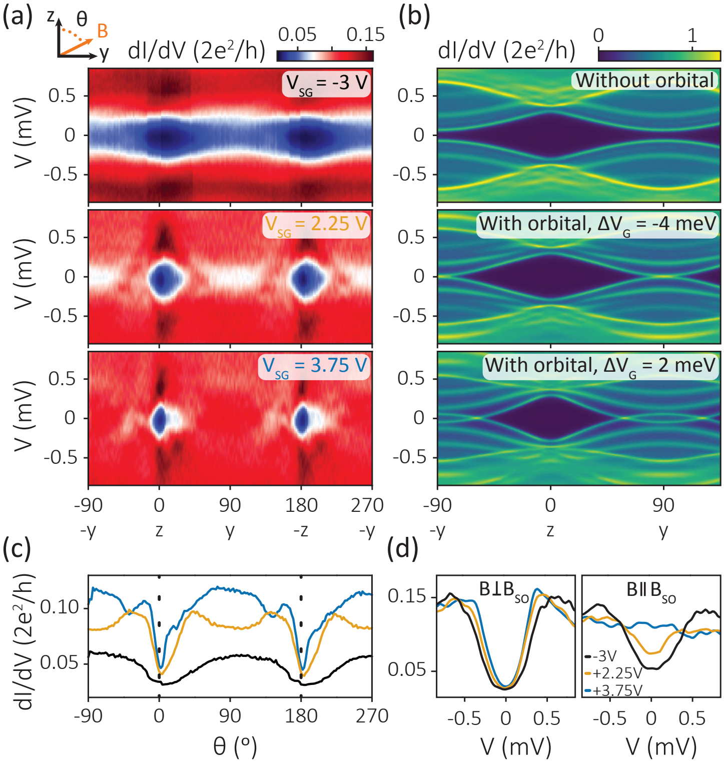

Figure 4.3: **(a)** Measured dI/dV as a function of V upon rotation of B at 0.3 T over angles Θ between z and y in device B (see Fig. S5 for the same behavior in device A). The voltage V_{SG} on the super gate (see insets) is varied in the three panels. **(b)** Simulated dI/dV as a function of Θ and V at 0.25 T. The top panel includes the Zeeman effect and SOI. The middle and bottom panels additionally include the orbital effect at two values of the potential difference ΔV_G between the top and middle of the wire. **(c)** Horizontal line cuts of (a) averaged over $|V| < 0.2$ V at $V_{\mathrm{SG}} = -3$, 2.25, and 3.75 V (black, orange, blue). Dashed lines indicate the z axis ($\Theta = 0°$). **(d)** Vertical line cuts of (a) at $\Theta = 0°$ (left) and $\Theta = 90°$ (right).

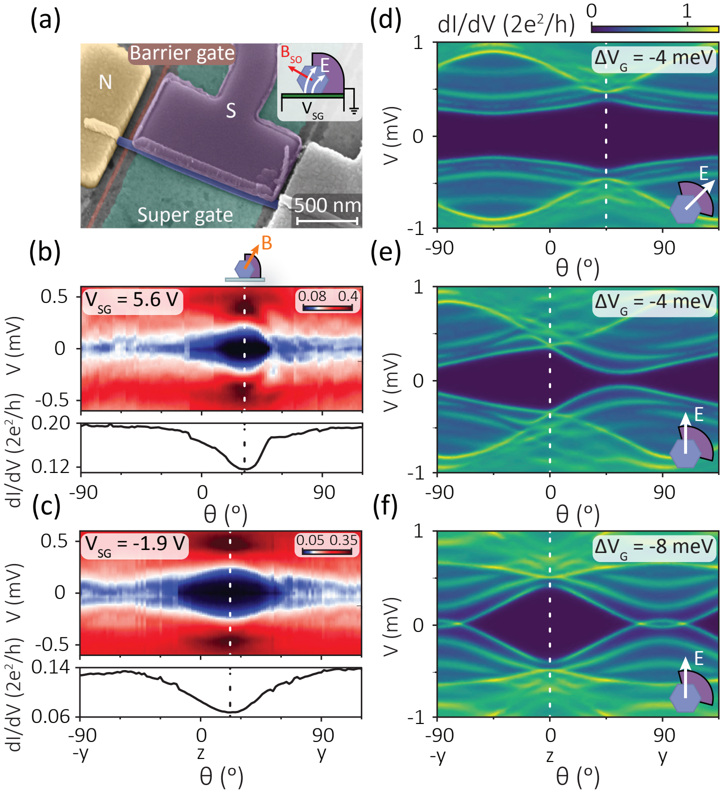

Figure 4.4: (a) Tilted view electron micrograph of Majorana nanowire device E, which is partially covered with NbTiN. In this device, the electric field E (and the associated spin-orbit field B_{SO}) can rotate away from the z axis (y axis), as illustrated in the inset. **(b)** Measured dI/dV as a function of V and angle Θ in the zy plane at $|B|$ = 75 mT and V_{SG} = 5.6 V, with a horizontal line cut averaged over $|V| < 0.25$ mV in the lower panel. The gap is maximum at $\Theta_{\max}$ = 32° as indicated by the dashed line. **(c)** Same as (b), but at V_{SG} = -1.9 V and $|B|$ = 0.15 T. $\Theta_{\max}$ is gate tuned to 22°. **(d)-(f)** Simulated dI/dV at 0.25 T at various ΔV_G (see inset) with the superconductor rotated to the side by 45° and including the Zeeman effect, SOI, and the orbital effect. The illustrations in the insets indicate the direction of E, which is rotated by 45° from z in (d).

dictated by the device geometry.

Now, we check whether the orbital effect changes $\Theta_{\max}$. The simulations in Fig. 4.3(b) show the effect of magnetic field rotation on the gap with $B_{\mathrm{SO}} \parallel y$, confirming that $\Theta_{\max}$ is, indeed, always given by the direction perpendicular to B_{SO}, i.e. $\Theta_{\max} = 0°$. Comparing the top panel (without the orbital effect) with the middle panel (with the orbital effect), we conclude that the orbital effect does not affect $\Theta_{\max}$. This conclusion also holds when we vary the potential difference ΔV_G between the middle and outer of the wire (corresponding to V_{SG}) in the middle panel and bottom panel. We note that, at ΔV_G = 2 meV (bottom panel) the wave function is moved towards the bottom of the nanowire, which increases the strength of the orbital effect by breaking the reflection symmetry about the z axis, as evidenced by the longer angle range over which the gap is closed compared to ΔV_G = -4 meV (middle panel). Experimentally, we also observe this in Fig. 4.3(a), with line cuts in Fig. 4.3(c), where the gap is closed over a significantly longer angle range with increasing V_{SG}. We note that we use small values of ΔV_G in the simulations, because we expect a weak gate response due to effective electrostatic screening by the superconductor, which covers five of the six nanowire facets [52].

Finally, we turn to a second type of device in which the superconducting film only partially covers the nanowire facets (see Fig. 4.4(a)). This partial superconductor coverage can modify the orientation of B_{SO} by changing the associated electric field direction [14], as sketched in the inset of Fig. 4.4(a). The electric field in the wire has two main origins. The first one originates from the work function difference between the superconductor and nanowire, which leads to charge redistribution. The resulting electric field is expected to rotate away from the z axis due to the partial superconductor coverage which breaks the spatial symmetry. In Fig. 4.4(b) we rotate B in the zy plane, perpendicular to the nanowire axis, and find that Θ_{max} is, indeed, no longer at zero, but at $32 \pm 2°$. The second contribution to the electric field arises from the applied V_{SG} and the electrostatic screening due to the grounded superconductor. Changing V_{SG} should, therefore, rotate the electric field for partial coverage. Indeed, we find that Θ_{max} shifts by 10° by adjusting V_{SG} by 7.5 V (see Fig. 4.4(c)). Field rotation at intermediate V_{SG} and magnetic field sweeps confirming the change of Θ_{max} are shown in the Supplemental Material. Our theory simulations confirm that Θ_{max} is still given by the direction orthogonal to B_{SO} when the electric field is not necessarily along a spatial symmetry axis of the partially covered device (see Fig. 4.4(d)) and 4(e)]. While the orbital effect does not change Θ_{max} (see Fig. 4.4(e)) and 4(f)], it can induce asymmetry in the energy spectrum around Θ_{max} resulting from wave function asymmetry when the electric field is not along the mirror plane of the device (see Fig. 4.4(b)) and Fig. 4.4(e)]. The significance of the orbital effect in our devices underlines the importance of including it in realistic simulations of Majorana nanowires.

4.3. CONCLUSION

In conclusion, the observed gap closing anisotropy for different magnetic field orientations demonstrates SOI in our Majorana nanowires, a necessary condition to create Majorana zero modes. Our experiments reveal that SOI is strongly affected by the work function difference at the nanowire-superconductor interface and the geometry of the superconductor, while electrostatic gating provides tunability of SOI.

ACKNOWLEDGEMENTS

We thank O.W.B. Benningshof, A. Geresdi, S. Goswami, M.W.A. de Moor, M. Quintero-Pérez and P. Rożek for valuable feedback and assistance. This work has been supported by the Netherlands Organization for Scientific Research (NWO), Foundation for Fundamental Research on Matter (FOM), European Research Council (ERC) and Microsoft Corporation Station Q. The work of F.N.R. and E.B. was supported by the Swedish Research Council Grant No. 642-2013-7837 and by Göran Gustafsson Foundation for Research in Natural Sciences and Medicine.

4.S. SUPPLEMENTAL MATERIAL

4.S.1. NANOWIRE GROWTH AND DEVICE FABRICATION

The InSb nanowires used here were grown using a Au-catalysed vapor-liquid-solid mechanism in a metal organic vapor phase epitaxy reactor, resulting in zinc blende nanowires grown along the [111] crystal orientation, which are free of stacking faults and dislocations [26]. Local gates, covered by a h-BN dielectric flake, were fabricated on a silicon substrate. The nanowires were individually placed over the gates using a micromanipulator [27]. The contacts are fabricated by exposing the chip to a mild oxygen plasma cleaning after resist development, followed by immersion in a saturated ammonium polysulphide solution diluted by water to a 1:200 ratio for 30 minutes at 60°C [28]. For the normal contacts, the wires are exposed to 30 seconds of in-situ helium ion milling, before evaporating 10 nm Cr and 110 nm Au. The NbTiN contacts are fabricated by exposing the nanowire to 5 seconds or Ar plasma etching at 25 W, followed by sputtering of 5 nm NbTi and 85 nm NbTiN [29, 52].

4.S.2. MEASUREMENT DETAILS

The measurements were performed in a dilution refrigerator at an electron temperature of ~50 mK using a three-axis vector magnet and standard lockin techniques.

4.S.3. SUPPLEMENTAL THEORETICAL DETAILS

Details of the tight binding simulations

The Hamiltonian defined in the main text is discretized on a lattice of a realistic nanowire geometry with a diameter of 70 nm and a length of 2 μm using a lattice spacing of 10 nm. The nanowire is covered by a 35 nm thick superconducting shell covering 3/8 of the circumference of the wire, posititioned on top of the wire (see Fig. 4.2, 4.3(b)) or rotated from the top to the side by 45° (see Fig. 4.4(b)). Transport calculations are performed by connecting the nanowire to semi-infinite normal leads, separated by a tunnel barrier on one side. The normal leads provide broadening of the peaks in the simulations [30, 31]. The superconducting proximity effect is implemented using the weak coupling approximation [6], in which the pairing gap $\Delta_0 = 0$ in the nanowire, which is tunnel coupled to a superconductor with $\Delta_0 > 0$ providing an induced gap of 0.45 meV at $B = 0\,\mathrm{T}$. The potential in the wire is given by $V(y,z) = \frac{\Delta V_G}{R}(z\cos(\Phi) + y\sin(\Phi))$, where ΔV_G is the potential difference between the middle and outer points of the wire, R is the radius of the nanowire, and Φ parametrizes the direction of the electric field $\hat{\mathbf{E}}$, which is set to $\Phi = 0°$ in all simulations, except for Fig. 4.4(d), where $\Phi = 45°$. The vector potential $\mathbf{A} = \left[B_y(z-z_0) - B_z(y-y_0), 0, B_x(y-y_0)\right]^T$ is chosen such that it does not depend on x and the offsets x_0, y_0, z_0 are chosen such that the vector potential averages to zero inside the superconductor, implying a total supercurrent of zero in the superconductor. This choice is supported by the negligible screening currents we observe in our Ginzburg-Landau simulations (see Fig. 4.S1). $\mathbf{A}$ is implemented in the tight-binding model by Peierls substitution in the hopping amplitudes [32].

Details of the Ginzburg-Landau simulations

To calculate the stray fields in the nanowire due to Meissner screening and vortex entry in the superconducting contact (results shown in Fig. 4.S1), we have performed simulations on the Ginzburg-Landau model [33] in a realistic three-dimensional geometry using the dimensions of device A. We used a penetration depth $\lambda = 290$ nm and a Ginzburg-Landau parameter $\kappa = \lambda/\xi = 50$, in line with the values expected for our NbTiN film, which has a room temperature resistivity of 95 $\mu\Omega\,\mathrm{cm}$ and a critical temperature of 15 K. The Ginzburg-Landau functional is discretized both inside the superconducting contact as well as in its surrounding space [34] using a second-order finite difference scheme at a maximum internode distance of 0.01λ. The resulting energy functional is minimized using the nonlinear conjugate gradient method and the code is implemented on a NVidia CUDA architecture with high parallelization. We obtain the energy of states with vortices at finite magnetic fields by first introducing artificial perturbations near the sample boundary, followed by energy minimization to find the local minimum corresponding to a specific number of vortices. The optimal number of vortices at a certain magnetic field is then determined by finding the state with the lowest energy globally. We note that non-optimal amounts of vortices can be metastable due to significant Bean-Livingston barriers for vortex entry, so the actual number of vortices is hysteretic and depends on the dynamics of the magnetic field.

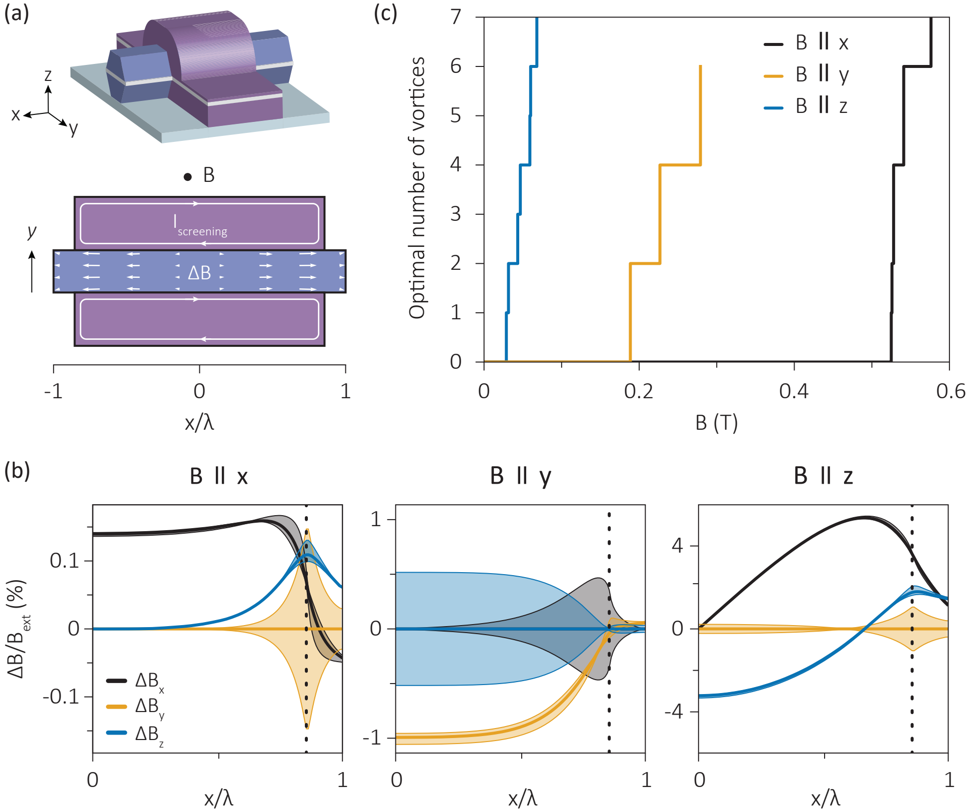

Figure 4.S1: Ginzburg-Landau simulations. **(a)** The top panel shows the schematic of the geometry used for Ginzburg-Landau simulations: a superconducting film covering a hexagonal nanowire. In a superconductor exposed to an external magnetic field B we calculate the screening currents $I_{\text{screening}}$, which induce stray magnetic fields ΔB in the nanowire. In the lower panel we show ΔB in the xy-plane in the middle of the nanowire, as indicated by the white line in (a). The bottom panel shows a top view of this xy-plane, where the arrows indicate the x and y components of ΔB in the nanowire for $B \parallel z$. **(b)** The x, y and z-components (black, yellow, blue) of ΔB relative to the external field B as a function of the position x along the nanowire axis, where $x = 0$ corresponds to the middle of the superconducting contact. The lines show the mean stray field and the shaded regions are bounded by the minimum and maximum stray field found along the nanowire width at a particular x. The end of the superconducting film is indicated by the dashed line. B is along x, y and z (left, middle and right panel). Since the device dimensions are comparable to the penetration depth $\lambda = 290$ nm, the magnetic screening in the superconductor is incomplete, leading to small screening currents and stray fields of at most 4% of B. These modifications are much smaller and do not match the anisotropy we observe in the measurements, which excludes Meissner screening as the origin of the observed anisotropic gap closing. We note that we have also evaluated ΔB at several different magnitudes of B as well as in the presence of vortices and find relative stray fields of very comparable magnitude. **(c)** Energetically most favorable number of vortices as a function of B along x, y and z (black, yellow, blue). Vortices form far more easily for $B \parallel z$. An anisotropic gap closing due to vortices near the nanowire would therefore cause the fastest gap closing along z, contrary to the anisotropic gap closing we observe, where the gap closes fastest for $B \parallel y$ [see e.g. Fig. 4.1(e)]. Furthermore, for $B \parallel y$ vortices only start to appear at $B > 0.2$ T, while the gap is already strongly suppressed at 0.2 T [see e.g. Fig. 4.1(e)], which excludes vortex formation as the origin of the gap closing for $B \parallel y$ and indicates that vortices do not have a strong effect on the size of the induced gap.

4.S.4. EXTRACTION OF SOI STRENGTH

Determination of SOI strength α from gap closing

In a Majorana nanowire the SOI strength α determines the shape of the gap closing along B-directions perpendicular to the spin-orbit field B_{SO} [46, 47] [see Fig. 4.S2(a)]. To find an analytical expression for the dependence of the gap closing on α, we start from the conventional one-dimensional Majorana nanowire Hamiltonian [4, 5], in which the gap size is given by the lowest energy eigenstate:

$$\Delta(B) = \min\left(\epsilon^2 + \epsilon_{\mathrm{SO}}^2 + \epsilon_Z^2 + \Delta(0)^2 \pm 2\sqrt{\epsilon^2(\epsilon_{\mathrm{SO}}^2 + \epsilon_Z^2) + \epsilon_Z^2\Delta(0)^2}\right)^{\frac{1}{2}} \tag{4.S1}$$

Here, $\epsilon = \hbar^2 k^2/2m^* - \mu$ represents the kinetic energy, with k the electron wave vector and $m^* = 0.015 m_e$ the effective mass. $\epsilon_{\mathrm{SO}} = \alpha k$ is the SOI term with α the SOI strength. $\epsilon_Z = \frac{1}{2} g \mu_B B$ is the Zeeman energy, with g the Landé g-factor and μ_B the Bohr magneton. $\Delta(0)$ is the induced superconducting gap at $B = 0$ T, which we measure in the experiments (as indicated in Fig. 4.1(b)).

For $B \parallel B_{\mathrm{SO}}$ (y-axis) and neglecting the orbital effect the gap closes linearly with the Zeeman energy due to tilting of the bands [24, 25]:

$$\Delta(B) = \Delta(0) - \frac{1}{2} g \mu_B B \tag{4.S2}$$

The orbital effect significantly enhances the gap closing in our devices [cf. Fig. 4.1,4.2], with a strong dependence on the potential difference ΔV_G in the three-dimensional model. Although the value of ΔV_G in our devices is unknown, we find that the orbital effect can be effectively taken into account in the one-dimensional model by adjusting the g-factor to match the gap closing along B_{SO}, where SOI disappears and only the Zeeman and orbital effect contribute to the gap closing. We emphasize that the g-factor extracted from the fits therefore does not correspond to the pure Zeeman g-factor used in our tight-binding calculations. The validity of this approximation is demonstrated in Fig. 4.S2(b), where the color map shows the gap closing resulting from our numerical calculations on the three-dimensional tight-binding model (taking the orbital effect into account and using $g = 50$) and the dashed white lines show the gap given by equation 4.S1 for $B \parallel x$ and by equation 4.S2 for $B \parallel y$ using $g = 65$.

To extract α from our measurements, we fit the model given by equation (S1) and (S2) to the measured gap closing both along the wire and along B_{SO} simultaneously. We prevent overfitting by independently constraining the free parameters. First, g is determined by the gap closing along B_{SO}, which only depends on the Zeeman effect. Then, μ follows from the critical field B_C along x, where $\frac{1}{2} g \mu_B B_C = \sqrt{\Delta(0)^2 + \mu^2}$ [4, 5] (note that B_C does not depend on α). The SOI strength α is now the only free parameter left to fit the curvature of the gap closing along x. This procedure is applied to four devices [see Fig. 4.1(f), Fig. 4.S4(b),(c), and Fig. 4.S7], resulting in a SOI strength of 0.15 – 0.35 eVÅ, corresponding to a spin-orbit energy $E_{\mathrm{SO}} = m^* \alpha^2/2\hbar^2$ of 20 – 120 μeV. The remaining parameters used for the fit of device A shown in Fig. 4.1(e) are $g = 90$, $\mu = 1.4$ meV. The values of g and μ found for the remaining devices are given in Fig. 4.S4. Table 4.S1 shows the range of values of the fitting parameters for which good fits can be obtained. Since α depends on the electric field in the wire, we expect the observed variation in the

Table 4.S1: Results of gap closing fitting procedure

	Device A	Device B	Device C	Device D
g	90 ± 10	60 ± 20	85 ± 5	160 ± 20
μ (meV)	1.5 ± 0.4	1.8 ± 0.8	2.75 ± 0.25	2.8 ± 0.6
α (eVÅ)	0.15 ± 0.05	0.3 ± 0.1	0.35 ± 0.05	0.35 ± 0.05

SOI strength of devices to be caused by differences in the applied gate voltages and wire diameter.

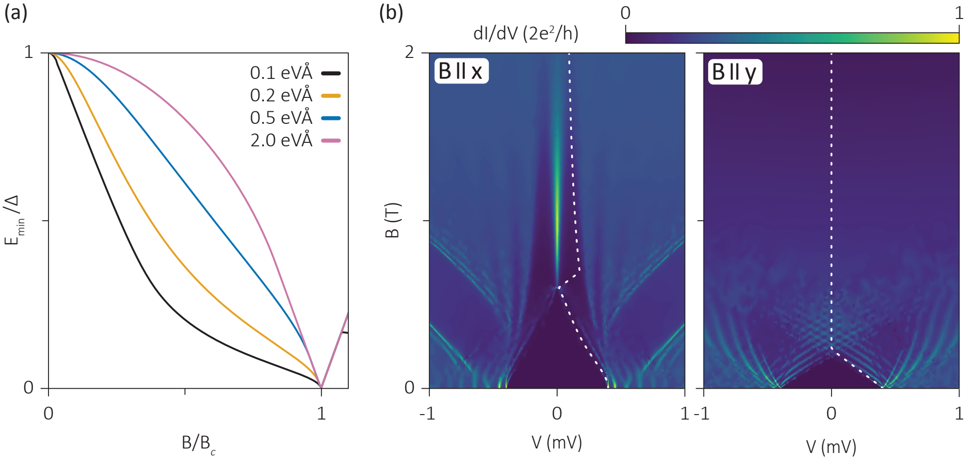

Figure 4.S2: Extracting SOI strength from gap closing curvature. **(a)** Lowest energy state E_{min} determining the gap in the one-dimensional model given by equation S1 as a function of magnetic field, B, in units of the critical field $B_c = \sqrt{\Delta^2 + \mu^2}$ for various spin-orbit strengths α. The curvature of the gap closing is strongly affected by α. Stronger SOI counteracts the Zeeman effect up to larger B/B_c, leading initially to a slow gap closing, followed by a sharp gap closing when approaching the critical field, where the lowest energy state is at $k \approx 0$ for which $B_{\text{SO}}(k)$ vanishes. The remaining parameters are: $\Delta(0) = 1$ meV, $\mu = 2$ meV. **(b)** Comparison of the numerical simulations on the 3D tight binding model, including the orbital effect (color map), with the 1D model given by equations (S1) and (S2) which does not account for the orbital effect (dashed lines). By adjusting the g-factor used in the Majorana nanowire model from $g = 50$ to 65 to match the gap closing for $B \parallel B_{\text{SO}}$, keeping all other parameters the same in both models, we find good agreement for the gap closing for $B \parallel x$. We use this same approach to take the orbital effect into account in an effective manner in fits of the experimentally observed gap closing. The remaining parameters used in the simulations shown here are $\Delta(0) = 0.45$ meV, $\mu = 0.95$ meV, $\alpha = 0.2$ eVÅ, $\Delta V_G = -10$ meV.

Estimation of SOI strength based on level repulsion
SOI induces coupling between states of different momentum and spin in finite length Majorana nanowires, which leads to level repulsion when energy levels are nearly degenerate [48]. Recently this level repulsion between longitudinal states within the same subband was used to estimate a SOI strength in epitaxial Al-InSb nanowires [20]. Here, we follow the same procedure to estimate the SOI strength in a seperate device with a NbTiN superconductor that exhibits such level repulsion. We consider a low energy model of two levels dispersing in the magnetic field due to the Zeeman effect, coupled to each other by SOI with the matrix element δ_{SO}:

$$H = \begin{bmatrix} E_0 + \frac{1}{2}g_0\mu_B B & \delta_{\mathrm{SO}} \\ \delta_{\mathrm{SO}} & E_1 - \frac{1}{2}g_1\mu_B B \end{bmatrix} \tag{4.S3}$$

We fit the eigenenergies of H to our experimental data (see Fig.)4.S3(a)] to extract δ_{SO}. The precise value of the coupling parameter δ_{SO} depends not only on α, but also on the details of the confinement and on the coupling strength to the superconductor [20]. A rough estimate, with reasonable agreement to numerical simulations, was proposed to be: $2\delta_{\mathrm{SO}} = \alpha\pi/L$, where L is the length of the wire. The extracted δ_{SO} is shown in Fig. 4.S3(b) for various values of the super gate voltage V_{SG}. As V_{SG} becomes more negative, we see an increase in δ_{SO}, consistent with an increasing electric field in the nanowire. We can estimate $\alpha \sim 0.4 - 0.55$ eVÅ. Considering the uncertainty in the relation between α and δ_{SO} and variation in the electrostatic environment of different devices, this magnitude is in line with our estimation based on the gap closing curvature.

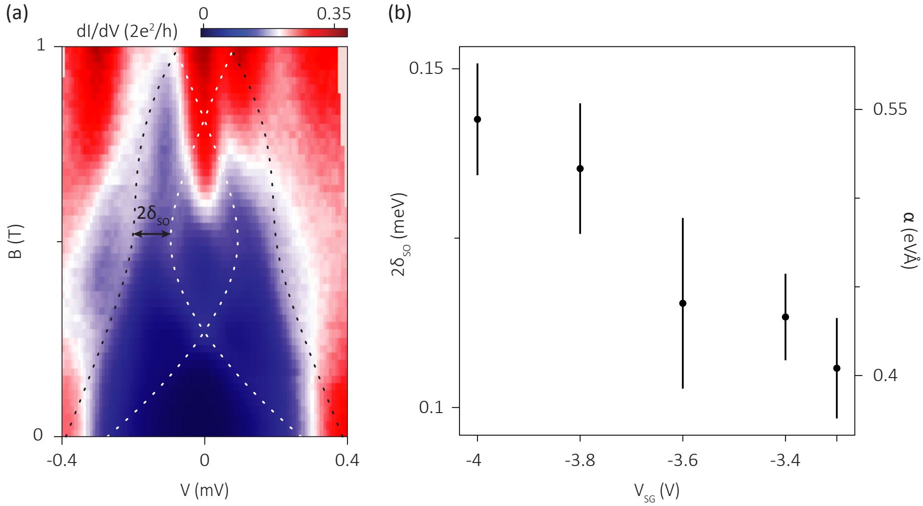

Figure 4.S3: Extracting the SOI strength from level repulsion. **(a)** dI/dV as a function of V and B at V_{SG} = -3.3 V, measured in device E. Two Andreev states come down from the gap edge and exhibit an avoided crossing around $B = 0.5$ T. The dashed lines indicate fits to the solution of equation (S3). The extracted coupling δ_{SO} between the Andreev levels is indicated by the arrow. **(b)** $2\delta_{SO}$ as a function of V_{SG}. The right axis shows the estimation of the SOI strength using $\alpha = 2\delta_{SO}L/\pi$ for the 1.2 μm long superconducting region. The errorbars show the standard deviation in δ_{SO} obtained from the fits.

4.S.5. SUPPLEMENTAL EXPERIMENTAL DATA

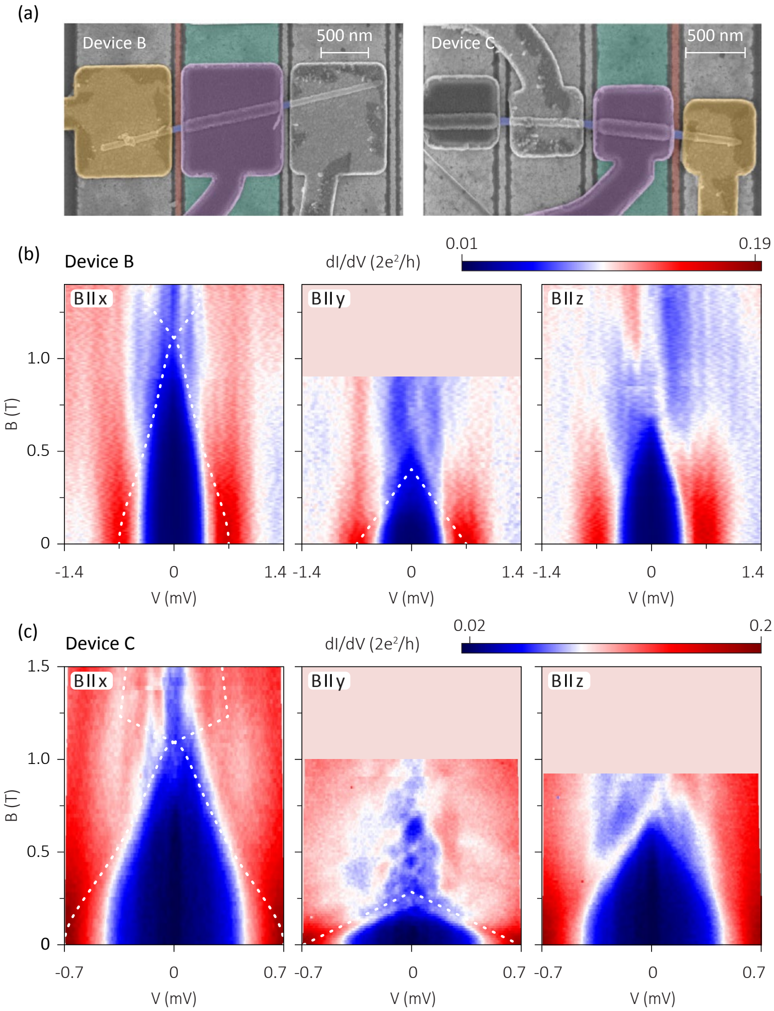

Figure 4.S4: Anisotropic gap closing in additional devices. (a) False colored scanning electron micrographs of additional devices B (used in Fig. 3) and C, showing anisotropy similar to the device in Fig. 4.1(e). **(b,c)** Differential conductance, dI/dV, as a function of the magnetic field, B, along the x, y, and z-axes (from left to right). The gap closes at much lower fields along the y-axis than the x and z-axes in all devices fully covered with the superconductor. The white dashed lines indicate fits to the gap closing from which we extract a spin-orbit strength α of 0.3 ± 0.1 eVÅ [for (b)] and 0.35 ± 0.05 eVÅ [for (c)], with g = 60, 85 and μ = 1.8, 2.7 meV as the remaining fit parameters for (b), (c) respectively. We note that we do not observe clear reopening of the gap in all devices, which theoretical studies have attributed to the negligible contribution to the tunneling conductance of the states associated with the gap reopening due to their spatial wave function extension into the middle of the wire leading to minimal weight near the tunnel barrier [35–37, 45]. The super gate was set to V_{SG} = -1.5 V, -2.6 V in (b), (c) respectively.

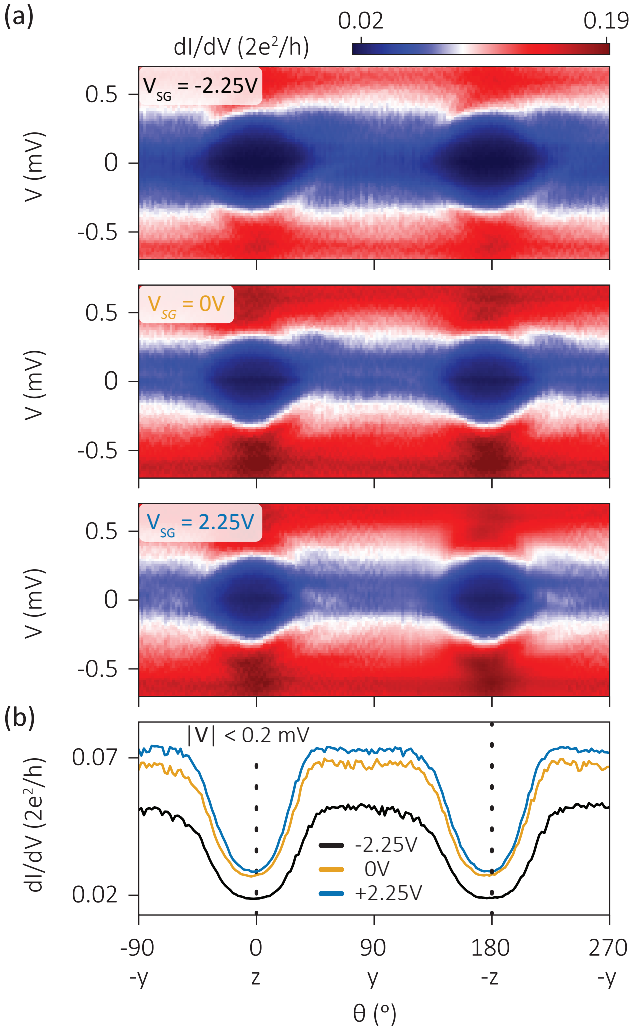

Figure 4.S5: Gap dependence on magnetic field orientation in *zy*-plane in device A. (a) Differential conductance, dI/dV, as a function of bias voltage, V, upon rotation of the magnetic field at 0.25 T over angles Θ between z and y with different voltages on the super gate V_{SG} in the three panels. This is the same device as presented in Fig 1. **(b)** Horizontal line cuts of (a) averaged over a bias range $|V| < 0.2$ mV, showing that the hardest gap is at $\Theta = 0$, and increased V_{SG} suppresses the gap when B is along y, the same behaviors observed in device B (see Fig. 3)].

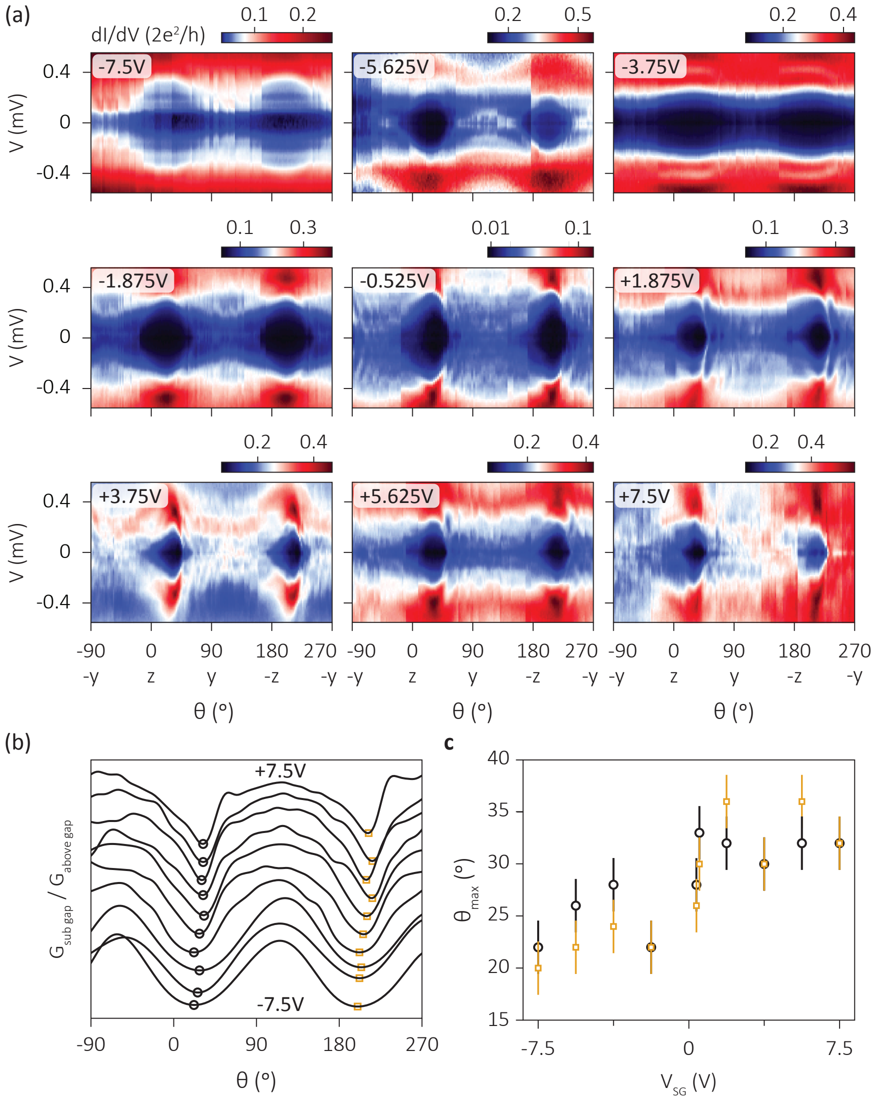

Figure 4.S6: Dependence of spin-orbit direction on super gate voltage in device D, which is partially covered by NbTiN. **(a)** Differential conductance, dI/dV, as a function of bias voltage, V, and angle Θ between z and y at various values of V_{SG} as indicated in the insets. The data is measured at slightly different field magnitudes between 0.1 and 0.2 T for the different V_{SG} to optimize the anisotropy between y and z. The discontinuities in dI/dV that are visible for some of the scans are likely caused by charge fluctuations in the dielectric environment. **(b)** The ratio between the sub gap conductance (averaged over $|V| < 0.2$ V) and the above gap conductance (averaged over $|V| > 0.4$ V) with V_{SG} increasing from bottom to top and offset for clarity. The minima of the curves signify the angle at which the gap is hardest, Θ_{max}, which shifts to higher angles at increasing V_{SG}. A lowpass filter is applied along the Θ direction to suppress the effect of the charge instabilities (this procedure does not affect the minima for the measurements without charge instabilities, such as in Fig. 4). **(c)** Θ_{max} as determined from the first (black) and second (yellow) minimum of the curves in (b) as a function of V_{SG}. The second minima (yellow) signify Θ_{max} at negative B and are subtracted by 180° accordingly.

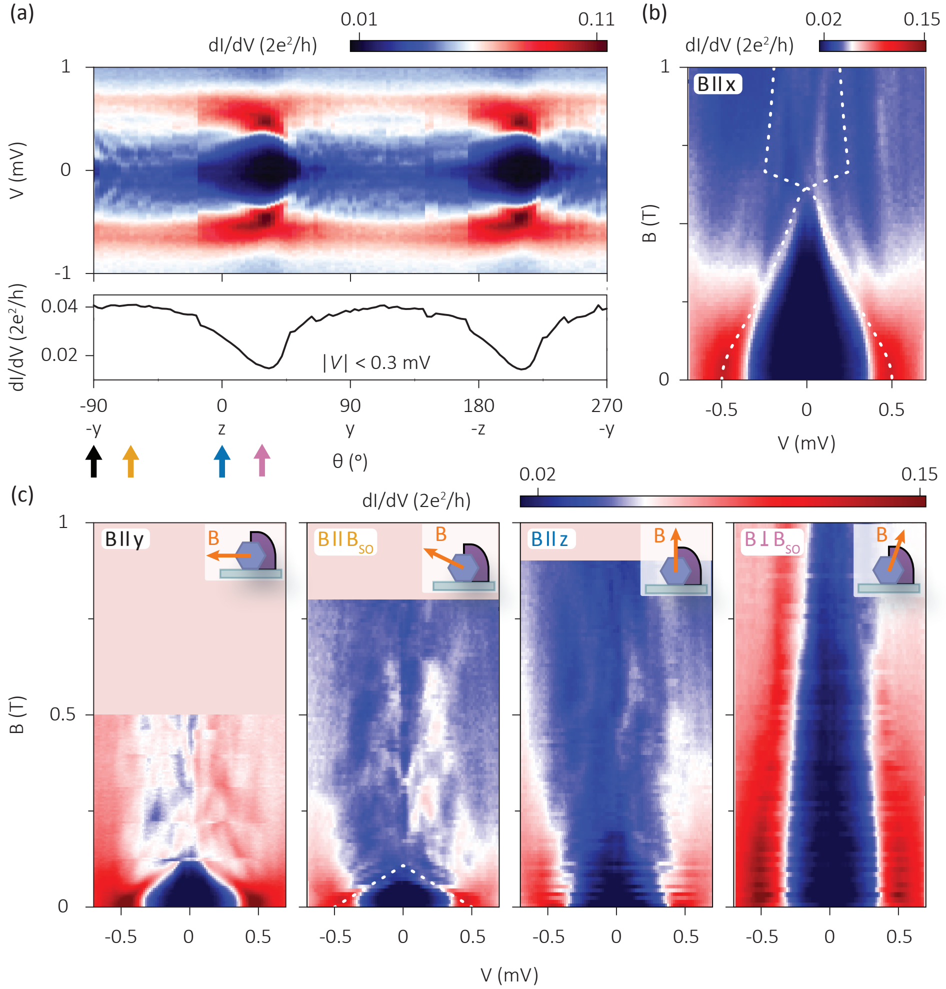

Figure 4.S7: Gap dependence on magnetic field orientation in device E, which is partially covered by NbTiN. **(a)** Differential conductance, dI/dV, as a function of the angle Θ between the z and y-axes at $V_{SG} = 0.525$ V and $B = 0.1$ T, with a horizontal line cut averaged over a bias range $|V| < 0.3$ mV in the lower panel. **(b)** dI/dV as a function of the magnetic field B along the nanowire axis, with the white dashed lines showing the fit to the gap closing, resulting in a spin-orbit strength α of 0.35 ± 0.05 eVÅ (the other fit parameters are $g = 160$, see $B \parallel B_{SO}$ in (c), and $\mu = 2.8$ meV). **(c)** dI/dV as a function of B along y, B_{SO}, z and perpendicular to B_{SO} from left to right, with the colors in the headers corresponding to the colored arrows in (a). The illustrations in the insets indicate the direction of the magnetic field. Note that due to the changed orientation of B_{SO}, B-sweeps along directions rotated by ~25° from the y-axis (second panel, $B \parallel B_{SO}$) and the z-axis (right panel, $B \perp B_{SO}$) now exhibit strong anisotropy, instead of the y and z-axes which show strong anisotropy in devices symmetrically covered by NbTiN.

REFERENCES

[1] A. Y. Kitaev, *Unpaired Majorana fermions in quantum wires,* Phys. Usp. **44**, 131 (2001).

[2] L. Fu and C. L. Kane, *Superconducting proximity effect and Majorana fermions at the surface of a topological insulator,* Phys. Rev. Lett. **100**, 096407 (2008).

[3] C. Nayak, S. H. Simon, A. Stern, M. Freedman, and S. Das Sarma, *Non-Abelian anyons and topological quantum computation,* Rev. Mod. Phys. **80**, 1083 (2008).

[4] R. M. Lutchyn, J. D. Sau, and S. Das Sarma, *Majorana fermions and a topological phase transition in semiconductor-superconductor heterostructures,* Phys. Rev. Lett. **105**, 077001 (2010).

[5] Y. Oreg, G. Refael, and F. von Oppen, *Helical liquids and Majorana bound states in quantum wires,* Phys. Rev. Lett. **105**, 177002 (2010).

[6] B. Nijholt and A. R. Akhmerov, *Orbital effect of magnetic field on the Majorana phase diagram,* Phys. Rev. B **93**, 235434 (2016).

[7] V. Mourik, K. Zuo, S. M. Frolov, S. R. Plissard, E. P. A. M. Bakkers, and L. P. Kouwenhoven, *Signatures of Majorana fermions in hybrid superconductor-semiconductor nanowire devices,* Science **336**, 1003 (2012).

[8] S. M. Albrecht, A. P. Higginbotham, M. Madsen, F. Kuemmeth, T. S. Jespersen, J. Nygård, P. Krogstrup, and C. M. Marcus, *Exponential protection of zero modes in Majorana islands,* Nature **531**, 206 (2016).

[9] M. T. Deng, S. Vaitiekėnas, E. B. Hansen, J. Danon, M. Leijnse, K. Flensberg, J. Nygård, P. Krogstrup, and C. M. Marcus, *Majorana bound state in a coupled quantum-dot hybrid-nanowire system,* Science **354**, 1557 (2016).

[10] Ö. Gül, H. Zhang, J. D. S. Bommer, M. W. A. de Moor, D. Car, S. R. Plissard, E. Bakkers, A. Geresdi, K. Watanabe, T. Taniguchi, and L. P. Kouwenhoven, *Ballistic Majorana nanowire devices,* Nat. Nanotech. **13**, 192 (2018).

[11] H. Zhang, C.-X. Liu, S. Gazibegovic, D. Xu, J. A. Logan, G. Wang, N. van Loo, J. D. S. Bommer, M. W. A. de Moor, D. Car, R. L. M. Op het Veld, P. J. van Veldhoven, S. Koelling, M. A. Verheijen, M. Pendharkar, D. J. Pennachio, B. Shojaei, J. S. Lee, C. J. Palmstrøm, E. P. A. M. Bakkers, S. D. Sarma, and L. P. Kouwenhoven, *Quantized Majorana conductance,* arXiv preprint arXiv:1710.10701 (2017).

[12] R. M. Lutchyn, E. P. A. M. Bakkers, L. P. Kouwenhoven, P. Krogstrup, C. M. Marcus, and Y. Oreg, *Majorana zero modes in superconductor-semiconductor heterostructures,* Nat. Rev. Mater. **3**, 52 (2018).

[13] R. Aguado, *Majorana quasiparticles in condensed matter,* Riv. Nuovo Cimento **40**, 523 (2017).

[14] A. Vuik, D. Eeltink, A. R. Akhmerov, and M. Wimmer, *Effects of the electrostatic environment on the Majorana nanowire devices,* New J. Phys. **18**, 033013 (2016).

[15] A. E. Antipov, A. Bargerbos, G. W. Winkler, B. Bauer, E. Rossi, and R. M. Lutchyn, *Effects of gate-induced electric fields on semiconductor Majorana nanowires,* Phys. Rev. X **8**, 031041 (2018).

[16] B. D. Woods, T. D. Stanescu, and S. Das Sarma, *Effective theory approach to the Schrödinger-Poisson problem in semiconductor Majorana devices,* Phys. Rev. B **98**, 035428 (2018).

[17] A. E. G. Mikkelsen, P. Kotetes, P. Krogstrup, and K. Flensberg, *Hybridization at superconductor-semiconductor interfaces,* Phys. Rev. X **8**, 031040 (2018).

[18] C. Fasth, A. Fuhrer, L. Samuelson, V. N. Golovach, and D. Loss, *Direct measurement of the spin-orbit interaction in a two-electron InAs nanowire quantum dot,* Phys. Rev. Lett. **98**, 266801 (2007).

[19] S. Nadj-Perge, V. S. Pribiag, J. W. G. van den Berg, K. Zuo, S. R. Plissard, E. P. A. M. Bakkers, S. M. Frolov, and L. P. Kouwenhoven, *Spectroscopy of spin-orbit quantum bits in indium antimonide nanowires,* Phys. Rev. Lett. **108**, 166801 (2012).

[20] M. W. A. de Moor, J. D. S. Bommer, D. Xu, G. W. Winkler, A. E. Antipov, A. Bargerbos, G. Wang, N. van Loo, R. L. M. O. het Veld, S. Gazibegovic, D. Car, J. A. Logan, M. Pendharkar, J. Sue Lee, E. P. A. M. Bakkers, C. J. Palmstrøm, R. M. Lutchyn, L. P. Kouwenhoven, and H. Zhang, *Electric field tunable superconductor-semiconductor coupling in Majorana nanowires,* New J. of Phys. **20**, 103049 (2018).

[21] A. E. Hansen, M. T. Björk, C. Fasth, C. Thelander, and L. Samuelson, *Spin relaxation in InAs nanowires studied by tunable weak antilocalization,* Phys. Rev. B **71**, 205328 (2005).

[22] I. van Weperen, B. Tarasinski, D. Eeltink, V. S. Pribiag, S. R. Plissard, E. P. A. M. Bakkers, L. P. Kouwenhoven, and M. Wimmer, *Spin-orbit interaction in InSb nanowires,* Phys. Rev. B **91**, 201413 (2015).

[23] J. Kammhuber, M. C. Cassidy, F. Pei, M. P. Nowak, A. Vuik, O. Gül, D. Car, S. R. Plissard, E. P. A. M. Bakkers, M. Wimmer, and L. P. Kouwenhoven, *Conductance through a helical state in an indium antimonide nanowire,* Nat. Commun. **8**, 478 (2017).

[24] J. Osca, D. Ruiz, and L. Serra, *Effects of tilting the magnetic field in one-dimensional Majorana nanowires,* Phys. Rev. B **89**, 245405 (2014).

[25] S. Rex and A. Sudbø, *Tilting of the magnetic field in Majorana nanowires: Critical angle and zero-energy differential conductance,* Phys. Rev. B **90**, 115429 (2014).

[26] D. Car, J. Wang, M. A. Verheijen, E. P. A. M. Bakkers, and S. R. Plissard, *Rationally designed single-crystalline nanowire networks,* Adv. Mater. **26**, 4875 (2014).

[27] K. Flöhr, M. Liebmann, K. Sladek, H. Y. Günel, R. Frielinghaus, F. Haas, C. Meyer, H. Hardtdegen, T. Schäpers, D. Grützmacher, and M. Morgenstern, *Manipulating InAs nanowires with submicrometer precision,* Rev. Sci. Instrum. **82**, 113705 (2011).

[28] D. B. Suyatin, C. Thelander, M. T. Björk, I. Maximov, and L. Samuelson, *Sulfur passivation for ohmic contact formation to InAs nanowires,* Nanotechnology **18**, 105307 (2007).

[29] O. Gül, H. Zhang, F. K. de Vries, J. van Veen, K. Zuo, V. Mourik, S. Conesa-Boj, M. P. Nowak, D. J. van Woerkom, M. Quintero-Pérez, M. C. Cassidy, A. Geresdi, S. Koelling, D. Car, S. R. Plissard, E. P. A. M. Bakkers, and L. P. Kouwenhoven, *Hard superconducting gap in InSb nanowires,* Nano Lett. **17**, 2690 (2017).

[30] C.-X. Liu, J. D. Sau, and S. Das Sarma, *Role of dissipation in realistic Majorana nanowires,* Phys. Rev. B **95**, 054502 (2017).

[31] J. Danon, E. B. Hansen, and K. Flensberg, *Conductance spectroscopy on Majorana wires and the inverse proximity effect,* Phys. Rev. B **96**, 125420 (2017).

[32] D. R. Hofstadter, *Energy levels and wave functions of Bloch electrons in rational and irrational magnetic fields,* Phys. Rev. B **14**, 2239 (1976).

[33] W. D. Gropp, H. G. Kaper, G. K. Leaf, D. M. Levine, M. Palumbo, and V. M. Vinokur, *Numerical simulation of vortex dynamics in type-II superconductors,* J. Comput. Phys. **123**, 254 (1996).

[34] Q. Du and X. Wu, *Numerical solution of the three-dimensional Ginzburg–Landau models using artificial boundary,* SIAM J. Numer. Anal. **36**, 1482 (1999).

[35] E. Prada, P. San-Jose, and R. Aguado, *Transport spectroscopy of NS nanowire junctions with Majorana fermions,* Phys. Rev. B **86**, 180503 (2012).

[36] F. Pientka, G. Kells, A. Romito, P. W. Brouwer, and F. von Oppen, *Enhanced zero-bias Majorana peak in the differential tunneling conductance of disordered multisubband quantum-wire/superconductor junctions,* Phys. Rev. Lett. **109**, 227006 (2012).

[37] T. D. Stanescu, S. Tewari, J. D. Sau, and S. Das Sarma, *To close or not to close: The fate of the superconducting gap across the topological quantum phase transition in Majorana-carrying semiconductor nanowires,* Phys. Rev. Lett. **109**, 266402 (2012).

[38] D. J. van Woerkom, A. Geresdi, and L. P. Kouwenhoven, *One minute parity lifetime of a NbTiN Cooper-pair transistor,* Nat. Phys. **11**, 547 (2015).

[39] W. Chang, S. M. Albrecht, T. S. Jespersen, F. Kuemmeth, P. Krogstrup, J. Nygård, and C. M. Marcus, *Hard gap in epitaxial semiconductor-superconductor nanowires,* Nat. Nanotech. **10**, 232 (2015).

[40] S. Gazibegovic, D. Car, H. Zhang, S. C. Balk, J. A. Logan, M. W. A. de Moor, M. C. Cassidy, R. Schmits, D. Xu, G. Wang, P. Krogstrup, R. L. M. Op het Veld, K. Zuo, Y. Vos, J. Shen, D. Bouman, B. Shojaei, D. Pennachio, J. S. Lee, P. J. van Veldhoven,

S. Koelling, M. A. Verheijen, L. P. Kouwenhoven, C. J. Palmstrøm, and E. P. A. M. Bakkers, *Epitaxy of advanced nanowire quantum devices,* Nature **548**, 434 (2017).

[41] S. Takei, B. M. Fregoso, H.-Y. Hui, A. M. Lobos, and S. Das Sarma, *Soft superconducting gap in semiconductor Majorana nanowires,* Phys. Rev. Lett. **110**, 186803 (2013).

[42] C. E. Pryor and M. E. Flatté, *Landé g factors and orbital momentum quenching in semiconductor quantum dots,* Phys. Rev. Lett. **96**, 026804 (2006).

[43] F. Qu, J. van Veen, F. K. de Vries, A. J. A. Beukman, M. Wimmer, W. Yi, A. A. Kiselev, B.-M. Nguyen, M. Sokolich, M. J. Manfra, F. Nichele, C. M. Marcus, and L. P. Kouwenhoven, *Quantized conductance and large g-factor anisotropy in InSb quantum point contacts,* Nano Lett. **16**, 7509 (2016).

[44] C. W. Groth, M. Wimmer, A. R. Akhmerov, and X. Waintal, *Kwant: a software package for quantum transport,* New J. Phys. **16**, 063065 (2014).

[45] C.-X. Liu, J. D. Sau, T. D. Stanescu, and S. Das Sarma, *Conductance smearing and anisotropic suppression of induced superconductivity in a Majorana nanowire,* Phys. Rev. B **99**, 024510 (2019).

[46] B. van Heck, J. I. Väyrynen, and L. I. Glazman, *Zeeman and spin-orbit effects in the Andreev spectra of nanowire junctions,* Phys. Rev. B **96**, 075404 (2017).

[47] H. Pan, J. D. Sau, T. D. Stanescu, and S. Das Sarma, *Curvature of gap closing features and the extraction of Majorana nanowire parameters,* Phys. Rev. B **99**, 054507 (2019).

[48] T. D. Stanescu, R. M. Lutchyn, and S. Das Sarma, *Dimensional crossover in spin-orbit-coupled semiconductor nanowires with induced superconducting pairing,* Phys. Rev. B **87**, 094518 (2013).

[49] T. D. Stanescu, R. M. Lutchyn, and S. Das Sarma, *Majorana fermions in semiconductor nanowires,* Phys. Rev. B **84**, 144522 (2011).

[50] W. S. Cole, S. Das Sarma, and T. D. Stanescu, *Effects of large induced superconducting gap on semiconductor Majorana nanowires,* Phys. Rev. B **92**, 174511 (2015).

[51] C. Reeg, D. Loss, and J. Klinovaja, *Metallization of a Rashba wire by a superconducting layer in the strong-proximity regime,* Phys. Rev. B **97**, 165425 (2018).

[52] H. Zhang, O. Gül, S. Conesa-Boj, M. P. Nowak, M. Wimmer, K. Zuo, V. Mourik, F. K. de Vries, J. van Veen, M. W. A. de Moor, J. D. S. Bommer, D. J. van Woerkom, D. Car, S. R. Plissard, E. P. A. M. Bakkers, M. Quintero-Pérez, M. C. Cassidy, S. Koelling, S. Goswami, K. Watanabe, T. Taniguchi, and L. P. Kouwenhoven, *Ballistic superconductivity in semiconductor nanowires,* Nat. Commun. **8**, 16025 (2017).

5

ELECTRIC FIELD TUNABLE SUPERCONDUCTOR-SEMICONDUCTOR COUPLING IN MAJORANA NANOWIRES

Michiel W.A. de Moor*, Jouri D.S. Bommer*, Di Xu*, Georg W. Winkler, Andrey E. Antipov, Arno Bargerbos, Guanzhong Wang, Nick van Loo, Roy L. M. Op het Veld, Sasa Gazibegovic, Diana Car, John A. Logan, Mihir Pendharkar, Joon Sue Lee, Erik P. A. M. Bakkers, Chris J. Palmstrøm, Roman M. Lutchyn, Leo P. Kouwenhoven, Hao Zhang

We study the effect of external electric fields on superconductor-semiconductor coupling by measuring the electron transport in InSb semiconductor nanowires coupled to an epitaxially grown Al superconductor. We find that the gate voltage induced electric fields can greatly modify the coupling strength, which has consequences for the proximity induced superconducting gap, effective g-factor, and spin-orbit coupling, which all play a key role in understanding Majorana physics. We further show that level repulsion due to spin-orbit coupling in a finite size system can lead to seemingly stable zero bias conductance peaks, which mimic the behavior of Majorana zero modes. Our results improve the understanding of realistic Majorana nanowire systems.

This chapter has been published in New Journal of Physics **20**, 103049 (2018)

*These authors contributed equally to this work.

5.1. INTRODUCTION

The hybrid superconductor-semiconductor nanowire system is the prime candidate to realize, control, and manipulate Majorana zero modes (MZMs) for topological quantum information processing [1–3]. Majorana zero modes can be engineered in these hybrid nanowire systems by combining the one dimensional nature of the nanowire, strong spin-orbit coupling, superconductivity, and appropriate external electric (to control the chemical potential) and magnetic fields (to control the Zeeman energy) to drive the system into a topologically non-trivial phase [4, 5]. To induce superconductivity in the semiconductor nanowire, it needs to be coupled to a superconductor. The electronic coupling between the two systems turns the nanowire superconducting [6], known as the proximity effect. Following this scheme, the first signatures of MZMs were observed in these hybrid systems, characterized by a zero bias peak (ZBP) in the tunneling conductance spectrum [7–10]. Since then, significant progress has been made in Majorana experiments [11–14], enabled by more uniform coupling between the superconductor and semiconductor nanowire. This has been achieved by improved interface engineering: through careful ex situ processing [15–17], by depositing the superconductor on the nanowires in situ [18, 19], and a combination of in situ and ex situ techniques [20], finally leading to the observation of ZBP heights near the conductance quantum $2e^2/h$ [13, 21].

However, the treatment of the superconductor-semiconductor coupling in the interpretation of experiments is often oversimplified. This coupling has recently been predicted to depend substantially on the confinement induced by external electric fields [22]. In this work, we experimentally show that the superconductor-semiconductor coupling, as parameterized by the induced superconducting gap, is affected by gate induced electric fields. Due to the change in coupling, the renormalization of material parameters is altered, as evidenced by a change in the effective g-factor of the hybrid system. Furthermore, the electric field is shown to affect the spin-orbit interaction, revealed by a change in the level repulsion between Andreev states. Our experimental findings are corroborated by numerical simulations.

5.2. EXPERIMENTAL SET-UP

We have performed tunneling spectroscopy experiments on four InSb-Al hybrid nanowire devices, labeled A-D, all showing consistent behaviour. The nanowire growth procedure is described in reference [20]. A scanning electron micrograph (SEM) of device A is shown in figure 5.1(a). Figure 5.1(b) shows a schematic of this device and the measurement set-up. For clarity, the wrap-around tunnel gate, tunnel gate dielectric and contacts have been removed on one side. A normal-superconductor (NS) junction is formed between the part of the nanowire covered by a thin shell of aluminum (10 nm thick, indicated in green, S), and the Cr/Au contact (yellow, N). The transmission of the junction is controlled by applying a voltage V_{Tunnel} to the tunnel gate (red), galvanically isolated from the nanowire by 35 nm of sputtered SiN_x dielectric. The electric field is induced by a global back gate voltage V_{BG}, except in the case of device B, where this role is played by the side gate voltage V_{SG}. Further details on device fabrication and design are included in Supplemental sections 5.S.1 and 5.S.2. To obtain information about the density of states in the proximitized nanowire, we measure the differential conductance

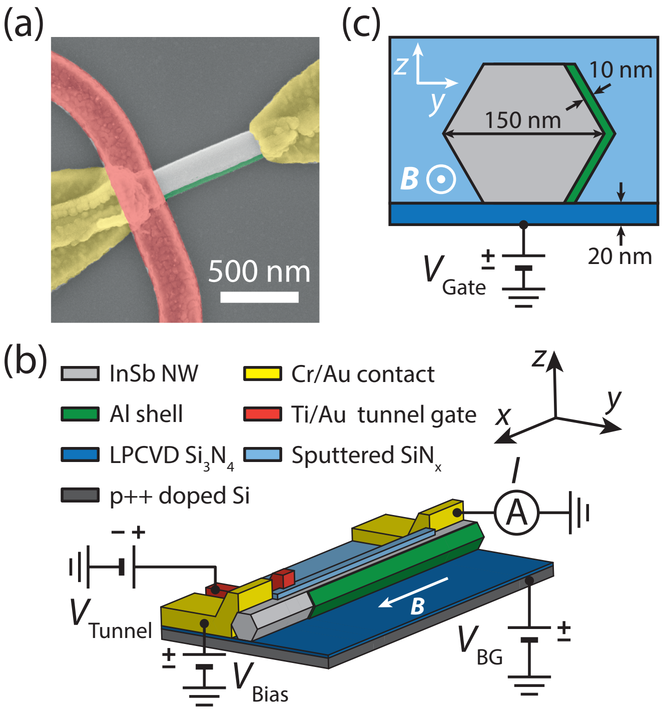

Figure 5.1: Device schematics. (**a**) SEM of device A, with InSb nanowire in gray, superconducting aluminum shell in green, Cr/Au contacts in yellow, and local tunnel gate in red. Scale bar is 500 nm. (**b**) Schematic of experimental set-up. The substrate acts as a global back gate. The magnetic field is applied along the nanowire direction (x-axis). (**c**) Geometry used in the numerical simulations. A uniform potential V_{Gate} is applied as a boundary condition at the interface between substrate and dielectric. The superconductor (green) is kept at a fixed potential, which is set by the work function difference at the superconductor-semiconductor interface.

$\mathrm{d}I/\mathrm{d}V_{\mathrm{Bias}}$ as a function of applied bias voltage V_{Bias}. In the following, we will label this quantity as $\mathrm{d}I/\mathrm{d}V$ for brevity. A magnetic field is applied along the nanowire direction (x-axis in figures 5.1(b),(c)). All measurements are performed in a dilution refrigerator with a base temperature of 20 mK.

5.3. THEORETICAL MODEL

The device geometry used in the simulation is shown in figure 5.1(c). We consider a nanowire oriented along the x-direction, with a hexagonal cross-section in the yz-plane. The hybrid superconductor-nanowire system is described by the Bogoliubov-de Gennes Hamiltonian

$$\begin{aligned} H = &\left[\frac{\hbar^2\mathbf{k}^2}{2m^*} - \mu - e\phi\right]\tau_z + \alpha_y(k_z\sigma_x - k_x\sigma_z)\tau_z \\ &+ \alpha_z(k_x\sigma_y - k_y\sigma_x)\tau_z + \frac{1}{2}g\mu_{\mathrm{B}}B\sigma_x + \Delta\tau_x. \end{aligned} \tag{5.1}$$

The first term contains contributions from the kinetic energy and the chemical potential, as well as the electrostatic potential ϕ. The second and third terms describe the Rashba spin-orbit coupling, with the coupling strength α_y (α_z) depending on the y-component (z-component) of the electric field. The Zeeman energy contribution, proportional to g, the Landé g-factor, is given by the fourth term. Finally, the superconducting pairing Δ is included as the fifth term. All material parameters are position dependent, taking different values in the InSb nanowire and the Al superconductor. For additional details about the simulation, see Supplemental sections 5.S.3 and 5.S.4.

If the coupling between the superconductor and semiconductor is small (compared to the bulk gap of the superconductor Δ, known as weak coupling), superconductivity can be treated as a constant pairing potential term in the nanowire Hamiltonian, with the induced superconducting gap being proportional to the coupling strength [23]. However, if the coupling becomes strong, the wave functions of the two materials hybridize, and the superconductor and semiconductor have to be considered on equal footing [24]. We achieve this by solving the Schrödinger equation in both materials simultaneously. When desired, the orbital effect of the magnetic field is added via Peierls substitution [25]. The simulations are performed using the `kwant` package [26].

The electrostatic potential in the nanowire cross-section is calculated from the Poisson equation, assuming an infinitely long wire. We use a fixed potential V_{Gate} as a boundary condition at the dielectric-substrate interface. The superconductor enters as the second boundary condition, with a fixed potential to account for the work function difference between superconductor and semiconductor [27]. We approximate the mobile charges in the nanowire by a 3D electron gas (Thomas-Fermi approximation). It has been demonstrated that the potentials calculated using this approximation give good agreement with results obtained by self-consistent Schrödinger-Poisson simulations [28]. The calculated potential for a given V_{Gate} is then inserted into the Hamiltonian (5.1). By solving the Schrödinger equation for a given electrostatic environment, we can see how the gate potential alters the electronic states in the nanowire, how they are coupled to the superconductor, and how this coupling affects parameters such as the induced gap, effective g-factor, and spin-orbit energy.

5.4. GATE VOLTAGE DEPENDENCE OF THE INDUCED SUPERCONDUCTING GAP

When the transmission of the NS-junction is sufficiently low (i.e., in the tunneling regime), the differential conductance $\mathrm{d}I/\mathrm{d}V$ is a direct measure of the density of states (DOS) in the proximitized nanowire [29]. In figure 5.2(a), we plot $\mathrm{d}I/\mathrm{d}V$ measured in device A as a function of applied bias voltage V_{Bias} and tunnel gate voltage V_{Tunnel}, for V_{BG} = -0.6 V. In the low transmission regime, we resolve the superconducting gap Δ around 250 μeV, indicated by the position of the coherence peaks. The ratio of sub-gap to above-gap conductance (proportional to the normal state transmission of the junction, T) follows the behavior expected from BTK theory [30, 31], indicating the sub-gap conductance is dominated by Andreev reflection processes (proportional to T^2). This is generally referred to as a hard gap. However, for more positive back gate voltages, the sub-gap conductance is larger and shows more resonances, as is illustrated in figure 5.2(b) for V_{BG} =

-0.3 V. Figure 5.2(c) shows line traces taken at a similar transmission (above-gap conductance) for both cases. The sub-gap conductance for V_{BG} = -0.3 V (black line) exceeds that of the hard gap case (red line) by an order of magnitude. This is indicative of a surplus of quasi-particle states inside the gap, referred to as a soft gap.

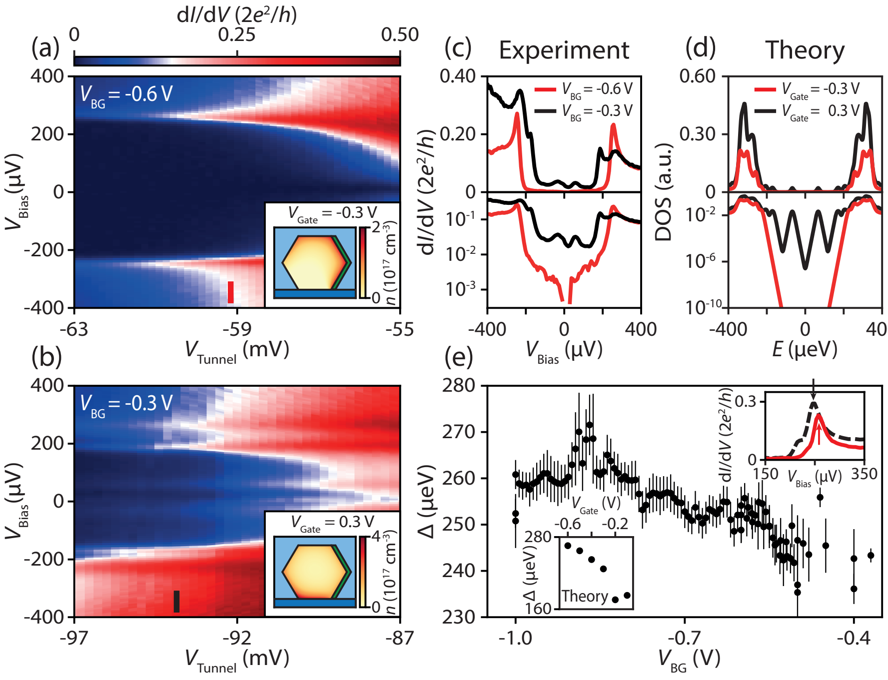

Figure 5.2: Gate dependence of the induced superconducting gap. (**a**,**b**) Differential conductance dI/dV measured in device A as a function of V_{Bias} and V_{Tunnel} for V_{BG} = -0.6 V (**a**) and V_{BG} = -0.3 V (**b**). Insets show the calculated electron density in the wire for V_{Gate} = -0.3 V and V_{Gate} = 0.3 V, respectively. (**c**) Line-cuts from (a) and (b), indicated by the colored bars, in linear (top) and logarithmic (bottom) scale. (**d**) Calculated DOS for the density profiles shown in the insets of (a) and (b), shown in red and black, respectively. (**e**) Induced gap magnitude Δ as a function of V_{BG}, showing a decrease for more positive gate voltages. Top right inset: line traces showing the coherence peak position (indicated by the arrow) for V_{BG} = -0.6 V (solid red line) and V_{BG} = -0.4 V (dashed black line). Bottom left inset: induced gap from the calculated DOS as a function of V_{Gate}, consistent with the experimental observation.

The gate voltage induced transition from soft to hard gap is generically observed in multiple devices. To understand this phenomenology, we calculate the electron density in the nanowire cross-section for different values of V_{Gate}. Because the charge neutrality point in our devices is unknown, there is a difference between the gate voltages used in the experiment and the values of V_{Gate} used in the simulation. By comparing the transition point between hard and soft gaps in the experiment and the simulation, we estimate that the experimental gate voltage range -0.6 V < V_{BG} < -0.4 V roughly corresponds to the simulated gate voltage range -0.4 V < V_{Gate} < -0.2 V.

For more negative V_{Gate}, the electric field from the gate pushes the electrons towards interface with the superconductor (inset of figure 5.2(a)). We solve the Schrödinger equation for the calculated electrostatic potential and find that this stronger confinement near the interface leads to a stronger coupling. This results in a hard gap, as illustrated by the calculated energy spectrum (figure 5.2(d), red line). However, for more positive voltages, the electrons are attracted to the back gate, creating a high density pocket far away from the superconductor (inset of figure 5.2(b)). These states are weakly coupled to the superconductor, as demonstrated by a soft gap structure (figure 5.2(d), black line, see also Supplemental section 5.S.5). We can therefore conclude that the electron tunneling between the semiconductor and the superconductor is strongly affected by the gate potential.

The change in superconductor-semiconductor coupling does not just affect the hardness, but also the size of the gap. For each back gate voltage, we fit the BCS-Dynes expression [32] for the DOS in order to extract the position of the coherence peaks, giving the gap size Δ. The results are shown in figure 5.2(e). Further details on the fitting procedure are given in Supplemental section 5.S.6. As V_{BG} becomes more positive, the superconductor-semiconductor coupling becomes weaker, reducing the size of the gap. From $V_{\mathrm{BG}} > \text{-}0.4\,\mathrm{V}$ onward it becomes difficult to accurately determine the gap, as it tends to become too soft and the coherence peaks are not always clearly distinguishable. The top right inset shows the shift of the coherence peak (indicated by the arrows) to lower bias voltage as V_{BG} is increased. The lower left inset shows the extracted coherence peak position from the numerical simulations, showing the same trend with gate voltage. However, the theoretically calculated induced gap is generally smaller than the experimentally observed gap. It has been demonstrated that disorder at the outer surface of the superconductor (e.g., due to oxidation) leads to an increase in the induced gap due to breaking of momentum conservation, which increases the superconductor-semiconductor hybridization [22]. Additionally, the gap decreases more slowly when the gate voltage is more positive. As this kind of disorder is present in our devices, but was not included in the simulation, this is a likely cause for the discrepancy between theory and experiment.

5.5. EFFECTIVE G-FACTOR

As the electric field induced by the back gate clearly has an important effect on the hybridization between the nanowire and the superconductor, we now look at the effect this has on the Zeeman term in the Hamiltonian. This term affects the energy dispersion of spinful states in a magnetic field. We study the dispersion of the states in the nanowire by measuring $\mathrm{d}I/\mathrm{d}V$ in device A as a function of applied bias voltage and magnetic field, as shown in figure 5.3(a) and figure 5.3(b). We define the effective g-factor as $g_{\mathrm{eff}} = \frac{2}{\mu_B}|\frac{\Delta E}{\Delta B}|$, with $|\frac{\Delta E}{\Delta B}|$ the absolute value of the average slope of the observed peak in the differential conductance as it disperses in magnetic field. This effective g-factor is different from the pure spin g-factor g_{spin}, as the dispersion used to estimate g_{eff} is generally not purely linear in magnetic field, and has additional contributions from the spin-orbit coupling, magnetic field induced changes in chemical potential, and orbital effects [22, 27, 33]. The effective g-factor is the parameter which determines the critical magnetic field required to drive the system through the topological phase transition [34]. We obtain the slope $\frac{\Delta E}{\Delta B}$ from a linear fit (shown as black dashed lines in figures 5.3(a,b), see appendix 5.S.7 for details) of the observed peak position. Figure 5.3(c) shows the extracted g_{eff} for device A, with more positive back gate voltages leading to larger g_{eff} (visible as a steeper slope). A similar result has recently been reported in hybrid InAs-Al nanowires [35].

We use our numerical model to calculate the DOS in the nanowire as a function of applied magnetic field, shown in figure 5.3(d) and figure 5.3(e). From the calculated spectrum, we apply the same procedure used to fit the experimental data to extract g_{eff} (white dashed lines). The results for different values of V_{Gate} are given in figure 5.3(f) as black circles. The applied back gate voltage changes the hybridization of the states in the InSb ($|g_{\mathrm{spin}}| = 40$ [36]) and the Al ($|g_{\mathrm{spin}}| = 2$). As a more positive gate voltage increases the weight of the wave function in the InSb, we expect the renormalized g-factor to increase as the gate voltage is increased, consistent with the results of figure 5.3(c) and figure 5.3(f).

To see how well g_{eff} describes the Zeeman term in the Hamiltonian, we turn our

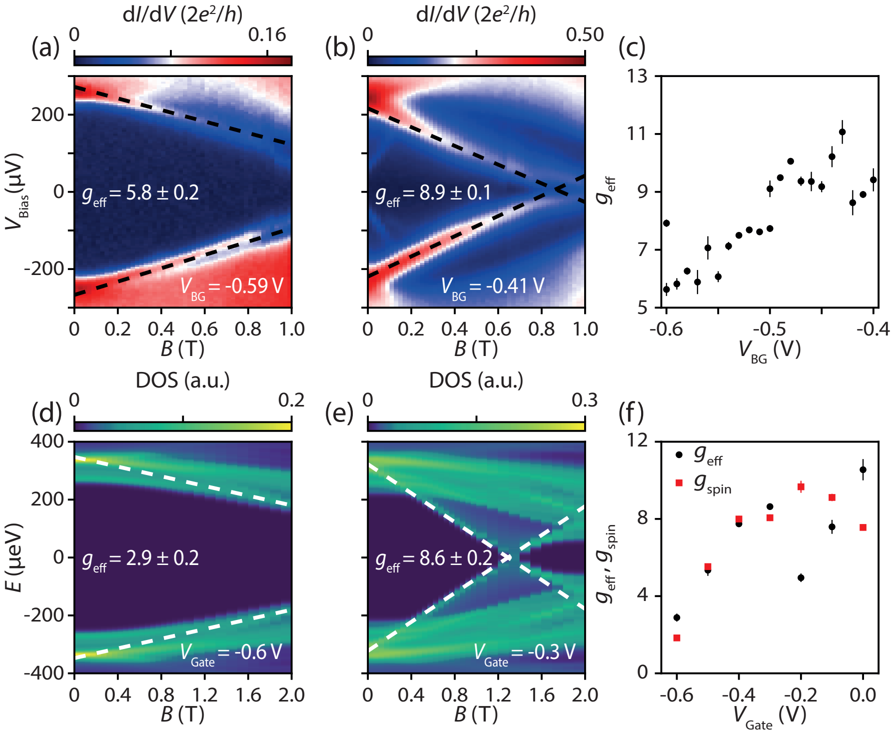

Figure 5.3: Effective g-factor. (**a**,**b**) $\mathrm{d}I/\mathrm{d}V$ measured in device A as a function of applied bias voltage V_{Bias} and magnetic field B for V_{BG} = -0.59 V and V_{BG} = -0.41 V, respectively. The effective g-factor is extracted from a linear fit of the lowest energy state dispersion (dashed lines). (**c**) g_{eff} as a function of V_{BG}, showing an increase as the gate voltage becomes more positive. Data from device A. (**d**,**e**) Simulated DOS in the nanowire as a function of magnetic field for V_{Gate} = -0.6 V and V_{Gate} = -0.3 V, respectively. (**f**) Extracted g_{eff} (based on lowest energy state in the spectrum, black circles) and g_{spin} (based on the spectrum at $k = 0$, red squares) from the simulation.

attention to the energy spectrum at $k = 0$. At this point, the effect of spin-orbit coupling vanishes. If orbital effects are excluded, we can then define the absolute value of the pure spin g-factor as $g_{\text{spin}} = \frac{2}{\mu_B}|\frac{\Delta E(k=0)}{\Delta B}|$. The resulting values for g_{spin} are shown as red squares in figure 5.3(f). By comparing the results for g_{eff} and g_{spin}, we can conclude that when the lowest energy state has a momentum near $k = 0$ (as is the case for $V_{\text{Gate}} <$ -0.2 V), the effect of spin-orbit coupling is negligible, and g_{eff} is a good proxy for the pure spin g-factor. However, when this is no longer the case, deviations can be observed, as is the case for $V_{\text{Gate}} \geq$ -0.2 V. As we expect the experimental gate voltage range of figure 5.3(c) to be comparable to values of $V_{\text{Gate}} <$ -0.2 V, we conclude that the experimentally obtained g_{eff} is a reasonable approximation of g_{spin} in this parameter regime. However, we stress once more that in general, one needs to be careful when interpreting the g_{eff} extracted from experimental data as the g-factor entering the Hamiltonian in the Zeeman term.

The increasing trend of g_{eff} does not change when the orbital effect of magnetic field is considered (see Supplemental section 5.S.7, figure 5.S11). However, there is a significant increase in the predicted values, in agreement with previous findings for InAs nanowires [33]. The values in figure 5.S11 are larger than the ones generally observed in our experiment (see figure 5.3(c)), suggesting that the orbital effect is not a dominant mechanism in determining the effective g-factor in these devices. We note that the data from device A used to make these plots was taken solely in the hard gap regime, where one expects a strong confinement near the superconductor. This suppresses the orbital contribution of the magnetic field. Another possible explanation for the discrepancy between the results of the simulation and the experimental data is an overestimation of the density in the nanowire, as higher sub-bands have a stronger contribution from the orbital effect. Minimizing the orbital effect is desirable for Majorana physics, as the orbital contributions of the magnetic field are detrimental to the topological gap [25].

5.6. LEVEL REPULSION DUE TO SPIN-ORBIT COUPLING

The term in the Hamiltonian that remains to be explored describes the Rashba spin-orbit coupling. The strength of the spin-orbit coupling is determined by the parameter α, which depends on the material (and thus, on the superconductor-semiconductor coupling), and the electric field [37–39]. Therefore, we expect that this term will be affected by the gate potential as well. In finite systems, the spin-orbit interaction can couple states with different orbitals and spins [40]. These states are thus no longer orthogonal to each other, and the spin-orbit mediated overlap between them causes energy splitting, leading to level repulsion [41–43]. This level repulsion, which is generic in class D systems in the presence of superconductivity, magnetic field and spin-orbit coupling [44, 45], can be extracted from the low energy nanowire spectrum as measured by tunneling spectroscopy [46].

In figures 5.4(a)-(c), we show the evolution of the level repulsion between the two lowest energy sub-gap states (labeled L_1 and L_2, as indicated by the white dashed lines in panel c) in device B. For these measurements, the global back gate is grounded, with the electric field being induced by applying a voltage to the side gate (side gate shown in Supplemental section 5.S.2).

We parameterize the level repulsion by two quantities: the coupling strength δ_{SO}, and the splitting A, defined as the maximum deviation of L_1 from zero energy after the first zero crossing. This splitting has previously been linked to the overlap between two MZM in a finite system [47]. In figure 5.4(e), we zoom in on the anti-crossing feature in panel figure 5.4(b), showing the minimum energy difference between L_1 and L_2 (given by $2\delta_{\mathrm{SO}}$) and the splitting A. We extract these parameters by a fit of the anti-crossing (solid green lines, with the uncoupled states shown by the dashed black lines, details of the fitting procedure are in Supplemental section 5.S.8). Because we expect finite size effects to be relevant, we cannot use our previous theoretical model, as it is based on an infinitely long nanowire. Therefore, we modify the model to take into account the finite size of the nanowire system, and calculate the low energy spectrum for different values of the Rashba spin-orbit strength (see Supplemental section 5.S.9). In figure 5.4(d), we plot the two lowest energy states in the nanowire as a function of the Zeeman energy ($E_Z = \frac{1}{2} g\mu_B B$), in units of the superconducting gap Δ. If $\alpha = 0$ (no spin-orbit coupling,

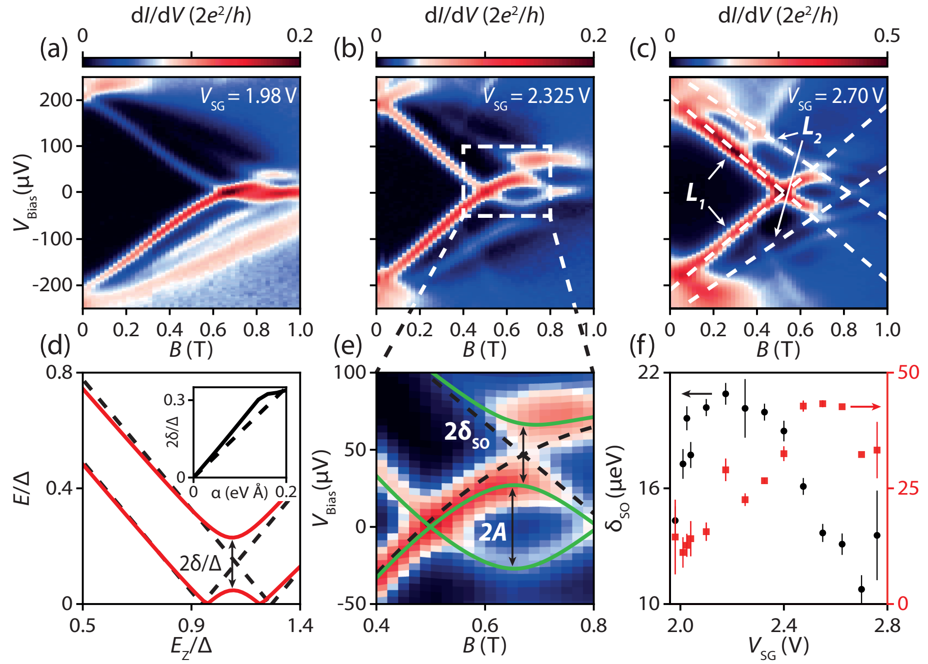

Figure 5.4: Spin-orbit coupling induced level repulsion. (**a**-**c**) dI/dV as a function of V_{Bias} for device B, showing the dispersion of subgap states in magnetic field, for V_{SG} = 1.98 V, 2.325 V, and 2.70 V, respectively. The two lowest energy states L_1, L_2, and their particle-hole symmetric partners are indicated by the white dashed lines. (**d**) Calculated low energy spectrum of the finite nanowire system as a function of the Zeeman energy E_Z for $\alpha = 0$ eV Å(dashed black lines) and $\alpha = 0.1$ eV Å(solid red lines), showing the opening of an energy gap 2δ due to spin-orbit coupling. Inset: the energy gap 2δ as a function of the Rashba α parameter (solid line), and the estimate $2\delta = \alpha\pi/l$ (dashed line), with l the nanowire length. All energy scales are in units of the superconducting gap Δ. (**e**) Zoom-in of the anti-crossing in (**b**), showing the splitting A and the coupling strength δ_{SO}. Green solid lines indicate a fit of the anti-crossing, with the dashed black lines showing the uncoupled energy levels. (**f**) Coupling δ_{SO} (black circles) and splitting A (red squares) as a function of V_{SG}, showing opposite trends for these parameters.

dashed black lines), there is no coupling between the states, and no level repulsion occurs. However, if spin-orbit coupling is included (e.g., $\alpha = 0.1\,\mathrm{eV\,Å}$, solid red lines), the levels repel each other, with the magnitude of the anti-crossing given by 2δ. The level repulsion strength scales with α (inset of figure 5.4(d)), providing a way to estimate α based on the low energy spectrum using $2\delta \sim \alpha\pi/l$, where l is the length of the nanowire.

In figure 5.4(f), we plot δ_{SO} (black circles) and A (red squares) as a function of the applied side gate voltage. The two parameters follow opposite trends, with A being maximal when δ_{SO} is minimal. When δ_{SO} is larger, the levels repel each other more, leading to L_1 being pushed closer to zero energy, reducing the splitting A. When $V_{\mathrm{SG}} < 2.0\,\mathrm{V}$, both parameters become smaller with decreasing V_{SG}. At this point, other states at higher energies become relevant for the lowest energy dispersion (a situation demonstrated in figure 5.4(a)), and our method to extract these parameters breaks down. We expect this method to be reliable when the energetically lowest two states can be clearly separated from the rest. Because δ_{SO} depends not only on α, but also on the details of the confinement potential, as well as the coupling to the superconductor, a precise estimate goes beyond the current approximations in our model. That being said, based on the observed magnitude of δ_{SO} and our simulations of the finite nanowire system, we can estimate the Rashba parameter α to be around $0.1\,\mathrm{eV\,Å}$ in this gate voltage range. This value is comparable to the values reported in InSb nanowire based quantum dots [48], and smaller than the values measured in weak anti-localization experiments [38]. A large value of α is beneficial for Majorana physics, as it determines the maximum size of the topological gap [49].

5.7. ZERO BIAS PEAK IN EXTENDED MAGNETIC FIELD RANGE

In the previous sections, we have described the effect of the gate induced electric field on the various terms in the Hamiltonian (5.1). As this Hamiltonian is known to describe Majorana physics, we now turn our attention to possible signatures of MZMs in this system. In particular, when $2\delta_{\mathrm{SO}}$ becomes comparable to the energy of L_2, we find that L_1 can become pinned close to zero bias over an extended range in magnetic field, as demonstrated in figure 5.5(b) (data from device A). Figure 5.5(d) shows that the state stays pinned to zero energy over a range of over 0.2 T, corresponding to a Zeeman energy of over 300 μeV, which is larger than the induced gap. The stability of the ZBP in terms of the ratio of Zeeman energy to induced gap is comparable to the most stable ZBPs reported in literature [11, 12]. When we fix the magnetic field to $B = 0.26\,\mathrm{T}$ and change the back gate voltage (figure 5.5(e)), it appears that there is a stable ZBP over a few mV as well.

We might be tempted to conclude that this stability implies this is a Majorana zero mode. However, if we change either the gate voltage (figure 5.5(a), figure 5.5(c)) or the magnetic field (figure 5.5(f)) a little bit, we observe that this stability applies only to very particular combinations of gate voltage and magnetic field. One should keep in mind that in a finite system, MZMs are not expected to be stable with respect to local perturbations if the system size is comparable to the Majorana coherence length, which is likely the case in our devices. This further complicates the determination of the origin of the observed peaks. As we find no extended region of stability, we conclude that it is unlikely that this state pinned to zero energy is caused by a topological phase transition. Rather,

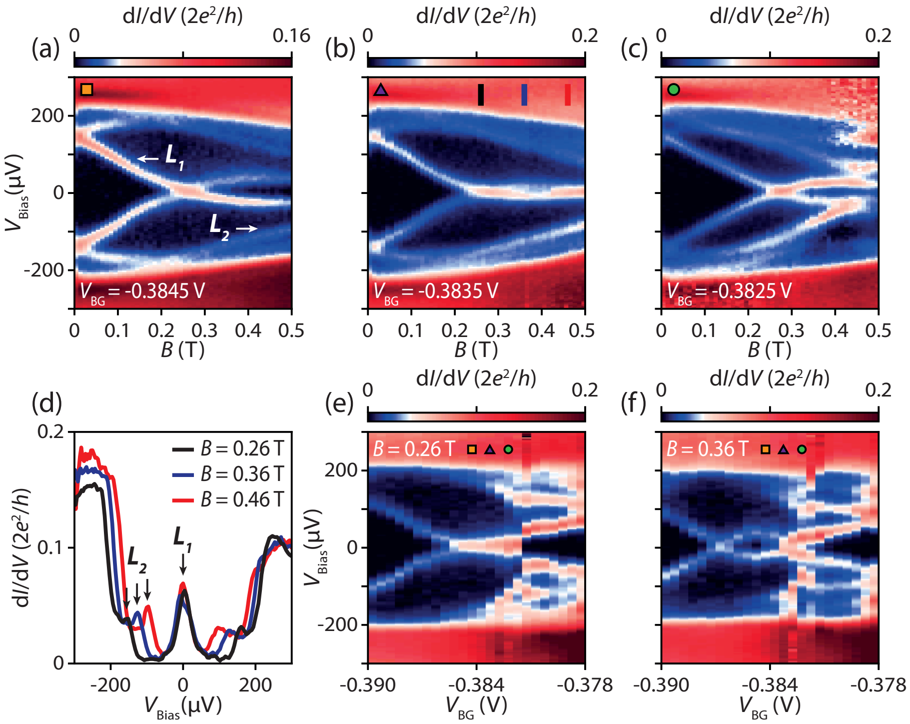

Figure 5.5: Zero bias pinning due to strong level repulsion. (**a**-**c**) dI/dV as a function of V_{Bias} for device A, showing the dispersion of L_1 and L_2 as a function of magnetic field for V_{BG} = -0.3845 V, -0.3835 V, and -0.3825 V, respectively. (**d**) Line traces at magnetic fields indicated by the colored bars in (b), showing the stable pinning of L_1 to zero bias voltage. (**e**,**f**) dI/dV measured as a function of V_{BG} at fixed magnetic field B = 0.26 T and 0.36 T, respectively. Gate voltages from (a), (b), and (c) are indicated by orange square, purple triangle, and green circle, respectively.

this seems to be due to a fine-tuned coincidence in which the repulsion between two states combined with particle-hole symmetry leads to one of the states being pinned to $E = 0$. We reiterate that simply having a stable zero energy state over an extended range in magnetic field is not sufficient to make claims about robust Majorana modes [50–52]. Further experimental checks, such as stability of the ZBP in an extended region of the parameter space spanned by the relevant gate voltages [11], as well as magnetic field, are required in order to assign a possible Majorana origin.

5.8. CONCLUSION & OUTLOOK

We have used InSb nanowires with epitaxial Al superconductor to investigate the effect of the gate voltage induced electric field on the superconductor-semiconductor coupling. This coupling is determined by the distribution of the wave function over the superconductor and semiconductor, and controls essential parameters of the Majorana Hamiltonian: the proximity induced superconducting gap, the effective g-factor, and spin-orbit coupling. Our observations show that the induced superconductivity, as parameterized by the hardness and size of the induced gap, is stronger when the electrons are confined to a region close to the superconductor. The stronger coupling leads to a lower effective g-factor. We also determine that the gate voltage dependence of the effective g-factor is dominated by the change in coupling to the superconductor, rather than by orbital effects of the magnetic field. Finally, we study the effect of level repulsion due to spin-orbit coupling. Appropriate tuning of the repulsion leads to level pinning to zero energy over extended parameter ranges, mimicking the behavior expected from MZMs. Our result deepens the understanding of a more realistic Majorana nanowire system. More importantly, it is relevant for the design and optimization of future advanced nanowire systems for topological quantum information applications.

AUTHOR CONTRIBUTIONS

M.W.A.d.M., J.D.S.B., D.X., and H.Z. fabricated the devices, performed the measurements, and analyzed the data. G.W.W., A.B., A.E.A., and R.M.L. performed the numerical simulations. N.v.L. and G.W. contributed to the device fabrication. R.L.M.o.h.V., S.G., and D.C. grew the InSb nanowires under the supervision of E.P.A.M.B.. J.A.L., M.P., and J.S.L. deposited the aluminum shell on the nanowires under the supervision of C.J.P.. L.P.K. and H.Z. supervised the project. M.W.A.d.M. and H.Z. wrote the manuscript with comments from all authors. M.W.A.d.M., J.D.S.B., and D.X. contributed equally to this work.

5.S. SUPPLEMENTAL MATERIAL

5.S.1. FABRICATION PROCEDURE

1. **Nanowire deposition**: a SEM-based nanomanipulator is used to deterministically place the InSb-Al nanowires unto a degenerately p-doped Si substrate covered by 20 nm of LPCVD Si_3N_4 (devices A, C, and D) or 285 nm of thermal SiO_2 (device B).

2. **Mask preparation & lithography**: for every fabrication step, we use standard electron beam lithography techniques to create the mask. The mask consists of a layer of PMMA 950KA6 spun at 4000 rpm. After writing, the mask is developed in a solution of MIBK:IPA (1:3 ratio) for 60 s, followed by a IPA rinse for 60 s. After each deposition step, liftoff is done using acetone.

3. **Contact preparation & deposition**: before depositing the contact material, the Al and AlO_x are locally removed by Ar plasma etch. The contacts are deposited by electron beam evaporation of Cr/Au (10/100-200 nm). For device B, the side gates are also evaporated in this step.

4. **Dielectric deposition**: as a top gate dielectric we sputter 35 nm of SiN_x (devices A, C, and D).

5. **Top gate deposition**: the top gates are deposited by electron beam evaporation of Ti/Au (10/200 nm) (devices A, C, and D).

5.S.2. DEVICE INFORMATION AND SCHEMATICS

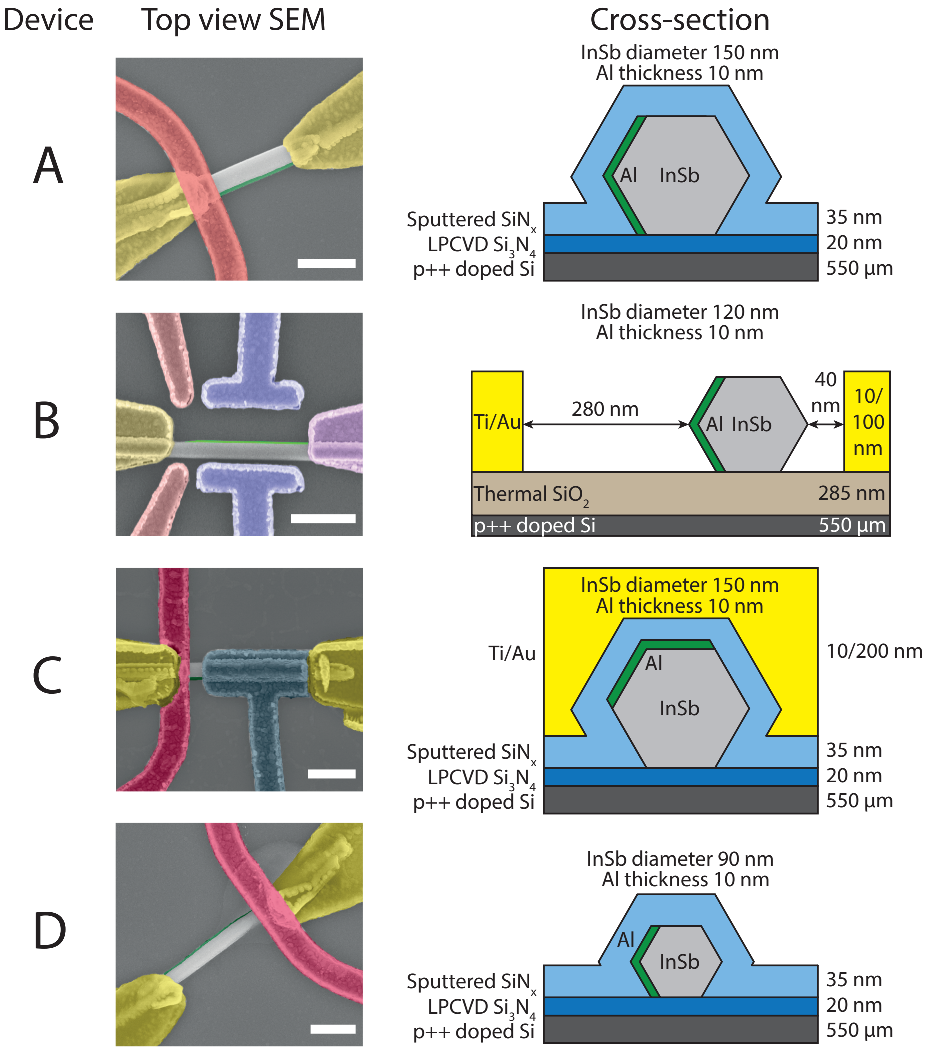

Figure 5.S1: SEM images and schematic cross-sectional views of the devices used as part of this research. Data from devices A and B is presented in the main text. Data from devices C and D is presented in the supplement for completeness. Note that the data for device B is obtained by changing the voltage on the side gate (V_{SG}), shown in blue in the SEM image. Scale bar is 500 nm.

5.S.3. SIMULATION OF ELECTROSTATICS AND NANOWIRE SPECTRUM

For the electrostatics simulations we use the geometry of device A (as shown in figure 5.1(c) of the main text). We describe the device as an infinite wire oriented along the x-direction, with a hexagonal cross-section in the yz-plane. The electrostatics are described by the Poisson equation

$$\nabla \cdot \big(\epsilon_r(\mathbf{r})\nabla\phi(\mathbf{r})\big) = \frac{\rho_{\text{tot}}[\phi(\mathbf{r})]}{\epsilon_0}, \tag{5.S1}$$

where $\rho_{\text{tot}}[\phi(\mathbf{r})]$ is a functional of the potential $\phi(\mathbf{r})$. We include four contributions to ρ_{tot},

$$\rho_{\text{tot}} = \rho_{\text{e}} + \rho_{\text{hh}} + \rho_{\text{lh}} + \rho_{\text{fixed}}, \tag{5.S2}$$

where ρ_{e}, ρ_{hh} and ρ_{lh} are the mobile charges of the conduction band, heavy hole band and light hole band of the InSb nanowire and ρ_{fixed} are the fixed charges in the system. For the mobile electron charges we assume a 3D electron gas density (Thomas-Fermi approximation)

$$\rho_{\text{e}}(\phi) = -\frac{e}{3\pi^2}\left(\frac{2m_{\text{e}}|\phi|\theta(-\phi)}{\hbar^2}\right)^{3/2}, \tag{5.S3}$$

with θ the Heaviside step function, and for the holes

$$\rho_i(\phi) = \frac{e}{3\pi^2}\left(\frac{2m_i|\phi - E_{\text{G}}|\theta(\phi - E_{\text{G}})}{\hbar^2}\right)^{3/2}, \tag{5.S4}$$

with E_{G} the band gap and i corresponding to the heavy hole (hh) and light hole (lh) band respectively. For the effective masses, we take the bulk InSb values [53]. We include hole bands to describe the additional screening when the electrochemical potential is in the valence band, which can become relevant for very negative gate voltages due to the narrow band gap of InSb. To model the influence of the sputtered dielectric on the nanowire surface, the wire is wrapped in a 1 nm surface layer of $2.5 \times 10^{18}\,\text{cm}^{-3}$ positive charge density. In the absence of other charges and gates this charge pins the conduction band of InSb at about -0.069 eV below the Fermi level at the surface. For the InSb-Al interface we assume the conduction band of InSb is pinned -0.08 eV below the Fermi level due to the work function difference between the two materials. A negative band offset of the semiconductor to the superconductor is required for a hard induced gap in the InAs-Al system [22], and we assume a similar situation in InSb-Al hybrid devices. While the precise numbers for the surface accumulation and band-offset at the InSb-Al interface are unknown, it is known that InSb wires have about a 10 times smaller density than InAs wires [19, 54], and the parameters were adjusted from the InAs ones accordingly. The Al layer is assumed to be grounded, and enters as a Dirichlet boundary condition which is set to +0.08 V. The boundary condition at the substrate-dielectric interface is set to the applied gate voltage, V_{Gate}. On the remaining three boundaries of the system we use Neumann conditions. For the dielectric constant of InSb, the sputtered SiN$_x$, and the LPCVD Si$_3$N$_4$ we take take 15.15, 7.5, and 8 respectively.

After the electrostatic potential has been calculated for a given V_{Gate}, we plug it into the Schrödinger equation and solve it for the cross-section of the device. We use a Rashba

Table 5.S1: Material parameters for InSb and Al.

Parameter	InSb	Al
m^*	0.0139 [53]	1
g	-40 [36]	2
Δ	0 meV	0.34 meV [55]
E_F	0 eV	10 eV [56]

Hamiltonian with a Bogoliubov-de Gennes (BdG) superconducting term [57]

$$\begin{aligned} H = &\frac{\hbar^2}{2m^*(y,z)}(k_x^2+k_y^2+k_z^2)\tau_z - (E_\mathrm{F}(y,z)+e\phi(y,z))\tau_z + \alpha_y(y,z)(k_z\sigma_x - k_x\sigma_z)\tau_z \\ &+ \alpha_z(y,z)(k_x\sigma_y - k_y\sigma_x)\tau_z + \frac{1}{2}g(y,z)\mu_\mathrm{B}B\sigma_x + \Delta(y,z)\tau_x, \end{aligned} \tag{5.S5}$$

where the effective mass m^*, the Fermi level E_F, the electrostatic potential ϕ, the Rashba parameters α_i, the g-factor and the superconducting pairing Δ are functions of the (y,z)-coordinates and depend on the material. Since ϕ is not solved in Al it is correspondingly set to zero there. The material parameters for InSb and Al are summarized in Tab. 5.S1. If desired, the orbital effect is added to Eq. (5.S5) by the Peierls substitution $k_z \rightarrow k_z - \frac{\pi}{\phi_0}B(y-y_0)$, with ϕ_0 the magnetic flux quantum. y_0 is chosen such that the average vector potential in Al is zero, resulting in a vanishing supercurrent [25]. The Hamiltonian is discretised on a quadratic mesh and constructed using the `kwant` package [26]. To accommodate the small Fermi wavelength of Al a discretisation length of 0.1 nm is used.

5.S.4. ELECTRIC FIELD DEPENDENCE OF SPIN-ORBIT COUPLING

The Rashba couplings α_y and α_z, which are nonzero only in the semiconductor region, result from the symmetry breaking by the electrostatic potential and are obtained from [53]

$$\alpha_i = \frac{eP^2}{3}\left[\frac{1}{E_0} - \frac{1}{(E_0+\Delta_0)^2}\right]\bar{\mathcal{E}}_i, \tag{5.S6}$$

where the average electric field in direction i is obtained by averaging $\mathcal{E}_i$ over the whole semiconductor region. Parameters for bulk InSb are used [53]: the Kane matrix element $P = 0.9641\,\mathrm{eV\,nm}$, the bandgap $E_0 = 0.237\,\mathrm{eV}$, and the spin-orbit gap $\Delta_0 = 0.810\,\mathrm{eV}$. The resulting Rashba parameters α_i are plotted in figure 5.S2(a).

We define the spin-orbit energy $E_{\mathrm{SO}} = \frac{m^*(\alpha_y^2+\alpha_z^2)}{2\hbar^2}$. The spin-orbit energy is plotted as a function of V_{Gate} in figure 5.S2(b). The average electric field in the nanowire increases as the applied gate voltage becomes more negative, leading to an enhancement of the spin-orbit coupling. At $V_{\mathrm{Gate}} = 0.08\,\mathrm{V}$, the average electric field in the nanowire becomes equal to 0 due to symmetry, eliminating the influence of spin-orbit coupling on the nanowire spectrum.

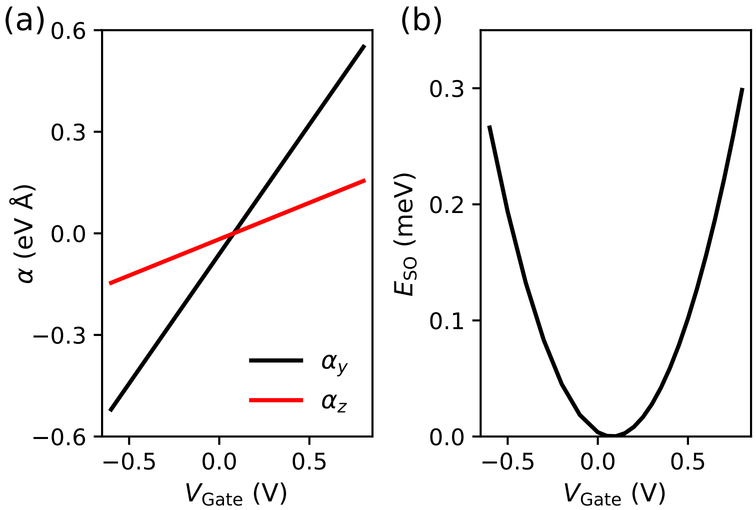

Figure 5.S2: (**a**) Rashba coefficients α_y and α_z as a function of V_{Gate}. At $V_{\mathrm{Gate}} = 0.08\,\mathrm{V}$, the average electric field in the wire goes to zero due to symmetry, leading to vanishing spin-orbit coupling. (**b**) Calculated E_{SO} as a function of V_{Gate}.

5.S.5. SIMULATED BAND STRUCTURE

The band structure of the superconductor-semiconductor nanowire system for different values of V_{Gate} is shown in figure 5.S3. To quantify the coupling of a given state to the superconductor, we calculate the weight of the state in the semiconducting region SM (see figure 5.1(c)) as $W_{\text{SM}} = \iint_{\text{SM}} |\Psi(k_{\text{F}})|^2 \, dy \, dz$.

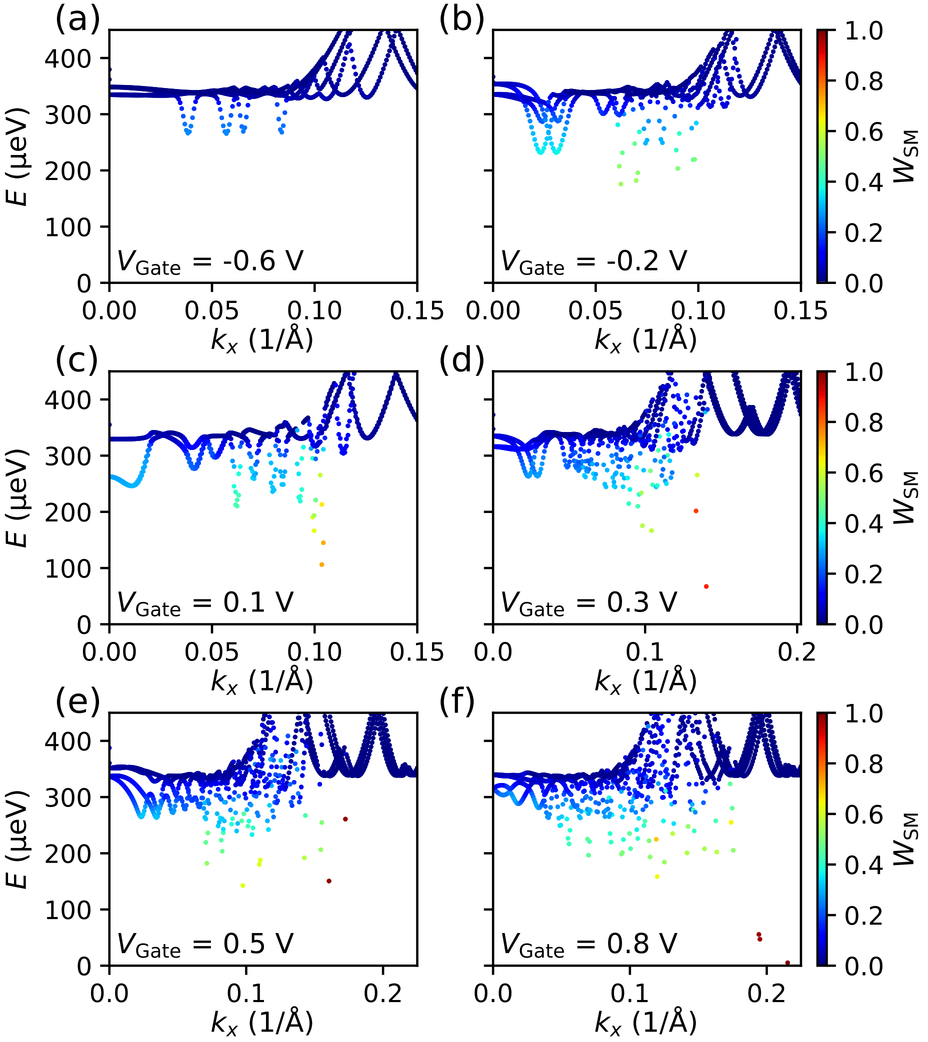

Figure 5.S3: Band structure of the hybrid system calculated at $B = 0\,\text{T}$ for different values of V_{Gate}. The color indicates the weight of a given state in the semiconducting region. As the gate voltage is increased, the population of states with higher W_{SM} leads to a soft gap.

5.S.6. GAP FITTING & ADDITIONAL DATA

To extract the gap, we measure the differential conductance $\mathrm{d}I/\mathrm{d}V$ as a function of V_{Bias} and tunnel gate voltage V_{Tunnel} for different back gate voltages V_{BG}. In the tunneling limit, $\mathrm{d}I/\mathrm{d}V$ is approximately proportional to the density of states. To ensure we are in this limit, we take only the traces where the conductance at high bias ($\sim 500\,\mu\mathrm{V}$) is between 0.03 and $0.08{\cdot}2e^2/h$. We use the BCS-Dynes expression for a dissipation broadened superconducting density of states [32] to arrive at the following expression for the conductance:

$$\frac{\mathrm{d}I}{\mathrm{d}V} = G_{\mathrm{N}}\mathrm{Re}\left\{\frac{V_{\mathrm{Bias}} - i\Gamma}{\sqrt{(V_{\mathrm{Bias}} - i\Gamma)^2 - \Delta^2}}\right\}. \tag{5.S7}$$

This equation is fitted to the data (separately for positive and negative bias), as shown in figure 5.S4 for V_{BG} = -0.6 V. We take the average of the extracted gap values for different values of V_{Tunnel}, with the errorbar given by the standard deviation (results plotted in figure 5.2(e)).

Device B shows similar behavior to device A: as the side gate voltage is increased, the observed gap becomes smaller (as illustrated in figure 5.S5).

In figure 5.S6, we show differential conductance traces as a function of V_{Bias} in device D for different values of the back gate voltage. The voltage on the tunnel gate is chosen such that the transmission through the junction (parameterized by G_{N}) is constant.

Although the sub-gap conductance is similar for all three gate voltages, there is a strong broadening of the coherence peak as the gate voltage becomes more positive. This broadening is associated with dissipation due to an increase in the number of quasiparticles, caused by pair breaking in the superconductor. We plot the extracted gap Δ and dissipation broadening Γ in figure 5.S7.

As in the other devices, the gap decreases for more positive gate voltages, although in this case the effect is minor. The size of the gap is quite stable over an extended range in gate voltage. We speculate that this is related to the diameter of the wire, which is smaller than in the other devices. The reduced thickness means the superconductor can screen

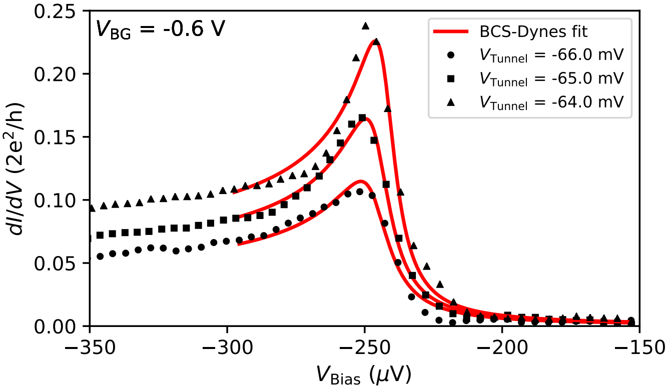

Figure 5.S4: Fit (red line) of equation (5.S7) to conductance data from device A (black circles, squares and triangles) for different values of the tunnel gate voltage.

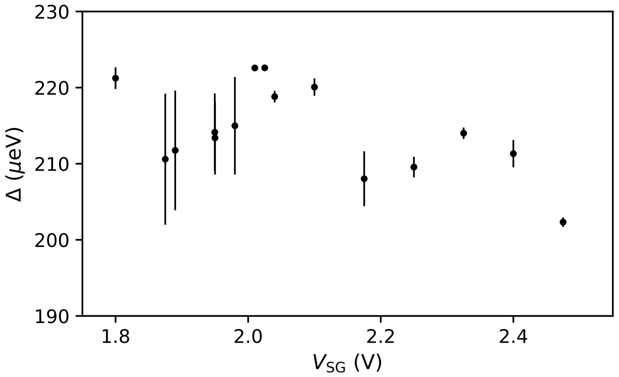

Figure 5.S5: Extracted gap Δ as a function of V_{SG} for device B.

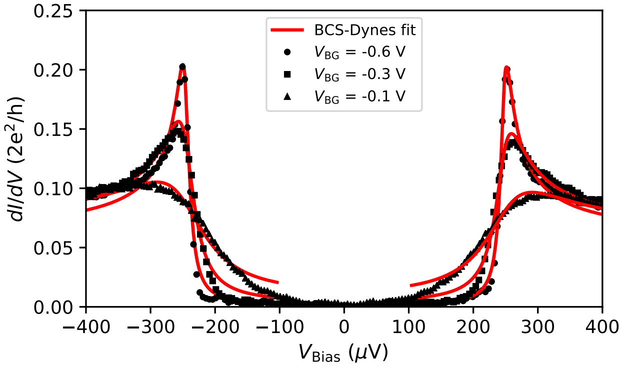

Figure 5.S6: Fit (red line) of equation 5.S7 to conductance data from device D (black circles, squares and triangles) for different V_{BG} at similar junction transparencies. The dissipation broadening sharply decreases for more negative gate voltages.

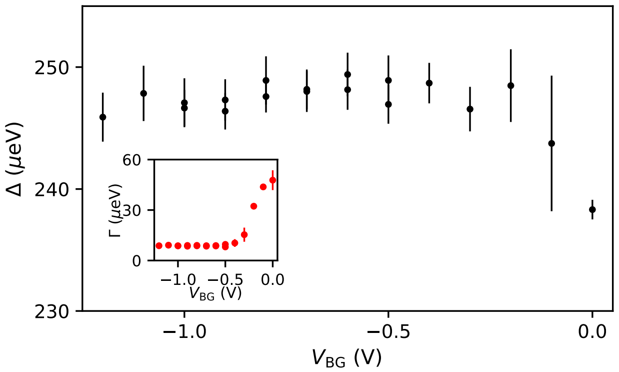

Figure 5.S7: Extracted gap Δ as a function of V_{BG} for device D. Inset: dissipation broadening Γ as a function of V_{BG}. A decrease in the gap is accompanied by an increase in broadening, signalling the emergence of a soft gap.

the gate voltage more effectively throughout the wire diameter, reducing the effect of the gate on the superconductor-semiconductor coupling.

5.S.7. G-FACTOR FITTING & ADDITIONAL DATA

For each back gate voltage, we measure the $\mathrm{d}I/\mathrm{d}V$ as a function of V_{Bias} and the magnetic field B. We then identify the lowest energy peak in the spectrum. The position of this peak at a given field is obtained by a peak finding algorithm, the results of which are shown as the green circles in figure 5.S8. The slope $|\frac{\Delta E}{\Delta B}|$ is determined by a linear fit (dashed black line in figure 5.S8). From the slope, we get g_{eff} by using the relation $|\Delta E| = \frac{1}{2} g_{\mathrm{eff}} \mu_{\mathrm{B}} |\Delta B|$ for a spin-$\frac{1}{2}$ particle, with μ_{B} the Bohr magneton. This procedure is performed separately for positive and negative bias. The reported g_{eff} is then calculated as a weighted average of the absolute value of the positive and negative bias results (weights determined by the variance of the fit parameters).

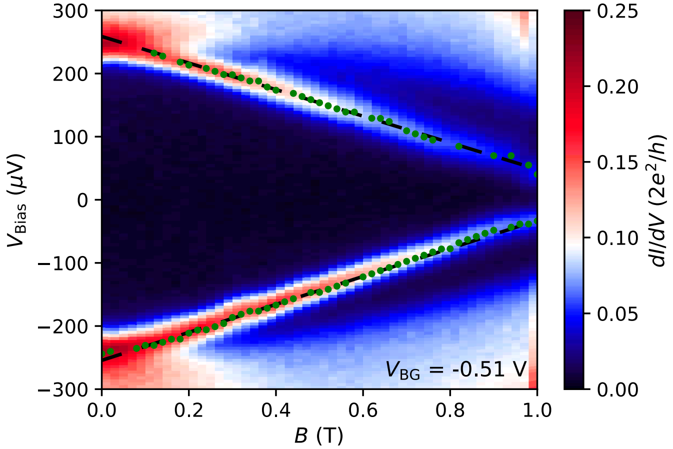

Figure 5.S8: Differential conductance as a function of V_{Bias} and magnetic field. We apply a linear fit (dashed black lines) to the extracted peak positions (green circles) to obtain the average slope $\frac{\Delta E}{\Delta B}$.

The effective g-factor for device A is reported in the main text (figure 5.3(c) and figure 5.4(d), respectively). In figure 5.S9, we plot the extracted g-factors of both L_1 and L_2 in device B. For completeness, data from device C is shown in figure 5.S10.

The effective g-factor of L_1 (black circles) changes appreciately when the side gate voltage is changed, with the effect comparable to the one observed in device A. In contrast, g_{eff} of L_2 (red squares) is almost unaffected by the gate and has a lower value. This may be due to L_2 being closely confined near the superconductor, leading to a decreased g-factor due to stronger hybridization, and a weaker gate response due to enhanced screening.

To determine the importance of orbital effects, we calculate the nanowire spectrum as a function of magnetic field including this effect (figures 5.S11(a),(b)). The orbital effect leads to an increase of the extracted values of g_{eff} and g_{spin} (figure 5.S11(c)). Note that the definition of g_{spin} used in the main text is no longer valid when the orbital effect is included. Nevertheless, for consistency we apply the same procedure. As we do not

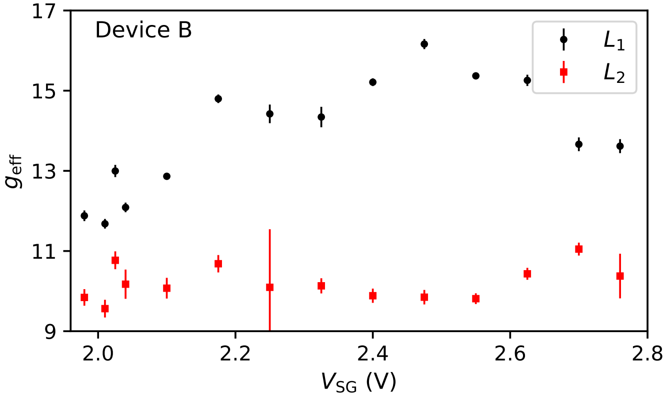

Figure 5.S9: Extracted values of g_{eff} as a function of V_{SG} for L_1 (black circles) and L_2 (red squares) in Device B.

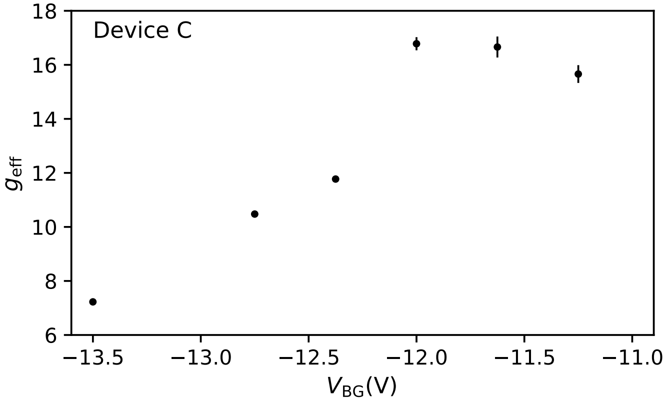

Figure 5.S10: Extracted values of g_{eff} for Device C.

observe these high g-factors in any of our devices, we conclude that the orbital effect does not give a significant contribution to the observed changes of g_{eff} with the gate voltage.

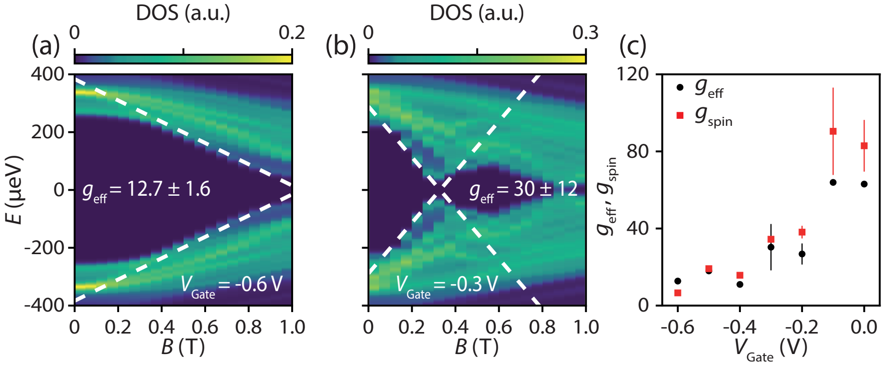

Figure 5.S11: (**a**,**b**) Simulated nanowire spectrum as a function of magnetic field including orbital effects. (**c**) Extracted g_{eff} (black circles) and g_{spin} (red squares) as a function of V_{Gate}.

5.S.8. ANTICROSSING FITTING

Near the anticrossing, we approximate the energy of the lowest subgap state L_1 as $E_1 + \frac{1}{2}g_1\mu_{\mathrm{B}}B + aB^2$. The linear term represents the Zeeman contribution to the energy, while the quadratic term is a correction to account for the curvature at high fields. This is possibly due to the presence of additional levels interacting with L_1 in this field range. As the dispersion of L_2 is mostly linear in the field range of interest, we approximate it as $E_2 - \frac{1}{2}g_2\mu_{\mathrm{B}}B$. Adding the coupling parameter δ_{SO}, we find the energy levels of the coupled system from the eigenvalues of the matrix

$$\begin{bmatrix} E_1 + \frac{1}{2}g_1\mu_{\mathrm{B}}B + aB^2 & \delta_{\mathrm{SO}} \\ \delta_{\mathrm{SO}} & E_2 - \frac{1}{2}g_2\mu_{\mathrm{B}}B \end{bmatrix}.$$

By fitting the expression for the eigenvalues to the data, we extract the parameters $E_{1,2}$, $g_{1,2}$, a, and δ_{SO}. To prevent overfitting, we use estimates for the uncoupled asymptotes to constrain the fit parameters. From the obtained parameters we also calculate the splitting A, defined as the maximum deviation from zero energy of the lowest energy state L_1, after the first zero energy crossing has occurred.

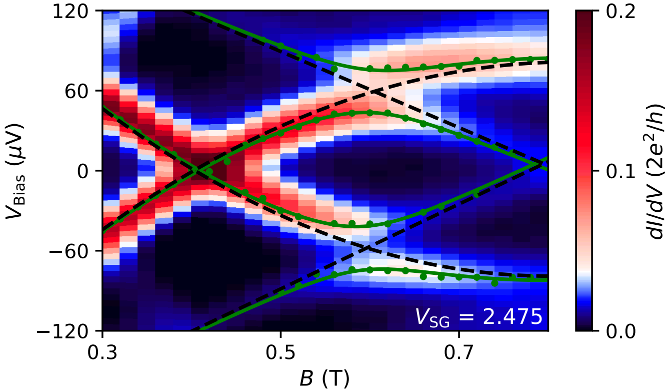

Figure 5.S12: Data from device B, showing the differential conductance $\mathrm{d}I/\mathrm{d}V$ as a function of V_{Bias} and B for $V_{\mathrm{BG}} = 2.475\,\mathrm{V}$. Green dots indicate the peak positions found using a peak finding algorithm. The fit to the data is shown in green, with the uncoupled asymptotes as the black dashed lines.

5.S.9. SIMULATION OF FINITE SIZE NANOWIRE SYSTEM

To simulate the finite nanowire system, we solve the Hamiltonian (5.1) in a simplified setup. We consider a rectangular cross-section in the yz-plane similar to the one used in reference [22], where the top facet of the rectangle is covered by the superconductor, and a uniform gate voltage V_{Gate} is applied to the bottom facet, as illustrated in figure 5.S13. First, we assume an infinitely long nanowire oriented in the x-direction, and calculate the electrostatic potential in the Thomas-Fermi approximation, similar to the procedure described in 5.S.3. The fermi level in the nanowire is tuned such that it supports the same number of transverse modes at $V_{\mathrm{Gate}} = 0$ as the hexagonal nanowire studied previously. We use the same material parameters as in the previous simulation, which can be found in table 5.S1.

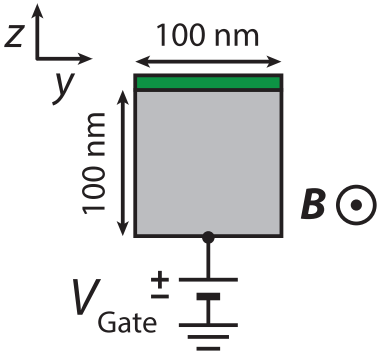

Figure 5.S13: Schematic cross-section of the geometry used to simulate the finite nanowire system. A potential V_{Gate} is applied to the bottom facet, while the potential at the top facet is fixed by the work function difference between the two materials. The magnetic field is applied in the x-direction, along length of the nanowire.

We then plug the resulting electrostatic potential into 5.1 and solve the Schrödinger equation to find the low energy spectrum of the finite nanowire. We take a length of 750 nm, similar to the studied devices. We calculate only the modes in the semiconductor, assuming a superconducting gap of $\Delta = 250\ \mu$eV. We find that the origin of the level repulsion between states is indeed spin-orbit coupling, which couples different longitudinal (along the x-direction) states within the same transverse (y- and z-directions) subband.

The result is illustrated in figure 5.S14, where we plot the low energy spectrum as a function of Zeeman energy E_Z for a fixed value of V_{Gate} and different values of α. An increase in the spin-orbit coupling strength leads to an increase in the level repulsion.

However, even if α is fixed, the magnitude of the level repulsion can be changed by changing the confinement potential, as demonstrated in figure 5.S15.

When the gate voltage is changed, it alters the confinement potential. This affects the energy of the levels coupled by the spin-orbit coupling, and as such directly influences the magnitude of δ, even though the spin-orbit coupling strength itself is not changed appreciatively. In figure 5.S16 we plot the calculated energy gap due to level repulsion, 2δ, and the maximum splitting from zero energy of the lowest energy state after the first zero crossing, A, as a function of V_{Gate}. The two parameters follow opposite trends, consistent with the experimental observation in figure 5.4(f).

However, the trend with gate voltage is opposite: δ increases with more positive gate voltage, whereas in the experiment it decreases. We note that the geometry used in this simulation is a simplified version of the one used in the experiment. The dependence of the confinement energy on gate voltage is strongly dependent on the geometry, which differs between the simulation and the experiment. It is therefore expected that the trend of δ with gate voltage is not universal, and requires the details of the systems to be very similar before comparisons can be made.

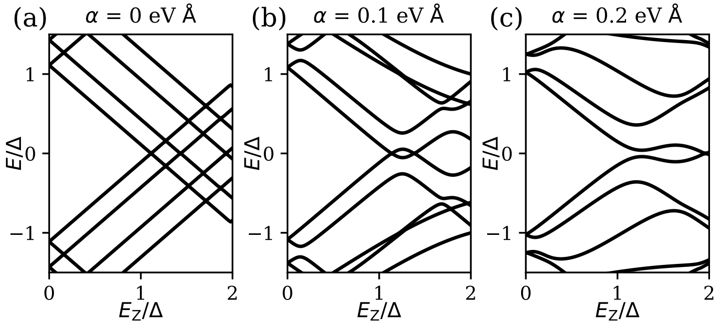

Figure 5.S14: Calculated low energy spectrum of the finite size nanowire as a function of Zeeman energy for different values of α. Values calculated for V_{Gate} = -0.536 V, which is also used in main text figure 5.4(d). All energy scales are in units of the superconducting gap Δ.

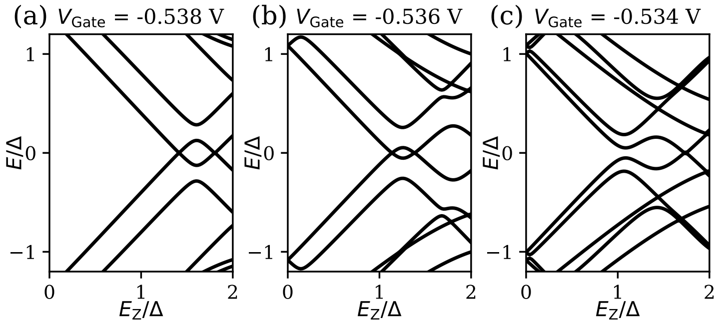

Figure 5.S15: Calculated low energy spectrum of the finite size nanowire as a function of Zeeman energy for different values of V_{Gate}. Values calculated $\alpha = 0.1$ eV Å, energy scales in units of Δ.

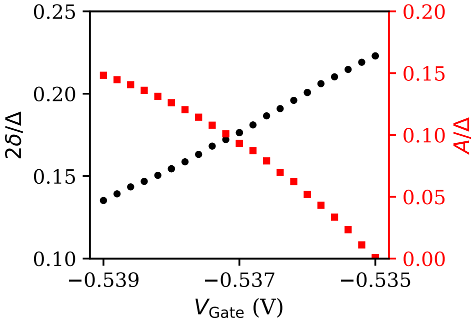

Figure 5.S16: Dependence of the energy gap 2δ and the splitting A, in units of Δ, on the gate voltage V_{Gate}.

5.S.10. ADDITIONAL ZBP DATA

Figure 5.S17(a) shows the differential conductance measured in device A as a function of V_{Bias} and V_{Tunnel}, for $B = 0.35$ T and $V_{\mathrm{BG}} = -0.37$ V. The low energy spectrum in this parameter regime does not depend on the transmission of the NS-junction. In figure 5.S17(b), we show line traces for different values of V_{Tunnel}. Even though the transmission of the junction is changed by a factor of two, the peak position of the low energy states are not affected. Data from main text figure 5 was obtained for $V_{\mathrm{Tunnel}} = -87$ mV.

Figure 5.S18 shows additional data on the evolution of the level repulsion between L_1 and L_2 in device A (supplementing the data presented in main text figures 5(a-c)) as the back gate voltage is increased. As discussed in the main text, we do not find an extended region in parameter space with a stable zero bias conductance peak.

In figure 5.S19 we show the low energy spectrum of device A as a function of V_{Bias} and V_{BG} for different magnetic fields (supplementing the data presented in main text figures 5(e,f)). For specific combinations of magnetic field and gate voltage, we can find a zero energy state. However, as we do not find an extended region in parameter space, it is unlikely that a topological phase transition is responsible for this observation.

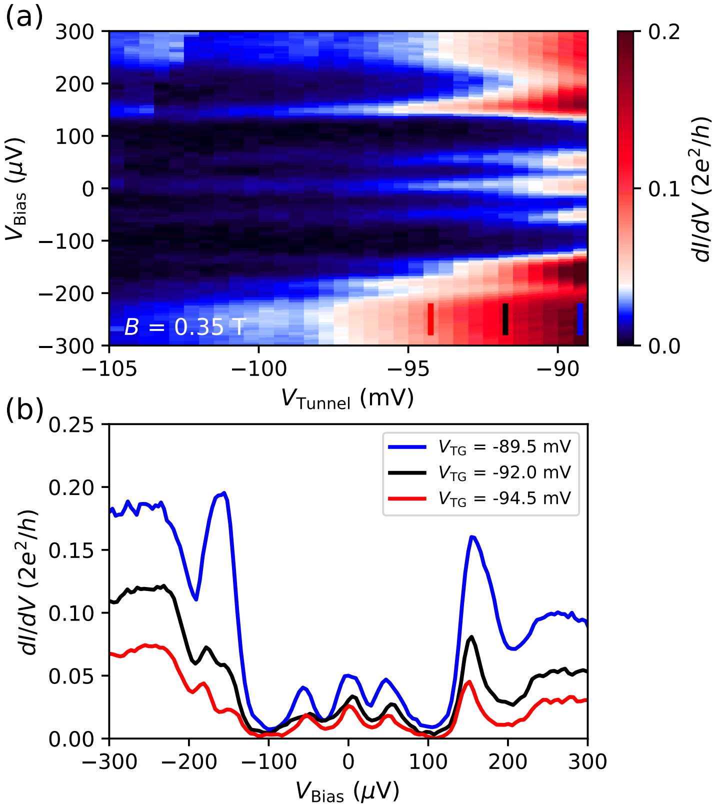

Figure 5.S17: (**a**) dI/dV measured in device A as a function of V_{Bias} and V_{Tunnel} for $B = 0.35$ T and V_{BG} = -0.37 V. (**b**) Line traces at the values of V_{Tunnel} indicated by the colored lines in panel (a).

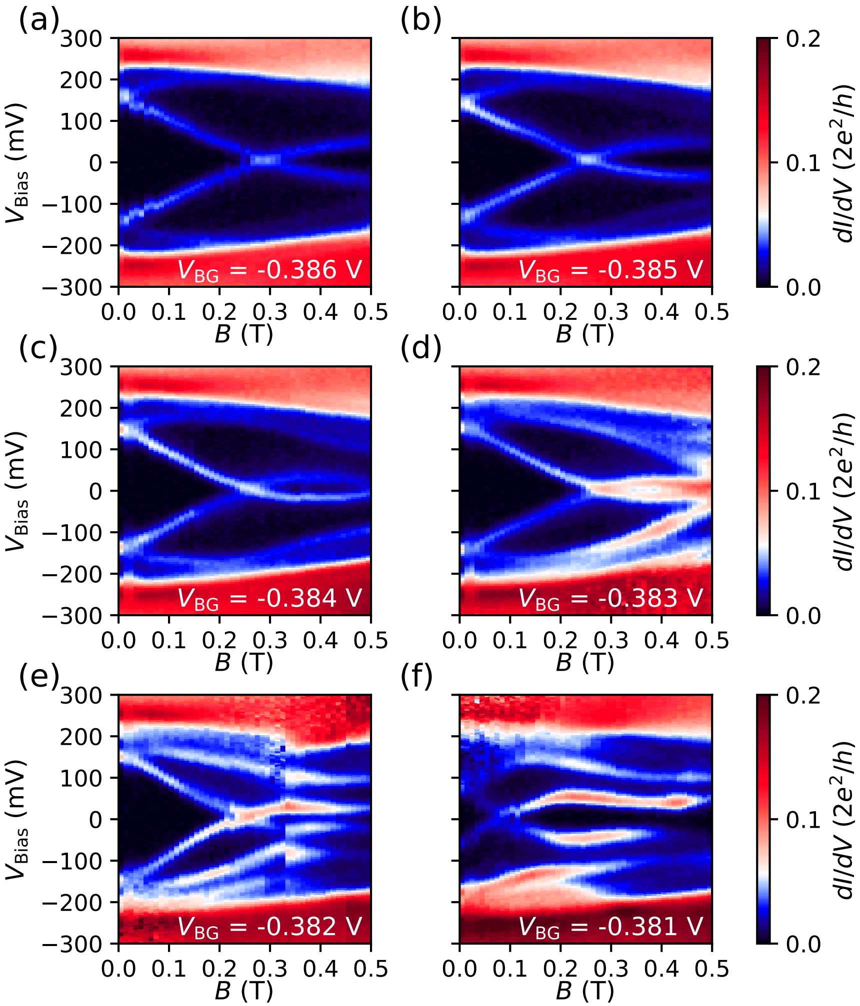

Figure 5.S18: Differential conductance as a function of V_{Bias} and magnetic field. Although the lowest energy state stays near zero over an extended magnetic field range for some gate voltages, this behavior is not robust.

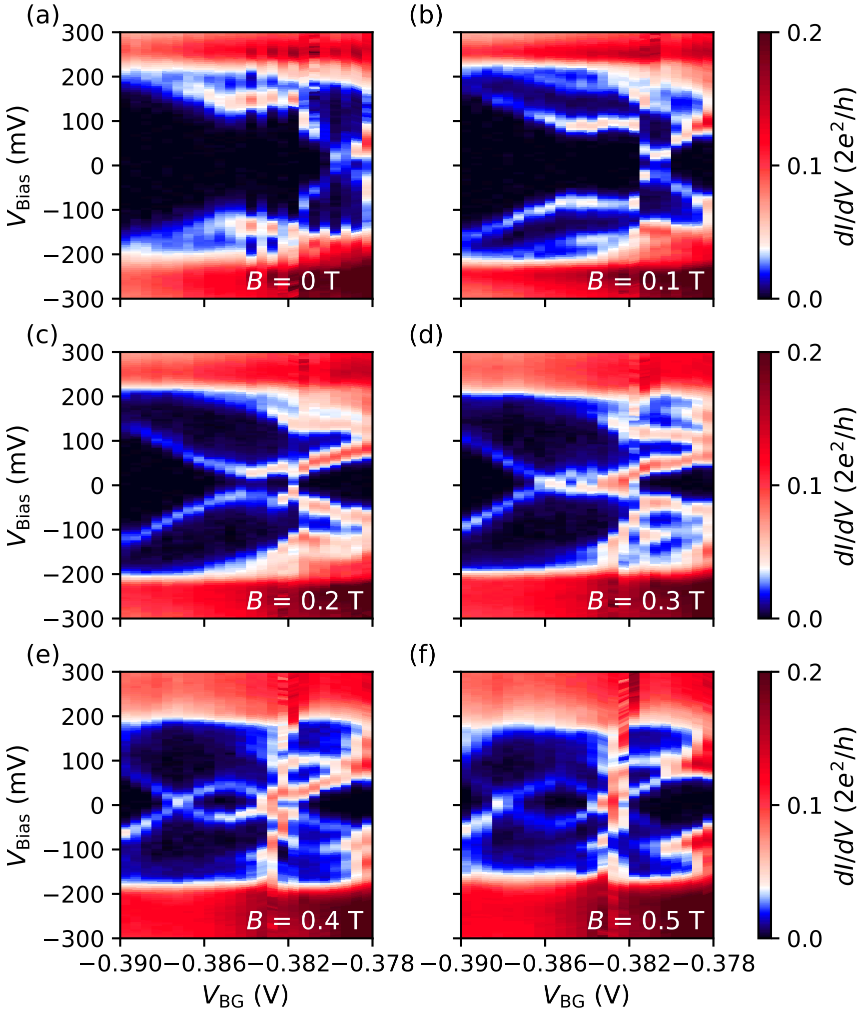

Figure 5.S19: Differential conductance as a function of V_{Bias} and V_{BG}. We find some stable ZBPs for certain ranges in back gate voltage at specific fields, but this is only true for fine tuned parameters.

REFERENCES

[1] C. Nayak, S. H. Simon, A. Stern, M. Freedman, and S. Das Sarma, *Non-Abelian anyons and topological quantum computation,* Rev. Mod. Phys. **80**, 1083 (2008).

[2] S. Plugge, A. Rasmussen, R. Egger, and K. Flensberg, *Majorana box qubits,* New J. Phys. **19**, 012001 (2017).

[3] T. Karzig, C. Knapp, R. M. Lutchyn, P. Bonderson, M. B. Hastings, C. Nayak, J. Alicea, K. Flensberg, S. Plugge, Y. Oreg, C. M. Marcus, and M. H. Freedman, *Scalable designs for quasiparticle-poisoning-protected topological quantum computation with Majorana zero modes,* Phys. Rev. B **95**, 235305 (2017).

[4] R. M. Lutchyn, J. D. Sau, and S. Das Sarma, *Majorana fermions and a topological phase transition in semiconductor-superconductor heterostructures,* Phys. Rev. Lett. **105**, 077001 (2010).

[5] Y. Oreg, G. Refael, and F. von Oppen, *Helical liquids and Majorana bound states in quantum wires,* Phys. Rev. Lett. **105**, 177002 (2010).

[6] P. G. de Gennes, *Boundary efects in superconductors,* Rev. Mod. Phys. **36**, 225 (1964).

[7] V. Mourik, K. Zuo, S. M. Frolov, S. R. Plissard, E. P. A. M. Bakkers, and L. P. Kouwenhoven, *Signatures of Majorana fermions in hybrid superconductor-semiconductor nanowire devices,* Science **336**, 1003 (2012).

[8] A. Das, Y. Ronen, Y. Most, Y. Oreg, M. Heiblum, and H. Shtrikman, *Zero-bias peaks and splitting in an Al–InAs nanowire topological superconductor as a signature of Majorana fermions,* Nat. Phys. **8**, 887 (2012).

[9] M. T. Deng, C. L. Yu, G. Y. Huang, M. Larsson, P. Caroff, and H. Q. Xu, *Anomalous zero-bias conductance peak in a Nb–InSb nanowire–Nb hybrid device,* Nano Lett. **12**, 6414 (2012).

[10] H. O. H. Churchill, V. Fatemi, K. Grove-Rasmussen, M. T. Deng, P. Caroff, H. Q. Xu, and C. M. Marcus, *Superconductor-nanowire devices from tunneling to the multichannel regime: zero-bias oscillations and magnetoconductance crossover,* Phys. Rev. B **87**, 241401 (2013).

[11] Ö. Gül, H. Zhang, J. D. S. Bommer, M. W. A. de Moor, D. Car, S. R. Plissard, E. Bakkers, A. Geresdi, K. Watanabe, T. Taniguchi, and L. P. Kouwenhoven, *Ballistic Majorana nanowire devices,* Nat. Nanotech. **13**, 192 (2018).

[12] M. T. Deng, S. Vaitiekėnas, E. B. Hansen, J. Danon, M. Leijnse, K. Flensberg, J. Nygård, P. Krogstrup, and C. M. Marcus, *Majorana bound state in a coupled quantum-dot hybrid-nanowire system,* Science **354**, 1557 (2016).

[13] H. Zhang, C.-X. Liu, S. Gazibegovic, D. Xu, J. A. Logan, G. Wang, N. van Loo, J. D. S. Bommer, M. W. A. de Moor, D. Car, R. L. M. Op het Veld, P. J. van Veldhoven, S. Koelling, M. A. Verheijen, M. Pendharkar, D. J. Pennachio, B. Shojaei, J. S. Lee,

C. J. Palmstrøm, E. P. A. M. Bakkers, S. D. Sarma, and L. P. Kouwenhoven, *Quantized Majorana conductance,* arXiv preprint arXiv:1710.10701 (2017).

[14] R. M. Lutchyn, E. P. A. M. Bakkers, L. P. Kouwenhoven, P. Krogstrup, C. M. Marcus, and Y. Oreg, *Majorana zero modes in superconductor-semiconductor heterostructures,* Nat. Rev. Mater. **3**, 52 (2018).

[15] O. Gül, H. Zhang, F. K. de Vries, J. van Veen, K. Zuo, V. Mourik, S. Conesa-Boj, M. P. Nowak, D. J. van Woerkom, M. Quintero-Pérez, M. C. Cassidy, A. Geresdi, S. Koelling, D. Car, S. R. Plissard, E. P. A. M. Bakkers, and L. P. Kouwenhoven, *Hard superconducting gap in InSb nanowires,* Nano Lett. **17**, 2690 (2017).

[16] H. Zhang, O. Gül, S. Conesa-Boj, M. P. Nowak, M. Wimmer, K. Zuo, V. Mourik, F. K. de Vries, J. van Veen, M. W. A. de Moor, J. D. S. Bommer, D. J. van Woerkom, D. Car, S. R. Plissard, E. P. A. M. Bakkers, M. Quintero-Pérez, M. C. Cassidy, S. Koelling, S. Goswami, K. Watanabe, T. Taniguchi, and L. P. Kouwenhoven, *Ballistic superconductivity in semiconductor nanowires,* Nat. Commun. **8**, 16025 (2017).

[17] S. T. Gill, J. Damasco, B. E. Janicek, M. S. Durkin, V. Humbert, S. Gazibegovic, D. Car, E. P. A. M. Bakkers, P. Y. Huang, and N. Mason, *Selective-area superconductor epitaxy to ballistic semiconductor nanowires,* Nano Lett. **18**, 6121 (2018).

[18] P. Krogstrup, N. L. B. Ziino, W. Chang, S. M. Albrecht, M. H. Madsen, E. Johnson, J. Nygård, C. M. Marcus, and T. S. Jespersen, *Epitaxy of semiconductor–superconductor nanowires,* Nat. Mater. **14**, 400 (2015).

[19] W. Chang, S. M. Albrecht, T. S. Jespersen, F. Kuemmeth, P. Krogstrup, J. Nygård, and C. M. Marcus, *Hard gap in epitaxial semiconductor-superconductor nanowires,* Nat. Nanotech. **10**, 232 (2015).

[20] S. Gazibegovic, D. Car, H. Zhang, S. C. Balk, J. A. Logan, M. W. A. de Moor, M. C. Cassidy, R. Schmits, D. Xu, G. Wang, P. Krogstrup, R. L. M. Op het Veld, K. Zuo, Y. Vos, J. Shen, D. Bouman, B. Shojaei, D. Pennachio, J. S. Lee, P. J. van Veldhoven, S. Koelling, M. A. Verheijen, L. P. Kouwenhoven, C. J. Palmstrøm, and E. P. A. M. Bakkers, *Epitaxy of advanced nanowire quantum devices,* Nature **548**, 434 (2017).

[21] F. Nichele, A. C. C. Drachmann, A. M. Whiticar, E. C. T. O'Farrell, H. J. Suominen, A. Fornieri, T. Wang, G. C. Gardner, C. Thomas, A. T. Hatke, P. Krogstrup, M. J. Manfra, K. Flensberg, and C. M. Marcus, *Scaling of Majorana zero-bias conductance peaks,* Phys. Rev. Lett. **119**, 136803 (2017).

[22] A. E. Antipov, A. Bargerbos, G. W. Winkler, B. Bauer, E. Rossi, and R. M. Lutchyn, *Effects of gate-induced electric fields on semiconductor Majorana nanowires,* Phys. Rev. X **8**, 031041 (2018).

[23] A. F. Volkov, P. H. C. Magnée, B. J. van Wees, and T. M. Klapwijk, *Proximity and Josephson effects in superconductor-two-dimensional electron gas planar junctions,* Physica C: Superconductivity **242**, 261 (1995).

[24] C. Reeg, D. Loss, and J. Klinovaja, *Metallization of a Rashba wire by a superconducting layer in the strong-proximity regime,* Phys. Rev. B **97**, 165425 (2018).

[25] B. Nijholt and A. R. Akhmerov, *Orbital effect of magnetic field on the Majorana phase diagram,* Phys. Rev. B **93**, 235434 (2016).

[26] C. W. Groth, M. Wimmer, A. R. Akhmerov, and X. Waintal, *Kwant: a software package for quantum transport,* New J. Phys. **16**, 063065 (2014).

[27] A. Vuik, D. Eeltink, A. R. Akhmerov, and M. Wimmer, *Effects of the electrostatic environment on the Majorana nanowire devices,* New J. Phys. **18**, 033013 (2016).

[28] A. E. G. Mikkelsen, P. Kotetes, P. Krogstrup, and K. Flensberg, *Hybridization at superconductor-semiconductor interfaces,* Phys. Rev. X **8**, 031040 (2018).

[29] J. Bardeen, *Tunnelling from a many-particle point of view,* Phys. Rev. Lett. **6**, 57 (1961).

[30] G. E. Blonder, M. Tinkham, and T. M. Klapwijk, *Transition from metallic to tunneling regimes in superconducting microconstrictions: Excess current, charge imbalance, and supercurrent conversion,* Phys. Rev. B **25**, 4515 (1982).

[31] C. W. J. Beenakker, *Quantum transport in semiconductor-superconductor microjunctions,* Phys. Rev. B **46**, 12841 (1992).

[32] R. C. Dynes, V. Narayanamurti, and J. P. Garno, *Direct measurement of quasiparticle-lifetime broadening in a strong-coupled superconductor,* Phys. Rev. Lett. **41**, 1509 (1978).

[33] G. W. Winkler, D. Varjas, R. Skolasinski, A. A. Soluyanov, M. Troyer, and M. Wimmer, *Orbital contributions to the electron g factor in semiconductor nanowires,* Phys. Rev. Lett. **119**, 037701 (2017).

[34] T. D. Stanescu, R. M. Lutchyn, and S. Das Sarma, *Majorana fermions in semiconductor nanowires,* Phys. Rev. B **84**, 144522 (2011).

[35] S. Vaitiekėnas, M.-T. Deng, J. Nygård, P. Krogstrup, and C. M. Marcus, *Effective g factor of subgap states in hybrid nanowires,* Phys. Rev. Lett. **121**, 037703 (2018).

[36] J. Kammhuber, M. C. Cassidy, H. Zhang, O. Gül, F. Pei, M. W. A. de Moor, B. Nijholt, K. Watanabe, T. Taniguchi, D. Car, S. R. Plissard, E. P. A. M. Bakkers, and L. P. Kouwenhoven, *Conductance quantization at zero magnetic field in InSb nanowires,* Nano Lett. **16**, 3482 (2016).

[37] J. Nitta, T. Akazaki, H. Takayanagi, and T. Enoki, *Gate control of spin-orbit interaction in an inverted* $In_{0.53}Ga_{0.47}As/In_{0.52}Al_{0.48}As$ *heterostructure,* Phys. Rev. Lett. **78**, 1335 (1997).

[38] I. van Weperen, B. Tarasinski, D. Eeltink, V. S. Pribiag, S. R. Plissard, E. P. A. M. Bakkers, L. P. Kouwenhoven, and M. Wimmer, *Spin-orbit interaction in InSb nanowires,* Phys. Rev. B **91**, 201413 (2015).

[39] Z. Scherübl, G. Fülöp, M. H. Madsen, J. Nygård, and S. Csonka, *Electrical tuning of Rashba spin-orbit interaction in multigated InAs nanowires,* Phys. Rev. B **94**, 035444 (2016).

[40] T. D. Stanescu, R. M. Lutchyn, and S. Das Sarma, *Dimensional crossover in spin-orbit-coupled semiconductor nanowires with induced superconducting pairing,* Phys. Rev. B **87**, 094518 (2013).

[41] E. J. Lee, X. Jiang, M. Houzet, R. Aguado, C. M. Lieber, and S. De Franceschi, *Spin-resolved Andreev levels and parity crossings in hybrid superconductor–semiconductor nanostructures,* Nat. Nanotech. **9**, 79 (2014).

[42] B. van Heck, J. I. Väyrynen, and L. I. Glazman, *Zeeman and spin-orbit effects in the Andreev spectra of nanowire junctions,* Phys. Rev. B **96**, 075404 (2017).

[43] E. C. T. O'Farrell, A. C. C. Drachmann, M. Hell, A. Fornieri, A. M. Whiticar, E. B. Hansen, S. Gronin, G. C. Gardner, C. Thomas, M. J. Manfra, K. Flensberg, C. M. Marcus, and F. Nichele, *Hybridization of subgap states in one-dimensional superconductor-semiconductor Coulomb islands,* Phys. Rev. Lett. **121**, 256803 (2018).

[44] D. I. Pikulin, J. P. Dahlhaus, M. Wimmer, H. Schomerus, and C. W. J. Beenakker, *A zero-voltage conductance peak from weak antilocalization in a Majorana nanowire,* New J. of Phys. **14**, 125011 (2012).

[45] S. Mi, D. I. Pikulin, M. Marciani, and C. W. J. Beenakker, *X-shaped and Y-shaped Andreev resonance profiles in a superconducting quantum dot,* J. Exp. Theor. Phys. **119**, 1018 (2014).

[46] R. V. Mishmash, D. Aasen, A. P. Higginbotham, and J. Alicea, *Approaching a topological phase transition in Majorana nanowires,* Phys. Rev. B **93**, 245404 (2016).

[47] S. M. Albrecht, A. P. Higginbotham, M. Madsen, F. Kuemmeth, T. S. Jespersen, J. Nygård, P. Krogstrup, and C. M. Marcus, *Exponential protection of zero modes in Majorana islands,* Nature **531**, 206 (2016).

[48] S. Nadj-Perge, V. S. Pribiag, J. W. G. van den Berg, K. Zuo, S. R. Plissard, E. P. A. M. Bakkers, S. M. Frolov, and L. P. Kouwenhoven, *Spectroscopy of spin-orbit quantum bits in indium antimonide nanowires,* Phys. Rev. Lett. **108**, 166801 (2012).

[49] J. D. Sau, S. Tewari, and S. Das Sarma, *Experimental and materials considerations for the topological superconducting state in electron- and hole-doped semiconductors: Searching for non-Abelian Majorana modes in 1D nanowires and 2D heterostructures,* Phys. Rev. B **85**, 064512 (2012).

[50] G. Kells, D. Meidan, and P. W. Brouwer, *Near-zero-energy end states in topologically trivial spin-orbit coupled superconducting nanowires with a smooth confinement,* Phys. Rev. B **86**, 100503 (2012).

[51] E. Prada, P. San-Jose, and R. Aguado, *Transport spectroscopy of NS nanowire junctions with Majorana fermions,* Phys. Rev. B **86**, 180503 (2012).

[52] C.-X. Liu, J. D. Sau, T. D. Stanescu, and S. Das Sarma, *Andreev bound states versus Majorana bound states in quantum dot-nanowire-superconductor hybrid structures: Trivial versus topological zero-bias conductance peaks,* Phys. Rev. B **96**, 075161 (2017).

[53] R. Winkler, S. J. Papadakis, E. P. De Poortere, and M. Shayegan, *Spin-orbit coupling effects in two-dimensional electron and hole systems,* Vol. 41 (Springer, 2003).

[54] S. R. Plissard, I. van Weperen, D. Car, M. A. Verheijen, G. W. G. Immink, J. Kammhuber, L. J. Cornelissen, D. B. Szombati, A. Geresdi, S. M. Frolov, L. P. Kouwenhoven, and E. P. A. M. Bakkers, *Formation and electronic properties of InSb nanocrosses,* Nat. Nanotech. **8**, 859 (2013).

[55] R. Meservey and P. M. Tedrow, *Properties of very thin aluminum films,* J. Appl. Phys. **42**, 51 (1971).

[56] N. Ashcroft and N. Mermin, *Solid state physics* (Saunders College Publishing, 1976).

[57] M. Tinkham, *Introduction to Superconductivity* (Dover Publications, 2004).

6

ZERO-BIAS CONDUCTANCE PLATEAUS DUE TO TOPOLOGICALLY TRIVIAL LOCAL MAJORANA STATES

> *How do I take off a mask when it stops being a mask,*
> *when it's as much a part of me as I am?*
>
> Elliot Alderson

Majorana zero-modes obey non-Abelian anyonic statistics and hold promise for topological quantum computing. When a semiconductor nanowire coupled to a superconductor is driven into the topologically nontrivial phase, a Majorana mode robustly pinned to zero energy appears at each end of the nanowire. In the topologically trivial phase, a smooth electrostatic confinement can stabilize an Andreev bound state at zero energy with comparable stability. A stable zero-energy Andreev bound state is composed of two overlapping yet decoupled local Majorana states, which also have a non-Abelian character. In tunneling spectroscopy, zero energy states are detected by a conductance peak at zero bias voltage. For both topological and local Majorana states, the height of the conductance is expected to be stable near $2e^2/h$ *(where e is the elementary charge and h is the Planck constant) while the tunneling strength is varied at low but finite temperature. Here, we track the dependence of zero-energy states on the tunneling barrier height and report the observation of conductance plateaus near* $2e^2/h$ *in indium antimonide nanowires coupled to an epitaxial aluminium superconductor. Based on dependence of the energy splitting on the electrostatic gates, we find that the states most likely originate in the tunnel junction, where local Majorana modes are expected to form. Our results improve the understanding that conductance plateaus near* $2e^2/h$ *do not yet uniquely identify a topological phase*

transition. Nevertheless, improved control over local Majorana states may offer an alternative direction for topological quantum computing.

6.1. INTRODUCTION

Majorana zero-modes (MZMs) are quasiparticles that appear in the at the edges of a topological superconductor and posses non-Abelian exchange statistics [1–3]. A topological quantum computer based on MZMs promises strong protection of the quantum information that can be stored in a pair of MZMs [4, 5]. Semiconductor nanowires coupled to a superconductor and exposed to an external magnetic field form a primary platform for investigation into MZMs [6, 7]. The presence of a MZM can be detected in an experimentally accessible way as a peak at zero bias voltage in the tunneling conductance. In particular, the height of the Majorana zero-bias peak (ZBP) is quantized at the conductance quantum $2e^2/h$, due to resonant Andreev reflection of a single (non-spin degenerate) mode [8]. The stability of the ZBP height upon variation of the tunnel barrier height, also in the presence of disorder [9], indicates the topological nature of the MZM. Indeed, the experimental verification of Majorana modes has largely focused around the observation of a ZBP in tunneling spectroscopy experiments, but generally the ZBP height has been limited to a fraction of the predicted quantized value [10–16]. More detailed theoretical studies revealed that the Majorana ZBP height can be lowered at finite temperatures, particularly if multiple subbands are occupied in the nanowire [17, 18] Dissipation broadening due to the presence of quasiparticle states within the superconducting gap forms another mechanism for reduced ZBP heights [19]. Due to the lack of the observation of a quantized peak height, the detection of MZMs through ZBPs has been controversial for some years. Recent experimental developments have shown a ZBP height close to $2e^2/h$ [20, 21]. However, new theoretical studies motivated by these results showed that a quantized conductance plateau can also emerge due to quasi-Majorana states [22], also referred to as partially separated Andreev bound states [23, 24]. In these theoretical studies, the chemical potential within the bulk of the nanowire is high and the nanowire is in the topologically trivial phase. When such a nanowire is exposed to a magnetic field and an inhomogeneous electrostatic potential profile along the nanowire, a local Andreev bound state (ABS) can stabilize at zero energy. We can understand this stabilization by separating the ABS into two MZM components. A smooth potential can decouple these MZM components through partial spatial separation and opposite spin polarization, resulting in a zero-energy state. Here, we will refer to such topologically trivial zero-energy states as local MZMs. When in addition only one of the MZMs is well coupled to the lead in the tunneling experiment, the ZBP height becomes quantized [22, 24]. Note that the strong spatial separation of MZMs at the ends of topological phase has results in the identical property of mutual MZM decoupling, with only a single MZM coupling to the lead. These commonalities make topological MZMs and local MZMs difficult to distinguish from each other in spectroscopy measurements. Detailed understanding of the circumstances under which zero-bias conductance plateaus near $2e^2/h$ can be found experimentally is essential to determine if their most likely origin is the emergence of MZMs at the edges of a topological phase, or local MZMs and a topologically trivial bulk.

Here, we investigate high ZBPs that typically occur in InSb nanowires proximitized by an epitaxial aluminium superconductor We find that the majority of these high ZBPs exhibit a strong instability upon variation of the electrostatic gate near the tunnel barrier. This points at an origin in the tunneling barrier region of the devices, where local

MZMs are expected to form. Interestingly, we find that appropriate tuning of the gates near the barrier can stabilize these states, leading to a zero-bias conductance plateau at $2e^2/h$. Additionally, we identify a zero-energy state that shows a stronger energy stability upon tunnel barrier variations. This state also displays plateaus near $2e^2/h$ while the tunneling barrier height is varied. Through theoretical analysis, we find that this state most likely also has a local origin, consistent with the formation of well decoupled local MZMs. Our results experimentally confirm the theoretical predictions that the observation of a plateau in the ZBP height at $2e^2/h$ upon variation of the tunnel strength is at this stage not a unique characteristic of a topological phase transition, and differentiation with local MZMs requires evidence of the nonlocality of the MZMs.

6.1.1. QUANTIZED ZERO-BIAS CONDUCTANCE AND ANDREEV BOUND STATES

Andreev bound states due to a smooth inhomogeneous electrostatic potential
Because a gate defined tunneling barrier by default creates an inhomogeneous potential profile, the presence of topologically trivial ABSs is unavoidable. Before diving into the experimental results, we first discuss in more detail how topologically trivial ABSs form in Majorana nanowires, how they can stabilize into zero-energy local MZMs, how local MZMs can result in a quantized ZBP height, and what the relation to topological MZMs is.

In general, MZMs form at the edges of a one-dimensional spinless p-wave superconductor [1, 2, 25, 26]. A semiconductor nanowire at a chemical potential μ (measured from the middle of the helical gap) with strong spin-orbit coupling, coupled to a superconductor which induces a superconducting gap Δ in the semiconductor nanowire, and exposed to a magnetic field induced Zeeman splitting E_Z behaves as such a topological superconductor when the criterion $|\mu| < \sqrt{(E_Z^2 - \Delta^2)}$ is satisfied in the bulk of the nanowire and only a single spin band is occupied [6, 7]. In the presence of an electrostatic potential barrier at the start of the nanowire, the edge where a MZM forms is defined by the point where the potential pushes the band bottom of the lowest spin subband up to the Fermi level [22], as illustrated in Fig. 6.1a. Following the reasoning of Kells *et al.* [27], the emergence of a topologically trivial ABS at the end of the nanowire can be explained in a similar fashion. We now consider the chemical potential of the nanowire to be high, such that both spin subbands are occupied and the bulk of the nanowire is in the topologically trivial phase ($\mu > E_Z > \Delta$). Due to the combined presence of superconductivity, spin-orbit coupling and the Zeeman field, both spin subbands exhibit p-wave superconductivity. Since for $E_Z > \Delta$ there are effectively two uncoupled one-dimensional p-wave superconductors of opposite spin, two overlapping local MZMs of opposite spin emerge at each end of the nanowire (see Fig. 6.1b). Due to their spatially overlapping character, these two MZMs typically couple strongly, together forming an ABS with a large energy splitting. Nevertheless, any fermionic ABS described by ψ_+ and its particle-hole symmetric partner ψ_- can be decomposed into two Majorana states $\psi_{\mathrm{M}\uparrow}$ and $\psi_{\mathrm{M}\downarrow}$ [2]:

$$\begin{aligned} \psi_{\mathrm{M}\uparrow} &= e^{i\varphi}\psi_+ + e^{-i\varphi}\psi_- \\ \psi_{\mathrm{M}\downarrow} &= ie^{i\varphi}\psi_+ - ie^{-i\varphi}\psi_- \end{aligned} \tag{6.1}$$

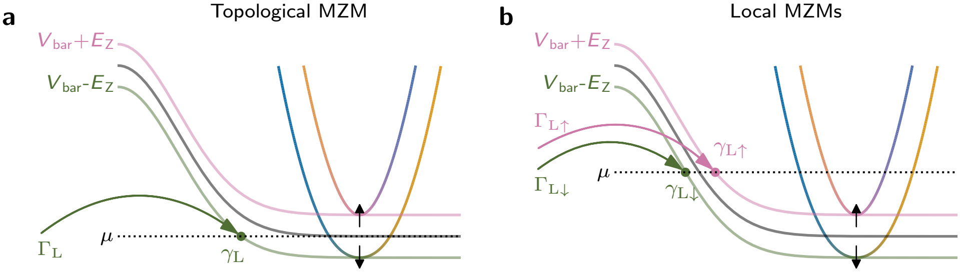

Figure 6.1: Illustration of the emergence of MZMs and their tunnel coupling through a potential barrier. **(a)** The bulk of the nanowire is in the topologically nontrivial phase, where only a single spin subband is occupied, so a single MZM (γ_L) appears at each end of the nanowire (only left end shown). In a long nanowire, where the left and right MZM are highly spatially separated, the left lead couples to only one of the MZMs with strength Γ_L. **(b)** The bulk of the nanowire is in the topologically trivial phase, with both spin subbands occupied. When both spin subbands have a p-wave character, they each contribute a set of opposite spin MZMs near the classical turning points $\mu - \left(V_{\mathrm{bar}}(x) \pm E_Z\right) = 0$ (green and pink dots), with distinct tunnel couplings $\Gamma_{L\downarrow}$ and $\Gamma_{L\uparrow}$.

where the phase φ can be chosen to define MZMs with optimal antiparallel spin. This decomposition is formally always possible, although the Majorana states are only true eigenstates at zero energy. Whereas this equivalent description of an ABS in terms of two local MZMs is not particularly informative for a conventional ABS, it does provide a natural framework to understand the properties of an ABS formed due to a smooth electrostatic potential, as we will see below.

To demonstrate the effect of varying degrees of coupling of the local MZMs, we look at simulations of a Majorana nanowire covered by a superconductor, except for the first 250 nm of the wire (the normal section). Strong coupling of the local MZMs occurs naturally at a sharp electrostatic barrier. Fig. 6.2a,e shows the effect of the coupling between the local MZMs for two slightly different sharp electrostatic potential profiles that have been used in literature previously [23, 24, 28–30]. In Fig. 6.2a the electrostatic potential in the normal section strongly exceeds the chemical potential μ, so the carrier density in the normal section is depleted, forming a high tunneling barrier. In this scenario, an ABS forms close to the superconducting gap, which has been referred to as an intrinsic ABS [30]. For the similar situation where the potential profile is sharp, but the potential in the normal section aligns with the chemical potential, an ABS can emerge at energies below the superconducting gap already at zero Zeeman field, since the wavefunction of the ABS has significant weight in the unproximitized normal section, reducing the induced superconducting coupling. When the Zeeman field is increased, these trivial ABSs [28, 29] spin split and decrease in energy, crossing zero energy, but without exhibiting stability of the peak splitting near zero energy (see Fig. 6.2e).

Since the MZMs that compose the ABSs discussed above have oppposite spin, their coupling (energy splitting) can only be caused by the spin-orbit coupling and the superconducting pairing. For a smooth electrostatic potential, the Rashba spin-orbit coupling term, which is proportional to the momentum, approaches zero at the end of the wire, where the electrostatic potential depletes the carrier density in the nanowire (momentum goes to zero). Additionally, at finite magnetic fields, the superconducting pairing is also suppressed in the absence of spin-orbit coupling [31]. As the region over which the coupling between the local MZMs is neglible increases, which happens for an increasingly smooth potential profile, the energy of the ABS starts to stabilize near zero energy (see Fig. 6.2b,f). For very smooth potentials, the ABS can stabilize near zero energy with an exponentially small energy splitting [22–24, 27] (Fig. 6.2c). Depending on the shape of the potential profile, these states have been referred to as quasi-MZMs [22] or partially-separated ABSs [23, 24]. Note that the decoupling of the local MZMs is not a result particular to the two potential profiles chosen in Fig. 6.1 [29]. The same general behavior also appears for two different variations of the potential profile, as shown in Fig. 6.S4.

We emphasize again that these stable zero-energy ABSs that emerge for very smooth potentials appear when the bulk of the nanowire is in the topologically trivial phase, and are as such often described as trivial ABSs in literature [23, 29]. However, these highly decoupled local MZMs do have a close connection to topological MZMs. As the Zeeman field is increased, the decoupled local MZMs spatially separate and eventually evolve smoothly into topological MZMs (see wavefunctions in Fig. 6.2d,h). For a smooth potential barrier, a stable zero-energy state is present both before and after the topological phase transition, complicating the association of a zero-energy state with the presence of either local MZMs or topological MZMs. This strong overlap between the local properties of decoupled local MZMs and topological MZMs also appears in other experimental signatures, including a ZBP height quantized at $2e^2/h$ [22, 24], as we discuss in more detail in the next paragraph, a 4π Josephson effect, and even braiding [22], which may make local MZMs candidate building blocks in quantum computing. The crucial difference between local MZMs and topological MZMs is that while topological MZMs are decoupled through their spatial separation by a topologically nontrivial bulk phase, providing them topological protection, local MZMs owe their decoupling to their opposite spin character combined with the local disappearance of the spin-orbit coupling and superconducting pairing. This difference in the locality only becomes apparent in nonlocal measurements, for example due to correlation of ZBPs on both ends of the nanowire [32], and the observation of a bulk gap closing and reopening through the nonlocal conductance [33].

Zero-bias conductance quantization due to local MZMs

The two local MZMs near the tunneling probe can each contribute a conductance of up to $2e^2/h$, resulting in a total zero-bias conductance in between 0 and $4e^2/h$ [29]. However, if the tunnel coupling to one of the local MZMs is strongly suppressed, an effectively quantized zero-bias conductance remains [22, 24]. A smooth potential creates this suppression in two ways. First, the Zeeman spin splitting of the subbands depletes the spin down subband closer to the tunneling probe than the spin-up subband, as is illustrated in 6.1b. The resulting spatial separation favors tunneling into the spin down local MZM [23, 24]. Second, the spin splitting of the tunneling barrier itself creates a lower barrier height for the spin down MZM than for the spin up MZM [22]. The tunnel coupling strengths to each of the local MZMs $\Gamma_\downarrow$ and $\Gamma_\uparrow$ also set the bias width of the ZBP. For exponentially different tunneling strengths, we therefore end up with a narrow $2e^2/h$

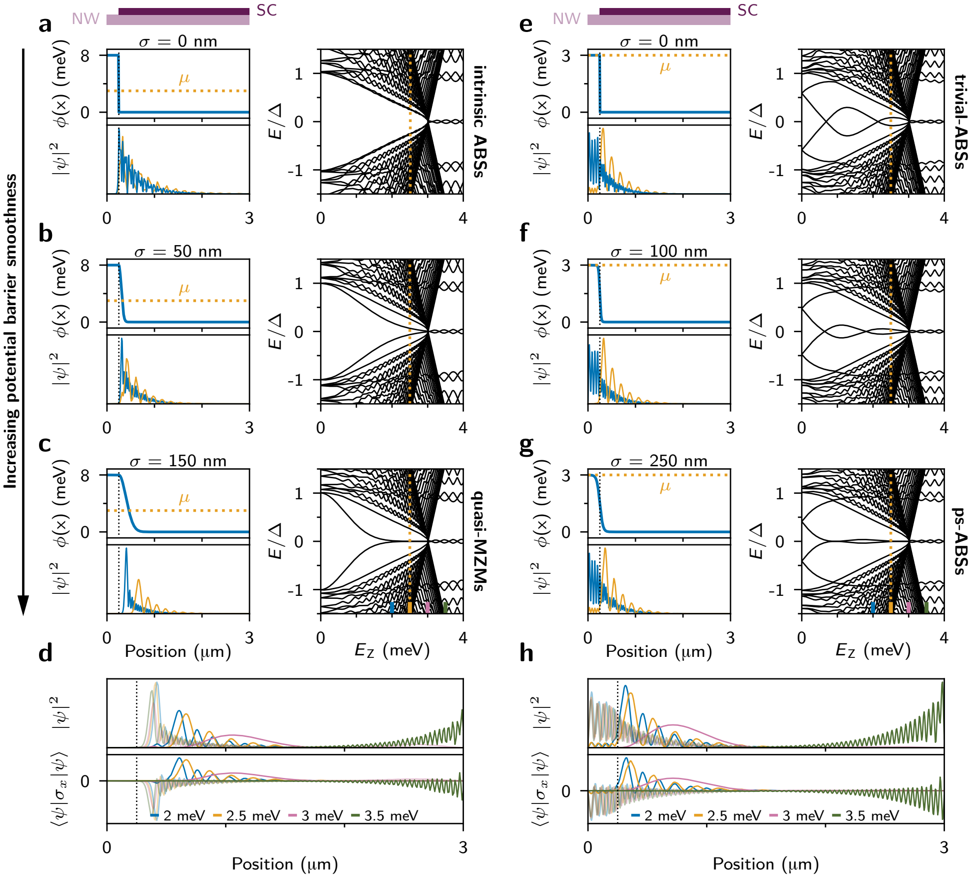

Figure 6.2: Overview of Andreev bound states due to smooth electrostatic potentials. We consider a nanowire with a length of 3 μm covered by a superconducting shell which induces a gap in the nanowire of $\Delta = 0.3\,\text{meV}$, except for the first 250 nm where the induced gap is set to zero. **(a-c)** The effect of an increasing potential barrier smoothness σ for a half-Gaussian confinement potential $\phi(x) = \phi_{\text{barrier}} \exp\left(-(x - L_{\text{N}})^2/2\sigma^2\right)$ for $x > L_{\text{N}} = 250\,\text{nm}$ and $\phi(x) = \phi_{\text{barrier}}$ for $x \leq x_0$ (normal section, boundary indicated by the dashed black line). Since we take the potential in the normal wire section to be high, $\phi_{\text{barrier}} = 8\,\text{meV}$, the carrier density in the normal wire section is completely depleted, creating a profile as in Vuik *et al.* [22]. For each panel the spatial profile of the electrostatic potential $\phi(x)$ is shown in the top left subpanel, the resulting energy spectrum as a function of the Zeeman energy E_{Z} is shown on the right, and the wavefunction distribution of the lowest energy state decomposed into the Majorana wavefunctions at $E_{\text{Z}} = 2.5\,\text{meV}$ is shown on the bottom left. **(d)** Majorana wavefunctions (top panel) and their spin densities (bottom panel) of the lowest energy states in **c** for an increasing Zeeman field. The lighter (darker) colored lines show the left (right) MZM. Below the topological phase transition at $E_{\text{Z}} \sim 3\,\text{meV}$, the local MZMs tend to separate further with increasing E_{Z} and have opposite spin-densities. After the topological phase transition (green lines), the right MZM moves to right end of the nanowire and both Majorana components have a negative spin density. **(e-g)** Same as **a** for a smooth potential step defined by $\phi(x) = \phi_{\text{barrier}}\left(1 - \left(1 + \tanh\left(\frac{x - L_{\text{N}}}{\sigma/4}\right)\right)/2\right)$, using $\phi_{\text{barrier}} = 3\,\text{meV}$, such that normal section of the nanowire is nearly depleted, as used in Moore *et al.* [23, 24]. **(h)** Same as **d**, for the lowest energy states in **g**. The model used to obtain this figure is described by equation 6.2, using the parameters $m^* = 0.03 m_{\text{e}}$, $\alpha = 0.5\,\text{eV\AA}$, and $\mu = 3\,\text{meV}$.

peak superimposed on a broad $2e^2/h$ peak. The finite temperature in an experimental setting broadens narrow peaks to $3.5k_\mathrm{B}T$, while significantly reducing their height (k_B is the Boltzmann constant). Therefore, when the height of the tunneling barrier is varied, a zero-bias conductance plateau effectively quantized at $2e^2/h$ remains as long as $\Gamma_\downarrow > 3.5k_\mathrm{B}T > \Gamma_\uparrow$.

6.2. DEVICE FABRICATION

The devices we study in this chapter consist of InSb nanowires covered on two of the hexagonal facets by a thin aluminium shell of a few nanometers thick, which induces a hard superconducting gap [34], that persists up to magnetic fields oriented along the nanowire exceeding 2 T. A gap in the aluminium coverage is formed through an in-situ shadowing technique [34], removing the need to selectively etch aluminium from InSb to create a gate-tunable semiconducting wire section. Using a micromanipulator in a scanning electron microscope, the nanowires are placed on a highly doped Si chip, covered by 20 nm of high quality LPCVD silicon nitride, which serves as an electrostatic back gate. The contacts to the nanowire are fabricated by etching in an argon plasma for 4 minutes at 3 mTorr and 100 W (in 20 s cycles followed by a 40 s cooldown, to limit sample heating), which removes most of the exposed nanowire and aluminium shell, followed by transfer into an electron beam evaporator, where 10 nm Cr and 100 nm Au is deposited. To fabricate local electrostatic gates the nanowires are covered by 35 nm of sputtered silicon nitride, followed by evaporation of Ti/Au electrodes. As is illustrated in the inset of Fig. 6.3a, the gates cover the top and sides of the nanowire, providing strong coupling, while limiting the cross capacitance of the gates through electrostatic screening, which is beneficial in the search of MZMs and to spatially resolve the position of low energy states. In the case of device A, an additional top gate was fabricated on top of the first top gate layer by depositing another 30 nm layer of sputtered silicon nitride, followed by 110 nm of niobium titanium nitride. All fabrication steps are performed at room temperature to preserve the sensitive interface between InSb and aluminium.

6.3. CONDUCTANCE PLATEAU WITH STRONG BARRIER POTENTIAL INSTABILITY

Following the advancement of the material quality with the arrival of hybrid InSb epitaxial aluminium nanowires [34], we now generally encounter high ZBPs approaching and in excess of $2e^2/h$ in virtually every device. Here, we first demonstrate a frequent behavior of such high ZBPs in this device design. We identify that they are predominantly located in the wire section in front of the superconducting region through the peak splitting induced by the different gates. Next, we show that in a particular nanowire device careful electrostatic tuning allows for the emergence of a zero-bias conductance plateau at $2e^2/h$. We note that although we focus on zero-energy states in the barrier region, our devices can also show ZBPs that are highly insensitive to tunnel barrier variations. These states appear to originate in the superconducting section of the nanowire and show features possibly indicating topological MZMs (see Fig. 6.S9).

Figure 6.3a shows hybrid nanowire device A, in which we perform tunneling spectroscopy by applying a bias voltage V between the contacts (yellow) while measuring the differential conductance $\mathrm{d}I/\mathrm{d}V$ using lock-in techniques. Our measurement circuit has a non-negligible reactive response at finite ac frequencies, which we take into account by correcting $\mathrm{d}I/\mathrm{d}V$ to correspond with the simultaneously measured dc differential conductance (see supplemental section 6.S.3 for details of the calibration procedure). The wrap around tunnel gate (blue) covers a section of the nanowire that is not covered by the aluminium shell and tunes the transmission of the tunnel barrier formed in the nanowire junction. The super gate next to it (purple) covers the nanowire section that is covered by the superconducting shell and tunes the carrier density in the superconducting region. After applying suitable voltages on the tunnel gate V_{TG} and the super gate V_{SG}, we apply a magnetic field B along the nanowire and observe the emergence of a ZBP, as shown in Fig. 6.3b. The conductance peaks at the edges of the superconducting gap at $B = 0\,\mathrm{T}$ continuously disperse with the magnetic field down to zero energy, where a ZBP forms with a height of $0.85\cdot 2e^2/h$ at $B = 1.2\,\mathrm{T}$, which splits into subgap states close to zero energy upon further increase of B (linecuts in the left panel of Fig. 6.3d). As the ZBP results from a crossing of the subgap states, it does not exhibit stability in the magnetic field, as is expected for a local state near the barrier. The magnetic field at which the ZBP occurs, depends sensitively on the applied gate voltages, as is apparent in Fig. 6.3c, where V_{SG} is increased to $-0.6\,\mathrm{V}$ and V_{TG} is decreased to keep the above-gap conductance approximately constant (linecuts in the right panel of Fig. 6.3d). The subgap states still emerge from the gap edge, but the ZBP is shifted to $B = 1.75\,\mathrm{T}$. The seemingly longer extent of the ZBP as compared to Fig. 6.3b results from the slower dispersion with magnetic field and does not imply the formation of a stable zero-energy state. To look into the effects of the gate voltages in more detail, we fix the magnetic field at $B = 1.7\,\mathrm{T}$, while we vary V_{TG} (Fig. 6.3e). Similar to the magnetic field dependence, the ZBP results from a level crossing and only extends over a $0.03\,\mathrm{V}$ range (the dependence on V_{TG2} is equivalent, as shown in Fig. 6.S5). Analogously, as V_{SG} is varied (Fig. 6.3g) the ZBP is easily split, although it remains near zero energy over a longer voltage range of $0.25\,\mathrm{V}$. The significantly stronger coupling of the ZBP to the tunnel gate indicates that the ZBP is located in the wire section between the normal contact and the super gate, where well coupled local MZMs (i.e. topologically trivial ABSs) are expected to form due to a inhomogeneous electrostatic potential [22–24, 27–29, 35]. The tendency of the low energy state to stick near zero energy over some finite gate ranges, as is particularly apparent in the super-gate dependence in Fig. 6.3g, could be because over those gate ranges the barrier potential is sufficiently smooth. Interestingly, looking at the ZBP height as a function of the gate voltages (see the linecuts in Fig. 6.3f,h) at $B = 1.7\,\mathrm{T}$ and as function of magnetic field in Fig. 6.3d, we find that the ZBP height reaches high values of $\sim 0.8\cdot 2e^2/h$ before the peak splits, while the transmission through the junction keeps increasing as the gates are increased (orange lines in Fig. 6.3f,h).

To explore the dependence of the ZBP and its height on the gate voltages in more detail, we measure the zero-bias conductance while varying V_{TG} and V_{SG} in Fig. 6.4a, where the ZBP appears as a diagonal peak with a negative slope, suggesting that an appropriate compensation of the two gates stabilizes subgap state at zero energy[1]. We investigate the

---

[1] Note that a peak as a function of gate voltages in the zero-bias conductance in Fig. 6.4a does not necessarily correspond to a ZBP in the conductance as a function of the bias voltage. However, in practice, we found the

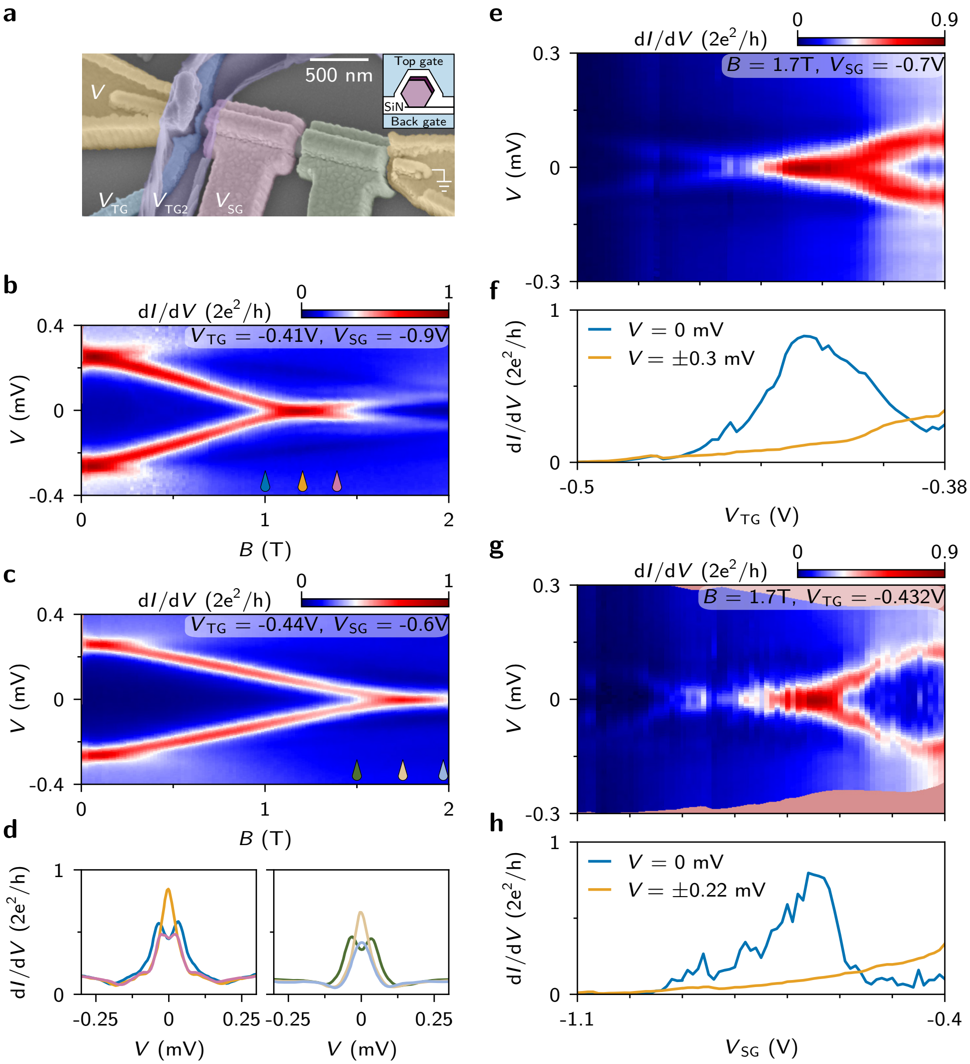

Figure 6.3: Typical high ZBPs in device A. **(a)** False-colored scanning electron micrograph of device A. The epitaxial aluminium-InSb nanowire is contacted by two gold contacts (yellow) and covered by the tunnel gate (blue) and a second overlapping tunnel gate (purple, set at $V_{TG2} = -0.5$V), which cover a section of the nanowire that is not covered by aluminium, and the super gate (pink). The additional gate at the far end of the nanowire (green) has no effect on any of the measurements in this device, so the set voltages are omitted. The global backgate is set to -0.25V. **(b)** Differential conductance dI/dV as a function of the magnetic field B and bias voltage V between the contacts at $V_{TG} = -0.41$V and $V_{SG} = -0.9$V. **(c)** Same as **b**. The ZBP shifts to a higher B with the gates at $V_{TG} = -0.44$V and $V_{SG} = -0.6$V. **(d)** Vertical linecuts of **b** (left panel) and **c** (right panel) at B indicated by the colored droplets. **(e)** Instability of the ZBP upon variation of the tunnel-gate voltage V_{TG} at $V_{SG} = -0.7$V and $B = 1.7$T. **(f)** Horizontal linecuts of **e** at zero bias (blue) and the above gap conductance, taken as the average of -0.3 and 0.3 mV (orange). **(g)** Instability of the ZBP upon variation of the super-gate voltage V_{SG} at $V_{TG} = -0.43$V and $B = 1.7$T. **(h)** Horizontal linecuts of **g** at zero bias (blue) and the above gap conductance, taken as the average of -0.22 and 0.22 mV (orange). $V_{TG2} = -0.5$V in all panels.

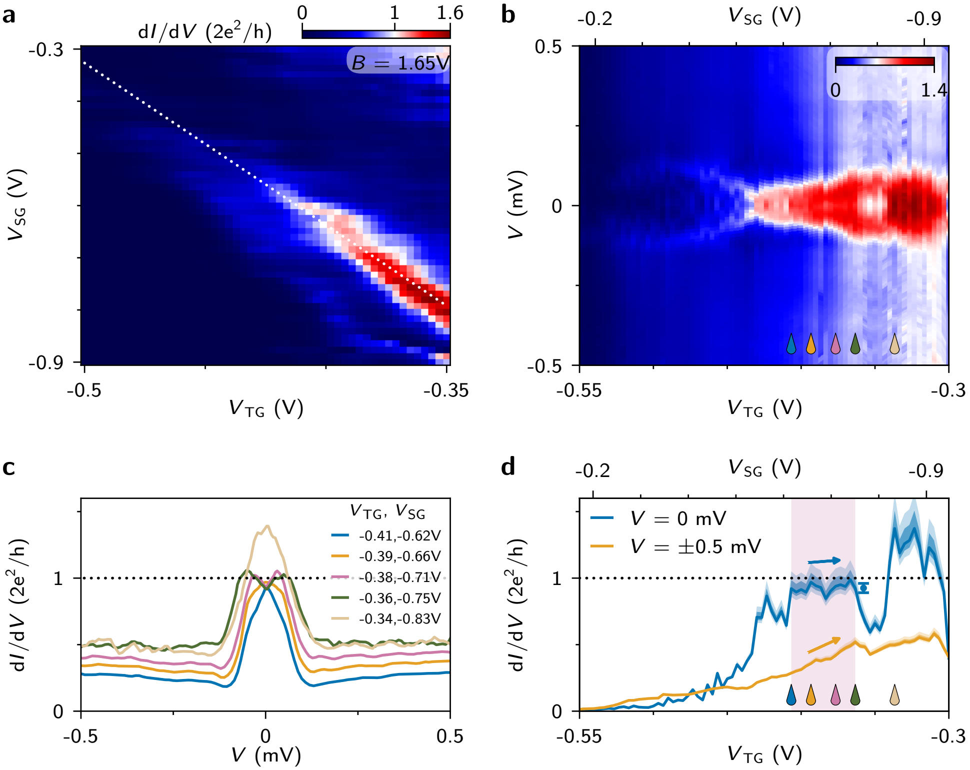

Figure 6.4: Zero-bias conductance plateau due to coupled local MZMs in device A. **(a)** The zero-bias $\mathrm{d}I/\mathrm{d}V$ at $B = 1.65\,\mathrm{T}$ and $V_{\mathrm{TG2}} = -0.69\,\mathrm{V}$ as a function of V_{TG} and V_{SG} shows that a ZBP is present if the two gates are appropriately compensated, as indicated by the dashed line. **(b)** $\mathrm{d}I/\mathrm{d}V$ against V while the tunnel gate and super gate are scanned over the dotted line in **a**, increasing the extent over which the ZBP is stable. We remark that the zero-bias conductance does not exactly reproduce **a**, likely due to gate hysteresis. **(c)** Vertical linecuts of **b** at the gate voltages indicated by the colored droplets in **b** and **d** showing the transition from a ZBP to a zero-bias conductance dip. **(d)** Horizontal linecuts of **b** at zero bias (blue line) showing a plateau in the conductance at $2e^2/h$ and the above-gap conductance (orange line), taken as the average at -0.5 and $0.5\,\mathrm{mV}$. The shaded blue region shows the $\mathrm{d}I/\mathrm{d}V$ uncertainty (as specified in supplemental section 6.S.1). The blue shade around the blue indicates the $\mathrm{d}I/\mathrm{d}V$ uncertainty, as specified in the supplemental section 6.S.1. The plateau region is indicated by the pink shade, and the blue arrow shows the average slope of the zero-bias conductance, which is six times smaller than the above-gap conductance slope (orange arrow). The mean zero-bias conductance on the plateau and its standard deviation are $0.93 \pm 0.04 \cdot 2e^2/h$ (blue errorbar). $V_{\mathrm{TG2}} = -0.69\,\mathrm{V}$ in all panels, the smooth connection to the ZBP in Fig. 6.3 measured at $V_{\mathrm{TG2}} = -0.5\,\mathrm{V}$ is visible in the V_{TG2} dependence in Fig. 6.S5).

stabilization of the low energy state in Fig. 6.4b, where V_{TG} and V_{SG} are swept following the white dotted line in 6.4a, which results in the appearance of the ZBP over an extended gate range. In fact, the zero-bias conductance (blue linetrace in Fig. 6.4d) stabilizes close to $2e^2/h$, while the above-gap conductance (orange linetrace in Fig. 6.4d) increases by a factor of two: a zero-bias conductance plateau forms[2]. The vertical linetraces in Fig.

---

two to be well correlated. A sweep of multiple gates at zero bias can therefore be considered as a good starting point in the search for a ZBP, after which its gate responses should be explored in more detail.

[2] We define a zero-bias conductance plateau as a region in parameter space where a ZBP appears and the standard deviation of the zero-bias conductance is no larger than 5 % of $2e^2/h$. Additionaly, we require the

6.4c confirm that a ZBP with a height of $2e^2/h$ is formed around $V_{\mathrm{TG}} = -0.41\,\mathrm{V}$ (blue and orange lines). Around $V_{\mathrm{TG}} = -0.38\,\mathrm{V}$ the zero-bias conductance remains near $2e^2/h$, but the conductance peaks now occur at non-zero bias voltage (pink and green lines). Eventually the split peak returns to a ZBP with a height of $1.5 \cdot 2e^2/h$ (beige line). For topological MZMs, a quantized zero-bias *peak* is expected to evolve into a quantized zero-bias *dip* when the tunnel barrier is reduced, and strong Andreev reflection raises the finite bias subgap conductance throughout the gap above $2e^2/h$ [9]. Although we do observe a peak to dip transition, we do not find the strong subgap conductance throughout the gap. In addition, the peak to dip transition is expected in the regime when both spinful modes acquire a transmission close to unity and the above-gap conductance approaches $2e^2/h$ [22]. In this particular case, the dip could instead be the result of a slight splitting of the ZBP, which is very sensitive upon the precise compensation of the gates. This sensitivity to the precise gate compensation and hysteresis is demonstrated in Fig. 6.S7, where we find less pronounced stabilization of the ZBP height near $2e^2/h$ for slightly different combinations of the tunnel gate and the super gate. Although in our experiments we focused on peak heights near $2e^2/h$, we do note that we find a similar state for which the ZBP height stabilizes around $1.35 \cdot 2e^2/h$ in the same device at a more negative back-gate voltage (Fig. 6.S8). This suggests that the formation of a stable zero-bias conductance over finite ranges of the voltages on the gates near the barrier may not be unique to $2e^2/h$. Although we commonly observe high ZBPs in our devices, we stress that the observation of plateau features is not generic. Our results show that a zero-bias conductance plateau could be generated by well-coupled local MZMs (trivial ABSs) by extremely precise tuning of the gate voltages near the tunneling barrier. The sensitivity of these plateau features, however, allows for a distinction from the more stable plateaus expected for strongly decoupled local MZMs and topological MZMs.

6.4. CONDUCTANCE PLATEAU WITH ENHANCED BARRIER POTENTIAL STABILITY

As we have found that a ZBP plateau can form near $2e^2/h$ due to a state in the tunneling region of the nanowire device by tuning both gates near the barrier simultaneously, a particularly important distinguishing characteristic for a $2e^2/h$ conductance plateau due to MZMs separated by a topological phase, is robustness at zero energy upon variation of the tunnel-gate voltage. In the following, we identify a ZBP that remains near zero energy and exhibits a plateau in the peak height near $2e^2/h$ as the tunneling barrier height is varied. Through comparison with a theoretical model of the nanowire system, we find that decoupled local MZMs provide a good explanation of the experimental observations. In addition, an analysis of the level repulsion with a higher energy state indicates an appreciable coupling to both local MZMs, consistent with the expected spatially overlapping character of local MZMs.

Experimental observations

We start by looking for a peak in $\mathrm{d}I/\mathrm{d}V$ that is unaffected by the tunnel gate by sweeping

---

positive slope of the zero-bias conductance with respect to the gate voltage to be at least a factor of three smaller than the slope of the above-gap conductance.

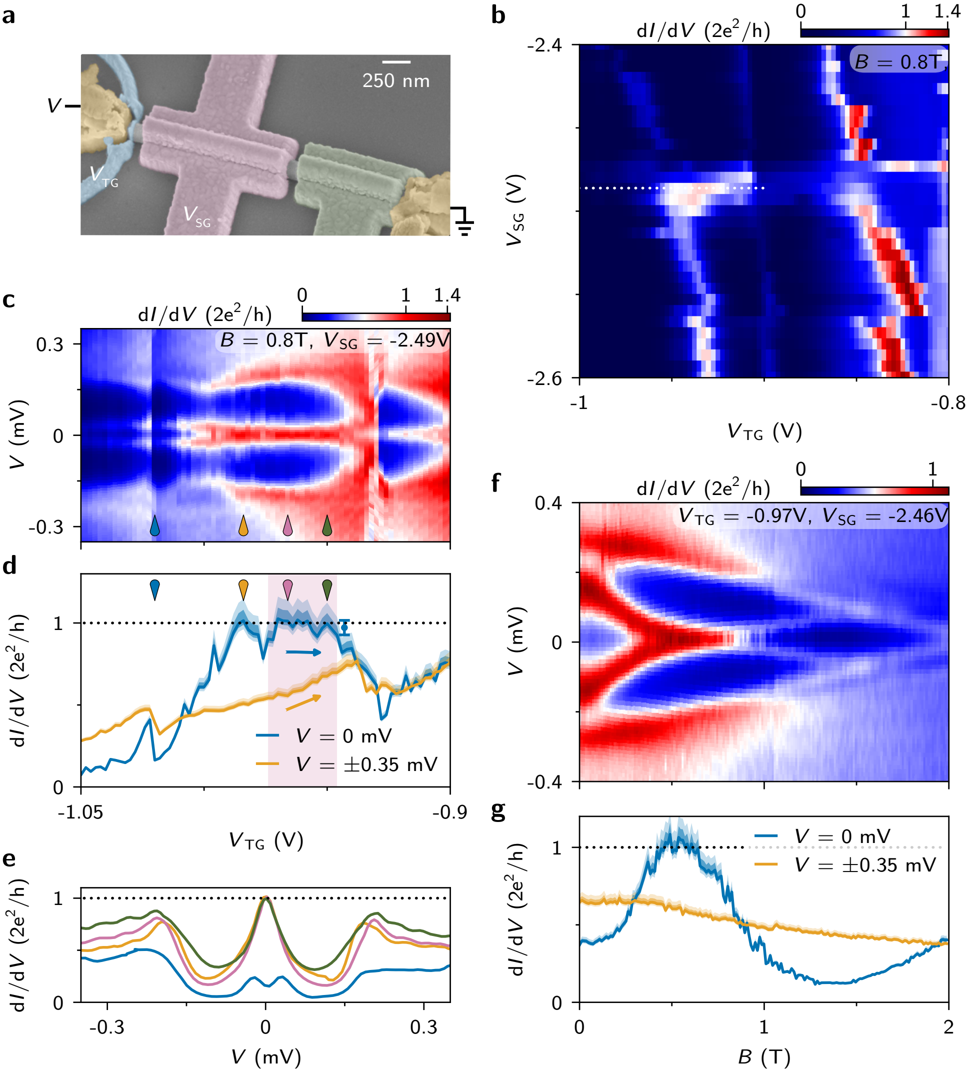

Figure 6.5: Zero-bias conductance plateau stable against tunnel gate variation at 0.8 T in device B. **(a)** False-color tilted view scanning electron micrograph of device B, using the same color coding as in Fig. 6.3a. The back-gate voltage is set to 0.1 V for all measurements in this device. **(b)** Zero-bias dI/dV at $B = 0.8$ T against V_{TG} and V_{SG}. The ZBP that is insensitive to changes in V_{TG} is highlighted by the white dashed line. **(c)** Scanning V_{TG} over the white dashed line ($V_{\mathrm{SG}} = -2.49$ V) in **b** shows the presence of subgap states close to zero energy merging into a ZBP. **(d)** Horizontal linecuts of **c**, showing the emergence of a zero-bias conductance plateau at $2e^2/h$ (blue line, with shade indicating the uncertainty). The above-gap conductance (orange line) is taken as the average of the conductance at −0.35 and 0.35 mV. On the plateau (pink shade) the mean and standard deviation of the zero-bias conductance are $0.97 \pm 0.04 \cdot 2e^2/h$ (blue errorbar) and the ratio of the slopes (blue, orange arrows) is −27. **(e)** Vertical linecuts at V_{TG} indicated by the colored droplets in **c** and **d** show the stability of the ZBP height on the plateau. **(f)** Magnetic field dependence of the ZBP at $V_{\mathrm{TG}} = -0.97$ V and $V_{\mathrm{SG}} = -2.47$ V. **(g)** Zero-bias linecut (blue) of **f** with the uncertainty indicated by the shaded region and the above-gap conductance (orange), taken as the average of the conductance at −0.35 mV and 0.35 mV.

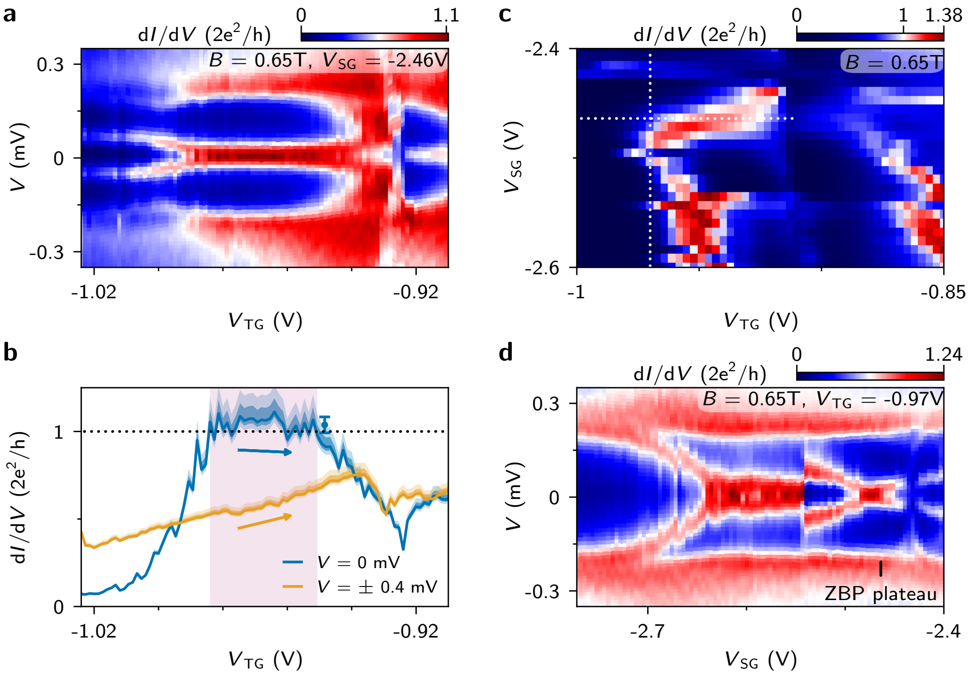

Figure 6.6: Zero-bias conductance plateau and super gate dependence at 0.65 T in device B. **(a)** A ZBP stable in tunnel gate variations analogous to Fig. 6.5c also forms at a slightly lower $B = 0.65\,\mathrm{T}$. V_{SG} is set to $-2.46\,\mathrm{V}$. **(b)** Horizontal linetraces of **a** at zero bias (blue) and averaged at -0.4 and $0.4\,\mathrm{mV}$ (orange). A plateau in the ZBP height emerges (pink shade), with an average zero-bias conductance and standard deviation of $1.05 \pm 0.05 \cdot 2e^2/h$ (blue errorbar). The slopes on the plateau (blue, orange arrows) have a ratio of -5. **(c)** Zero-bias conductance against V_{TG} and V_{SG} analogous to Fig. 6.5a. The white dotted lines indicate the gate voltages where **a** and **d** are taken. **(d)** Super gate dependence at the ZBP plateau in **a** at $V_{\mathrm{TG}} = -0.97\,\mathrm{V}$. The ZBP appears as a level crossing upon variation of V_{SG}. At lower V_{SG} a ZBP appears over an extended V_{SG} range, which likely results from the trivial ABS located close to the tunnel gate, to which it couples only weakly (see **c**).

V_{TG} against V_{SG} at zero bias voltage, at a magnetic field of 0.8 T (Fig. 6.5b) in device B (scanning electron micrograph in Fig. 6.5a). Like in the previous section, we find prominent diagonal peaks, which are unstable when V_{TG} or V_{SG} are varied individually. Now, we additionally find a narrow V_{SG} range around $V_{\mathrm{SG}} = -2.49\,\mathrm{V}$ where a horizontal peak appears over an extended tunnel-gate voltage range, as indicated by the dotted line. We investigate this peak by fixing V_{SG} to $-2.49\,\mathrm{V}$ and sweep V_{TG} against the bias voltage V in Fig. 6.5c and find that the state is slightly split at low V_{TG} and merges to form a ZBP that is stable against variations of the tunnel barrier over a significant gate voltage range. Further increase of V_{TG} induces splitting of the ZBP, coinciding with a state coming down in energy from the superconducting gap edge, followed by a possible discontinuity in the electrostatic environment, after which the conductance decreases and the ZBP returns. The linecuts in 6.5d show that the zero-bias conductance forms a plateau at the conductance quantum $2e^2/h$. At the same time, the conductance at bias voltages exceeding the superconducting gap keeps increasing, which indicates that the transmission of the tunnel barrier keeps increasing (also see the vertical linecuts in Fig. 6.5e).

We investigate the stability of the ZBP upon a changing magnetic field in Fig. 6.5f, by fixing V_{TG} at $-0.97\,\mathrm{V}$, where we observe a plateau in the zero-bias conductance when V_{TG} is varied. Starting at $B = 0\,\mathrm{T}$, we find a pair of subgap states at 0.15 mV, which merge to form a ZBP at 0.45 T, which extends over a range of 0.35 T before splitting away from zero energy towards the gap edge. Although the peak position is stable over an extended range of the magnetic field, the peak height is not robustly fixed to $2e^2/h$ (see the linecut at zero bias in 6.5g). The ZBP height at 0.8 T in the magnetic field dependence is reduced compared to Fig. 6.5c due to a slightly higher super-gate voltage (c.f. Fig. 6.5b). We note that at 0.65 T a plateau in the ZBP height as a function of V_{TG} can also be found by adjusting V_{TG} (Fig. 6.6a,b). At this magnetic field the average conductance on the plateau is slightly higher and consists of points exceeding $2e^2/h$. Although the height of a ZBP due to a topological MZM from a single band cannot exceed $2e^2/h$, if multiple subbands are occupied in the nanowire junction, Andreev reflection into lower lying subbands can cause a nonzero background conductance [36, 37], which can raise the zero-bias conductance above the expected quantized value [9]. A small excess ZBP height therefore does not necessarily disprove an interpretation involving topological MZMs. As is already suggested by the sharpness of the peak in the zero-bias conductance along the super gate axis in Fig. 6.5b and the analogous measurement at 0.65 T shown in Fig. 6.6c, the zero-energy state is very sensitive to the super-gate voltage, indicating a partial weight of the zero-energy state underneath the super gate. Likely related to this V_{SG} sensitivity, direct comparison of the parameters between different datasets is complicated by small charge fluctuations along the nanowire and hysteresis (e.g. sweep direction).

Theoretical model

To understand our experimental observations in more detail we perform numerical simulations of the one-dimensional Majorana nanowire Hamiltonian [6, 7]. As we found above that zero-energy states can originate in the tunneling region of the nanowire, we use a smooth electrostatic potential profile to investigate if we can explain our observations with local MZMs. The Hamiltonian is given by:

$$H = \left(\frac{\hbar^2 k_x^2}{2m^*} - \mu(x) + \phi(x) - \alpha k_x \sigma_y\right)\tau_z + E_Z\sigma_x + \Delta(x)\tau_x \qquad (6.2)$$

Where k_x is the wavevector along the nanowire axis, $\mu(x)$ is the chemical potential measured from the middle of the helical gap, $\phi(x)$ is the electrostatic potential along the nanowire, and α is the Rashba spin-orbit strength. As we expect the ZBPs to originate in the tunneling barrier region of the nanowire, where the spin-orbit interaction is expected to be larger than in the superconducting nanowire section, we take $\alpha = 0.75\,\mathrm{eV\AA}$ [38]. E_Z is the Zeeman energy that splits states of opposite spin due to a magnetic field along the nanowire. $\Delta(x) = \Delta_0(x)(1-(E_Z/E_{Z,c})^2)$ is the superconducting energy gap induced in the nanowire, where we account for the closing of the gap of the aluminium superconducting shell by the magnetic field at a critical Zeeman energy $E_{Z,c} = 1.5\,\mathrm{meV}$. σ_i and τ_i are the Pauli matrices that operate in spin and particle-hole space respectively, $\hbar$ is the reduced Planck's constant and $m^* = 0.015 m_{\mathrm{e}}$ is the effective mass for InSb with m_{e} the electron mass. We consider a nanowire length of 1.5 µm, comparable to the length of the super gate in the experiment. The profile of the electrostatic potential and superconducting gap is illustrated in Fig. 6.7a. To account for the presence of subgap states at zero magnetic field, we include a normal wire section of length $L_\mathrm{N} = 200\,\mathrm{nm}$ in front of the superconducting nanowire by setting the induced superconducting gap $\Delta_0(x) = 0$ for $x < L_\mathrm{N}$, while in the superconducting wire $\Delta_0(x) = 0.3\,\mathrm{meV}$ for $x \geq L_\mathrm{N}$. We note that a smooth transition of the superconducting gap between the normal and superconducting parts of the nanowire, does not qualitatively affect the results. Motivated by calculations of the shape of the potential profile in the barrier using the geometry of our device, resulting in a smooth shape of the potential profile [39], we set the chemical potential to μ_N in the normal part of the wire, which smoothly transitions into $\mu_\mathrm{SC} = 0.85\,\mathrm{meV}$ in the superconducting wire section over a length scale of $2\sigma_\mu = 75\,\mathrm{nm}$:

$$\mu(x) = \mu_\mathrm{N} + \frac{\mu_\mathrm{SC} - \mu_\mathrm{N}}{2}\left(\tanh\left(\frac{x - L_\mathrm{N}}{\sigma_\mu}\right) + 1\right) \tag{6.3}$$

We note that we have checked that a different choice of the smooth potential profile, such as a Gaussian step leads to qualitatively equivalent results.

Finally, we include a sharp electrostatic potential barrier of height $\phi_\mathrm{barrier} = 10\,\mathrm{meV}$ with a width $\sigma = 5\,\mathrm{nm}$ centered around $x_0 = 0\,\mathrm{nm}$ to provide a peak broadening comparable to the experiment, without affecting the ZBP height, as shown in Fig. 6.S6:

$$\phi(x) = \phi_\mathrm{barrier} \exp\left(\frac{-(x - x_0)^2}{2\sigma^2}\right) \tag{6.4}$$

The KWANT package is used to discretize and diagonalize the Hamiltonian to obtain the energy spectrum. Transport calculations are obtained using the scattering matrix method [40]. Temperature broadening is included in the transport simulations by convolution with the derivative of the Fermi-Dirac distribution at 50 mK, the estimated electron temperature in our nanowire devices.

ZBP plateau due to local MZMs

We start by considering the effect of the magnetic field on the low energy levels by sweeping the Zeeman energy in Fig. 6.7b. At zero Zeeman energy we find an ABS below the superconducting gap edge, signifying it is located in the tunnel junction, where the states are not fully proximitized by the superconducting shell. As the Zeeman energy increases, the ABS moves towards zero energy, where it sticks until the superconducting nanowire section transitions into the topological phase at $E_Z = \sqrt{\Delta^2 + \mu_\mathrm{SC}^2}$, as indicated by the white dashed line. As is typically encountered in transport simulations, the closing and reopening of the gap at the phase transition is not well resolved, as this is governed by states that extend throughout the superconducting part of the nanowire with little weight in the tunneling region where $\mathrm{d}I/\mathrm{d}V$ is measured [17, 28, 41]. The height of the ZBP is illustrated in Fig. 6.7c. Similar to the experiment, the ZBP height at first slightly exceeds $2e^2/h$, after which it approaches $2e^2/h$ more accurately, until the ZBP splits. We note that the stabilization of the zero-bias conductance is aided by the finite temperature broadening, since it broadens sharp peaks or dips near zero bias, which generally appear in the simulations at zero temperature. To understand the reason for the near quantization of the ZBP, we can look into the Majorana wavefunctions of the zero-energy state

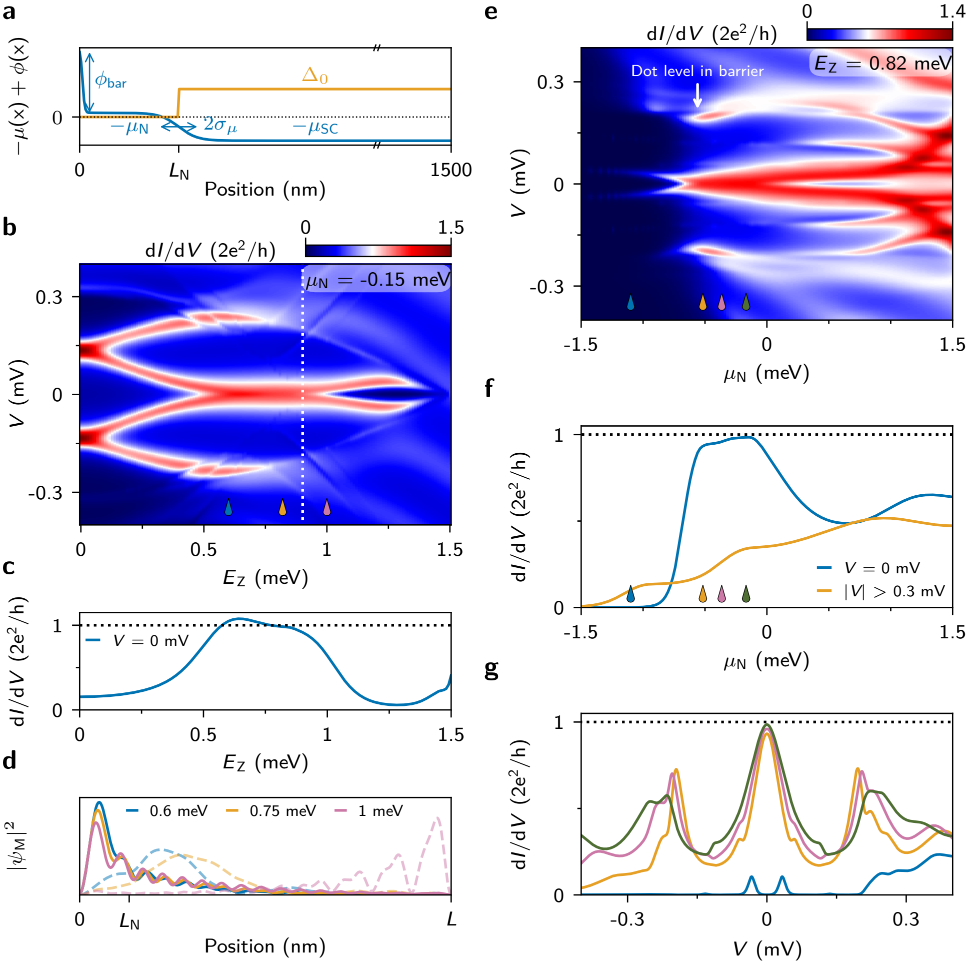

Figure 6.7: Simulated zero-bias conductance plateau due to local MZMs. **(a)** Schematic of the electrostatic potential profile $-\mu(x)+\phi(x)$ (blue) and the superconducting gap $\Delta(x)$ used in the simulations. The Fermi level $-\mu(x)+\phi(x)=0$ is indicated by the black dotted line. **(b)** dI/dV as a function of the Zeeman energy E_Z obtained from transport calculations. The white dashed line indicates the critical Zeeman field above which the superconducting part of the nanowire transitions into the topological phase. **(c)** Zero-bias linetrace of **b**, showing that the ZBP height stabilizes near $2e^2/h$. **(d)** Majorana wavefunctions of the zero-energy state at three different values of E_Z, indicated by the colored droplets in **b**. The lighter dashed lines show the right MZM, which moves further away from the normal section as E_Z increases. **(e)** Variation of the chemical potential in the normal wire section μ_N at $E_Z = 0.82\,\text{meV}$ shows a set of low energy states at low μ_N which evolves into a ZBP at $2e^2/h$ as μ_N is increased. The merging of the subgap states at zero energy coincides with the appearance of an ABS near the gap edge indicated by the white arrow. **(f)** Horizontal linecuts of **e** at zero bias (blue) and averaged over $|V| \geq 0.3\,\text{mV}$, representing the above-gap conductance (orange). **(g)** Vertical linetraces of **e** at μ_N indicated by the colored droplets.

in Fig. 6.7d. The solid lines show the left MZM, which is located inside the tunneling region at any magnetic field. This MZM contributes a conductance of $2e^2/h$, provided that the tunneling rate exceeds the temperature broadening of the peak [17]. At the start of the ZBP at $E_Z = 0.6\,\mathrm{meV}$ (blue lines), we see that the right MZM (dashed light blue line) is partially separated from the left MZM, but still has a considerable weight in the tunneling region. Therefore, a finite tunneling rate to the right MZM remains, which can slightly raise the ZBP height [22, 24]. Upon further increase of the Zeeman energy (orange lines), the right MZM moves further away from the barrier and the barrier becomes more spin selective, reducing the coupling of the right MZM to the lead and leading to a peak height close to $2e^2/h$. When the Zeeman field is increased beyond the critical field of the topological phase transition, the right MZM moves to the other end of the device (pink lines) and the ZBP quickly splits due to the oscillatory peak splitting of overlapping MZMs [32]. It may appear surprising that the ZBP splitting in the topological phase is stronger than for local MZMs, since the spatial wavefunction overlap is reduced when the right MZM moves to the end of the nanowire. However, local MZMs are also decoupled due to opposite spin polarization of the MZMs [22] or separation in momentum space [35], which can lead to stronger decoupling than in the topological regime, where only the spatial separation provides decoupling.

To compare the simulations with the observed tunnel gate dependence, we set the Zeeman field to 0.82 meV and vary the chemical potential in the tunneling barrier region μ_N in Fig. 6.7e. At low μ_N a split low energy state remains at nearly constant energy, after which it comes down to form a ZBP. The height of the ZBP is stable around $2e^2/h$ (blue horizontal linetrace in Fig. 6.7f, and vertical linetraces in Fig. 6.7g), while the above-gap conductance keep increasing (orange linetrace in Fig. 6.7f): a zero-bias conductance plateau emerges near $2e^2/h$.

We note that local MZMs have a tendency to stick near zero energy as the Zeeman field is increased. Additionally, a change in the chemical potential in the superconducting part of the nanowire μ_{SC} is expected to only weakly affect the zero-energy stability. In our model the ZBP does not readily split to the degree that we observe in the experiment when we vary B (Fig. 6.5f) and V_{SG} (Fig. 6.6d). There are several tentative explanations for these deviations. One is the emergence of a topological phase, where overlap of the MZMs induces energy splitting oscillations [32]. However, further evidence of repeated peak splitting oscillations would be required to support this scenario. Another possibility is the presence of finite size effects due to a short nanowire length. As a final suggestion, the zero-energy stability could be aided by a Fabry-Perot type resonance where the spin-orbit interaction strength is commensurate with the nanowire length [42]. A change in chemical potential and the associated spin-orbit interaction strength can detune from resonance and the resonance condition is expected to break down at high magnetic fields. The resonance by itself is not expected to lead to a ZBP with stability around $2e^2/h$. Such stability may however arise when combined with a smooth potential profile.

Interaction of the ZBP with a dot level

Interestingly, like in the experiment, the formation of the ZBP as a function of μ_N in Fig. 6.7e coincides with the emergence of a state near the gap edge, as indicated by the white arrow. The interaction of this state with the local MZMs can be used to estimate the locality of this state. Fig. 6.8a,b show the band spectrums corresponding to Fig. 6.7b,e. In the band spectrum, we see this state coming down towards low energy twice as μ_N is varied (orange line in Fig. 6.8b). Based on its evolution with μ_N, we can expect the state to be located inside the barrier, which we can confirm by looking into the wavefunction of this state, as shown by the orange line in Fig. 6.8c. Indeed, we find that this ABS is predominantly located in the barrier, analogous to a quantum dot level, with a tail extending into the superconducting part of the nanowire. The interaction of a dot level with a near zero-energy state has been proposed as a method to determine the coupling strength between the two MZMs composing the zero-energy state and the fermionic dot level, which can be related to the spatial separation of the MZMs [43, 44]. For local MZMs, both the left and the right MZM (blue and light blue lines in Fig. 6.8c) have an appreciable overlap with the barrier ABS, resulting in comparable coupling strengths ($t_L \sim t_R$, where $t_{L/R}$ is the coupling strength between the dot level and the left/right MZM). This results in level repulsion between the dot level and the zero-energy state as indicated by the black arrows in Fig. 6.8b. Conversely, for well-separated MZMs that result from a topological phase transition in the superconducting section of the nanowire, the coupling to the right MZM is suppressed ($t_L \gg t_R$). If we lower the chemical potential in the superconducting part of the nanowire μ_{SC} in the simulations, a ZBP appears as a function of Zeeman energy after the topological phase transition (Fig. 6.8d). In the dependence on the chemical potential in the normal section of the nanowire (Fig. 6.8e), the dot levels (orange lines) are again apparent, but now the ZBP (blue line) remains close to zero energy upon resonance with the dot. The lack of coupling between the dot level and the right MZM is reflected in the wavefunctions shown in Fig. 6.8f, where the right MZM (light blue) has negligible overlap with the dot level (orange).

Returning to the experimental observations, in the tunnel gate dependence at both $B = 0.65\,\mathrm{T}$ and $0.8\,\mathrm{T}$ (Fig. 6.6a and 6.5b) we observe significant level repulsion of the ZBP with the dot level, similar to the simulations in Fig. 6.8b. By fitting the level repulsion using the method described in Prada *et al.* [43], we can extract the coupling strengths between the dot and MZMs, yielding $\sqrt{t_R/t_L} = 0.75$ at $B = 0.65\,\mathrm{T}$ and $\sqrt{t_R/t_L} = 0.68$ at $B = 0.8\,\mathrm{T}$ (for the fitting procedure see Supplemental Material, with the fits shown in Fig. 6.S2), indicating a significant overlap of the dot level and the right MZM, consistent with the picture of local MZMs. Interestingly, the coupling to the right MZM decreases with increasing magnetic field, which is also expected for local MZMs as the right MZM moves further into the superconducting part of the nanowire (Fig. 6.7d). Although many aspects of the experimental data, such as the magnetic field dependence and the emergence of a zero-bias conductance plateau at $2e^2/h$ in the tunnel strength dependence are also expected for MZMs associated with a topological phase transition in the nanowire, the observed level repulsion with the dot level is difficult to explain within this picture. We note that stable ZBPs resembling the experimental data can also form for well coupled local MZMs (sometimes referred to as a trivial ABS), as a result of finite size effects, as shown in the supplementary section 6.S.3. However, in this situation the ZBP height does not preferentially stabilize near $2e^2/h$ and extremely precise finetuning of the tunneling barrier height is required for the emergence of a zero-bias conductance plateau.

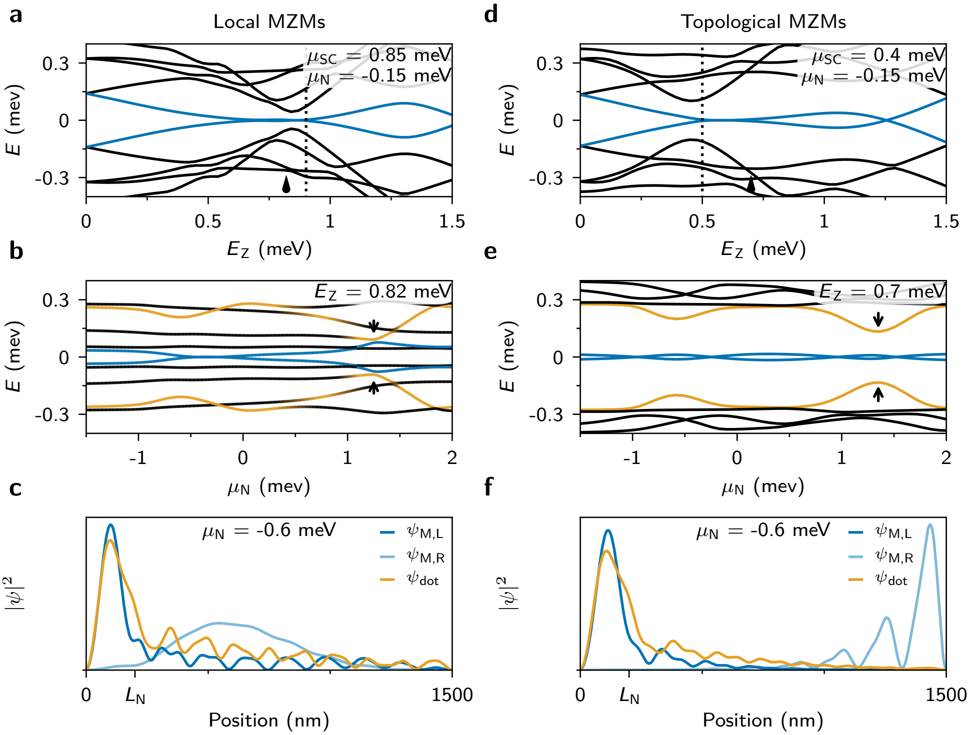

Figure 6.8: Interaction of ZBP with barrier ABS. **(a)** Band spectrum as a function of Zeeman energy, corresponding to Fig. 6.7b. The black dotted line indicates the topological phase transition. **(b)** Band spectrum upon variation of the chemical potential in the normal wire section, corresponding to Fig. 6.7e. The local MZMs are shown in blue, and the dot level in orange. The black lines at low energy are bulk states in the superconducting part of the nanowire. **(c)** The wavefunction of the local MZM decomposed into its Majorana components (blue, light blue) and the fermionic wavefunction of the dot level (orange). **(d)** Band spectrum as a function of Zeeman energy for the same parameters, except for a reduced μ_{SC}. The black dotted line indicates the topological phase transition. **(e)** Band spectrum as a function of μ_N corresponding to the parameters in **d**. **(f)** Wavefunctions corresponding to **e**.

6.5. DISCUSSION

We have found ZBPs emerging at finite magnetic fields with a peak height near $2e^2/h$, which can be split varying the potential in the tunneling barrier region. From this tunnel barrier dependence we conclude that these states originate in the normal nanowire section in front of the proximity induced superconducting nanowire section. We have found that upon appropriate tuning of the electrostatic gates bordering the tunneling region, ZBPs can be kept at zero energy, while the tunneling transmission is increased, revealing a zero-bias conductance plateau near the quantized value of $2e^2/h$. For the conductance plateaus observed here, we find that the zero-energy state can be easily split by different electrostatic gates near the barrier, or upon resonance with dot levels in the barrier. These observations indicate that these zero-energy states predominantly originate in the tunneling barrier section of the nanowire devices. By using a model involving decoupled local MZMs, we find good agreement with the observed stabilization of the peak height near $2e^2/h$. We note that we have only observed plateau formation while varying the tunneling potential, while theoretically plateaus expected in the dependence on other parameters, such as as the magnetic field. The influence of orbital effects[45] and electronic interactions [32, 46, 47] on the effective chemical potential in the nanowire junction could explain this deviation.

Motivated by theory predictions of zero-bias conductance plateaus at $2e^2/h$, we aimed our experimental efforts at ZBPs near $2e^2/h$. A limitation of this of approach is that we cannot claim that highly stable plateaus only occur at this conductance value. Establishing if plateaus are indeed special to $2e^2/h$ is infeasible using the relatively slow lock-in technique applied here in the inherently large parameter space of magnetic field and the multiple gate voltages. Future studies can make use of fast readout techniques to investigate the occurrence of plateaus at arbitrary conductance value.

We focused our interpretation of the experimental results on zero-energy states induced by a (long range) inhomogeneous electrostatic potential. Another mechanism that is known to induce zero-energy states is (short range) disorder along the nanowire [48–50]. However, the ZBPs here originate in the normal section of the nanowire, which has a low degree of disorder [45, 51, 52]. Disorder also is associated with a large number of states within the superconducting gap, contrary to our observations.

Our observations experimentally confirm that a zero-bias conductance plateau at $2e^2/h$ alone cannot definitively confirm the presence of a MZM at the edge of a topological superconductor. Instead, demonstration of a ZBPs near the conductance quantum should be supplemented with additional evidence supporting a topological phase transition, preferably addressing the nonlocality of the MZMs. However, it is interesting to note that as decoupled local MZMs in many ways essentially behave as an isolated MZM, they may be useful by themselves as the building block in topological quantum computation and to demonstrate braiding operations [22]. To explore this possibility further, it would be useful to investigate if the local MZMs can become highly decoupled by deliberately designing a smooth potential profile.

CONTRIBUTIONS TO THE PROJECT

The InSb nanowires were grown by Sasa Gazibegovic and Roy op het Veld, under the supervision of Erik Bakkers at Eindhoven University of Technology. The aluminium superconductor was grown on the nanowires by John Logan, Mihir Pendharkar and Joon Sue Lee, under the supervision of Chris Palmstrøm at the University of California, Santa Barbara. The nanowire devices were fabricated and the measurements were performed and analyzed by **Jouri Bommer** in collaboration with Hao Zhang, Michiel de Moor, and Di Xu. The simulations were performed by **Jouri Bommer**, using code kindly provided by Adriaan Vuik and adapted by Michiel de Moor. The project was supervised by Leo Kouwenhoven. We gratefully acknowledge Chun-Xiao Liu for valuable input on the potential profile of the tunneling barrier and Önder Gül and Michael Wimmer for useful comments on the manuscript.

DATA AVAILABILITY

The measurement and simulation data, data processing scripts, and analysis scripts that create the figures in this chapter are available at Ref. [53].

6.S. SUPPLEMENTAL MATERIAL

6.S.1. DETERMINATION OF THE DEVICE DIFFERENTIAL CONDUCTANCE

Because observation of quantization of the ZBP height relies on accurate determination of the differential conductance, in this section we provide the details of the calibration required to obtain the differential conductance of the nanowire devices from the measurements of the complete electronic circuit and we estimate the uncertainty in the obtained conductance values.

The measurement circuit that we use consists of a voltage source which applies a dc voltage V_{bias} superimposed with a small low frequency (83.19 Hz) ac excitation voltage v_{ac}, which is fed into three stages of RC-filters before reaching the nanowire sample, and goes through another three stages of RC-filters before reaching a M1b current-to-voltage converter [54], which amplifies the current with an adjustable gain A. We measure the output of the current-to-voltage converter simultaneously both at dc using a Keithley 2000 multimeter and at ac using a SR830 lock-in amplifier, which yields both the magnitude and the phase of the ac current. The measured output voltages are converted into the dc and ac currents I_{dc} and i_{ac} using the set gain A. Since we measure in a two terminal setup, voltage drops over the filter resistances, the output impedance of the voltage source, and the input impedance of the current-to-voltage converter (taken together the series resistance R_{series}) decrease the voltage over the sample below the applied bias voltage and needs to be compensated for. Since the contact resistance between the leads and the nanowire is not well known, we only take it into account in the conductance uncertainty (see below).

The current-to-voltage converter we used is optimized to send a very low energy back to the sample, favoring low noise measurements, by a strongly decreasing open-loop-gain as a function of ac frequency, with a bandwidth of ~ 200 Hz. The decreasing open-loop-gain at increased frequencies has the consequence of an increased input impedance and, to a small degree, a reduced current-to-voltage gain, and an associated phase shift. Therefore, the ac current obtained at finite frequency is underestimated when the dc gain and input resistance are used to convert the output of the current-to-voltage converter into the dc current. Due to the presence of the reactive elements in the circuit (from the RC-filters, and unknown parasitic capacitance, and possible parasitic inductance), these ac circuit complications depend on the sample resistance, which makes calculating back the device conductance extremely involved and imprecise (more detailed information on the ac effects is available at [55]). However, since the circuit intricacies have an ac nature, the measured dc data *is* accurate. Therefore, to account for the ac effects of the circuit, we determine an ac-to-dc correction factor by mapping the differential conductance obtained from the magnitude of the lock-in signal ($g_{\mathrm{ac}} = i_{\mathrm{ac}}/v_{\mathrm{ac}}$) to the dc differential conductance obtained by numerically differentiating[3] the dc current with respect to the dc bias voltage ($g_{\mathrm{dc}} = \Delta I/\Delta V$), using multi-

---

[3] For each bias value the numerical derivative is determined from the two adjacent data points of an I-V curve to ensure that the numerical differential conductance is determined for the same dc bias value as the lock-in differential conductance. No (lowpass) filtering is applied. Outliers in g_{dc} removed more than four standard deviations from the mean are excluded from the fits. The correction factors obtained from independent calibration measurements on Ohmic resistors from the linear slope of the I-V traces, correspond well with the method involving numerical differentiation described here, showing that the numerical derivative provides a reliable determination of the differential conductance (see Fig. 6.S1e,f).

	A (MV/A)	R_{series} (kΩ)	f_{cor}
Device A	10	17.023 ± 0.074	$0.3696 g_{\text{ac}} + 0.9066$
Device B	1	8.777 ± 0.019	$0.0199 g_{\text{ac}} + 0.9992$

Table 6.S1: Measurement settings and data processing parameters. Note that the difference in the series resistance of device A and B is solely caused by a different gain setting of the voltage source and the current-to-voltage converter. The stated correction factors are appropriate for a conductance g_{ac} in units of $2e^2/h$.

ple large datasets (~ 3,000 to 40,000 datapoints per dataset) from multiple devices with each a broad range of sample conductances (a single dataset illustrating the procedure is shown in Fig. 6.S1a). Although the dc signal and the numerical derivation procedure are subject to noise, the effect of stochastic noise on the correction factor is suppressed by the large sample size we use. We note that we determine this correction using the complete circuit conductance, without subtracting any series resistance. As we find that nonlinearity in the conversion between the ac and the dc data is well captured by a second order polynomial term, we fit each dataset with (see Fig. 6.S1b):

$$g_{\text{dc}} = a g_{\text{ac}}^2 + b g_{\text{ac}}, \tag{6.S1}$$

resulting in an ac-to-dc correction factor:

$$f_{\text{cor}}\left(g_{\text{ac}}\right) = \frac{g_{\text{dc}}}{g_{\text{ac}}} = a g_{\text{ac}} + b. \tag{6.S2}$$

The correction we eventually apply to the data is the average of each individual fit, weighted by the mean squared error of the fit (see Fig. 6.S1c-f). After applying the correction factor we subtract the series resistance to obtain the differential conductance reported in this chapter:

$$\frac{\mathrm{d}I}{\mathrm{d}V} = \left(\left(\frac{i_{\text{ac}}}{v_{\text{ac}}} f_{\text{cor}}\left(g_{\text{ac}}\right)\right)^{-1} - R_{\text{series}}\right)^{-1} \tag{6.S3}$$

In the datasets where the bias is varied, the bias axis is corrected for the voltage drop over the series resistance:

$$V = V_{\text{bias}} - I_{\text{dc}} R_{\text{series}} \tag{6.S4}$$

Uncertainty estimation

To determine the uncertainty in differential conductance, we consider three errors which propagate in eq. 6.S3: the noise in the ac current, the uncertainty in the correction factor, and uncertainty in the series resistance. The noise in the lock-in signal is estimated from the standard deviation of repeated measurements as 1.5 % of the conductance (determined before subtracting the series resistance). The uncertainty in f_{cor} is given by the weighted covariance of the individual fits and accounts for the variability in the correction obtained from different datasets. The value and the uncertainty of the series resistance is determined from independent calibration measurements of the RC-filters, the output resistance of the voltage source, and the input resistance of the current-to-voltage amplifier. The uncertainties stated in Table. 6.S1 are defined by the standard

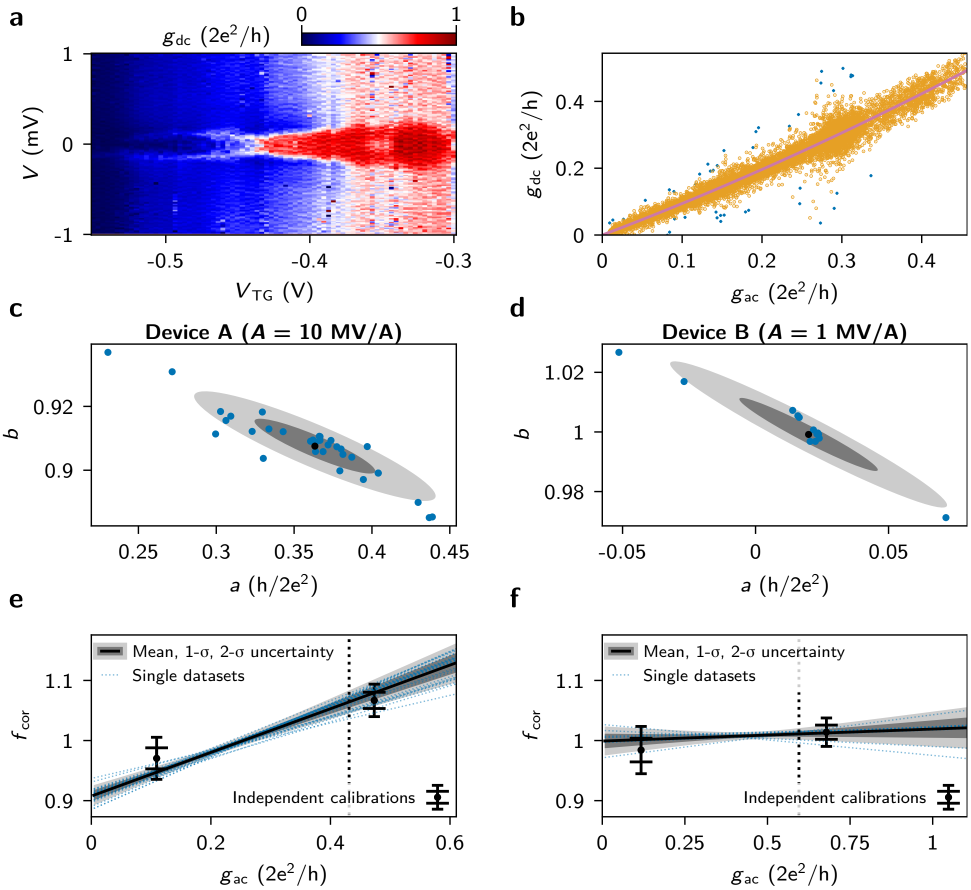

Figure 6.S1: Correction of differential conductance for ac circuit non-idealities. **(a)** The dc differential conductance g_{dc} obtained by numerically differentiating the dc I-V traces for the dataset shown in Fig. 6.4b. Note that the circuit series resistance is not subtracted, nor is the bias axis corrected for the voltage drop over the series resistance. **(b)** The ac conductance g_{ac} determined from the lock-in amplifier signal (without subtracting the series resistance) is plotted against g_{dc} (dots) and fitted with a second order polynomial with zero intercept (pink line) to determine the ac-to-dc correction factor $f_{cor} = g_{dc}/g_{ac} = a g_{ac} + b$ for this dataset. Outliers, defined as being separated by more than four standard deviations from the mean, are excluded from the fits (blue dots) **(c)** The procedure shown in **a,b** is repeated for 33 datasets from device A and two independent devices all using the same ac excitation frequency and current-to-voltage converter gain setting $A = 10\,\mathrm{MV/A}$ as was used to obtain the data in device A. The blue dots show the spread in the obtained fitting parameters, and the black dot and the shaded covariance ellipses show the weighted mean, 1-σ, and 2-σ uncertainty obtained from the individual fits respectively. **(d)** Same as **c** for a gain setting $A = 1\,\mathrm{MV/A}$ as used for the measurements on device B using a total of 13 datasets from device B and another device not discussed in this chapter. **(e)** The obtained correction factor f_{cor} (black line) and its associated 1-σ and 2-σ uncertainty (grey shades) for $A = 10\,\mathrm{MV/A}$. The individual fits are shown by the blue dotted lines. The black dot and errorbars show the correction factor and its 1-σ and 2-σ uncertainty obtained from independent measurements of a $10\,\mathrm{k\Omega}$ and a $100\,\mathrm{k\Omega}$ resistor cooled down and measured under the same measurement conditions. As the I-V traces of the independent resistor calibration are ohmic, the dc conductance is determined from a linear fit of the I-V traces. The vertical black dotted line indicates the conductance that corresponds to the conductance quantum after subtracting the series resistance. **(f)** Same as **e** for $A = 1\,\mathrm{MV/A}$.

deviation in the resistance values obtained from measurements of different fridge lines of the setup used, and of multiple units of the voltage source and the current-to-voltage amplifier of the the same type used in the experiments. In addition to the series resistance discussed above, there is a possible resistance between the metal leads and the nanowire. Because of the two probe nature of nanowire experiments, this value is difficult to estimate. Based on (superconducting) quantum point contact plateaus in device B, we estimate an upper bound of 0.5 kΩ to 1 kΩ. Note that the contact resistance is a one-sided uncertainty which only contributes to the upper uncertainty range. The total uncertainty is shown in the relevant figure as a dark shade for the 1-σ plus 0.5 kΩ uncertainty and as a light shade for the 2-σ plus 1 kΩ uncertainty.

6.S.2. ESTIMATION OF MAJORANA NONLOCALITY

For completeness, we first discuss the procedure to extract the ratio of the tunnel coupling to two MZMs $\Sigma \sim \sqrt{t_\mathrm{R}/t_\mathrm{L}}$, as described in Prada *et al.* [43]. The coupling of a quantum dot to a fermionic state in the nanowire, which is decomposed into two Majorana modes, is described by the effective low energy Hamiltonian:

$$H = \left(d_\uparrow^\dagger, d_\downarrow^\dagger, d_\uparrow, d_\downarrow, \gamma_L, \gamma_R\right) \check{H} \left(d_\uparrow, d_\downarrow, d_\uparrow^\dagger, d_\downarrow^\dagger, \gamma_L, \gamma_R\right)^T$$

$$\check{H} = \begin{bmatrix} E_\mathrm{Z} + U\langle n_\downarrow\rangle + \epsilon_0 & 0 & 0 & 0 & 2t_\mathrm{L}\sin\left(\frac{\theta_\mathrm{L}}{2}\right) & -2i\,t_\mathrm{R}\sin\left(\frac{\theta_\mathrm{R}}{2}\right) \\ 0 & -E_\mathrm{Z} + U\langle n_\uparrow\rangle + \epsilon_0 & 0 & 0 & -2t_\mathrm{L}\cos\left(\frac{\theta_\mathrm{L}}{2}\right) & -2i\,t_\mathrm{R}\cos\left(\frac{\theta_\mathrm{R}}{2}\right) \\ 0 & 0 & -E_\mathrm{Z} - U\langle n_\downarrow\rangle - \epsilon_0 & 0 & -2t_\mathrm{L}\sin\left(\frac{\theta_\mathrm{L}}{2}\right) & -2i\,t_\mathrm{R}\sin\left(\frac{\theta_\mathrm{R}}{2}\right) \\ 0 & 0 & 0 & E_\mathrm{Z} - U\langle n_\uparrow\rangle - \epsilon_0 & 2t_\mathrm{L}\cos\left(\frac{\theta_\mathrm{L}}{2}\right) & -2i\,t_\mathrm{R}\cos\left(\frac{\theta_\mathrm{R}}{2}\right) \\ 2t_\mathrm{L}\sin\left(\frac{\theta_\mathrm{L}}{2}\right) & -2t_\mathrm{L}\cos\left(\frac{\theta_\mathrm{L}}{2}\right) & -2t_\mathrm{L}\sin\left(\frac{\theta_\mathrm{L}}{2}\right) & 2t_\mathrm{L}\cos\left(\frac{\theta_\mathrm{L}}{2}\right) & 0 & i\delta \\ 2i\,t_\mathrm{R}\sin\left(\frac{\theta_\mathrm{R}}{2}\right) & 2i\,t_\mathrm{R}\cos\left(\frac{\theta_\mathrm{R}}{2}\right) & 2i\,t_\mathrm{R}\sin\left(\frac{\theta_\mathrm{R}}{2}\right) & 2i\,t_\mathrm{R}\cos\left(\frac{\theta_\mathrm{R}}{2}\right) & -i\delta & 0 \end{bmatrix} \tag{6.S5}$$

Here, d_σ and γ_i denote the operator of the quantum dot and Majorana states, E_Z is the Zeeman energy, U is the charging energy of the quantum dot, $\langle n_\sigma\rangle$ is the expectation value of the dot number operators, ϵ_0 is the quantum dot energy and δ is the energy of the Majoranas due to wavefunction overlap. The quantum dot is coupled to the left and right Majorana with strength t_L and t_R. The spin texture of the Majoranas just after the quantum dot is captured in the spin canting angles $\theta_\mathrm{L,R}$.

At the two resonances (- for the lower and + for the higher dot), the lowest energy states of the Majorana mode $E_\mathrm{M}^\pm$ and dot level $E_\mathrm{D}^\pm$ can be found by projecting out the off-resonance dot level:

$$\begin{aligned} E_\mathrm{M,D}^- &= \sqrt{\delta^2/2 + s_\mathrm{L}^2 + s_\mathrm{R}^2 \mp \sqrt{\left(\delta^2/2 + s_\mathrm{L}^2 + s_\mathrm{R}^2\right)^2 - 4s_\mathrm{L}^2 s_\mathrm{R}^2}} \\ E_\mathrm{M,D}^+ &= \sqrt{\delta^2/2 + c_\mathrm{L}^2 + c_\mathrm{R}^2 \mp \sqrt{\left(\delta^2/2 + c_\mathrm{L}^2 + c_\mathrm{R}^2\right)^2 - 4c_\mathrm{L}^2 c_\mathrm{R}^2}} \\ s_\mathrm{i} &= 2t_\mathrm{i}\sin\left(\theta_\mathrm{i}/2\right) \\ c_\mathrm{i} &= 2t_\mathrm{i}\cos\left(\theta_\mathrm{i}/2\right) \end{aligned} \tag{6.S6}$$

In the experimental data we identify the four energies $E_\mathrm{M}^\pm$ and $E_\mathrm{D}^\pm$ at the two anticrossings and determine δ at low V_TG, away from the resonances. Using these values we can solve eq. 6.S6 for t_i and θ_i, which provides a unique solution for t_L and t_R, and thus a

Table 6.S2: Fit parameters of the quantum dot-Majorana model used in Fig. 6.S2.

B (T)	δ (meV)	t_L (meV)	t_R (meV)	θ_L (rad)	θ_R (rad)	$\sqrt{t_R/t_L}$
0.65	0.0552	0.0582	0.0393	8.78	0.962	0.82
0.80	0.0236	0.0541	0.0256	8.95	0.669	0.69

unique estimation of the wavefunction overlap $\Sigma \sim \sqrt{t_R/t_L}$. The found parameters and the resulting nonlocality estimation are shown in table 6.S2. Having obtained the nonlocality estimation, we also examine the agreement of the full spectrum away from the resonances. To do so, we find the eigenvalues of eq. 6.S5. For the required quantum dot parameters, we choose $U = 0$ and use $E_Z = \frac{1}{2} g \mu_B B$, where μ_B is the Bohr magneton, and g is the g-factor. To obtain agreement with the experimentally observed spectrum we choose $g = 12$ (in agreement with earlier observation of states proximitized by an aluminium superconductor [56]). In addition, we need to pick the correct values out of the multiple solutions for θ_L and θ_R to eq. 6.S6. To convert ϵ_0 to the gate voltage, we determine the capacitive coupling by linearly transforming the gate voltages at the two resonances to the resonant dot energies $\epsilon_0 = -U - E_Z$ and $\epsilon_0 = E_Z$. The resulting energy spectrum is in excellent agreement with the data (Fig. 6.S2).

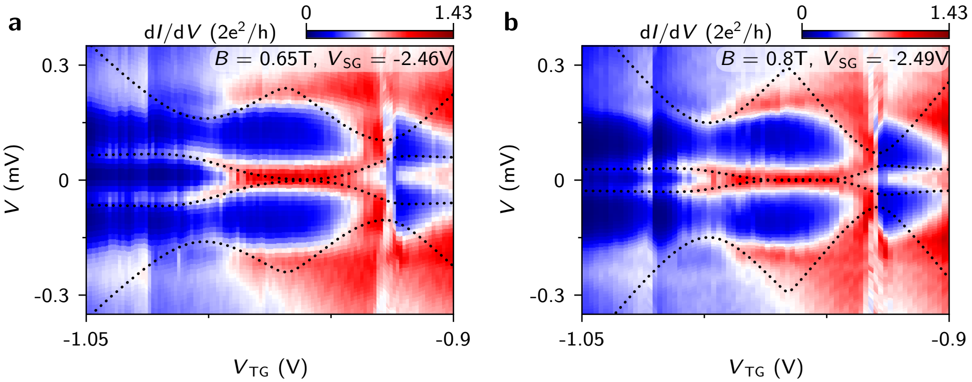

Figure 6.S2: Energy spectrum obtained with quantum dot-Majorana model applied to device B. Calculated spectrum obtained from the effective Hamiltonian (eq. 6.S5) using the parameters in table 6.S2 (dotted black lines) and overlaid on the experimental plots Fig. 6.6a (at 0.65 T in **a**) and Fig. 6.5b (at 0.8 T in **b**). After the right anticrossing a reproducible discontinuity in the electrostatic environment occurs, which causes the model to deviate from the experimental data on the righthand side.

6.S.3. ZERO-BIAS CONDUCTANCE PLATEAU DUE TO FINITE SIZE EFFECTS FOR WELL COUPLED LOCAL MZMS

The simulations in the main text describe a situation where an ABS forms in the tunneling barrier, of which the MZMs components become decoupled. This decoupling is driven by the occupation of a single spin-polarized subband in the barrier. However, ABSs can also form when both spin-polarized subbands remain occupied. In this case, the MZM components do not decouple significantly, which we refer to here as a trivial

ABS. A trivial ABS can form a ZBP stable in Zeeman field [29, 42], but its peak height is not quantized and can reach up to $4e^2/h$ [29]. Nevertheless, fine-tuning of the system parameters could lead to plateau in the zero-bias conductance as a function of μ_N. To look into this scenario, we consider the potential profile shown in Fig. 6.S3a, with a significantly higher chemical potential in the normal section of the nanowire (of length $L_\mathrm{N} = 210\,\mathrm{nm}$) than in the main text. Due to the high μ_N, a sharp Gaussian potential barrier (with $\phi_\mathrm{barrier} = 14.3\,\mathrm{meV}$ and $\sigma = 10\,\mathrm{nm}$ centered around $x_0 = 20\,\mathrm{nm}$) is now essential to control the transmission through the barrier section. We consider a short superconducting wire of $1\,\mu\mathrm{m}$, close to the length of the super gate in the experiment, and a spin-orbit strength of $\alpha = 0.31\,\mathrm{eV\AA}$. The chemical potential is set to $\mu_\mathrm{SC} = 2.7\,\mathrm{meV}$ in the superconducting wire section and we consider Zeeman fields below $\sqrt{\Delta^2 + \mu_\mathrm{SC}^2}$, the critical field of the topological phase transition. For the field at which the host superconducting gap closes, we use $E_\mathrm{Z,c} = 1.4\,\mathrm{meV}$. We also implement an additional subband 2.5 meV lower in energy, which allows for a high above-gap conductance without excessive broadening of the low energy states of interest, which stem from the highest subband. We note that we do not consider interband coupling, so that the low energy spectrum is unaffected by the presence of the second band.

The response to a Zeeman field is shown in Fig. 6.S3b, where The wavefunctions of the two lowest energy states at $E_\mathrm{Z} = 0.7\,\mathrm{meV}$ are shown in Fig. 6.S3f, where we see that the lowest energy state (MZM components shown by the blue and orange blue lines) is located mostly inside the barrier, without significant separation of its MZM components. Figure 6.7b shows the differential conductance $\mathrm{d}I/\mathrm{d}V$ as function of the Zeeman field and the bias voltage. We see a subgap state coming down towards zero energy where it sticks near zero energy over an extended Zeeman field range between 0.6 and 0.9 meV due to fine-tuned interaction with the finite energy states. The height of the zero-bias peak is close to $2e^2/h$, but since the ZBP is caused by a trivial ABS, the peak height is not quantized as a function of magnetic field, as is clear from the linecut shown in Fig. 6.7c. Next, we fix E_Z to 0.7 meV and consider the effect of the tunnel-gate voltage by changing μ_N in the simulation (Fig. 6.7d). Increasing μ_N simultaneously lowers the height of the tunnel barrier measured from the Fermi level, increasing the transmission through the barrier. Like in the experiment, we find two finite energy subgap states at low μ_N, which merge to form a ZBP as μ_N is increased, before it strongly splits. The formation of the ZBP sensitively relies on the energy of the ABS in the normal section, which is tuned by changing μ_N. Nevertheless, the simulation shows that this does not necessarily lead to a sharp level crossing as a function of the chemical potential in the normal section and a ZBP can form over an extended range. As the tunneling rate to the highest subband is only weakly affected by changing μ_N, the ZBP height remains stable at $2e^2/h$ (blue linecut in Fig. 6.7e). The above-gap conductance is dominated by the lower lying second subband, which experiences a lower tunneling barrier, for which small changes of μ_N have a relatively stronger effect on the tunneling rate, which allows the above-gap conductance (orange linecut) to change significantly.

Although a trivial ABS can result in a zero-bias conductance plateau at $2e^2/h$, it does require extremely precise fine tuning of the system parameters, such as the height of the sharp tunneling barrier, as demonstrated in Fig. 6.S6. Furthermore, the potential profile, in particular the sharp peak preceding the normal nanowire is not expected based on

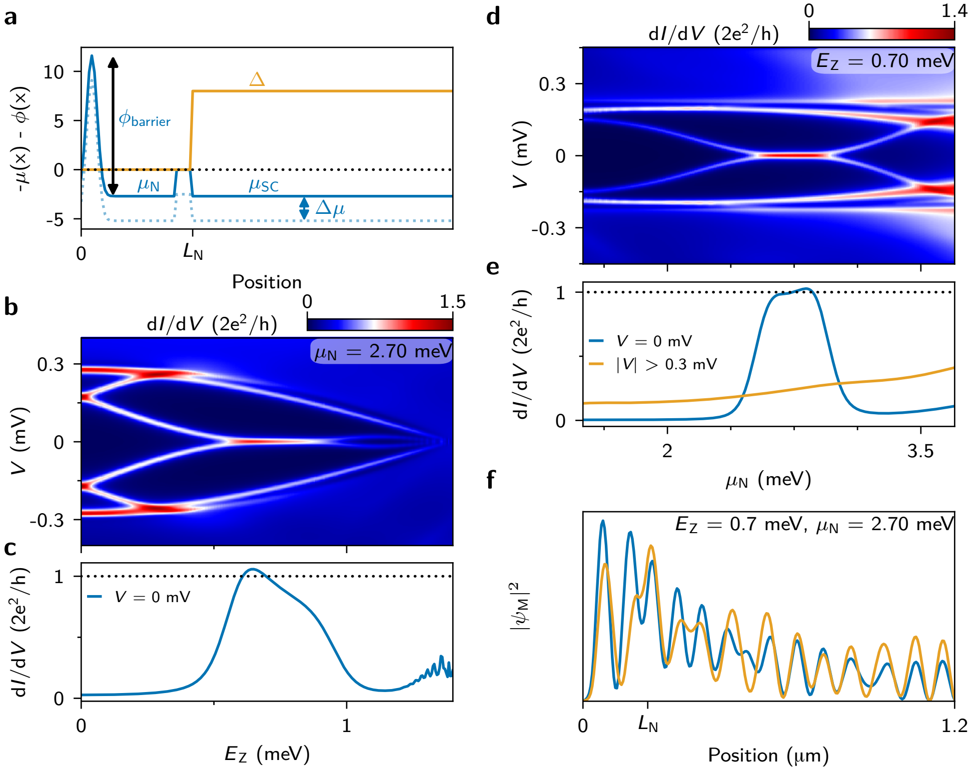

Figure 6.S3: Simulated zero-bias conductance plateau due to a trivial ABSs. **(a)** Schematic of the electrostatic potential profile $-\mu(x)+\phi(x)$ (blue) and the superconducting gap $\Delta(x)$ used in the simulations. The normal and superconducting parts of the nanowire are weakly decoupled to allow for a zero field ABS at an energy comparable to the experiment, by setting $\mu(x)=0$ for the last 30 nm of the normal section. The blue dotted line indicates the potential for the second subband, which is lower in energy by $\Delta\mu = 2.5$ meV, and is only implemented in the conductance simulations in **d-g**. **(b)** The differential conductance dI/dV as a function of V and E_Z obtained from transport calculations shows the appearance of a ZBP over an extended Zeeman field range. **(c)** Zero-bias linecut of **d** showing a ZBP height close to, but without stability at, $2e^2/h$. **(d)** Variation of the chemical potential in the normal wire section μ_N at $E_Z = 0.65$ meV leads to a ZBP over an extended μ_N range. **(e)** Horizontal linecuts of **f** at zero bias (blue) and averaged over $|V| \geq 0.3$ mV, representing the above-gap conductance (orange). **(f)** Majorana wavefunctions of the ZBP. The strong overlap of the MZM components signifies the ABS character of these states.

electrostatic simulations of our device, which displays a smooth potential profile [39], favoring an interpretation of decoupled local MZMs.

6.S.4. SUPPLEMENTAL FIGURES

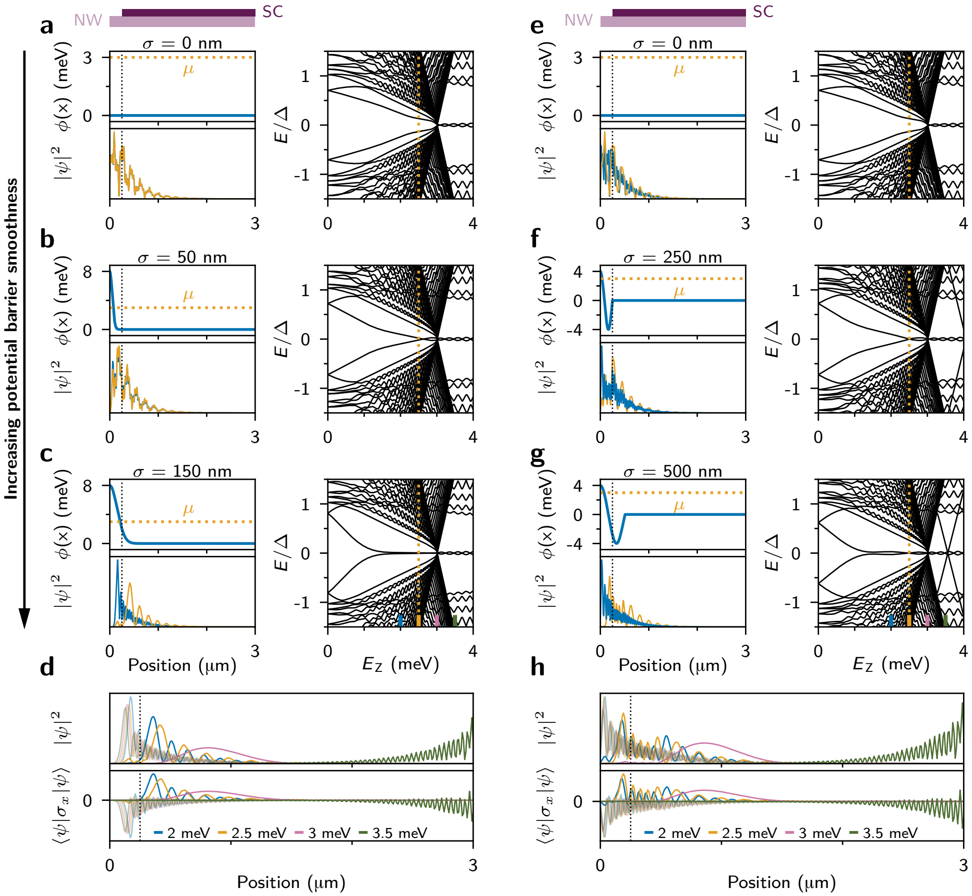

Figure 6.S4: ABSs in Majorana nanowires for additional potential profiles. **(a-c)** ABSs due to a half-Gaussian potential barrier defined by $\phi(x) = \phi_{\text{barrier}} \exp\left(-(x-L_{\text{N}})^2/2\sigma^2\right)$ with increasing width σ (smoothness) going from the top to the bottom panel. In contrast to the potential profile in Fig. 6.2a, the Gaussian is centered at the start of the nanowire, which has an induced gap of $\Delta = 0$. Since the wavefunction of the ABS now extend into the unproximitized nanowire region, the states can detach from the superconducting gap edge already at zero Zeeman field. Nevertheless, stable zero-energy states form for a smooth barrier (see **c**). **(d)** Wavefunction profile (top panel) and spin polarization (bottom panel) of the lowest energy states at four different Zeeman fields in **c**. Similar to the observations in Fig. 6.2, the MZM wavefunctions tend to separate more as the Zeeman field increases, until the bulk of the nanowire transitions into the topological phase (E_Z>3.01 meV). **(e-g)** For a barrier potential of a peak, followed by a dip, modeled as $\phi(x) = V_0 \cos(3\pi x/2\sigma)$ for $0 \leq x \leq \sigma$ and $\phi(x) = 0$ for $x > \sigma$, an increasing smoothness σ again leads to increased stability of zero-energy states. The appearance of the sharp level crossing at high Zeeman field is likely related to the dip in the potential, causing confined quantum dot like states. **(h)** Same as **d**, for the lowest energy states in **g**.

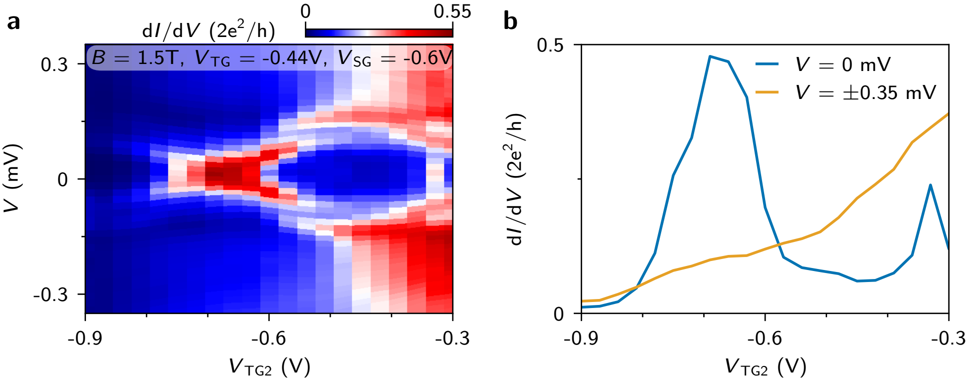

Figure 6.S5: Dependence of the ZBP in device A shown in Fig. 6.3 on the additional tunnel gate. (**a**) As the voltage on the additional tunnel gate V_{TG2} (see Fig. 6.3a) is varied, the subgap state comes down from finite energy, crosses zero energy to form a ZBP, and then splits off again, analogous to the dependence on the primary tunnel gate (Fig. 6.3e). **(b)** Horizontal linecuts of **a** at zero bias (blue) and the above-gap conductance, taken as the average of -0.3 and 0.3 mV.

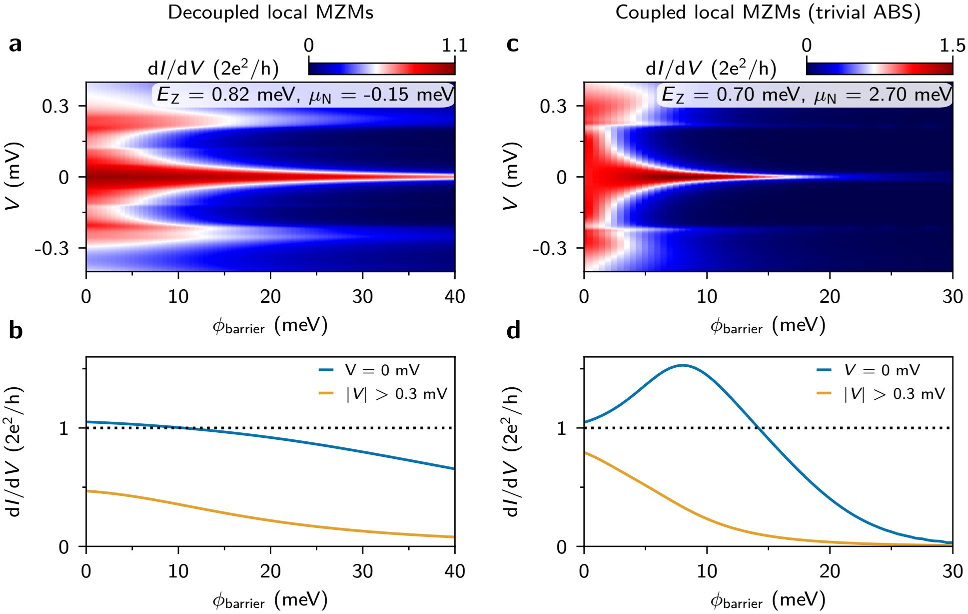

Figure 6.S6: Dependence of the ZBP height on the sharp Gaussian barrier height. In the simulations we have included a sharp barrier of height ϕ_{barrier} at the start of the normal nanowire section, which has a starkly different effect on the ZBP peak height for decoupled local MZMs and coupled local MZMs [24] (often called a trivial ABS). **(a)** Dependence on the barrier height for the decoupled local MZMs scenario using the parameters used in Fig. 6.7. **(b)** Horizontal linetraces of **a** at zero bias (blue) and averaged over $|V| > 0.3$ mV (orange). The ZBP height saturates close to $2e^2/h$ when the barrier height is lowered. Due to finite transmission to the second MZM, the conductance is increased slightly above $2e^2/h$. **(c)** Dependence on the barrier height for the trivial ABS scenario using the parameters used in Fig. 6.S3, using a single band model that only includes the subband giving rise to the ZBP to such that the peak height can be traced in isolation from Andreev reflection stemming from the lower subband. **(d)** Horizontal linetraces of **a** at zero bias (blue) and averaged over $|V| > 0.3$ mV (orange). The ZBP height crosses $2e^2/h$ and significantly exceeds it as the barrier height is lowered. The drop in the peak height that appears upon further reduction of the barrier height, is due to a slight peak splitting induced by the changing barrier potential.

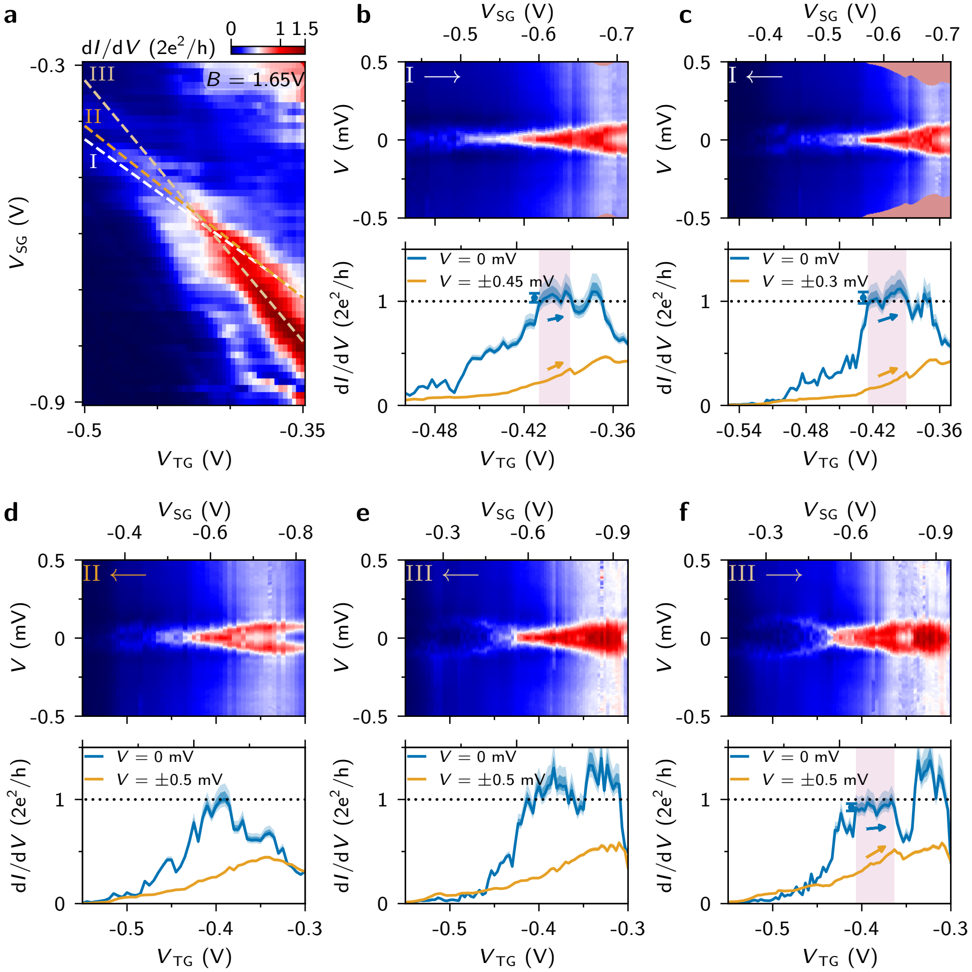

Figure 6.S7: Dependence of the ZBP in device A shown in Fig. 6.3 and 6.4 on the tunnel gate-super gate compensation. **(a)** The zero-bias dI/dV as a function of V_{TG} and V_{SG} shows that a ZBP is present if the two gates are appropriately compensated. Three different gate compensations are used, labeled I–III, and indicated by the dashed lines. **(b–f)** Top panels: The bias and compensated V_{TG}-V_{SG} dependence of dI/dV. The specific gate compensation and the sweep direction are indicated by the Roman numeral and arrow on the top left of each panel. The colorscale is the same as in **a**. Bottom panels: Zero-bias linetraces (blue) and above-gap linetraces averaged over positive and negative bias voltage (orange). The stability of the zero-bias conductance plateau is sensitive to the precise electrostatic environment, which is also affected by hysteretic gate effects. For comparison, in **b** and **c** we indicate relatively flat regions of the zero-bias conductance (pink shade). These regions do not meet our definition of plateaus however, with a ratio of slopes (blue, orange arrows) of ~ 1 and a mean zero-bias conductance and standard deviation of 1.03 ± 0.04, 1.03 ± 0.06 in **b**, **c** respectively. Note that the data in **a** and **f** are also shown in Fig. 6.4a,b. $B = 1.65\,\mathrm{T}$ and $V_{TG2} = -0.69\,\mathrm{V}$ in all panels.

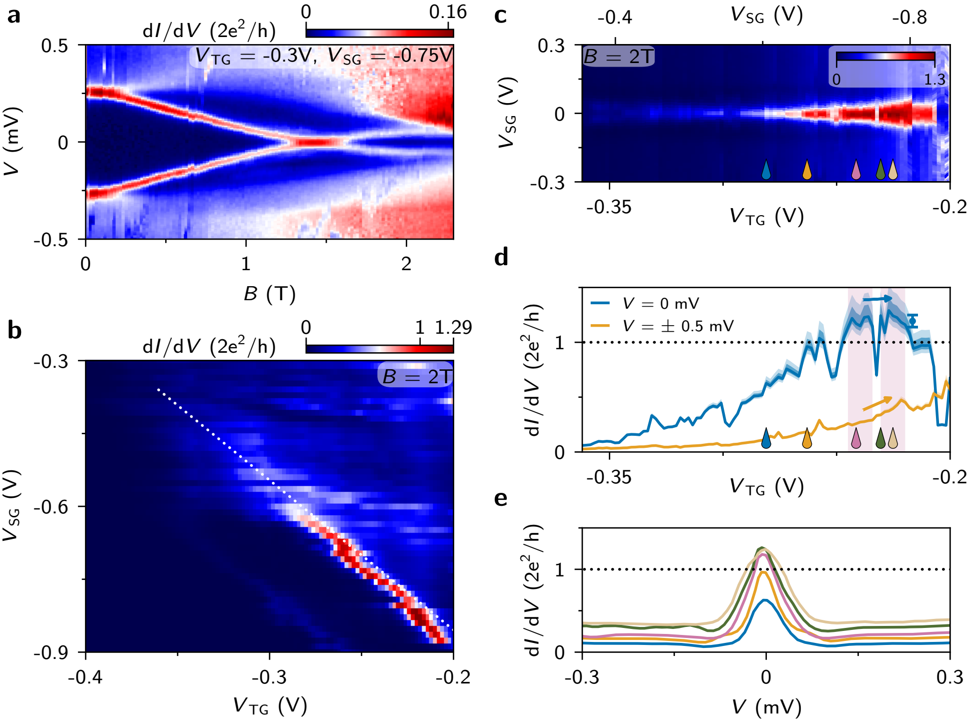

Figure 6.S8: Zero-bias conductance saturation at $1.35 \cdot 2e^2/h$ in device A. A saturation of the zero-bias peak height at a conductance different from $2e^2/h$ can be found by careful fine tuning of the gate compensation for various electrostatic configurations of the device. In this dataset, the backgate voltage is set to $-1.5\,$V, instead of $-0.25\,$V as in Fig. 6.3 and 6.4. **(a)** Magnetic field dependence shows that the ZBP results from a zero-energy crossing. The peak height is lower than $2e^2/h$ due to a low tunnel-gate voltage. The gates are set to: $V_{TG} = -0.3\,$V, $V_{SG} = -0.75\,$V. **(b)** The zero-bias conductance at $B = 2\,$T shows that a ZBP only appears when the tunnel gate and super gate are appropriately compensated, with a strong dependence on the tunnel-gate voltage, indicating that the zero-energy state is located close to the tunnel barrier. **(c)** When V_{TG} and V_{SG} are scanned over the dotted line in **b**, the subgap state remains pinned close to or at zero energy. The dotted line in **b** does not exactly overlap the ZBP due to hysteresis in the gate sweeps. **(d)** Horizontal linecuts of **c** at zero bias (blue line, uncertainty in shade) and the averaged linetraces at -0.5 and $0.5\,$V indicating the above-gap conductance (orange). The pink shade indicates a region where the zero-bias conductance saturates at a mean value and standard deviation of $1.19 \pm 0.06 \cdot 2e^2/h$ (blue errorbar, single outlier outside of pink shade excluded). The ratio of the slopes (blue, orange arrows) is 7. The zero-bias conductance variation in the saturation region exceeds our limit for a plateau. The peak height saturates at $\sim 1.35 \cdot 2e^2/h$ for $V_{TG} > -0.245\,$V. Simultaneously, the above gap conductance continues to increase. **(e)** Vertical linecuts of **c** at the gate voltages indicated by the colored droplets in **c**. The ZBP height stabilizes, while the peak width and above-gap conductance keep increasing. $V_{TG2} = -0.5\,$V in all panels.

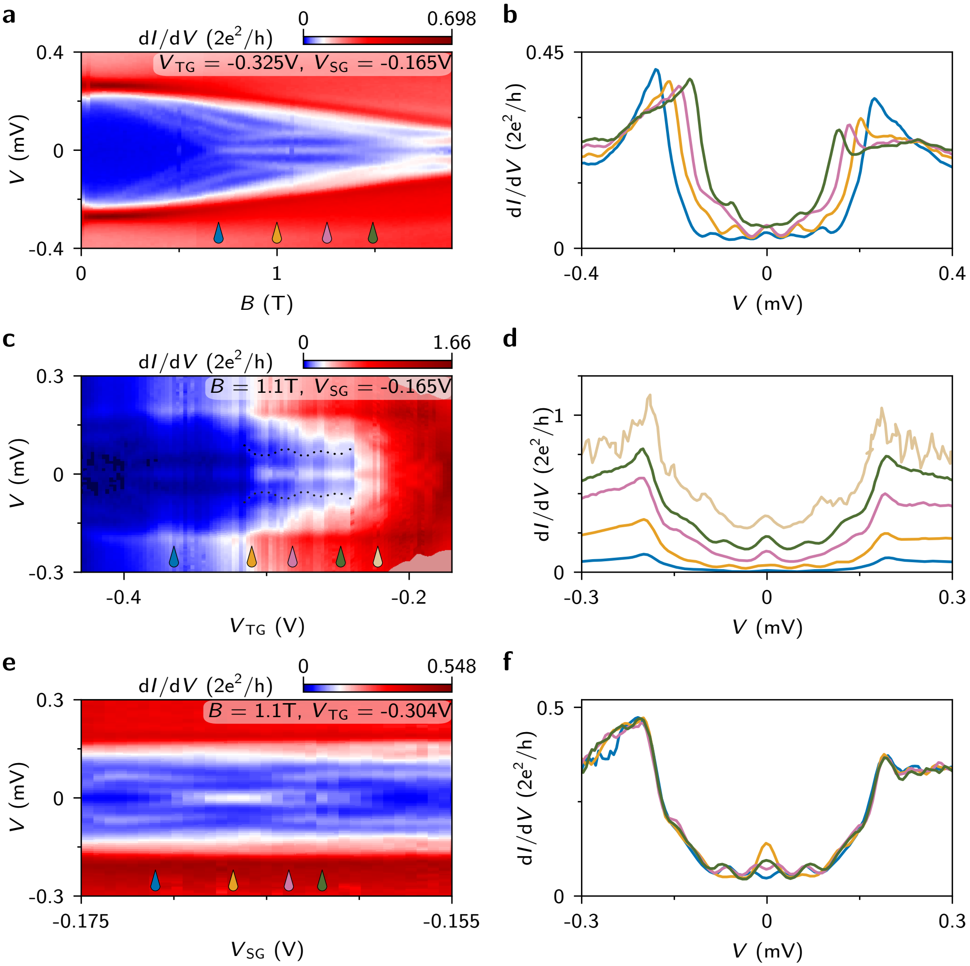

Figure 6.S9: Stable ZBP with gap reopening features in device A. **(a)** Magnetic field dependence of the ZBP. Subgap states come down from the gap edge and form a ZBP stable over a range of 0.65 T. As the ZBP forms, the higher energy subgap states increase in energy. This behavior is expected for a finite size Majorana nanowire: the trivial gap closes and reopens with the appearance of a ZBP upon the transition into the topological phase [6, 7]. However, this feature could be mimicked by a trivial ABS in in multimode nanowires with interband coupling [57], which we cannot exclude based on our dataset. **(b)** Linecuts of **a** at B indicated by the colored droplets. **(c)** Tunnel gate dependence of the ZBP at $B = 1.1\,\mathrm{T}$. The ZBP is stable over the entire tunnel gate range, strongly indicating that the ZBP originates underneath the superconductor. Higher energy states come down towards the ZBP multiple times (dotted lines), without splitting the ZBP, which could indicate that the zero energy state has a nonlocal character [43, 44]. $V_{\mathrm{SG}} = -0.165\,\mathrm{V}$. **(d)** Linecuts of **c** at V_{TG} indicated by the colored droplets. **(e)** Super gate dependence of the ZBP at $B = 1.1\,\mathrm{T}$. Starting from low V_{SG}, subgap states come down in energy to form a ZBP over a limited V_{SG} range, after which it splits and oscillates around zero energy once. **(f)** Linecuts of **c** at V_{SG} indicated by the colored droplets, showing the oscillating behavior of the ZBP. The backgate is set to $-1.0\,\mathrm{V}$ and $V_{\mathrm{TG2}} = -0.5\,\mathrm{V}$ in all panels.

REFERENCES

[1] N. Read and D. Green, *Paired states of fermions in two dimensions with breaking of parity and time-reversal symmetries and the fractional quantum Hall effect,* Phys. Rev. B **61**, 10267 (2000).

[2] A. Y. Kitaev, *Unpaired Majorana fermions in quantum wires,* Phys. Usp. **44**, 131 (2001).

[3] L. Fu and C. L. Kane, *Superconducting proximity effect and Majorana fermions at the surface of a topological insulator,* Phys. Rev. Lett. **100**, 096407 (2008).

[4] A. Y. Kitaev, *Fault-tolerant quantum computation by anyons,* Annals of Physics **303**, 2 (2003).

[5] S. Das Sarma, M. Freedman, and C. Nayak, *Topological quantum computation,* Phys. Today **59**, 32 (2006).

[6] R. M. Lutchyn, J. D. Sau, and S. Das Sarma, *Majorana fermions and a topological phase transition in semiconductor-superconductor heterostructures,* Phys. Rev. Lett. **105**, 077001 (2010).

[7] Y. Oreg, G. Refael, and F. von Oppen, *Helical liquids and Majorana bound states in quantum wires,* Phys. Rev. Lett. **105**, 177002 (2010).

[8] K. T. Law, P. A. Lee, and T. K. Ng, *Majorana fermion induced resonant Andreev reflection,* Phys. Rev. Lett. **103**, 237001 (2009).

[9] M. Wimmer, A. R. Akhmerov, J. P. Dahlhaus, and C. W. J. Beenakker, *Quantum point contact as a probe of a topological superconductor,* New J. of Phys. **13**, 053016 (2011).

[10] V. Mourik, K. Zuo, S. M. Frolov, S. R. Plissard, E. P. A. M. Bakkers, and L. P. Kouwenhoven, *Signatures of Majorana fermions in hybrid superconductor-semiconductor nanowire devices,* Science **336**, 1003 (2012).

[11] A. Das, Y. Ronen, Y. Most, Y. Oreg, M. Heiblum, and H. Shtrikman, *Zero-bias peaks and splitting in an Al–InAs nanowire topological superconductor as a signature of Majorana fermions,* Nat. Phys. **8**, 887 (2012).

[12] M. T. Deng, C. L. Yu, G. Y. Huang, M. Larsson, P. Caroff, and H. Q. Xu, *Anomalous zero-bias conductance peak in a Nb–InSb nanowire–Nb hybrid device,* Nano Lett. **12**, 6414 (2012).

[13] M. T. Deng, S. Vaitiekėnas, E. B. Hansen, J. Danon, M. Leijnse, K. Flensberg, J. Nygård, P. Krogstrup, and C. M. Marcus, *Majorana bound state in a coupled quantum-dot hybrid-nanowire system,* Science **354**, 1557 (2016).

[14] J. Chen, P. Yu, J. Stenger, M. Hocevar, D. Car, S. R. Plissard, E. P. A. M. Bakkers, T. D. Stanescu, and S. M. Frolov, *Experimental phase diagram of zero-bias conductance peaks in superconductor/semiconductor nanowire devices,* Sci. Adv. **3**, e1701476 (2017).

[15] Ö. Gül, H. Zhang, J. D. S. Bommer, M. W. A. de Moor, D. Car, S. R. Plissard, E. Bakkers, A. Geresdi, K. Watanabe, T. Taniguchi, and L. P. Kouwenhoven, *Ballistic Majorana nanowire devices,* Nat. Nanotech. **13**, 192 (2018).

[16] A. Grivnin, E. Bor, M. Heiblum, Y. Oreg, and H. Shtrikman, *Concomitant opening of a bulk-gap with an emerging possible Majorana zero mode,* Nat. Commun. **10**, 1940 (2019).

[17] F. Pientka, G. Kells, A. Romito, P. W. Brouwer, and F. von Oppen, *Enhanced zero-bias Majorana peak in the differential tunneling conductance of disordered multisubband quantum-wire/superconductor junctions,* Phys. Rev. Lett. **109**, 227006 (2012).

[18] F. Setiawan, C.-X. Liu, J. D. Sau, and S. Das Sarma, *Electron temperature and tunnel coupling dependence of zero-bias and almost-zero-bias conductance peaks in Majorana nanowires,* Phys. Rev. B **96**, 184520 (2017).

[19] C.-X. Liu, J. D. Sau, and S. Das Sarma, *Role of dissipation in realistic Majorana nanowires,* Phys. Rev. B **95**, 054502 (2017).

[20] F. Nichele, A. C. C. Drachmann, A. M. Whiticar, E. C. T. O'Farrell, H. J. Suominen, A. Fornieri, T. Wang, G. C. Gardner, C. Thomas, A. T. Hatke, P. Krogstrup, M. J. Manfra, K. Flensberg, and C. M. Marcus, *Scaling of Majorana zero-bias conductance peaks,* Phys. Rev. Lett. **119**, 136803 (2017).

[21] H. Zhang, C.-X. Liu, S. Gazibegovic, D. Xu, J. A. Logan, G. Wang, N. van Loo, J. D. S. Bommer, M. W. A. de Moor, D. Car, R. L. M. Op het Veld, P. J. van Veldhoven, S. Koelling, M. A. Verheijen, M. Pendharkar, D. J. Pennachio, B. Shojaei, J. S. Lee, C. J. Palmstrøm, E. P. A. M. Bakkers, S. D. Sarma, and L. P. Kouwenhoven, *Quantized Majorana conductance,* arXiv preprint arXiv:1710.10701 (2017).

[22] A. Vuik, B. Nijholt, A. R. Akhmerov, and M. Wimmer, *Reproducing topological properties with quasi-Majorana states,* SciPost Phys. **7**, 061 (2019).

[23] C. Moore, T. D. Stanescu, and S. Tewari, *Two-terminal charge tunneling: Disentangling Majorana zero modes from partially separated Andreev bound states in semiconductor-superconductor heterostructures,* Phys. Rev. B **97**, 165302 (2018).

[24] C. Moore, C. Zeng, T. D. Stanescu, and S. Tewari, *Quantized zero-bias conductance plateau in semiconductor-superconductor heterostructures without topological Majorana zero modes,* Phys. Rev. B **98**, 155314 (2018).

[25] C. Nayak, S. H. Simon, A. Stern, M. Freedman, and S. Das Sarma, *Non-Abelian anyons and topological quantum computation,* Rev. Mod. Phys. **80**, 1083 (2008).

[26] R. Aguado, *Majorana quasiparticles in condensed matter,* Riv. Nuovo Cimento **40**, 523 (2017).

[27] G. Kells, D. Meidan, and P. W. Brouwer, *Near-zero-energy end states in topologically trivial spin-orbit coupled superconducting nanowires with a smooth confinement,* Phys. Rev. B **86**, 100503 (2012).

[28] E. Prada, P. San-Jose, and R. Aguado, *Transport spectroscopy of NS nanowire junctions with Majorana fermions,* Phys. Rev. B **86**, 180503 (2012).

[29] C.-X. Liu, J. D. Sau, T. D. Stanescu, and S. Das Sarma, *Andreev bound states versus Majorana bound states in quantum dot-nanowire-superconductor hybrid structures: Trivial versus topological zero-bias conductance peaks,* Phys. Rev. B **96**, 075161 (2017).

[30] Y. Huang, H. Pan, C.-X. Liu, J. D. Sau, T. D. Stanescu, and S. Das Sarma, *Metamorphosis of Andreev bound states into Majorana bound states in pristine nanowires,* Phys. Rev. B **98**, 144511 (2018).

[31] J. D. S. Bommer, H. Zhang, O. Gül, B. Nijholt, M. Wimmer, F. N. Rybakov, J. Garaud, D. Rodic, E. Babaev, M. Troyer, D. Car, S. R. Plissard, E. P. A. M. Bakkers, K. Watanabe, T. Taniguchi, and L. P. Kouwenhoven, *Spin-orbit protection of induced superconductivity in Majorana nanowires,* Phys. Rev. Lett. **122**, 187702 (2019).

[32] S. Das Sarma, J. D. Sau, and T. D. Stanescu, *Splitting of the zero-bias conductance peak as smoking gun evidence for the existence of the Majorana mode in a superconductor-semiconductor nanowire,* Phys. Rev. B **86**, 220506 (2012).

[33] T. O. Rosdahl, A. Vuik, M. Kjaergaard, and A. R. Akhmerov, *Andreev rectifier: A nonlocal conductance signature of topological phase transitions,* Phys. Rev. B **97**, 045421 (2018).

[34] S. Gazibegovic, D. Car, H. Zhang, S. C. Balk, J. A. Logan, M. W. A. de Moor, M. C. Cassidy, R. Schmits, D. Xu, G. Wang, P. Krogstrup, R. L. M. Op het Veld, K. Zuo, Y. Vos, J. Shen, D. Bouman, B. Shojaei, D. Pennachio, J. S. Lee, P. J. van Veldhoven, S. Koelling, M. A. Verheijen, L. P. Kouwenhoven, C. J. Palmstrøm, and E. P. A. M. Bakkers, *Epitaxy of advanced nanowire quantum devices,* Nature **548**, 434 (2017).

[35] M. W. A. de Moor, *Quantum transport in nanowire networks,* Ph.D. thesis, Delft University of Technology (2019), chapter 8: Bound states in 1D Majorana nanowires.

[36] G. E. Blonder, M. Tinkham, and T. M. Klapwijk, *Transition from metallic to tunneling regimes in superconducting microconstrictions: Excess current, charge imbalance, and supercurrent conversion,* Phys. Rev. B **25**, 4515 (1982).

[37] C.-X. Liu, F. Setiawan, J. D. Sau, and S. Das Sarma, *Phenomenology of the soft gap, zero-bias peak, and zero-mode splitting in ideal Majorana nanowires,* Phys. Rev. B **96**, 054520 (2017).

[38] I. van Weperen, B. Tarasinski, D. Eeltink, V. S. Pribiag, S. R. Plissard, E. P. A. M. Bakkers, L. P. Kouwenhoven, and M. Wimmer, *Spin-orbit interaction in InSb nanowires,* Phys. Rev. B **91**, 201413 (2015).

[39] C.-X. Liu, Personal communication (2019).

[40] C. W. Groth, M. Wimmer, A. R. Akhmerov, and X. Waintal, *Kwant: a software package for quantum transport,* New J. Phys. **16**, 063065 (2014).

[41] D. Rainis, L. Trifunovic, J. Klinovaja, and D. Loss, *Towards a realistic transport modeling in a superconducting nanowire with Majorana fermions,* Phys. Rev. B **87**, 024515 (2013).

[42] C. Reeg, O. Dmytruk, D. Chevallier, D. Loss, and J. Klinovaja, *Zero-energy Andreev bound states from quantum dots in proximitized Rashba nanowires,* Phys. Rev. B **98**, 245407 (2018).

[43] E. Prada, R. Aguado, and P. San-Jose, *Measuring Majorana nonlocality and spin structure with a quantum dot,* Phys. Rev. B **96**, 085418 (2017).

[44] D. J. Clarke, *Experimentally accessible topological quality factor for wires with zero energy modes,* Phys. Rev. B **96**, 201109 (2017).

[45] J. Kammhuber, M. C. Cassidy, H. Zhang, O. Gül, F. Pei, M. W. A. de Moor, B. Nijholt, K. Watanabe, T. Taniguchi, D. Car, S. R. Plissard, E. P. A. M. Bakkers, and L. P. Kouwenhoven, *Conductance quantization at zero magnetic field in InSb nanowires,* Nano Lett. **16**, 3482 (2016).

[46] A. Vuik, D. Eeltink, A. R. Akhmerov, and M. Wimmer, *Effects of the electrostatic environment on the Majorana nanowire devices,* New J. Phys. **18**, 033013 (2016).

[47] B. D. Woods, T. D. Stanescu, and S. Das Sarma, *Effective theory approach to the Schrödinger-Poisson problem in semiconductor Majorana devices,* Phys. Rev. B **98**, 035428 (2018).

[48] D. I. Pikulin, J. P. Dahlhaus, M. Wimmer, H. Schomerus, and C. W. J. Beenakker, *A zero-voltage conductance peak from weak antilocalization in a Majorana nanowire,* New J. of Phys. **14**, 125011 (2012).

[49] H. Pan and S. Das Sarma, *Physical mechanisms for zero-bias conductance peaks in Majorana nanowires,* Phys. Rev. Research **2**, 013377 (2020).

[50] H. Pan, W. S. Cole, J. D. Sau, and S. Das Sarma, *Generic quantized zero-bias conductance peaks in superconductor-semiconductor hybrid structures,* Phys. Rev. B **101**, 024506 (2020).

[51] O. Gül, D. J. van Woerkom, I. van Weperen, D. Car, S. R. Plissard, E. P. A. M. Bakkers, and L. P. Kouwenhoven, *Towards high mobility InSb nanowire devices,* Nanotechnology **26**, 215202 (2015).

[52] H. Zhang, O. Gül, S. Conesa-Boj, M. P. Nowak, M. Wimmer, K. Zuo, V. Mourik, F. K. de Vries, J. van Veen, M. W. A. de Moor, J. D. S. Bommer, D. J. van Woerkom, D. Car, S. R. Plissard, E. P. A. M. Bakkers, M. Quintero-Pérez, M. C. Cassidy, S. Koelling, S. Goswami, K. Watanabe, T. Taniguchi, and L. P. Kouwenhoven, *Ballistic superconductivity in semiconductor nanowires,* Nat. Commun. **8**, 16025 (2017).

[53] J. D. S. Bommer, *Zero-energy states in Majorana nanowire devices,* Zenodo Dataset (2020).

[54] *Qt designed instrumentation -modules-m1b-,* http://qtwork.tudelft.nl/~schouten/ivvi/doc-mod/docm1b.htm.

[55] G. Wang, J. D. S. Bommer, and M. W. A. De Moor, *Notes on transport measurements using a lock-in,* https://forum.kavli.tudelft.nl/t/lock-in-measurement-common-issues-and-guidelines/85 (2020).

[56] M. W. A. de Moor, J. D. S. Bommer, D. Xu, G. W. Winkler, A. E. Antipov, A. Bargerbos, G. Wang, N. van Loo, R. L. M. O. het Veld, S. Gazibegovic, D. Car, J. A. Logan, M. Pendharkar, J. Sue Lee, E. P. A. M. Bakkers, C. J. Palmstrøm, R. M. Lutchyn, L. P. Kouwenhoven, and H. Zhang, *Electric field tunable superconductor-semiconductor coupling in Majorana nanowires,* New J. of Phys. **20**, 103049 (2018).

[57] B. D. Woods, J. Chen, S. M. Frolov, and T. D. Stanescu, *Zero-energy pinning of topologically trivial bound states in multiband semiconductor-superconductor nanowires,* Phys. Rev. B **100**, 125407 (2019).

7

NONLOCAL ELECTROSTATIC GATING OF MAJORANA NANOWIRES

7.1. INTRODUCTION

Majorana zero-modes (MZMs), which can be regarded as special half-electron-like quasiparticles, forming in a pair at the edges of a topological superconductor, have attracted significant interest, owing to their non-Abelian exchange statistics [1], and technological application as the building blocks of a topological quantum computer. Topological quantum bits promise an inherent protection against local noise, which provides an improved stability of the quantum bits over other quantum computing platforms [1–3]. At the basis of this topological quantum bit protection, lies a spatial separation of the pair of MZMs, which prevents their mutual interaction, while the quantum information is stored nonlocally in the zero-energy electronic state formed by the pair of MZMs. The prime platform for the creation of MZMs is a semiconducting nanowire with strong spin-orbit interaction, coupled to an ordinary *s*-wave superconductor [4, 5]. The experimental efforts to detect MZMs have largely focused on the observation of a zero-bias conductance peak (ZBP) in tunneling spectroscopy. Following the initial observations of MZM signatures [6–8], shortcomings of the original nanowire systems, including a soft induced superconducting gap and ZBP heights far below the predicted quantized value of $2e^2/h$ [9–12], have been addressed through significant material science improvements [13–16]. However, as the previous tunneling experiments could only address the MZM adjacent to the tunnel probe, the nonlocal properties of MZMs, which ultimately reflect their topological nature, have remained elusive. In parallel with the experimental progress, the understanding of alternative explanations of the ZBPs have also developed with the realization that a smooth electrostatic potential profile can stabilize a topologically trivial Andreev bound state (ABS) at zero-energy [17–19]. In the presence of a particularly smooth potential, these trivial ABSs are referred to as quasi-Majorana modes [20] or partially separated ABSs [21, 22] and can be understood as being composed of two local MZMs with negligible or weak spatial separation, but with a nevertheless strongly suppressed mutual interaction. Owing to this suppressed interaction, local MZMs mimick the local properties of spatially separated MZMs.

Here, we approach the question of locality by using a remote electrostatic gate far removed from the tunneling barrier (dubbed the nonlocal gate), which only manipulates states that extend throughout the nanowire, whereas localized states are unaffected. We present ZBPs exhibiting peak splitting oscillations induced by the nonlocal gate, for zero-energy states that display strong robustness against variations of the tunneling barrier, with peak heights approaching $2e^2/h$, consistent with nonlocal MZMs in a short nanowire device. Meanwhile, we distinguish two types of local states by the absence of a nonlocal gating effect and a distinct response to the local gates and magnetic field.

7.2. EXPERIMENTAL SETUP

We perform tunneling spectroscopy on InSb nanowire device coupled to a thin ~ 10 nm aluminium shell that covers two of the six nanowire facets, where a short section of the nanowire is left uncovered with the superconductor through an in-situ shadowing technique [16]. Here, we focus on the first device shown in Fig. 7.1a, with a schematic in Fig. 7.1b. The results from the second device are discussed in the Supplementary section

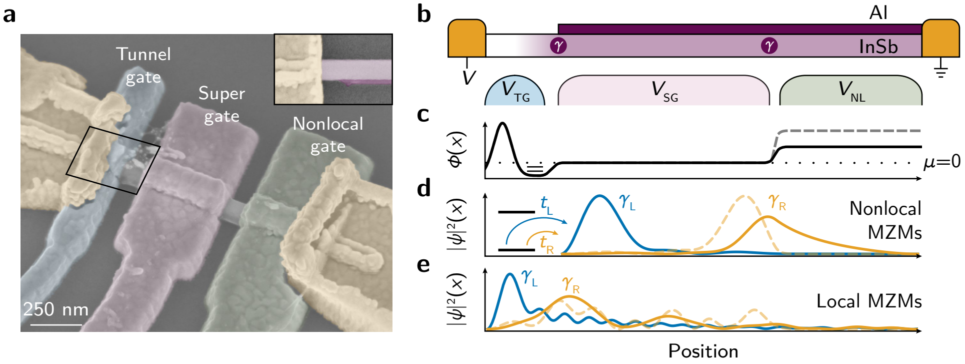

Figure 7.1: Device overview. (a) Tilted-view false-colored scanning electron micrograph of the device studied. The InSb epitaxial aluminium nanowire is contacted by two contacts (yellow). The left contact is positioned on the wire section that is left uncovered with aluminium (see top right inset: micrograph taken before gate deposition, with aluminium is shown in purple). The nanowire and contacts are covered by a 35 nm thick SiN dielectric layer before placement of the wrap-around gates (blue, purple and green), as illustrated by the cross section shown in the bottom left inset. **(b)** Device schematic (not to scale). The tunnel gate (TG) induces a tunneling barrier. The super gate (SG) adjusts the chemical potential in the proximitized nanowire, so that MZMs (γ) can form at the edges of the super gate. The nonlocal gate (NL) tunes the potential at the far end of the nanowire. **(c)** Schematic electrostatic potential along the nanowire axis two different values of V_{NL} (solid and dotted lines). Unintentional dot states form near the tunneling barrier, illustrated by the lines in the potential well. **(d)** Majorana wavefunctions for two different values of V_{NL} (solid and dotted lines). A change of the potential at the far end of the nanowire slightly moves the right MZM, and hence affects the overlap with the left MZM, which is detectable as a modulation of the peak splitting measured at the tunneling barrier. **(e)** Same as **d**, but for local MZMs induced by a smooth tunneling barrier profile.

7.S.4. The nanowire is contacted at the edge of the uncovered nanowire section, where a bias voltage V is applied, and at the end of the nanowire where the aluminium shell is grounded and current is drained. We measure the differential conductance, $\mathrm{d}I/\mathrm{d}V$, using lock-in techniques, and correct for the non-device resistances and calibrate out AC effects due to the reactive response of the measurement circuit to obtain accurate conductance values (see the supplemental section 7.S.1 for the details of the procedure). A back gate is located globally underneath the device, separated by a 20 nm thick SiN dielectric layer, and is set to −1.04 V throughout the experiment, unless specified otherwise. Three top gates, separated from the nanowire by a 35 nm thick SiN layer, wrap around the nanowire, minimizing the cross coupling of each gate to the electron density in the nanowire underneath the adjacent gates. The tunnel gate (blue) covers the nanowire section that is uncovered by aluminium and can deplete the nanowire to induce a tunneling barrier. The super gate (purple) controls the chemical potential in the nanowire, which allows for the creation of MZMs at the ends of the super gate when a magnetic field B is applied along the nanowire [4, 5]. The left MZM, located next to the tunneling barrier, shows up as a zero-bias peak (ZBP) in the tunneling experiment. The right MZM, on the other hand, is typically inaccessible in experiments, which lies at the basis of the lingering debate around the nonlocality of the zero-energy states observed previously. Here, we use a short super gate length of 450 nm, to ensure that the wavefunctions of the MZMs we aim to create overlap, which is expected to induce oscillations in the ZBP splitting as a function of the magnetic field and the chemical potential [23]. Similarly, by adjusting the voltage on the nonlocal gate, positioned near the right MZM, the position of right MZM can be manipulated slightly, which consequently changes the wavefunction overlap and is detectable at the tunneling barrier through ZBP splitting oscillations, as illustrated in Fig. 7.1c,d. By contrast, localized states should be insensitive to the nonlocal gate. In the case of local MZMs resulting from a smooth tunneling barrier potential, a weak nonlocal gating effect could be induced by the manipulation of the tails of the wavefunctions that extend throughout the nanowire (see Fig. 7.1e), but a distinct dependence on the local gates is expected.

7.3. RESULTS

Nonlocal gating of zero-bias peaks

We start our transport spectroscopy experiment by applying a magnetic field B along the nanowire axis in Fig. 7.2a (with linecuts in Fig. 7.2e), where we find a state coming down from the gap edge, which crosses zero energy around 0.7 T, after which it splits and remains close to zero-energy (highlighted by the white dotted line). The observation of this nearly zero-energy state is our first indication of overlapping MZMs. We note that at zero magnetic field we also find high subgap peaks, which result from an ABS formed in an unintentional quantum dot near the tunnel barrier, and which move towards the superconducting gap edge at $B = 0.2\,\mathrm{T}$ (detailed characterization of the dot state is shown in Fig. 7.S3). Simarly, another low energy subgap state at zero magnetic field spin splits and crosses zero energy before moving towards the gap edge when the magnetic field is increased. Now, we explore the effect of the chemical potential on the near zero-energy state at 0.7 T by varying the voltage on the super gate V_{SG} in Fig. 7.2b. At low V_{SG} a pair of states come down to form a ZBP over an extended gate range, with two small oscillations, which can result from the overlap of MZMs. We ascribe the subgap states at higher bias to bulk states, which show up as discrete states in finite length nanowires [24]. To spatially resolve the origin of the ZBP, we vary the voltage on the tunnel gate V_{TG} (Fig. 7.2c, with linecuts in 7.2g), and we find that the energy of the ZBP is completely stable at zero, indicating that the zero-energy state originates underneath the super gate, where the effect of the tunnel gate is insignificant due to the strong electrostatic screening of the wrap-around super gate. Importantly, MZMs are expected to form underneath the super gate, whereas a strong V_{TG} stability over extended gate ranges is not expected for topologically trivial zero-energy modes generated by electrostatic potential inhomogeneities, which are particularly expected near the tunneling barrier. The discrete bulk states at finite energy, which are best visible at $V_{\mathrm{TG}} > -110\,\mathrm{mV}$, are equally stable against V_{TG} variations. We emphasize that we consistently observe this tunnel gate stability of the states underneath the super gate, irrespective of the magnetic field or super gate voltage. Not all states we encounter are located underneath the super gate, however. In Fig. 7.2b we also observe states that do depend on V_{TG}, namely two sharp zero-energy crossings and a level smoothly evolving in between the crossing. The V_{TG} dependence indicates that these are dot states originate near the tunneling barrier, where due to proximity coupling to the superconducting shell, Andreev bound states (ABSs) can form in the dot. We will return to a detailed discussion of the interaction of the dot ABS with the nanowire states. First, we explore the nonlocal character of the ZBP through its response to the voltage

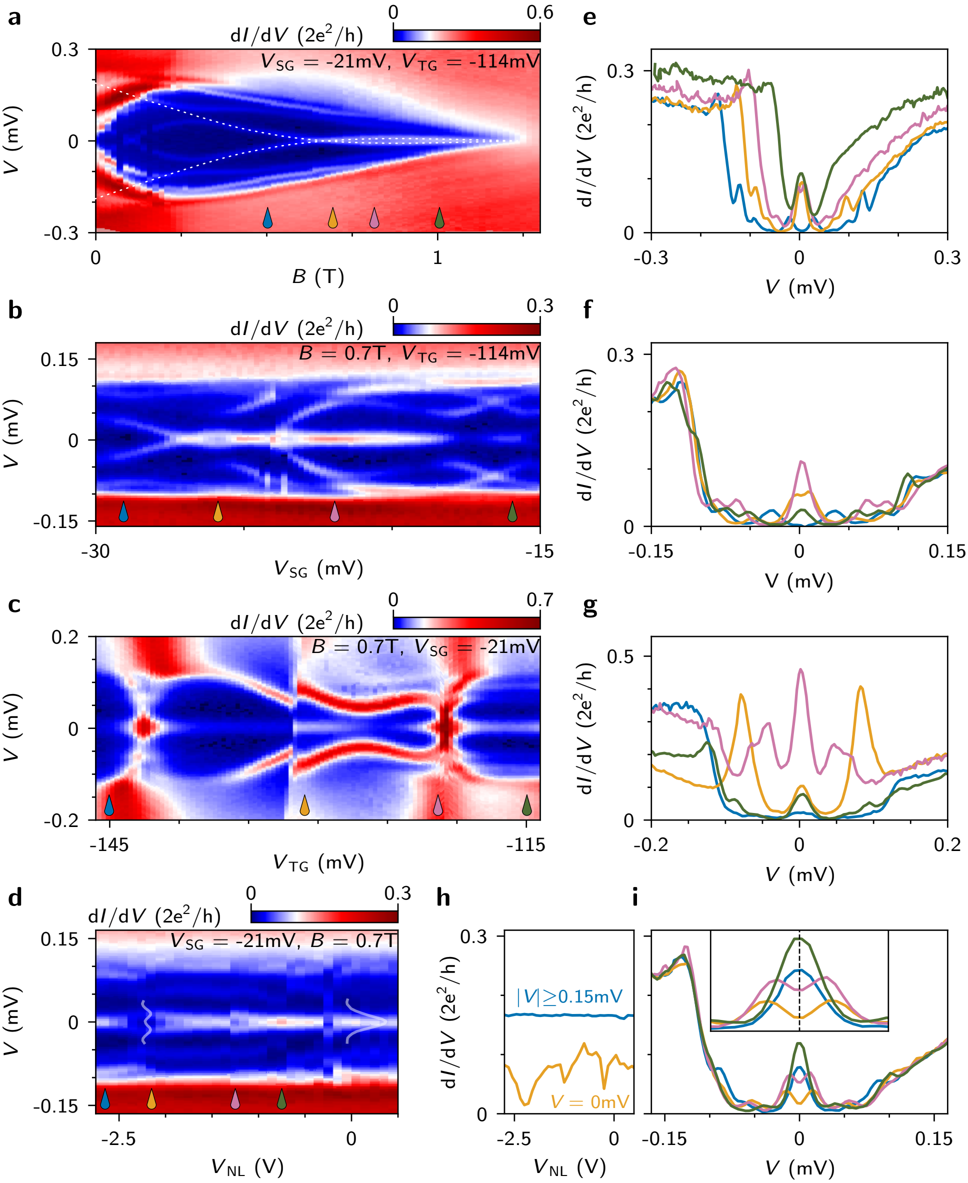

Figure 7.2: ZBP characterization. **(a)** Differential conductance dI/dV as a function of bias voltage V and magnetic field B oriented along the nanowire axis. The dotted line indicates the state that comes down to form a near zero-energy state. **(b)** Super gate (V_{SG}) dependence of the ZBP showing stability near zero energy with small occasional peak splittings. **(c)** Tunnel gate (V_{TG}) dependence showing stability of the ZBP at zero energy. **(d)** Nonlocal gate (V_{NL}) dependence showing ZBP peak splitting modulation. **(e,f,g,i)** Vertical linecuts of **(a,b,c,d)** respectively, at the positions indicated by the colored droplets in the adjacent panels. **(h)** Horizontal linecuts of **d**. $|V| > 0.15\,\mathrm{mV}$ (blue) shows a stable above-gap conductance, despite a large change of V_{NL} of 3.25 V. The zero-bias conductance (orange), does vary significantly. In all panels, $V_{\mathrm{TG}} = -114\,\mathrm{mV}$ and $V_{\mathrm{NL}} = 0\,\mathrm{V}$, unless the parameter is swept.

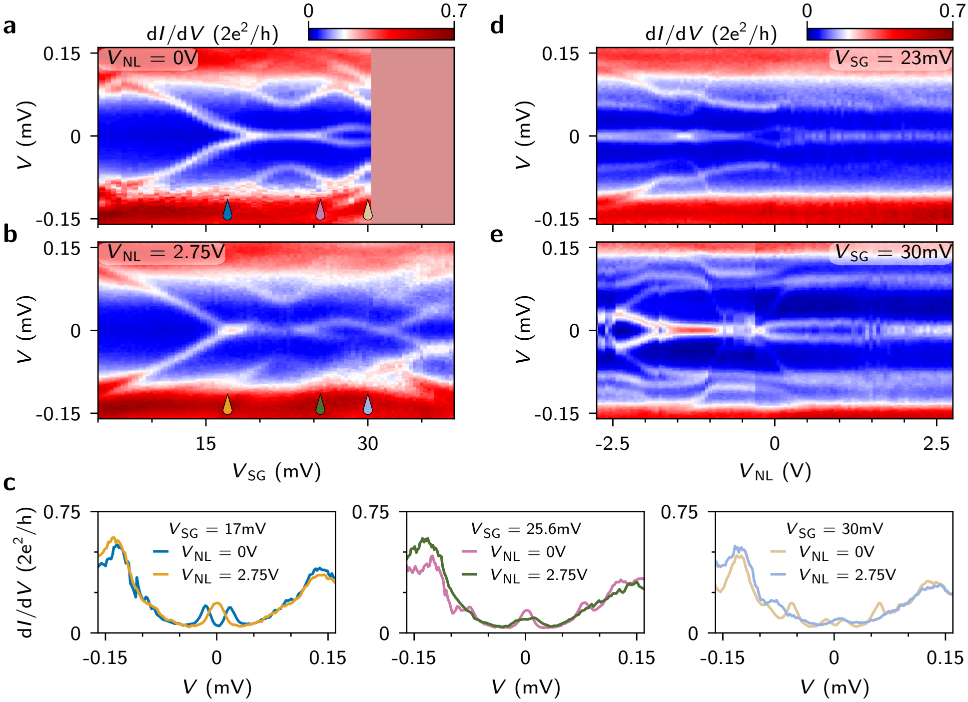

Figure 7.3: Nonlocal gating behavior at a magnetic field of 0.4T. (a,b) dI/dV against V and V_{SG} at $V_{\mathrm{NL}} = 0\,\mathrm{V}$ and 2.75 V respectively. The nonlocal gate adjusts the ZBP splitting oscillations. **(c)** Linecuts of **a** and **b** at the super gate voltages indicated by the colored droplets. **(c,d)** dI/dV against V and V_{NL} at $V_{\mathrm{SG}} = 23\,\mathrm{mV}$ and 30 mV, directly showing the ZBP splitting effect. We note that hysteretic effects of V_{NL}cause small differences when the V_{SG} and V_{NL} sweeps are compared, while hysteresis in V_{SG} is accounted for in **a** and **b** by sweeping in the same direction.

on the nonlocal gate V_{NL} in Fig. 7.2d, with linecuts in Fig. 7.2i. The ZBP we observe at $V_{\mathrm{NL}} = 0\,\mathrm{V}$ splits and moves back to zero energy twice as V_{NL} is decreased, consistent with the modulation of the outer MZM. We exclude cross-coupling of the nonlocal gate to the tunneling barrier region as the cause of the nonlocal gate effect based on the constant above-gap conductance over a large V_{NL} range of 3.25 V, as shown by the blue line in Fig. 7.2h, a behavior consistently observed for the nonlocal gate. The second device shows similar dependence on the magnetic field and gate voltages, including a nonlocal gating effect (Fig. 7.S8).

The nonlocal gating effect is also present at a lower magnetic field of 0.4 T, where we explore it in more detail by first varying V_{SG} at two different values of V_{NL} in Fig. 7.3a,b. Again, we observe a state coming down from the gap edge to form a ZBP with oscillating peak splitting behavior as V_{SG} is increased further (B dependence and V_{TG} stability is shown in Fig. 7.S1). The oscillations observed here deviate from the periodic oscillations expected from an ideal Majorana nanowire model [4, 5], which is expected when orbital effects [25] and electronic interactions [23, 26] are considered. Comparing the oscillatory peak splitting behavior at $V_{\mathrm{NL}} = 0\,\mathrm{V}$ and $V_{\mathrm{NL}} = 2.75\,\mathrm{V}$, we see that the nonlocal gate can change a split peak into a ZBP and vice versa, as highlighted in the linecuts shown in Fig. 7.3c. The peak splitting modulation becomes directly visible when we vary V_{NL} with the other gates fixed. The modulation can have an oscillatory behavior (Fig. 7.3d), or induce a smooth transition between a peak at zero-bias and a split peak, with regions where the ZBP remains pinned at zero energy (Fig. 7.3e). The shape of the peak splitting oscillations as a function of V_{SG} and V_{NL} depends on the overlap of the MZM wavefunctions, which is expected to sensitively depend on the confining electrostatic potential in the nanowire, and other system parameters, such as non-uniform spin-orbit coupling [27], interband interaction in nanowires with multiple occupied subbands [28], and disorder in the electrostatic potential along the nanowire [29]. Besides the energy splitting defined by wavefunction overlap of the MZMs, ZBPs can also be pinned to zero energy over extended regions of parameters such as the magnetic field and the chemical potential due to interactions with bound charges in the dielectric [26]. We note that the discrete bulk states at higher energy also display a nonlocal gating effect, as they are extended underneath the super gate towards the nonlocal gate [30].

ZBP stability upon level repulsion with dot levels and ZBP height

Nonlocal gating is one approach to detect the outer MZM. In addition, we can indirectly probe the outer MZM by employing the unintentional quantum dot that forms after the tunneling barrier, as it turns out that the interaction between a dot level and a pair of MZMs is distinctly different for well separated and strongly overlapping MZMs [31–33]. If the dot level is on resonance with well separated zero-energy MZMs, the MZM energy remains fixed at zero, whereas for overlapping MZMs the level repulsion induces an energy splitting, as illustrated in Fig. 7.4b. Perhaps unintuitively, this analysis does not assume that the MZMs are the result of the emergence of a topological phase. Instead, in this context a fermionic state is formally decomposed into a pair of MZMs, which do not need to be eigenstates of the system. An effective model describing the level repulsion spectrum can be obtain by considering distinct tunnel couplings between the dot state and the left MZM (t_{L}), and the dot state and the right MZM (t_{R}). If the MZMs are highly overlapping, then $t_{\mathrm{L}} \approx t_{\mathrm{R}}$, while for spatially separated MZMs $t_{\mathrm{L}} \gg t_{\mathrm{R}}$ (as illustrated in Fig. 7.4a). This method has been proposed [31–33], and used experimentally [34], as a tool to estimate the overlap of the MZM wavefunctions as $\Omega \sim \sqrt{(t_R/t_L)}$.

We now investigate the interaction with dot levels in detail at a magnetic field of 0.6 T, where we again observe ZBP splitting oscillations upon variation of V_{SG}, alternated with regions where the subgap state remains pinned at zero energy (Fig. 7.4c). The nonlocal gate dependence at this magnetic field is shown in Fig. 7.S5. Having found a ZBP at $V_{\mathrm{SG}} = 1\,\mathrm{mV}$, we now bring it in resonance with the dot states by varying V_{TG} in Fig. 7.4d. We observe complete stability of the energy of the subgap states, also upon crossing with the dot levels, in line with the spectrum expected for separated MZMs. Since the tunneling to the zero-energy state occurs through the dot in the tunneling barrier, only cotunneling processes are allowed when the dot is off-resonance, and the ZBP height is suppressed significantly (blue linetraces in Fig. 7.4d,f). However, on resonance with the dot level the ZBP height approaches the quantized conductance value expected for a MZM of $2e^2/h$ [35] within 5 % (blue linetrace in the upper panel of Fig. 7.4d and green, pink, and beige linetraces in Fig. 7.4f). Importantly, the zero-bias conductance does not exceed $2e^2/h$, which would be incompatible with a Majorana peak.

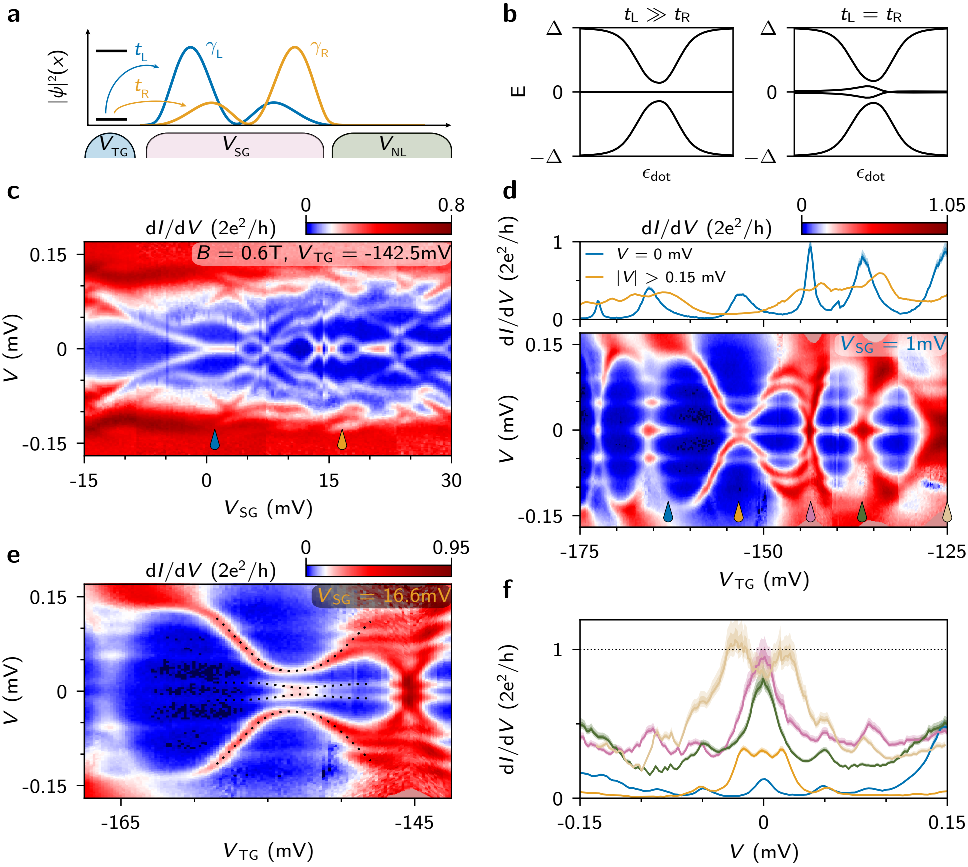

Figure 7.4: Dot anticrossing at 0.6T. **(a)** Illustration of the tunnel coupling between the dot states (horizontal lines) and the MZMs. The small amplitude of the wavefunction of the right MZM near the dot leads to a reduced t_R. **(b)** Dot ABS-MZM level repulsion spectrum as function of the energy of the dot state ϵ_{dot} for well separated MZMs ($t_L \gg t_R$, left), where the ZBP remains pinned at zero energy, and for a local ABS ($t_L = t_R$, right), where the ZBP splits on resonance with the dot state. **(c)** Super gate dependence of the ZBP showing oscillatory peak splitting behavior. **(d)** Lower panel: tunnel gate dependence of the ZBP at $V_{SG} = 1\,$mV, indicated by the blue droplet in **c**, showing complete stability of the position of the ZBP. Upper panel: horizontal linetraces at zero-bias (blue) and the above-gap conductance taken as the average conductance at $|V| \geq 0.15\,$mV (orange). The 1-σ and 2-σ uncertainty of the zero-bias conductance is indicated by shaded regions around the linetraces. **(e)** The tunnel gate dependence of the split peak at $V_{SG} = 16.6\,$mV, indicated by the orange droplet in **c**, exhibiting slight level repulsion with the dot ABS. The black dotted lines show the best fit to the spectrum, resulting in $\sqrt{t_R/t_L} \sim 0.5$. Full fit parameters are detailed in the Supplemental Material. **(f)** Vertical linecuts of **d** at V_{TG} indicated by the colored droplets. On resonance with the dot, the zero-bias conductance approaches, but does not exceed, $2e^2/h$. The shaded colored regions around the linetraces indicate the 1-σ and 2-σ uncertainty (see Supplemental Material). A very weak cross capacitance of 1% of the tunnel gate to the states underneath the super gate is compensated by adjusting V_{SG} simultaneously by 0.5 mV and 0.25 mV in **d** and **e** respectively. $V_{NL} = -1.45\,$V in all panels.

Although we observe no peak splitting upon dot resonances for the ZBP in Fig. 7.4d, small splittings could be obscured by the finite broadening of the peaks. To quantify the coupling strengths t_L and t_R, we set V_SG to 16.6 mV, at a maximum of the oscillatory peak splitting in Fig. 7.4c, so small changes in the energy of the peaks are easier to distinguish. As we vary V_TG in Fig. 7.4e, we notice that the peak splitting remains constant until the dot ABS comes down and pushes the split state slightly closer towards zero-energy. We fit this level repulsion by using an extension of the effective model introduced by Prada *et al.* [31]. We model the dot ABS as a spinful quantum dot level coupled to a superconductor implemented using a self-energy renormalization [36]. This dot ABS is coupled to the pair of MZMs, characterized by an energy splitting δ due to their mutual interaction. Further details of the model and the determination of the ABS parameters are discussed in supplemental section 7.S.2. The best fit to this model, shown by the black dotted line in Fig. 7.4e indicates $\sqrt{t_R/t_L} \sim 0.5$, which signifies an appreciable, but incomplete overlap of the two MZMs, consistent with our conjecture of overlapping MZMs in a short nanowire, for which peak splitting oscillations as a function of V_SG and a nonlocal gating effect are expected. We note that in the context of local MZMs, Vuik *et al.* [20] showed that t_R can be suppressed due to Zeeman field induced spin-splitting of the tunneling barrier, which effectively decouples one of the spin-polarized MZMs, without requiring spatial separation of the MZMs. However, a local MZM results from smoothness of the electrostatic potential profile, which is expected to occur near the tunneling barrier. Local MZMs should therefore be sensitive to the tunnel gate voltage, opposite to the strong tunnel gate stability we observe for this ZBP.

Trivial ABS underneath the super gate

The zero-energy states we have discussed so far, exhibit a nonlocal gate effect and weak level repulsion on resonance with dot levels. We also find states underneath the super gate with the opposite behavior: no nonlocal gate effect and strong peak splitting upon dot resonances. This is expected for a localized state, with nearly completely overlapping MZMs as illustrated in Fig. 7.5a. We first characterize the super gate dependence at a low magnetic field of 0.2 T in Fig. 7.5b, which shows a set of loops sharply cross zero-energy, typical of a trivial ABS in a confined potential [36–38]. We finely tune V_SG to the second zero-energy crossing and vary V_NL in Fig. 7.5c. The ZBP is completely insensitive to V_NL over more than 5 V, even though the ZBP only appears over a V_SG range of less than 1 mV. We now check the response to V_TG in Fig. 7.5d, where in addition to the zero-energy state, we observe two subsequent loops (four zero-energy crossings) stemming from two dot ABSs. In between the zero crossings of the dot ABSs, the ZBP remains pinned near zero energy, signifying that the ZBP originates underneath the super gate. On resonance with the dot ABSs, on the other hand, the ZBP splits and merges with the dot ABS (see the zoom-in of the zero crossings in Fig. 7.5e and the linetraces in Fig. 7.5f), as is expected for a localized state. Quantitatively, the best fit to the spectrum confirms the local character, yielding $\sqrt{t_R/t_L} \sim 0.9$ (black dotted lines in Fig. 7.5d,e). We have found other trivial states that are insensitive to the nonlocal gate and exhibit level repulsion with dot states at a slightly larger V_SG (see Fig. 7.S4) and in a second device (see Fig. 7.S7). The exact origin of the localized states underneath the super gate is unclear, but we speculate that it may be caused by remaining disorder in the device, for example due to impurity scattering in the superconducting shell [39].

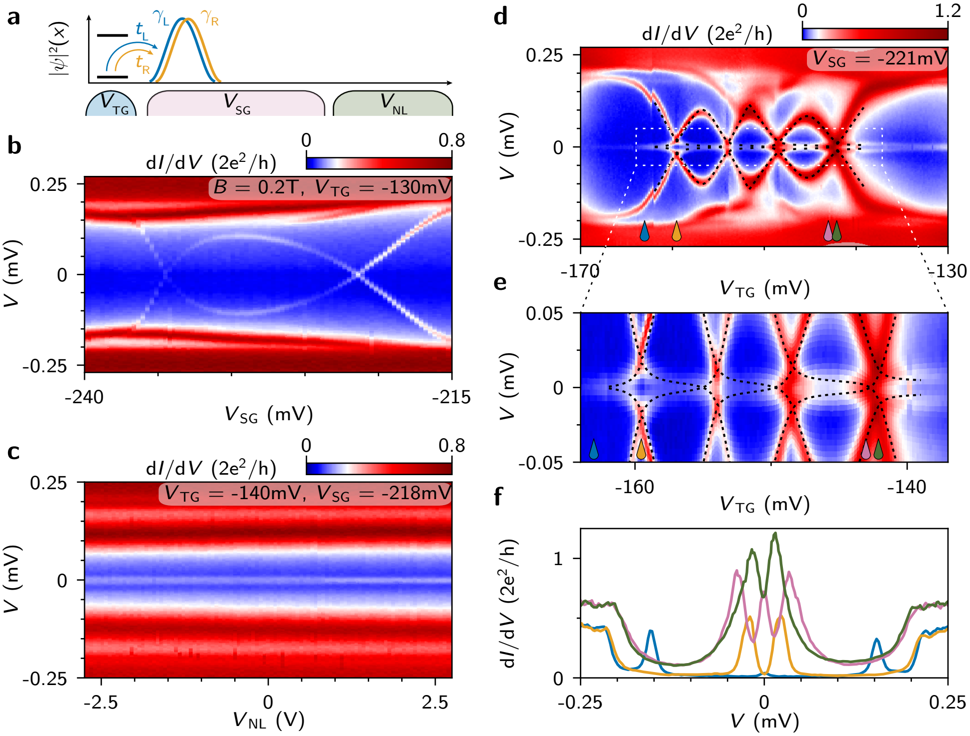

Figure 7.5: Trivial ABS underneath the super gate. **(a)** Illustration of the tunnel coupling between the dot states and the strongly overlapping MZMs for a local ABS for which $t_L \sim t_R$. **(b)** Super gate dependence of a trivial ABS crossing zero-energy twice. **(c)** Nonlocal gate dependence of the fine-tuned zero-energy ABS, showing complete insensitivity of the ZBP on V_{NL}. Compared to **b**, V_{TG} is slightly adjusted to optimize the visibility of the ZBP. **(d)** Tunnel gate dependence of the trivial ABS fine-tuned to zero-energy. The ZBP splits and fully hybridizes on resonance with the dot. The dotted lines show the best fit to the anticrossings, resulting in $\sqrt{t_R/t_L} \sim 0.9$ (see full fit parameters in Supplemental Material). **(e)** Same as **d**, zoomed in on the level repulsions in the white dashed box in **d**. **(f)** Linecuts of **d** and **e** at V_{TG} indicated by the colored droplets. V_{NL} = 0 V in **b**,**d**,**e** and the back gate voltage is 0 V in all panels.

Evolution of dot state into high ZBP

Up to this point, we have focused on ZBPs originating underneath the super gate. Most of the lingering alternative explanations of ZBPs that strongly resemble the emergence of a topological phase with spatially separated MZMs, involve smoothness of parameters near the tunneling barrier, such as the electrostatic potential, and induced superconducting gap [17, 19–22]. Here we show that, within the same device, indeed, the dot states near the tunneling barrier can evolve into a stable ZBP with a peak height approaching $2e^2/h$, the quantized conductance expected for MZMs [35]. However, this ZBP displays a characteristically different response to the various gates. With V_{TG} set to -126 mV, we increase the magnetic field and observe a state coming down from the gap edge to form a ZBP stable from 0.8 T up until the gap closing at around 1.25 T in Fig. 7.6a. With B set to 0.95 T, where the ZBP height is maximal, we notice that this ZBP is easily split by changing V_{TG} (lower panel Fig. 7.6b), in line with the behavior expected for an

ABS in a dot, and in stark contrast with the ZBPs we have discussed before. Investigating the zero-bias conductance (blue line) in the top panel of Fig. 7.6b, we notice that the ZBP height stabilizes around $0.65 \cdot 2e^2/h$, coinciding with a stable above-gap conductance (orange line), which is a measure of the tunneling strenght. We emphasize this is different from the plateaus observed in chapter 6, where the above-gap conductance increases with V_{TG} while the zero-bias conductance remains constant. In the present case, a constant tunneling rate can explain the stable zero-bias conductance. As a function of V_{SG}, the ZBP remains close to zero energy over a significant range (Fig. 7.6d), again in contrast with the ZBPs underneath the super gate that we investigated previously. The ZBP due to the dot ABS also exhibits irregular peak splitting behavior induced by level repulsion with the states underneath the super gate, inducing slight peak splittings (also see linetraces in 7.6f). Finally, the ZBP does not show an oscillatory peak splitting behavior in the nonlocal gate response (Fig. 7.6e). Instead, there is only a weak irregular

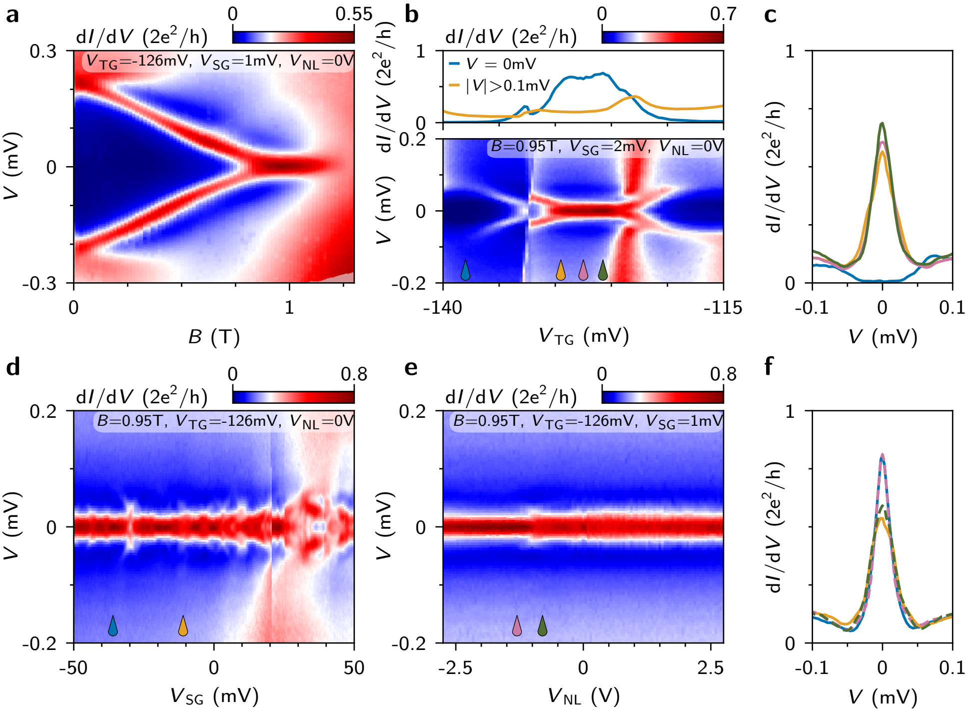

Figure 7.6: Development of high ZBP from a dot ABS (a). Magnetic field dependence of the dot ABS, which forms a ZBP stable from 0.8 T up to the gap closing. **(b)** Bottom panel: tunnel gate dependence of the ZBP at $B = 0.95\,\mathrm{T}$. The ZBP only appears over a short V_{TG} range. Top panel: The zero-bias linetrace (blue line) which shows a ZBP height stabilizing around $0.65 \cdot 2e^2/h$, coinciding with a stable above-gap conductance (orange line). **(c)** Linetraces of the lower panel of **b** at V_{TG} indicated by the colored droplets. **(d)** Super gate dependence of the ZBP at $B = 0.95\,\mathrm{T}$ showing that the ZBP remains close to zero energy over a long V_{SG} range. **(e)** Nonlocal gate dependence of the ZBP at $B = 0.95\,\mathrm{T}$, which lacks oscillatory peak splitting behavior. **(f)** Linetraces of **d** (solid lines) and **e** (dashed lines), at V_{SG} and V_{NL} indicated by the colored droplets. Changes in V_{SG} and V_{NL} affect the peak height, which reaches a maximum value of $0.8 \cdot 2e^2/h$. The backgate voltage is set to $-1.04\,\mathrm{V}$.

modulation of the ZBP, analogous to the V_{SG} dependence, which we attribute to the coupling of the nonlocal gate to the states extended throughout the nanowire. In both the V_{NL} and V_{SG} dependence the ZBP height reaches a maximum of $0.8 \cdot 2e^2/h$ (blue and purple dotted line in Fig. 7.6f). The relative instability to the tunnel gate, the stability to changes of the super gate, and the high peak height all indicate that the state originates at the tunneling barrier, where smoothness in the electrostatic potential profile can give rise to remarkably stable ZBPs [17–22].

7.4. CONCLUSION AND OUTLOOK

We have identified ZBPs that emerge at a finite magnetic field, which exhibit peak splitting oscillations as the chemical potential is varied and whose peak position is insensitive to tunnel barrier variations, showing that the zero-energy states originate in the nanowire section underneath the superconductor, instead of in the tunneling region, where topologically trivial zero-energy states, mimicking local signatures of MZMs, are suspected to form easily [17–22] . Furthermore, the nonlocal gate on the far end of the nanowire device induces an oscillatory ZBP splitting and the observed ZBPs are weakly repelled upon interaction with dot states, both of which indicate a nonlocal distribution of the zero-energy states. Finally, we observed that upon opening of the tunneling barrier, the ZBP height reaches $2e^2/h$. All of these observations are consistent with the observation of spatially separated MZMs in a short Majorana nanowire device. At present, a scenario involving topologically trivial zero-energy states due to a smooth electrostatic tunnel barrier potential profile is an unlikely explanation of our observations, in particular due to the strong stability to the tunnel gate potential. Although our observations do not point at the formation of topologically trivial states in the tunneling region of the nanowire, at this point we cannot fully exclude the formation of topologically trivial states underneath the superconductor, which could be induced through interband interaction when many orbital subbands are occupied in the superconducting region [28, 40] or interaction with disorder induced impurity levels [40, 41]. The spatial distribution of such states throughout the superconducting nanowire and the resulting consequences for nonlocal detection techniques is an interesting direction for future studies.

We note that although we have found nonlocal gating effects in two devices, many other short devices showed a complete insensitivity to the nonlocal gate, which we speculate could be related to disorder in the chemical potential in the nanowire in those devices, for example due to a spatially inhomogeneous strain induced when the aluminium covering the nanowire consists of multiple grains with different crystallographic orientations. Experiments involving multiple tunnel probes along the nanowire could shed more light on possible chemical potential disorder. The next crucial step is to test if the nonlocal character is maintained in long devices, where the overlap of the MZMs can be minimized to obtain the complete topological protection required to build topological quantum bits, which can be achieved through the observation of correlated ZBPs on both ends of the nanowire device, concurring with the observation of the closing and reopening of the induced superconducting gap [23, 42].

CONTRIBUTIONS TO THE PROJECT

The InSb nanowires were grown by Sasa Gazibegovic, Roy op het Veld, and Diana Car, under the supervision of Erik Bakkers at Eindhoven University of Technology. The aluminium superconductor was grown on the nanowires by Jay Logan, Mihir Pendharkar and Joon Sue Lee, under the supervision of Chris Palmstrøm at the University of California, Santa Barbara. The nanowire devices were fabricated and the measurements were performed and analyzed by **Jouri Bommer** in collaboration with Hao Zhang, Michiel de Moor, and Di Xu. The project was supervised by Leo Kouwenhoven.

DATA AVAILABILITY

The measurement data, data processing scripts, and analysis scripts that create the figures in this chapter are available at Ref. [43].

7.S. SUPPLEMENTAL MATERIAL

7.S.1. DETERMINATION OF THE DEVICE DIFFERENTIAL CONDUCTANCE

We perform measurements of the differential conductance by applying a small amplitude AC bias voltage of typically ~ 5 µV at 83.17 Hz superimposed on a DC bias voltage, while measuring the AC current of the circuit with a lock-in amplifier and the DC current with a Keithley multimeter. The nanowire device, which is loaded in a dilution refrigerator with an estimated electron temperature of ~ 50 mK, is connected to the room temperature measurement equipment through several stages of lowpass filters. Determination of the exact conductance of the device therefore requires the subtraction of the filter resistances and the input and output impedances of the measurement equipment. The total subtracted resistance was independently measured to be 17.023 ± 0.074 kΩ. In addition, we need to correct for the limited bandwidth of the current amplifier and the filter capacitances, which effectively induces a frequency dependent circuit impedance [44]. The details of the calibration procedure used are discussed in length in section 6.S.1 of the previous chapter. We note that the validity of the calibration procedure has been verified through independent measurements using the same setup on samples of known resistance.

Propagation of the uncertainty in the circuit resistance and the recalibration procedure, as is also discussed in section 6.S.1 of the previous chapter, yields the uncertainty ranges shown in Fig. 7.4d,f.

7.S.2. EXTRACTION OF TUNNEL COUPLING BETWEEN DOT AND MZM FROM LEVEL REPULSION SPECTRUM

The coupling of a quantum dot level to a fermionic mode in the nanowire, which can formally always be considered as a pair of (overlapping) MZMs, leads to level repulsion of the energy levels of the dot and nanowire states. The shape of the anticrossing spectrum contains information on the coupling strength between the dot and the MZMs, which has been proposed as an estimator of the wavefunction overlap of the MZMs [17, 32, 33]. To analyze the shape of the spectrum, we follow the effective model of Prada *et al.* [31], which consists of a single spinful quantum dot level at energy ϵ_0, with a charging energy U and Zeeman spin-splitting energy E_Z and two possibly overlapping MZMs characterized by a mutual coupling strength (energy splitting) δ. The dot is coupled to the leftmost MZM by a tunnel coupling t_L, and to the rightmost MZM by a tunnel coupling t_R. The spin structure of the MZMs is incorporated in the spin canting angles θ_L and θ_R for the left and the right MZM respectively. The Hamiltonian, with the creation operator $d_\sigma^\dagger$ for the dot level with spin σ and Majorana operators γ_i for the nanowire state, for the system is:

$$H = \left(d_\uparrow^\dagger, d_\downarrow^\dagger, d_\uparrow, d_\downarrow, \gamma_L, \gamma_R\right) \check{H} \left(d_\uparrow, d_\downarrow, d_\uparrow^\dagger, d_\downarrow^\dagger, \gamma_L, \gamma_R\right)^T$$

$$\check{H} = \begin{bmatrix} \epsilon_0 + U + E_Z/2 & 0 & 0 & 0 & 2t_\mathrm{L}\sin\left(\frac{\theta_\mathrm{L}}{2}\right) & -2i\,t_\mathrm{R}\sin\left(\frac{\theta_\mathrm{R}}{2}\right) \\ 0 & \epsilon_0 - E_Z/2 & 0 & 0 & -2t_\mathrm{L}\cos\left(\frac{\theta_\mathrm{L}}{2}\right) & -2i\,t_\mathrm{R}\cos\left(\frac{\theta_\mathrm{R}}{2}\right) \\ 0 & 0 & -\epsilon_0 - U - E_Z/2 & 0 & -2t_\mathrm{L}\sin\left(\frac{\theta_\mathrm{L}}{2}\right) & -2i\,t_\mathrm{R}\sin\left(\frac{\theta_\mathrm{R}}{2}\right) \\ 0 & 0 & 0 & -\epsilon_0 + E_Z/2 & 2t_\mathrm{L}\cos\left(\frac{\theta_\mathrm{L}}{2}\right) & -2i\,t_\mathrm{R}\cos\left(\frac{\theta_\mathrm{R}}{2}\right) \\ 2t_\mathrm{L}\sin\left(\frac{\theta_\mathrm{L}}{2}\right) & -2t_\mathrm{L}\cos\left(\frac{\theta_\mathrm{L}}{2}\right) & -2t_\mathrm{L}\sin\left(\frac{\theta_\mathrm{L}}{2}\right) & 2t_\mathrm{L}\cos\left(\frac{\theta_\mathrm{L}}{2}\right) & 0 & i\delta \\ 2i\,t_\mathrm{R}\sin\left(\frac{\theta_\mathrm{R}}{2}\right) & 2i\,t_\mathrm{R}\cos\left(\frac{\theta_\mathrm{R}}{2}\right) & 2i\,t_\mathrm{R}\sin\left(\frac{\theta_\mathrm{R}}{2}\right) & 2i\,t_\mathrm{R}\cos\left(\frac{\theta_\mathrm{R}}{2}\right) & -i\delta & 0 \end{bmatrix} \tag{7.S1}$$

The quantum dot in this model is in the normal state, while we observe loop shaped resonances in the experiment, indicating proximity induced superconductivity in the dot. We account for this by extending the model of Prada *et al.* [31] by including a coupling to the aluminium superconductor implemented as a self-energy renormalization Σ parameterized by a tunneling rate to the superconductor Γ and the superconducting gap Δ of the superconducting aluminium. We account for closing of the aluminium gap in a magnetic field B with a critical field B_c, by using $\Delta = \Delta_0\left(1 - B^2/B_c^2\right)$ [45], where Δ_0 is the superconducting gap at zero magnetic field.

$$\Sigma(\omega) = \begin{bmatrix} -\frac{\Gamma\omega}{\sqrt{\Delta^2-\omega^2}} & 0 & 0 & -\frac{\Delta\Gamma}{\sqrt{\Delta^2-\omega^2}} & 0 & 0 \\ 0 & -\frac{\Gamma\omega}{\sqrt{\Delta^2-\omega^2}} & \frac{\Delta\Gamma}{\sqrt{\Delta^2-\omega^2}} & 0 & 0 & 0 \\ 0 & \frac{\Delta\Gamma}{\sqrt{\Delta^2-\omega^2}} & -\frac{\Gamma\omega}{\sqrt{\Delta^2-\omega^2}} & 0 & 0 & 0 \\ -\frac{\Delta\Gamma}{\sqrt{\Delta^2-\omega^2}} & 0 & 0 & -\frac{\Gamma\omega}{\sqrt{\Delta^2-\omega^2}} & 0 & 0 \\ 0 & 0 & 0 & 0 & 0 & 0 \\ 0 & 0 & 0 & 0 & 0 & 0 \end{bmatrix} \tag{7.S2}$$

We obtain the energy spectrum from the Green's function $G(\omega)^{-1} = \omega - \check{H} - \Sigma(\omega)$ by solving $\det\left(G(\omega)^{-1}\right) = 0$ numerically.

Fit parameters for Fig. 7.4

Before fitting the level repulsion spectrum in Fig. 7.4c, we first determine the parameters that characterize the dot ABS from its dependence on V_{TG} at various magnetic fields, as shown in Fig. 7.S1. We model the ABS using eqs. 7.S1 and 7.S2, but without the presence of the MZMs. Δ is determined from the zero-field energy gap, and Γ and U together determine how far down the ABS comes in energy at zero magnetic field. The critical magnetic field of the aluminium film B_c is taken to correspond with the closing of the superconducting gap found in the magnetic field dependence in e.g. Fig. 7.2a. The Zeeman field is given by $E_Z = g\mu_B B$, where μ_B is the Bohr magneton and where the g-factor is determined from the magnetic field dependence of the ABS spectrum. Finally, we extract the conversion between energy and gate voltage $\epsilon_0 = C(V_{\mathrm{TG}} - V_0)$ from the ABS position and width. The complete list of ABS parameters is:

Table 7.S1: Dot ABS parameters for Fig. 7.4e.

Δ (meV)	U (meV)	Γ (meV)	B_c (T)	g	V_0 (mV)	C (eV/V)
0.23	0.05	0.8	1.2	41	-151.5	0.208

We then use these ABS parameters to perform a least-squares fit of the complete model to extract the interaction strength of lowest energy state with the ABS. The value of δ is extracted from the energy splitting away from resonance and kept fixed. The resulting level repulsion parameters are:

Table 7.S2: Dot-MZM coupling parameters for Fig. 7.4e.

δ (µeV)	t_{L} (µeV)	t_{R} (µeV)	θ_{L}	θ_{R}	$\sqrt{t_{\mathrm{R}}/t_{\mathrm{L}}}$
13	24.3	6.59	137°	270°	0.52

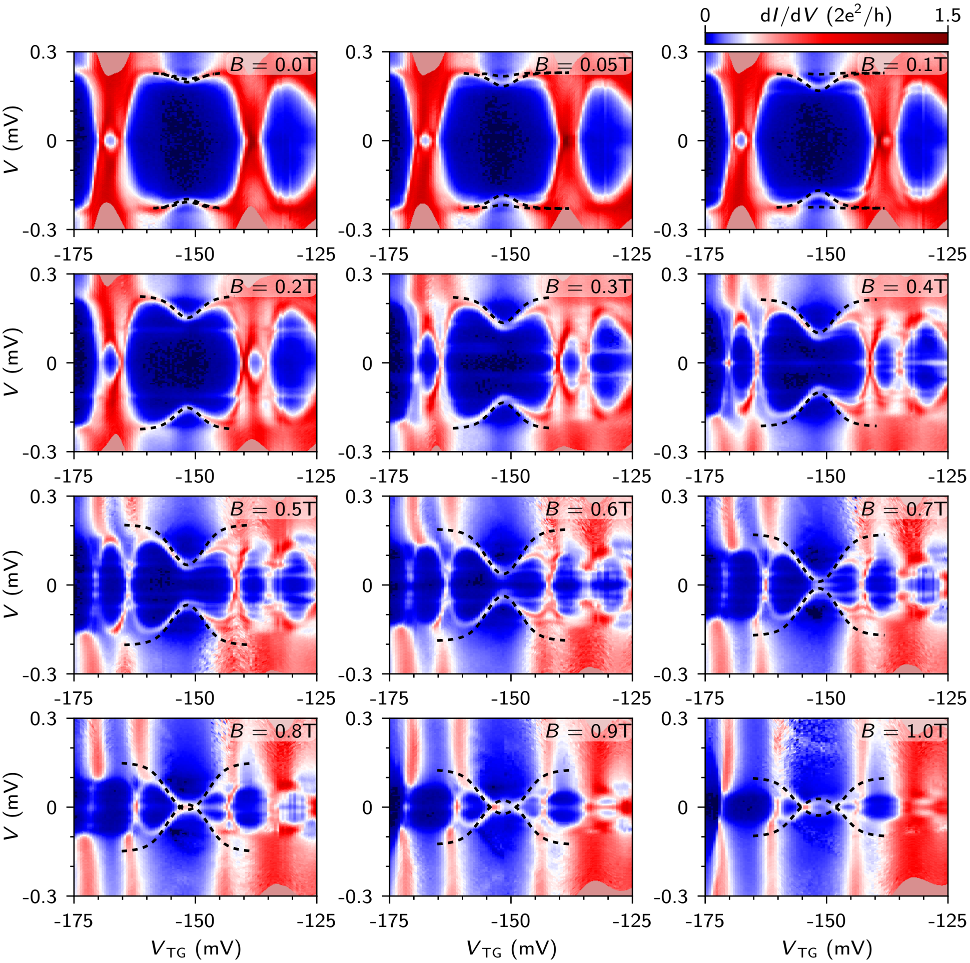

Figure 7.S1: Extraction of the dot ABS parameters in Table 7.S1. The colormap shows the spectrum of the dot ABS upon variation of V_{TG} at increasing magnetic fields. The black dotted lines show the ABS spectrum obtained from the model. We note that we observe some small deviations between the model and the data since we do not take interaction with subgap states underneath the super gate into account here. $V_{SG} = 22\,\text{mV}$, $V_{NL} = 0\,\text{V}$ in all panels.

Fit parameters for Fig. 7.5d,e

In the gate regime of Fig. 7.5, where we observe the local ZBP, we observe two dot ABSs right after each other. We account for the two dot states simultaneously by adding an additional dot state in the Hamiltonian H and self energy Σ using two sets of independent parameters for the dots. We determine the parameters characterizing the two dot ABSs from the spectrum at a magnetic field of 0 T, 0.1 T and 0.2 T (see Fig. 7.S2), resulting in:

Table 7.S3: Dot ABS parameters for Fig. 7.5d,e.

	Δ (meV)	B_c (T)	U (meV)	Γ (meV)	g	V_0 (mV)	C (eV/V)
Dot 1	0.23	1.0	0	0.05	31	-157	0.0625
Dot 2	0.23	1.0	0	0.05	27	-145.3	0.0469

In the fit of the anticrossing in Fig. 7.5d,e, we allow for different tunneling strengths between each dot state and the MZMs. We take the spin canting angles are equal for both dot-MZM crossings, as those are a property of the MZMs and not expected to depend on V_{TG}. The parameters stated in the table below are extracted using the expressions for the two lowest energy levels on resonance from Prada *et al.* [31], instead of fitting the complete spectrum. We then use the extracted parameters in the complete model described above to obtain the fits in Fig. 7.5d,e.

Table 7.S4: Dot-MZM coupling parameters for Fig. 7.5d,e.

	δ (μeV)	t_{L} (μeV)	t_{R} (μeV)	θ_{L}	θ_{R}	$\sqrt{t_{\mathrm{R}}/t_{\mathrm{L}}}$
Dot 1	3	9.81	8.27	−76.9°	70.3°	0.9
Dot 2	3	7.96	5.57	−76.9°	70.3°	0.84

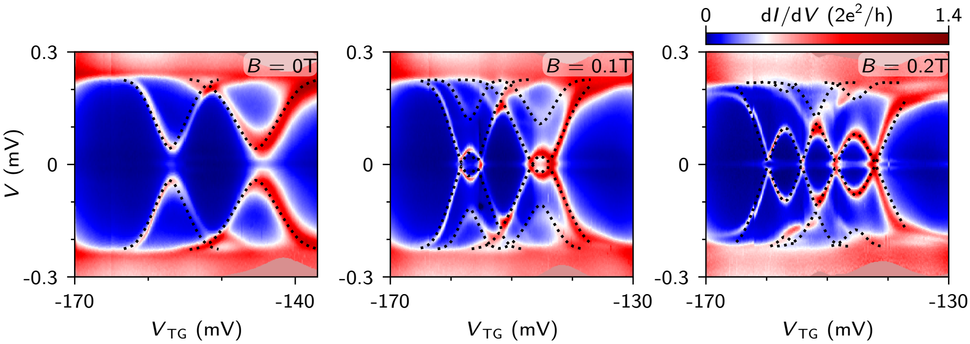

Figure 7.S2: Extraction of the dot ABS parameters in Table 7.S3. The colormap shows the spectrum of the dot ABS upon variation of V_{TG} at increasing magnetic fields. The black dotted lines correspond to the ABS spectrum obtained from the model for the two dot states, without coupling to the states underneath the super gate. At $B = 0$T the black lines appear slightly shifted, which is likely due to gate hysteresis, which could be accounted for by a slight shift of V_0. At each magnetic field V_{SG} is fine-tuned to the zero crossing of the same trivial ABS underneath the super gate ($V_{\mathrm{SG}} = -220, -218, -221$mV for $B = 0, 0.1, 0.2$T), causing a faint ZBP. The back gate voltage is set to 0 V.

7.S.3. SUPPLEMENTAL FIGURES FOR MAIN TEXT DEVICE

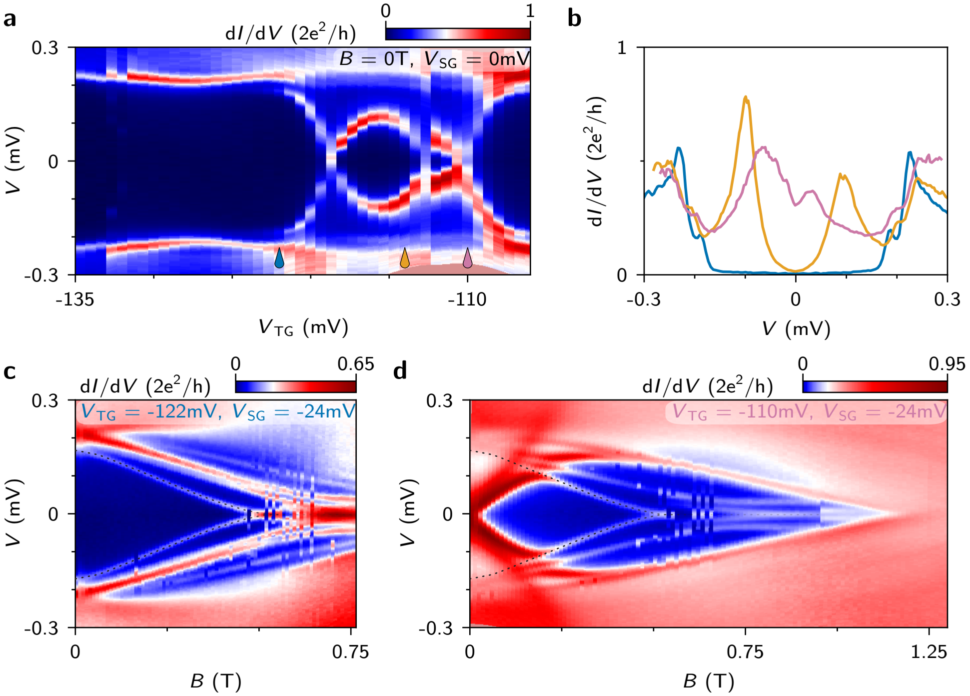

Figure 7.S3: Dot ABS and its appearance in magnetic field sweeps. **(a)** Sweeping V_{TG} at zero magnetic field shows the appearance of a loop state, as expected for an ABS in a quantum dot [36–38]. Between the two zero energy crossings, the dot is in the doublet state, where the ABS moves to higher energies as the magnetic field is increased. Outside of this regime the ABSs spin-split as a magnetic field is applied, with one of the states coming down towards zero energy, which obscures observation of the states underneath the super gate. To optimize the finite field visibility of states underneath the super gate we therefore set $V_{TG} = -114\,\text{mV}$ (orange droplet) in Fig. 7.2a. **(b)** Vertical linecuts of **a** at V_{TG} indicated by the colored droplets. At $V_{TG} = -122\,\text{mV}$ (blue linetrace, used in **c**) a well-defined, hard gap is visible, with the dot ABS just below the gap edge. Within the doublet region, the dot ABS induces prominent subgap peaks (orange linetrace at $V_{TG} = -114\,\text{mV}$ and pink linetrace at $V_{TG} = -110\,\text{mV}$, used in **d**). **(c)** Magnetic field sweep at $V_{TG} = -122\,\text{mV}$ (blue droplet in **a**) with the dot ABS in the singlet state and close to the superconducting gap edge at zero field. As B increases, two states come down towards zero energy, with the lowest energy and lower magnitude state corresponding to a state underneath the super gate (highlighted by the black dotted line), and with the higher magnitude peak corresponding to the spin-split dot ABS. Around $B = 0.7\,\text{T}$ the dot ABS comes down to zero energy. Due to the broad peak of the dot ABS the states underneath the super gate become difficult to track. **(d)** Magnetic field sweep with the dot ABS in the doublet state at $V_{TG} = -122\,\text{mV}$, corresponding to the pink droplet in **a**, and similar to Fig. 7.2a, but with $V_{SG} = -24\,\text{mV}$. The dot ABS only appears near zero magnetic field and quickly splits away, so that states underneath the super gate can be observed without hindrance for $B > 0.2\,\text{T}$. The black dotted line is the same as in **c**, showing that the evolution of the lowest energy state is unaffected by the change in V_{TG}, reflecting that the state originates underneath the super gate. The second lowest energy state comes down in energy up to $B = 0.7\,\text{T}$, after which it kinks and increases in energy, which could either be an indication of closing and reopening of the gap in a finite size nanowire [24], or interaction of states in the nanowire [28]. We note that the discontinuities for B from 0.5 T to 0.7 T, are likely caused by small instabilities of the electrostatic environment at the super gate induced by the changing magnetic field.

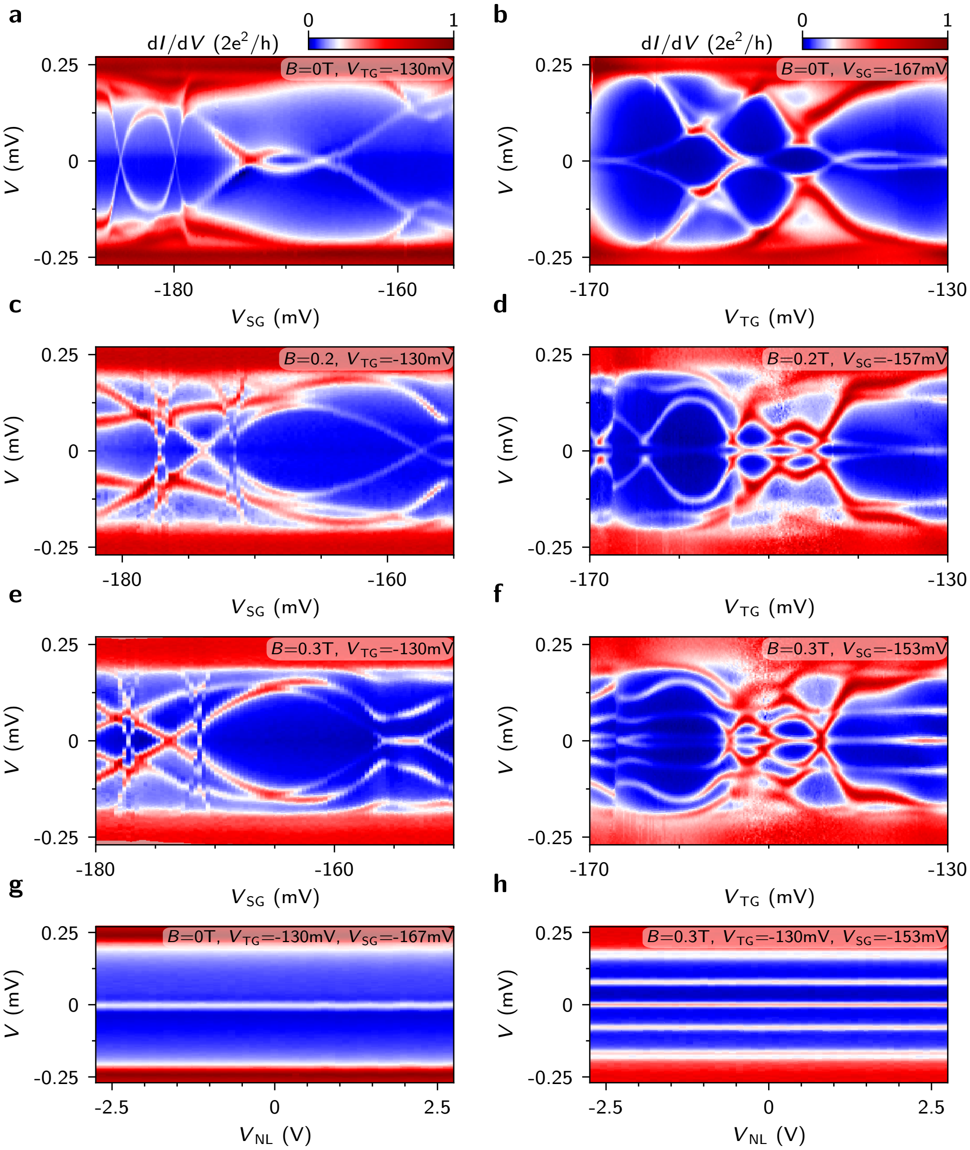

Figure 7.S4: Additional dataset trivial ABSs underneath the super gate. Analogous to Fig. 7.5, we observe ABSs that disperse quickly with V_{SG} (**a**,**c**,**e** at $B = 0\,\mathrm{T}$, $0.2\,\mathrm{T}$, $0.3\,\mathrm{T}$), which cross zero-energy, allowing for fine-tuned ZBPs. Away from the dot resonances, these ZBPs are insensitive to V_{TG}, while they strongly split on resonance with dot states (**b**,**d**,**f**), characteristic of a highly local state. Correspondingly, these fine-tuned ZBPs are completely insensitive to the nonlocal gate (see **g** for $B = 0\,\mathrm{T}$ and **h** for $B = 0.3\,\mathrm{T}$). Interestingly, level repulsion between states underneath the super gate at $B = 0.3\,\mathrm{T}$ and $V_{\mathrm{SG}} = -153\,\mathrm{mV}$ induces a ZBP over an extended range (see **e**). However, the nonlocal gate insensitivity is maintained (see **h**), starkly contrasting the nonlocal gate induced oscillatory peak splitting we discuss in the main text. The back gate is set to 0 V in all panels.

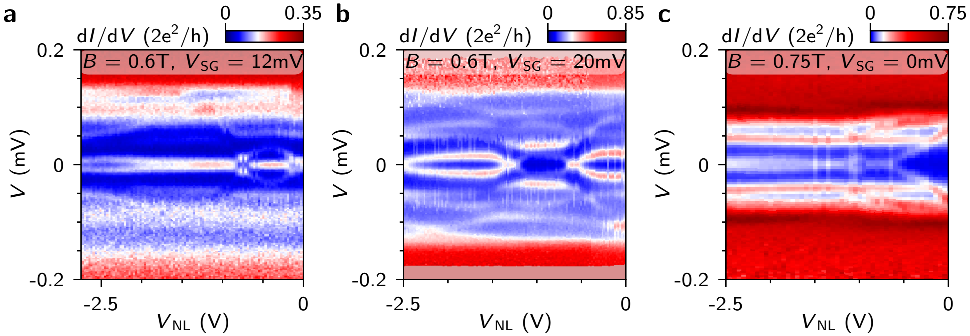

Figure 7.S5: Additional nonlocal gate dependences. (**a,b**) Nonlocal gate dependence of the ZBP in Fig. 7.4 showing peak splitting modulation at $V_{SG} = 12\,\text{mV}$, $V_{SG} = 20\,\text{mV}$ and $V_{TG} = -162\,\text{mV}$, $V_{TG} = -137\,\text{mV}$ in **a**,**b** respectively. **(c)** At $B = 0.75\,\text{T}$ we observe two small peak splitting oscillations, after which the ZBP fully splits towards the gap edge. $V_{TG} = -150\,\text{mV}$.

7.S.4. NONLOCAL DEPENDENCE IN SECOND DEVICE

In this section we demonstrate the nonlocal gate dependencies of zero-energy states that originate underneath the super gate in a second device, labeled device B. Compared to device A, this second device has a thinner aluminium shell of $\sim 5\,\text{nm}$, significantly increasing the magnetic field resilience to above 2 T. The layout of device B is very similar to device A with a super gate width of 500 nm. In addition to the gates available in device A, device B has a second tunnel gate, which covers the nanowire region in between the tunnel gate and the super gate, and is separated by an additional 30 nm thick layer of sputtered silicon nitride dielectric (device image and schematic in Fig. 7.S6). This second tunnel gate was, however, ineffective and can be considered to floating in the experiment. The back gate voltage was kept grounded for all measurements in device B.

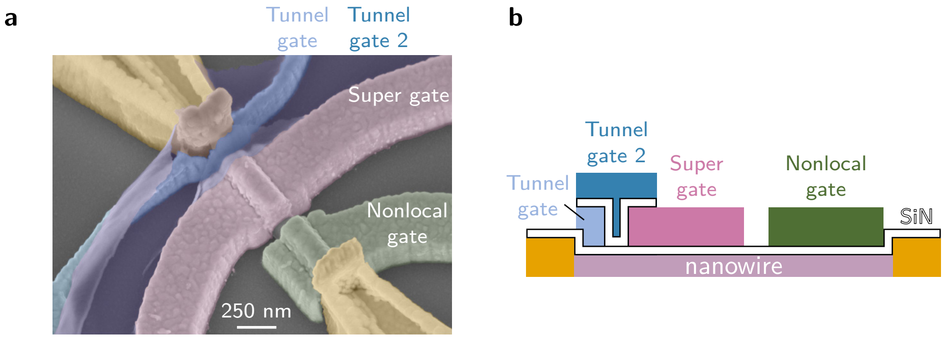

Figure 7.S6: Overview of device B. (a) False color tilted view scanning electron micrograph of device B. **(b)** Side view schematic of device B, cut through the center of the nanowire (not to scale). The layout of the wrap gates is similar to the device discussed in the main text, with the exception of the presence of a second tunnel gate, which overlaps the gap between the tunnel gate and the super gate.

Local state underneath the super gate

We first discuss a local state likely located underneath the super gate, analogous to the trivial ABS studied in Fig. 7.5. Fig. 7.S7a shows the magnetic field dependence for an increasing V_{SG} in the four panels. In all panels, a state comes down from the gap edge towards zero energy, as B increases. Depending on the super gate voltage, the low energy states repel (left panel), form a ZBP over an extended magnetic field range (middle panels), or cross zero-energy (right panel). To investigate the stability of the ZBP with respect to the gate voltages, we first set V_{SG} to 150 mV (third panel) at $B = 1.5$ T and vary V_{TG} in Fig. 7.S7b. Over the complete V_{TG} range, the ZBP remains close to zero energy while the tunnel barrier height varies significantly, indicating a weak presence of the zero-energy state in the tunneling barrier. The occasional small peak splittings may be induced by interaction with the dot states in the tunneling region. Next, varying V_{SG} in Fig. 7.S7c instead, we find that the ZBP that appears near a super gate voltage of 150 mV is the result of a level crossing as the chemical potential in the nanowire is varied, analogous to the trivial ABS observed in Fig. 7.5 and Fig. 7.S4. Although the magnetic field and tunnel gate dependence are in line with the expected characteristics of a nonlocal MZM, the sharp level crossing behavior as a function of V_{SG} instead, is not expected in a topological Majorana scenario. The localized character of this state is underpinned by the lack of nonlocal gate dependence, as shown at two different V_{SG} values in Fig. 7.S7d,e, corresponding respectively to the ZBP in the second panel and the split peak in the right panel of 7.S7a. Although some higher energy states do respond to the nonlocal gate, the position of the lowest energy state is unaffected.

Nonlocal state underneath the super gate

At a lower magnetic field and an increased V_{TG}, the states that do depend on the nonlocal gate become more clearly visible. In the B dependence shown in Fig. 7.S8a, we observe low amplitude peaks appearing at a magnetic field of ∼ 0.5 T, which oscillate around zero-energy before forming a ZBP that remains visible up to ∼ 1 T. Note that the higher amplitude state that approaches zero-energy at a higher magnetic field of 1.3 T is the state we discussed in Fig. 7.S7. Setting the magnetic field to 0.85 T, where we find a zero-energy state, and varying V_{TG} in Fig. 7.S8b, we find no evidence of peak splitting behavior, hinting at a lack of sensitivity of the energy splitting to the tunnel-barrier details, although the ZBP is only visible (sufficiently high) over short gate voltage ranges. When varying V_{SG} in Fig. 7.S8c we observe that the ZBP remains pinned near zero-energy over a small gate voltage range around 132 mV and splits at significantly higher and lower V_{SG}values. In the dependence on the nonlocal gate, we observe a variation in the peak splitting of the zero-energy states, similar to the behavior observed in device A, indicating a spatial extension of the zero-energy state towards the nonlocal gate.

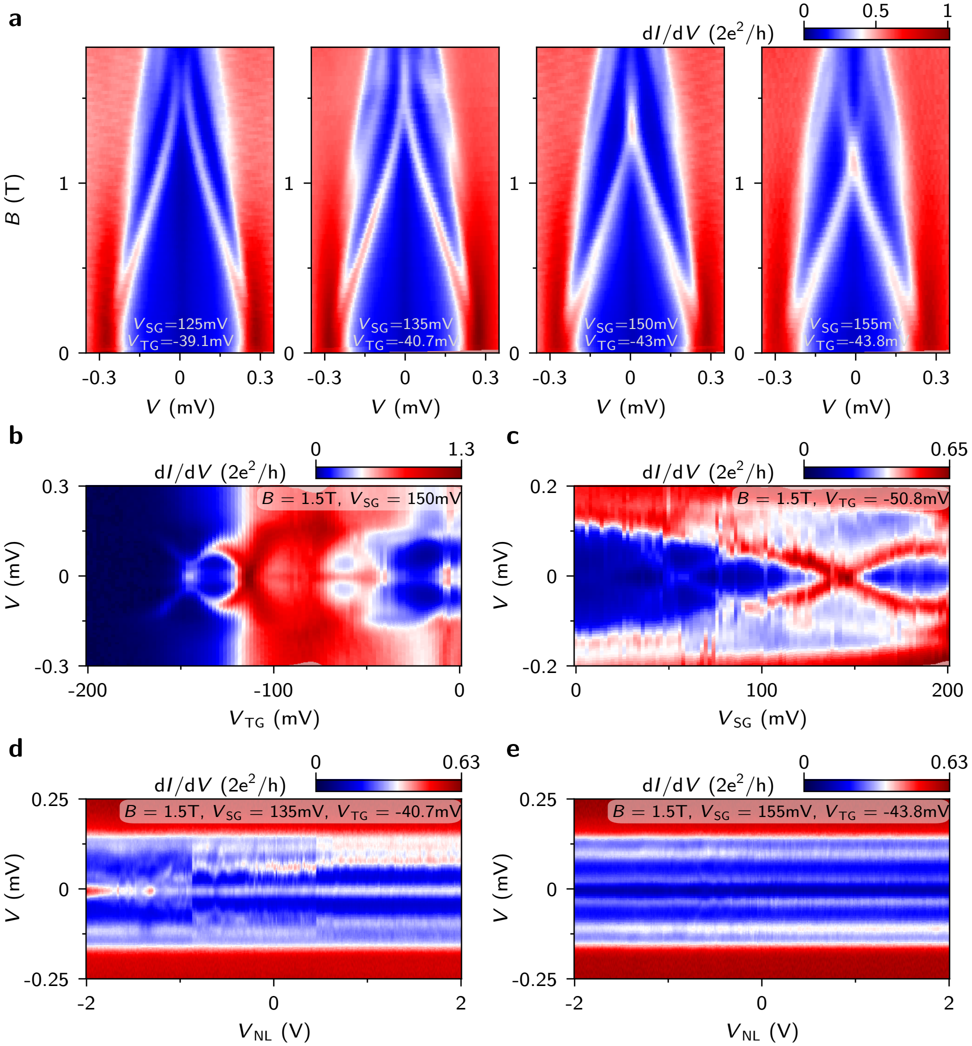

Figure 7.S7: Local zero-energy state underneath the super gate in device B. (a) Magnetic field dependence of the zero-energy state at an increasing super gate voltage. A ZBP stable in magnetic field appears over a small range of super gate voltage. The tunnel gate voltage is slightly adjusted to keep the above-gap conductance constant. $V_{\mathrm{NL}} = 2\,\mathrm{V}$ in the first and third panel and $0\,\mathrm{V}$ in the second and fourth panel (see also **d,e**). **(b)** The ZBP in the third panel of **a** remains close to zero-energy as the tunnel gate voltage is varied. $V_{\mathrm{NL}} = 0\,\mathrm{V}$. **(c)** The ZBP appears as a crossing upon variation of the super gate voltage. $V_{\mathrm{NL}} = 0\,\mathrm{V}$. **(d,e)** At $B = 1.5\,\mathrm{T}$, the ZBP in the second panel of **a** and the split peak in the last panel of **a** remain at the same energy over large ranges of the nonlocal gate voltage. The discontinuities in **d** are likely due to a stochastic change in the electrostatic environment of the nanowire, which does not affect the zero-energy state, nor the above-gap conductance.

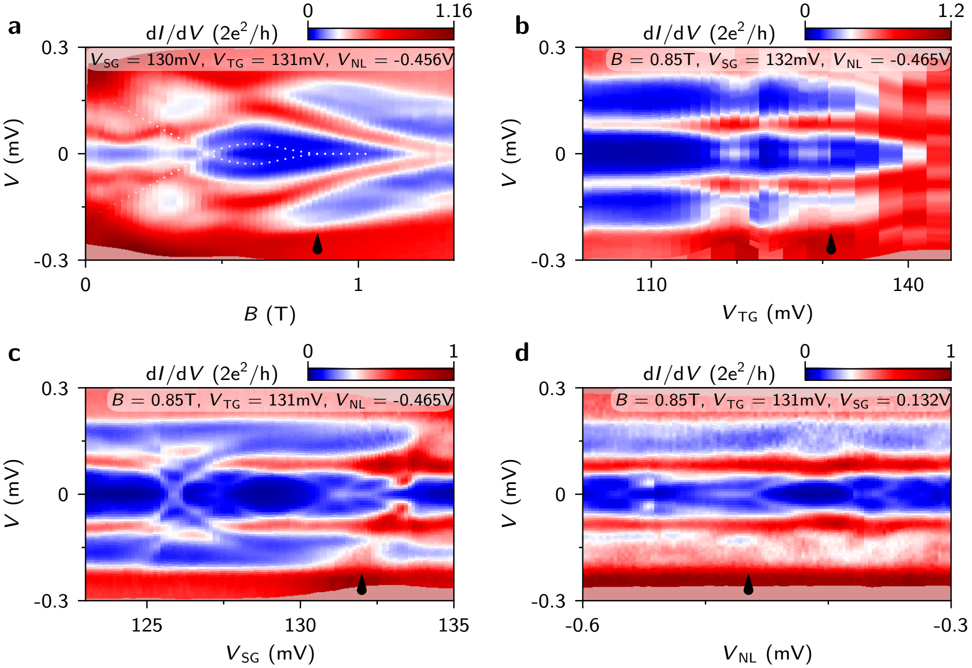

Figure 7.S8: Nonlocal state underneath the super gate in device B. **(a)** Magnetic field dependence of the zero-energy state. The dotted lines indicate the energy of the low energy state under study. The black droplet indicates the magnetic field used in the following datasets. **(b)** Upon variation of the tunnel gate voltage, the zero-energy state shows no signs of peak splitting. The black droplet indicates the tunnel gate voltage used in the other panels. **(c)** The dependence on the super gate voltage shows that the low energy state tend to vary around zero-energy, with a gate voltage window around 132 mV over which the zero-energy states remains at zero-energy. The black droplet indicates the super gate voltage used in panels **b,d**. Note that the ZBP in **a** appears at a slightly lower V_{SG}, which is likely the result of a small hysteresis in the gate response. **(d)** The dependence on the nonlocal gate voltage shows that the energy splitting oscillates around zero-energy, with regions where the state remains fixed at zero-energy. The black droplet indicates the nonlocal gate voltage used in the other panels.

REFERENCES

[1] N. Read and D. Green, *Paired states of fermions in two dimensions with breaking of parity and time-reversal symmetries and the fractional quantum Hall effect*, Phys. Rev. B **61**, 10267 (2000).

[2] A. Y. Kitaev, *Unpaired Majorana fermions in quantum wires*, Phys. Usp. **44**, 131 (2001).

[3] L. Fu and C. L. Kane, *Superconducting proximity effect and Majorana fermions at the surface of a topological insulator*, Phys. Rev. Lett. **100**, 096407 (2008).

[4] R. M. Lutchyn, J. D. Sau, and S. Das Sarma, *Majorana fermions and a topological phase transition in semiconductor-superconductor heterostructures*, Phys. Rev. Lett. **105**, 077001 (2010).

[5] Y. Oreg, G. Refael, and F. von Oppen, *Helical liquids and Majorana bound states in quantum wires*, Phys. Rev. Lett. **105**, 177002 (2010).

[6] V. Mourik, K. Zuo, S. M. Frolov, S. R. Plissard, E. P. A. M. Bakkers, and L. P. Kouwenhoven, *Signatures of Majorana fermions in hybrid superconductor-semiconductor nanowire devices*, Science **336**, 1003 (2012).

[7] M. T. Deng, C. L. Yu, G. Y. Huang, M. Larsson, P. Caroff, and H. Q. Xu, *Anomalous zero-bias conductance peak in a Nb–InSb nanowire–Nb hybrid device*, Nano Lett. **12**, 6414 (2012).

[8] A. Das, Y. Ronen, Y. Most, Y. Oreg, M. Heiblum, and H. Shtrikman, *Zero-bias peaks and splitting in an Al–InAs nanowire topological superconductor as a signature of Majorana fermions*, Nat. Phys. **8**, 887 (2012).

[9] Ö. Gül, H. Zhang, J. D. S. Bommer, M. W. A. de Moor, D. Car, S. R. Plissard, E. Bakkers, A. Geresdi, K. Watanabe, T. Taniguchi, and L. P. Kouwenhoven, *Ballistic Majorana nanowire devices*, Nat. Nanotech. **13**, 192 (2018).

[10] M. T. Deng, S. Vaitiekėnas, E. B. Hansen, J. Danon, M. Leijnse, K. Flensberg, J. Nygård, P. Krogstrup, and C. M. Marcus, *Majorana bound state in a coupled quantum-dot hybrid-nanowire system*, Science **354**, 1557 (2016).

[11] F. Nichele, A. C. C. Drachmann, A. M. Whiticar, E. C. T. O'Farrell, H. J. Suominen, A. Fornieri, T. Wang, G. C. Gardner, C. Thomas, A. T. Hatke, P. Krogstrup, M. J. Manfra, K. Flensberg, and C. M. Marcus, *Scaling of Majorana zero-bias conductance peaks*, Phys. Rev. Lett. **119**, 136803 (2017).

[12] H. Zhang, C.-X. Liu, S. Gazibegovic, D. Xu, J. A. Logan, G. Wang, N. van Loo, J. D. S. Bommer, M. W. A. de Moor, D. Car, R. L. M. Op het Veld, P. J. van Veldhoven, S. Koelling, M. A. Verheijen, M. Pendharkar, D. J. Pennachio, B. Shojaei, J. S. Lee, C. J. Palmstrøm, E. P. A. M. Bakkers, S. D. Sarma, and L. P. Kouwenhoven, *Quantized Majorana conductance*, arXiv preprint arXiv:1710.10701 (2017).

[13] P. Krogstrup, N. L. B. Ziino, W. Chang, S. M. Albrecht, M. H. Madsen, E. Johnson, J. Nygård, C. M. Marcus, and T. S. Jespersen, *Epitaxy of semiconductor–superconductor nanowires,* Nat. Mater. **14**, 400 (2015).

[14] W. Chang, S. M. Albrecht, T. S. Jespersen, F. Kuemmeth, P. Krogstrup, J. Nygård, and C. M. Marcus, *Hard gap in epitaxial semiconductor-superconductor nanowires,* Nat. Nanotech. **10**, 232 (2015).

[15] H. Zhang, O. Gül, S. Conesa-Boj, M. P. Nowak, M. Wimmer, K. Zuo, V. Mourik, F. K. de Vries, J. van Veen, M. W. A. de Moor, J. D. S. Bommer, D. J. van Woerkom, D. Car, S. R. Plissard, E. P. A. M. Bakkers, M. Quintero-Pérez, M. C. Cassidy, S. Koelling, S. Goswami, K. Watanabe, T. Taniguchi, and L. P. Kouwenhoven, *Ballistic superconductivity in semiconductor nanowires,* Nat. Commun. **8**, 16025 (2017).

[16] S. Gazibegovic, D. Car, H. Zhang, S. C. Balk, J. A. Logan, M. W. A. de Moor, M. C. Cassidy, R. Schmits, D. Xu, G. Wang, P. Krogstrup, R. L. M. Op het Veld, K. Zuo, Y. Vos, J. Shen, D. Bouman, B. Shojaei, D. Pennachio, J. S. Lee, P. J. van Veldhoven, S. Koelling, M. A. Verheijen, L. P. Kouwenhoven, C. J. Palmstrøm, and E. P. A. M. Bakkers, *Epitaxy of advanced nanowire quantum devices,* Nature **548**, 434 (2017).

[17] E. Prada, P. San-Jose, and R. Aguado, *Transport spectroscopy of NS nanowire junctions with Majorana fermions,* Phys. Rev. B **86**, 180503 (2012).

[18] G. Kells, D. Meidan, and P. W. Brouwer, *Near-zero-energy end states in topologically trivial spin-orbit coupled superconducting nanowires with a smooth confinement,* Phys. Rev. B **86**, 100503 (2012).

[19] C.-X. Liu, J. D. Sau, T. D. Stanescu, and S. Das Sarma, *Andreev bound states versus Majorana bound states in quantum dot-nanowire-superconductor hybrid structures: Trivial versus topological zero-bias conductance peaks,* Phys. Rev. B **96**, 075161 (2017).

[20] A. Vuik, B. Nijholt, A. R. Akhmerov, and M. Wimmer, *Reproducing topological properties with quasi-Majorana states,* SciPost Phys. **7**, 061 (2019).

[21] C. Moore, T. D. Stanescu, and S. Tewari, *Two-terminal charge tunneling: Disentangling Majorana zero modes from partially separated Andreev bound states in semiconductor-superconductor heterostructures,* Phys. Rev. B **97**, 165302 (2018).

[22] C. Moore, C. Zeng, T. D. Stanescu, and S. Tewari, *Quantized zero-bias conductance plateau in semiconductor-superconductor heterostructures without topological Majorana zero modes,* Phys. Rev. B **98**, 155314 (2018).

[23] S. Das Sarma, J. D. Sau, and T. D. Stanescu, *Splitting of the zero-bias conductance peak as smoking gun evidence for the existence of the Majorana mode in a superconductor-semiconductor nanowire,* Phys. Rev. B **86**, 220506 (2012).

[24] R. V. Mishmash, D. Aasen, A. P. Higginbotham, and J. Alicea, *Approaching a topological phase transition in Majorana nanowires,* Phys. Rev. B **93**, 245404 (2016).

[25] O. Dmytruk and J. Klinovaja, *Suppression of the overlap between Majorana fermions by orbital magnetic effects in semiconducting-superconducting nanowires,* Phys. Rev. B **97**, 155409 (2018).

[26] F. Domínguez, J. Cayao, P. San-Jose, R. Aguado, A. L. Yeyati, and E. Prada, *Zero-energy pinning from interactions in Majorana nanowires,* npj Quantum Mater. **2**, 13 (2017).

[27] Z. Cao, H. Zhang, H.-F. Lü, W.-X. He, H.-Z. Lu, and X. C. Xie, *Decays of Majorana or Andreev oscillations induced by steplike spin-orbit coupling,* Phys. Rev. Lett. **122**, 147701 (2019).

[28] B. D. Woods, J. Chen, S. M. Frolov, and T. D. Stanescu, *Zero-energy pinning of topologically trivial bound states in multiband semiconductor-superconductor nanowires,* Phys. Rev. B **100**, 125407 (2019).

[29] H. Pan and S. Das Sarma, *Physical mechanisms for zero-bias conductance peaks in Majorana nanowires,* Phys. Rev. Research **2**, 013377 (2020).

[30] T. D. Stanescu, S. Tewari, J. D. Sau, and S. Das Sarma, *To close or not to close: The fate of the superconducting gap across the topological quantum phase transition in Majorana-carrying semiconductor nanowires,* Phys. Rev. Lett. **109**, 266402 (2012).

[31] E. Prada, R. Aguado, and P. San-Jose, *Measuring Majorana nonlocality and spin structure with a quantum dot,* Phys. Rev. B **96**, 085418 (2017).

[32] D. J. Clarke, *Experimentally accessible topological quality factor for wires with zero energy modes,* Phys. Rev. B **96**, 201109 (2017).

[33] F. Peñaranda, R. Aguado, P. San-Jose, and E. Prada, *Quantifying wave-function overlaps in inhomogeneous Majorana nanowires,* Phys. Rev. B **98**, 235406 (2018).

[34] M.-T. Deng, S. Vaitiekėnas, E. Prada, P. San-Jose, J. Nygård, P. Krogstrup, R. Aguado, and C. M. Marcus, *Nonlocality of Majorana modes in hybrid nanowires,* Phys. Rev. B **98**, 085125 (2018).

[35] K. T. Law, P. A. Lee, and T. K. Ng, *Majorana fermion induced resonant Andreev reflection,* Phys. Rev. Lett. **103**, 237001 (2009).

[36] J.-D. Pillet, C. H. L. Quay, P. Morfin, C. Bena, A. L. Yeyati, and P. Joyez, *Andreev bound states in supercurrent-carrying carbon nanotubes revealed,* Nat. Phys. **6**, 965– (2010).

[37] E. J. Lee, X. Jiang, M. Houzet, R. Aguado, C. M. Lieber, and S. De Franceschi, *Spin-resolved Andreev levels and parity crossings in hybrid superconductor–semiconductor nanostructures,* Nat. Nanotech. **9**, 79 (2014).

[38] A. Jellinggaard, K. Grove-Rasmussen, M. H. Madsen, and J. Nygård, *Tuning Yu-Shiba-Rusinov states in a quantum dot,* Phys. Rev. B **94**, 064520 (2016).

[39] D. E. Liu, E. Rossi, and R. M. Lutchyn, *Impurity-induced states in superconducting heterostructures,* Phys. Rev. B **97**, 161408 (2018).

[40] H. Pan, W. S. Cole, J. D. Sau, and S. Das Sarma, *Generic quantized zero-bias conductance peaks in superconductor-semiconductor hybrid structures,* Phys. Rev. B **101**, 024506 (2020).

[41] S. Mi, D. I. Pikulin, M. Marciani, and C. W. J. Beenakker, *X-shaped and Y-shaped Andreev resonance profiles in a superconducting quantum dot,* J. Exp. Theor. Phys **119**, 1018 (2014).

[42] T. O. Rosdahl, A. Vuik, M. Kjaergaard, and A. R. Akhmerov, *Andreev rectifier: A nonlocal conductance signature of topological phase transitions,* Phys. Rev. B **97**, 045421 (2018).

[43] J. D. S. Bommer, *Zero-energy states in Majorana nanowire devices,* Zenodo Dataset (2020).

[44] G. Wang, J. D. S. Bommer, and M. W. A. De Moor, *Notes on transport measurements using a lock-in,* https://forum.kavli.tudelft.nl/t/lock-in-measurement-common-issues-and-guidelines/85 (2020).

[45] M. Tinkham, *Introduction to Superconductivity* (Dover Publications, 2004).

8

CONCLUSIONS AND OUTLOOK

8.1. CONCLUSIONS

Chapter 3

Following optimization of the interface between InSb nanowires and a NbTiN superconductor [1], we demonstrate zero-bias peaks that remain stable upon variation of magnetic fields and gate voltages using a nanowire junction that exhibits ballistic transport. The observations of zero-bias peaks are consistent with the presence of Majorana zero-modes and the ballistic junction indicates a low degree of disorder, which excludes alternative interpretations of zero-bias peaks based on disorder and quantum dot formation in the tunneling barrier.

Chapter 4

We track the effect of magnetic fields oriented along various directions on the induced superconducting gap in InSb nanowires coupled to a NbTiN superconductor, and show a strong anisotropy in the magnetic field resilience of superconductivity. Through comparison with realistic simulations of the nanowire device, we identify that Rashba spin-orbit interaction with a strength of 0.15 eVÅ to 0.35 eVÅ protects the superconducting gap from closing, which is an effect essential for the creation of Majorana zero-modes in nanowires, as it lies at the basis of the size of the topological gap. The gap closing anisotropy also reveals the spin-orbit direction, which depends on the geometry of the superconductor and the applied voltages on the electrostatic gates.

Chapter 5

Through the electrical transport properties of InSb nanowires coupled to an epitaxial aluminium superconductor, we study the effect of electric fields induced by electrostatic gates on the coupling between the semiconductor and the superconductor. We find that the electric field affects the strength of the semiconductor-superconductor coupling, which affects the size of the induced superconducting gap, the effective g-factor, and the spin-orbit strength, all essential parameters in Majorana physics. Additionally, we observe that spin-orbit coupling of subgap states in a finite length nanowire can result in zero-bias peaks with a degree of stability to the magnetic field and the gate voltage, resembling Majorana characteristics. The improved understanding of realistic situations in hybrid semiconductor-superconductor nanowires contributes to the knowledge required to interpret Majorana experiments.

Chapter 6

In InSb nanowires coupled to an epitaxial aluminium superconductor, we find zero-bias peaks which lead to zero-bias conductance plateaus at $2e^2/h$ when the tunneling barrier strength is varied. We identify that the $2e^2/h$ plateaus, which are also expected for topological Majorana zero-modes, result from low energy states located near the tunneling barrier, based on the instability of the low energy states upon variation of the electrostatic gates near the tunneling barrier and their interaction with other states localized in the tunneling region. Through comparison with theoretical models, we verify that the presence of nearly quantized conductances plateaus can be explained by smooth electrostatic potentials that induce zero-energy states in the topologically trivial phase, which can be described as a set of local Majorana modes. Although a quantized conductance plateau cannot be considered as definitive evidence of topological Majorana zero-modes, local Majorana modes could provide a promising alternative route to non-Abelian physics and quantum bits.

Chapter 7
We investigate short InSb nanowires coupled to an epitaxial aluminium superconductor, where separate electrostatic gates allow individual control of the tunnel barrier strength, the electron density in the nanowire section after the tunnel barrier, and the electron density in a section remote from the tunnel barrier, which allows for the modulation of the energy splitting of delocalized nanowire states as a tool to study the nonlocal properties of subgap states. Through the dependence of low energy subgap states on the electrostatic gates we identify zero-energy states that originate in the nanowire section covered by the superconductor, instead of near the tunneling barrier, where topologically trivial Andreev bound states may easily form. These zero-energy states respond to the remote gate by showing an oscillatory peak splitting behavior and display a weak interaction with localized states near the tunneling barrier, both indicating a degree of a spatially nonlocal distribution, consistent with overlapping Majorana zero-modes. Additionally, for highly transparent barriers, the zero-bias conductance closely approaches $2e^2/h$. We contrast the results on this type of nonlocal state with distinctly different zero-energy states in the same device, which have a highly local nature, or originate near the tunneling barrier, which could result from disorder or spatially inhomogeneous electrostatic potentials.

8.2. OUTLOOK

8.2.1. TOPOLOGICAL MAJORANA MODES

Three terminal correlation devices
Since the first observation of signatures of Majorana zero-modes in 2012 [2], advancements in material growth and device fabrication have significantly improved nanowire devices and have addressed concerns such as the presence of a background subgap density of states (a soft gap), and low zero-bias peak heights [3–10]. So far, the state of the art experiments show consistency with an interpretation of Majorana zero-modes[5, 6, 9–11] and can exclude several non-Majorana scenarios for the presence of zero-energy states[12–14]. However, the majority of the experiments to date have used *local* measurement techniques, such as the tunneling spectroscopy often used throughout this thesis. The characteristic properties of topological Majorana zero-modes, on the other hand, stem from their *nonlocal* behavior: two correlated Majorana modes appear at the edge of a topological superconductor, which exhibits an inverted (topologically non-trivial) band gap. The next experimental steps in this field should therefore focus on nonlocal detection techniques. The prime experimental setup for this, contains tunnel probes on both ends of a nanowire covered by a grounded superconductor, as illustrated in 8.1a. The simplest signature in such a setup is the simultaneous observation of zero-bias peaks on both ends of the device, although this cannot exclude the accidental presence of two topologically trivial zero-energy states on both ends of the

nanowire. A stronger signature could be observed in shorter nanowires, where overlap of the Majorana zero-modes at the two ends induces an energy splitting which is oscillatory upon variation of system parameters such as the Zeeman energy and the chemical potential in the nanowire [15]. Crucially, since the two Majorana modes together form a single fermionic state, this energy splitting must be equal on both sides of the device, with an expected growing amplitude of the energy splitting oscillations for an increasing magnetic field. Furthermore, the correlation setup allows for the detection of the bulk gap closing through the nonlocal conductance [16]. Because the correlation setup consists of three terminals, a nonlocal conductance is possible, where the application of a bias voltage at one lead can induce a current in the other lead. In long nanowires (of length exceeding the coherence length in the proximitized nanowire) a nonzero nonlocal conductance emerges at energies in between the induced superconducting gap in the nanowire and the bulk superconducting gap of the superconducting contact, because there is a finite quasiparticle density of states, which allows for the transmission of an incoming electron either as an electron (direct transfer) or as a hole (crossed Andreev reflection). At energies below the induced gap, the nanowire spectrum is gapped, which suppresses any nonlocal conductance response. The nonlocal conductance thus provides a measure of the induced superconducting gap. Since the emergence of Majorana modes at the ends of a topological phase is characterized by a closing and reopening of the induced superconducting gap, the topological phase transition can be detected through the nonlocal conductance. Since zero-bias peaks which have a topologically trivial origin do not coincide with a bulk gap closing, the nonlocal conductance can play a crucial role in determining the topological nature of a zero-energy state. The combined observation of gap inversion through the nonlocal conductance with the emergence of correlated zero-bias peaks at both ends in the local conductance (see Fig. 8.1b), would therefore provide strong evidence of the presence of topological Majorana zero-modes.

The relevance of such correlation measurements have not gone unnoticed and are currently being undertaken [17, 18]. Most recently, this has led to the observation of a gap closing in the nonlocal conductance and zero-bias peaks on both sides of the device in the local conductance, although the gap appears to not stay open over the full extent of the zero-bias peaks, which is not expected for a clean topological superconductor [19]. In similar experiments [17, 18], and in the experimental data in chapter 7 a large number of discrete subgap states are typically found. These states could spatially extend throughout the nanowire, which is a possible explanation for a finite nonlocal conductance near zero-bias. The origin of the large number of subgap states has not been clearly established yet, while an improved understanding of these subgap states is crucial for further development of Majorana nanowire devices and experiments. A likely factor in the presence of the large number of subgap states is some kind of disorder along the nanowire [20, 21] or interaction of states stemming from different subbands when a large number of orbital subbands is occupied in the nanowire [21, 22]. Below, we will first discuss how the fabrication of nanowire devices could be optimized for correlation measurements and how their successful implementation can be detected in transport experiments. Afterwards, we will discuss the possible candidates for disorder in more detail and address strategies of how the origin of possible disorder can be studied to guide further material improvements.

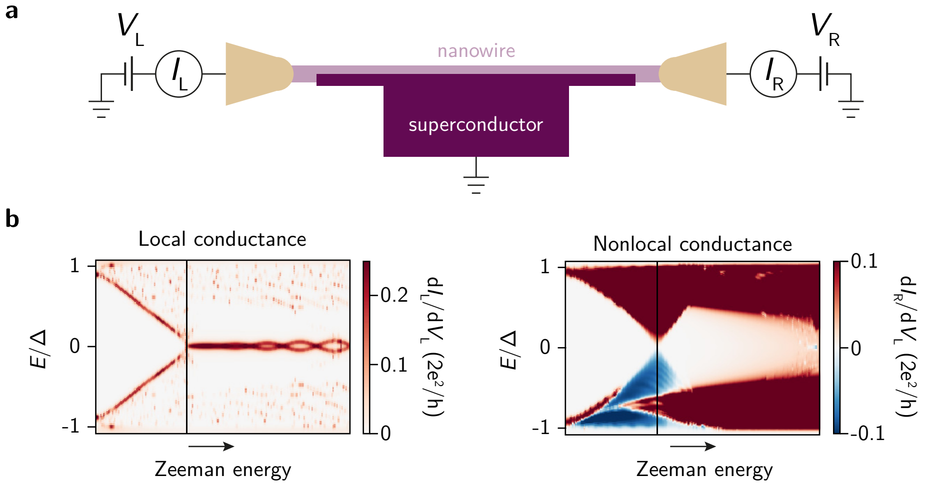

Figure 8.1: Measurement setup to detect correlated Majorana zero modes. (a) Illustration of the experimental setup. Leads connect to the nanowire on both sides. On each side a bias voltage can be applied and the current through the lead is measured. The nanowire is covered by a grounded superconductor. Due to the presence of multiple leads, a nonlocal conductance can arise. **(b)** Simulation of the local (left) and the nonlocal conductance (right) behavior expected for Majorana zero-modes as the Zeeman energy is increased from zero. At the critical Zeeman field where the nanowire transitions into the topological phase, indicated by the vertical black lines, a zero-bias peak emerges in the local conductance. Due to overlap of the Majorana modes, oscillations in the peak splitting arise, which should be equal in the local signal on both sides of the nanowire. In the nonlocal conductance, the closing of the bulk superconducting gap is visible. At the topological phase transition, the gap approaches zero and increases at higher Zeeman fields. Adapted from Rosdahl *et al.* [16].

Device design considerations to suppress topologically trivial states

Ideally, correlation devices are designed to minimize the occurrence of topologically trivial states that mimick topological Majorana modes. Although the power of a correlation measurement is that topologically trivial states can in principle be distinguished through distinct tunneling behavior on both sides of the nanowire, their presence can slow down experimental progress as a larger number of candidate states needs to be investigated. Furthermore, when topologically trivial states coexist with topological Majorana modes, the trivial states could obscure or interact with the desired Majorana signatures.

We begin discussing how states that originate in the tunneling regions of the nanowire devices may be avoided. Unintentional quantum dots are known to sometimes arise in nanowire devices [11, 23] and are associated with several topologically trivial scenarios [13, 14, 24]. Such quantum dot states occur when confinement presents itself in an unpredictable way, for example due to non-ideal electrical contacts to the nanowire, due to stacking faults in the nanowires, or due to poor quality dielectrics covering the nanowire. In devices with optimized contacts and high quality dielectrics, quantum dot states can be ruled out through the observation of ballistic transport when the tunnel probe is tuned to a highly transmitting quantum point contact [1, 6]. However, ballistic transport may coexist with a smooth electrostatic potential profile of the tunneling barrier [25–30], or a Fabry-Perot type resonance in the unproximitized nanowire section, both of which can stabilize topologically trivial Andreev bound states at zero energy at finite Zeeman field. Since these states originate near the tunneling barrier, they should have a dependence on electrostatic gates near the tunneling barrier. To limit the occurrence of such states, the tunneling region of the device can be made as narrow as possible, with a sharp potential barrier [31]. A possible approach to induce a very sharp tunneling barrier is to implement a built-in barrier by implementing a narrow section of a higher bandgap semiconductor along the nanowire axis [32–34], if the challenge of placing the barrier right next to the superconductor can be met. Interestingly, the devices used in chapters 3 and 4, where the nanowires were covered around five of the six facets by a superconducting NbTiN contact, rarely showed subgap states with a dependence on the tunnel gate. This observation suggests that with the help of electrostatic screening from the contacts a sharper potential barrier could be formed than in nanowires which are only covered by aluminium on two or three of the nanowire facets. Unfortunately, the gain in sharpness of the tunneling barrier with increased superconductor coverage comes at the cost of a reduced gate control over the chemical potential in the superconducting part of the nanowire. This limitation could be circumvented by first fabricating a wrap-around gate around the superconducting part of the nanowire using a thin dielectric to take on the role of screening the tunnel barrier potential, and then using either a side gate or an overlapping wrap-around gate to induce the tunneling barrier.

A successful optimization of the tunneling region of a correlation device would lead to a lack of tunnel barrier dependent subgap states, excluding most origins of topologically trivial zero-energy states, except for topologically trivial states that could form underneath the superconductor. When a large number of subbands is occupied underneath the superconductor, interband coupling can cause topologically trivial low energy states to stick near zero energy [22]. This scenario is similar to the more general observation from random matrix theory that in a class D superconductor (which only has particle-hole symmetry) there is a tendency for states to remain close to zero energy without requiring a topological phase transition [21, 35]. An effectively random Hamiltonian could result from the occupancy of a large number of subbands or due to disorder induced impurity levels in the nanowire [21]. Reducing the number of occupied subbands could therefore be beneficial to obtain cleaner transport results. The obvious approach of applying a negative gate potential to reduce the chemical potential may have limited effectiveness in nanowires with strong band bending which aids strong coupling to the superconductor [36–40]. Further investigation into inducing a hard superconducting gap while limiting band bending effects may therefore be necessary. In the next paragraph we discuss how the understanding of disorder in the nanowires can be improved. Although disorder can unlikely be eliminated completely, a correlation experiment should be able to distinguish zero-bias peaks with a random origin, as the randomness of the disorder should appear in different ways at the two ends of the nanowire [35].

Characterizing disorder in Majorana nanowires

The disorder in the semiconductor nanowires themselves is relatively well studied through mobility and quantum point contact characterization, showing relatively long mean free paths [4, 41–46]. However, in particular approaches, a surface treatment takes place before deposition of the superconductor, which is essential in obtaining high quality induced superconductivity [47–49]. It may therefore be worthwhile to study nanowire devices before and after the surface treatments, without actual deposition of the superconductor, so that the effect on normal transport properties, such as mobility and conductance quantization in short nanowires can be evaluated. As opposed to the well studied normal state properties of nanowires, disorder related to the presence of the superconductor, is not understood in detail. The semiconductor-superconductor coupling strength is very sensitive on the interface properties [3, 48], in which the workfunction mismatch between the semiconductor and the superconductor plays a large role [36–40]. As the workfunction mismatch is not only dependent on the material properties, but also on the surface preparation before deposition of the superconductor, this parameter could vary spatially. The workfunction mismatch controls the band bending at the semiconductor-superconductor interface, which affects the strength of hybridization of semiconductor and superconductor states, affecting critical nanowire parameters, including the g-factor, the induced superconducting gap, and the spin-orbit strength, as we found in chapter 5. In addition, the band bending affects the carrier density in the nanowire, which translates into the effective chemical potential in the nanowire. So spatial inhomogeneity in the workfunction mismatch can in turn induce a spatial dependence of the conditions appropriate to induce topological superconductivity. In other words, a topological gap could open up only in some parts of the nanowire. Analogously, if the superconductor is not monocrystalline over the full length of the nanowire and grain boundaries are located near the interface, differences in strain and epitaxy can induce spatial inhomogeneity in the nanowire properties. Similar effects might also occur when a dielectric material covers the nanowire.

Currently, it has not yet been established if these effects play a major role in Majorana nanowires, but if they do, they could well be a roadblock for successful measurements of correlated Majorana modes and future experiments aimed at topological qubits. Correlation experiments themselves can give some indirect information on spatial inhomogeneity in Majorana nanowires, for example through the local BCS charge densities of subgap states measured on both ends of the device [50]. However, experiments directly aimed at detecting spatial variations in the electronic structure of Majorana nanowires will give more detailed information and will provide better feedback to optimize the material growth. Studying the electronic structure of the nanowire can additionally provide information on the subband structure in the nanowire and the number of occupied subbands in the nanowires covered by a superconductor, which is a related topic of which the precise experimental details are yet unclear [51]. Ideally, the electronic structure would be obtained using scanning tunneling spectroscopy (STS) using a scanning tunneling microscope or using nanoscale angle resolved photoemission spectroscopy (nano-ARPES). To ensure that the electronic structure measurements are representative of the experimental situation in which Majorana zero-modes would be created and to obtain a small energy resolution, low temperatures are required[1]. These techniques do require highly specialized experimental setups however, especially at low temperatures.

Lacking sufficient access to such advanced experimental setups, valuable information can also be obtained from tunneling spectroscopy by patterning multiple tunnel

---

[1] Temperatures on the order of 1 Kelvin could be sufficient. The superconducting material can be in the normal state, since superconductivity is not essential to find spatial variations in for example the workfunction difference and the chemical potential. In fact, the results will be easier to interpret in the normal state.

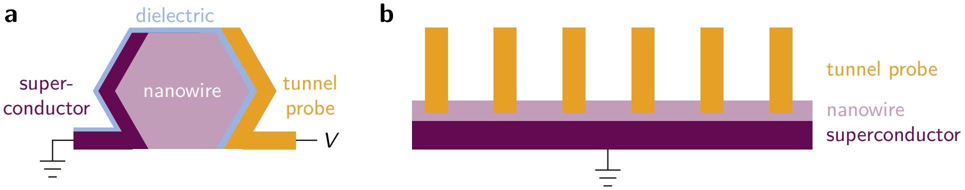

Figure 8.2: Measurement setup to investigate spatial variation of the electronic stucture in nanowires. (a) Cross-sectional view of the proposed setup. A semiconductor nanowire (light purple) is first contacted by a superconductor (purple), which can be grounded through a superconducting lead. A thin dielectric (blue) covers the nanowire and serves as a tunneling barrier to tunnel probes (yellow) on which a bias voltage V can be applied. The tunnel probes are located on nanowires facet(s) which are not covered by the superconductor to study the semiconductor density of states. **(b)** Top view of the setup. By implementing multiple identical tunnel probes at different points along the nanowire, spatial variations in the tunneling spectra can be investigated.

probes on a nanowire (see Fig. 8.2a). To avoid the formation of Andreev bound states due to smooth tunnel barriers, sharp tunneling barriers can be created by using thin dielectric tunneling barriers, instead of gate defined barriers. For example, to create the dielectric tunneling barrier, a thin aluminium layer could be deposited and controllably oxidized all around the nanowire in-situ, after the superconductor is deposited. By using multiple narrow tunnel probes along the nanowire (illustrated in Fig. 8.2b), spatial variations in the density of states can be detected, and by comparing different devices, device reproducibility can be tested. Note that a similar setup can be used to study Majorana signatures [8], if effects of the tunnel probes on the electrostatic potential profile (chemical potential) along the nanowire can be shown to be negligible. For the purpose of measuring the spatial fluctuations in the electronic structure, however, invasive effects of the tunnel probes on the electrostatic potential in the nanowire are acceptable, if the invasiveness of the probes can be assumed to be the same for each probe. When biasing a single tunnel probe, a measurement of the nonlocal conductance induced in the adjacent tunnel probes can furthermore give an estimate of the currently unknown induced superconducting coherence length ξ, since the nonlocal conductance at voltages below the induced gap exponentially decays with the ratio l/ξ, where l is the distance from the biased tunnel probe [16].

8

8.2.2. LOCAL MAJORANA MODES

In chapter 6 we found plateaus in the zero-bias conductance near $2e^2/h$ and argued that these plateaus can be interpreted in terms of local Majorana modes which form in the tunneling region of a nanowire device due to a smooth electrostatic potential profile. The emergence of these states remains sensitive on precise tuning of the electrostatic gates and magnetic fields, likely because in a short tunneling region a sufficiently smooth electrostatic potential profile only forms for specific gate settings. Local Majorana modes may provide an alternative route towards demonstration of non-Abelian braiding and could be useful building blocks for a quantum computer, provided that the energy splitting due to the mutual overlap of the Majorana modes can be highly suppressed [28, 52]. Since the decoupling of local Majorana modes is directly related to the smoothness of the electrostatic potential profile, creating a highly smooth potential by design is a logical step to improve the stability of local Majorana modes near zero-energy. A complicating factor in typical Majorana nanowire device designs is the significant uncertainty in the strength of effect of electrostatic gates on nanowires covered by a superconductor due to strong screening effects from the superconducting shell and the unknown value of the workfunction difference at the interface between the semiconducting nanowire and the superconductor [36–40]. Furthermore, the presence of the superconductor might introduce disorder, as we discussed in the previous section. Interestingly though, in a nanowire which is only partially covered by a superconducting shell, local Majorana modes can also stabilize due a smooth potential in the bare section of the nanowire [29, 30, 52], where the effect of gates is stronger and understood much better. This way, the nanowire can be easily tuned into the single spin subband regime required to generate local Majorana modes. Additionally, in the absence of direct contact with a superconductor, we know that the nanowire is relatively disorder free through measurements of the mobility and the observation of conductance quantization [4, 41–46], which could be beneficial for making reliable and reproducible devices using the presently available fabrication techniques.

To create a smooth electrostatic barrier potential by design, we propose to use a semiconductor nanowire, where the first section of the nanowire ($\sim 1\,\mu\text{m}$)[2] is left uncovered, and the last part of the nanowire is covered by a superconducting shell. The nanowire can be placed on top of a back gate, which can be used to control the overall electron density in the nanowire to tune the uncovered nanowire section slightly above the band bottom of the first subband. Source and drain contacts are formed at the ends of the nanowire. A smooth potential can then be created in the uncovered nanowire section using tapered side gates, as illustrated in Fig. 8.3a. Although side gates typically have a relatively weak capacitive coupling, its gating effect should be sufficient due to the lack of electrostatic screening from metallic part near the uncovered section. By applying a negative voltage on the side gates, the nanowire can be depleted gradually in between the left contact and the superconducting section of the nanowire, as shown in the electrostatic potential profile in Fig. 8.3b, which is calculated by solving the Poisson equation with the Thomas-Fermi approximation for the proposed geometry (details in the caption of Fig. 8.3). Based on the electrostatics calculations, the smoothness of the electrostatic potential is largely controlled by the tapering angle of the side gates, with finite angles of 5° or less resulting in the smoothest profiles. To check whether this potential profile indeed induces the mutual decoupling of the local Majorana modes and results in stable zero-energy states, Fig. 8.3c shows a simulation of the conductance using the potential profile created by the tapered design as a function of the Zeeman energy. At zero Zeeman field, there are two energy states below the gap which are largely located in the uncovered nanowire section and therefore experience a reduced coupling to the superconductor. When the Zeeman field is increased, these states split and one pair moves towards zero energy at a Zeeman field of around 1 meV, where it remains upon further increase of the Zeeman field. A similar stability of the zero-energy states is expected when the side-gate voltage is varied at a fixed Zeeman field, as shown in Fig.

---

[2] We note that similar results are obtained for normal sections of 500 nm, with slightly reduced zero-energy stability.

8.3d.

In addition to the decoupling of the local Majorana modes, the smooth potential profile also creates a strongly spin-dependent coupling to the left lead at finite Zeeman energies. An exponentially different lead-local Majorana coupling causes the emergence of a zero-bias conductance plateau at $2e^2/h$ for a broad range of magnetic field and tunnel-coupling strength [28], as is visible in the linetraces in Fig. 8.3e,f. Looking at the tunneling strength between the left lead and each of the local MZMs shown in Fig. 8.3g,h directly, we find that the difference in coupling strengths can exceed three orders of magnitude in this geometry. The spin selective transmission of the barrier is also reflected in the appearance of spin-split quantized plateaus at integer multiples of e^2/h in the above-gap conductance (orange line in Fig. 8.3f). Experimental observation of zero-bias conductance plateaus at $2e^2/h$ upon variation of the magnetic field and the side-gate voltage would provide a good indication that the tapered gate design produces the desired local Majorana modes. Additionally, the transition of a zero-bias conductance of essentially zero to the quantized value of $2e^2/h$ with an increasing side-gate voltage would indicate that it is possible to switch between coupling to neither of the local Majorana modes and coupling to a single local Majorana mode, which is required in measurement based braiding protocols [28, 53, 54].

Within the simple one-dimensional tight binding model used in this preliminary evaluation of the proposed setup, even long uncovered nanowire sections exceeding a micron appear to be suitable to create local Majorana modes, while maintaining a well defined superconducting gap away from the directly proximitized nanowire region. Long normal sections allow for a smoother potential profile with improved decoupling of the local Majorana modes and small residual energy splittings, which are essential for the purposes of braiding and quantum computing. It is presently unknown, however, if such a long range proximity effect is realized under experimental conditions, in particular in the presence of (small amounts of) disorder or when taking into account the finite nanowire width which could suppress the induced gap [16, 36]. Therefore, there is likely a trade-off in the choice of the length of the normal section, as for shorter normal sections, zero-energy stability will become more compromised. Other effects that could influence the formation of local Majorana modes are the orbital effect of the magnetic field and multiband occupation of the nanowire in the region covered by the superconducting shell. These are interesting factors to address in more advanced device simulations, to provide more detailed input on the device geometry.

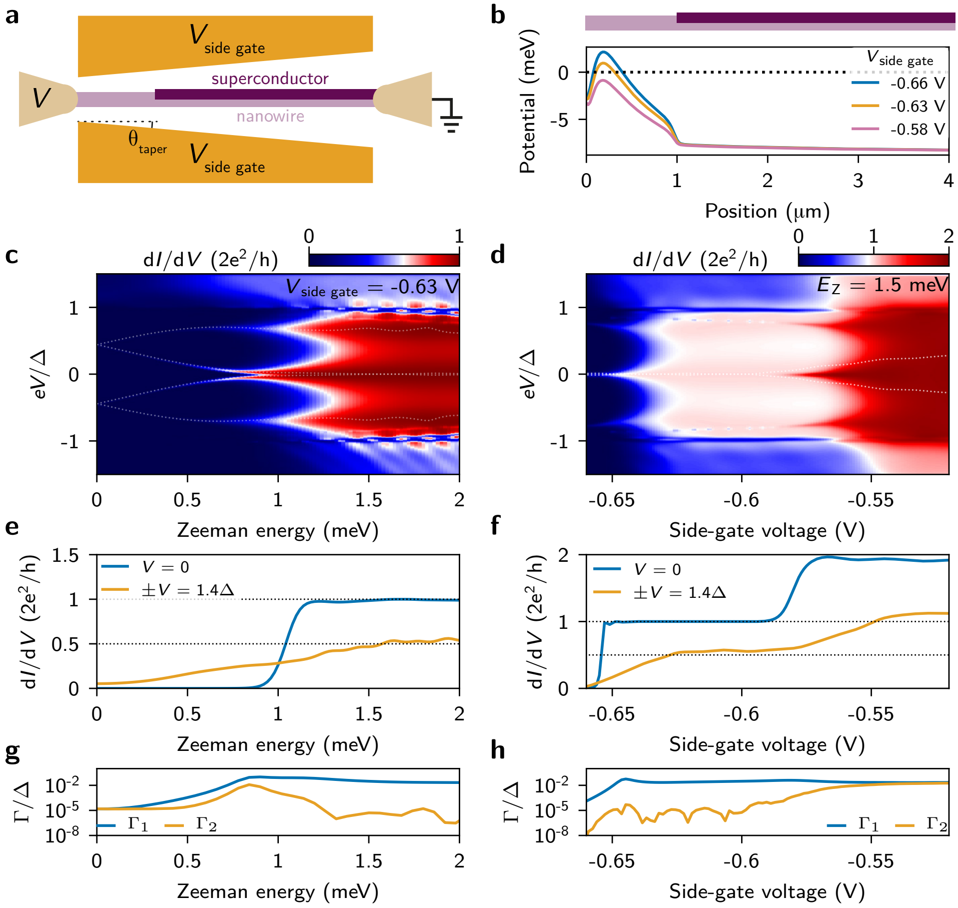

Figure 8.3: Local Majorana modes induced by a tapered side-gate design. **(a)** Top view of the proposed design. θ_{taper} indicates the tapering angle of the side gates. A back gate located below the nanowire is not shown. **(b)** The electrostatic potential profile induced by the proposed design measured from the conductance band bottom (black dotted line) obtained from a three-dimensional electrostatics simulation of the Poisson equation using the Thomas-Fermi approximation with the effective masses (electrons and holes) appropriate for InSb (relative permittivity of 16.8), equivalent to the model used in chapter 5 [39]. In the simulations, the tapering angle of the side gates is set to 5°, the nanowire is 4 μm long, with the first 1 μm uncovered by the superconductor, using a 30 nm thick SiN back-gate dielectric (relative permittivity of 8), with the back gate set to 0.1 V. The potential shown is evaluated in the middle of the nanowire. **(c)** The conductance as a function of the bias voltage normalized to the superconducting gap and the Zeeman energy for the potential shown in **b**. The nanowire is in the topologically trivial phase over the full Zeeman range (the topological transition here only occurs for $E_Z \gtrsim 0.8\,\text{meV}$). The conductance is obtained for a one-dimensional tight-binding simulation [55, 56] using KWANT and an effective mass of $0.015 m_e$ (m_e is the electron mass) and a Rashba spin-orbit strength of 0.5 eVÅ. All conductance plots are thermally broadened at a temperature of 25 mK. The white dotted lines indicate the two lowest energy states of the energy spectrum for clarity. **(d)** Same as **c**, but as a function of the side-gate voltage at a fixed Zeeman energy of 1.5 meV. **(e,f)** Zero-bias linetrace (blue) and above-gap linetrace taken as the average of the conductance at positive and negative 1.4Δ (orange) of **c** and **d** respectively. Note that the above-gap linetraces show ballistic transport through a single or two spinful modes in the junction and saturate slightly above e^2/h and $2e^2/h$ because the linetraces are taken close to the gap edge where Andreev reflection is not fully suppressed [57]. **(g,h)** Tunnel-coupling strength of the lead to each of the local MZMs corresponding to **c,d** respectively. Calculated using the method described in Vuik *et al.* [28].

REFERENCES

[1] H. Zhang, O. Gül, S. Conesa-Boj, M. P. Nowak, M. Wimmer, K. Zuo, V. Mourik, F. K. de Vries, J. van Veen, M. W. A. de Moor, J. D. S. Bommer, D. J. van Woerkom, D. Car, S. R. Plissard, E. P. A. M. Bakkers, M. Quintero-Pérez, M. C. Cassidy, S. Koelling, S. Goswami, K. Watanabe, T. Taniguchi, and L. P. Kouwenhoven, *Ballistic superconductivity in semiconductor nanowires,* Nat. Commun. **8**, 16025 (2017).

[2] V. Mourik, K. Zuo, S. M. Frolov, S. R. Plissard, E. P. A. M. Bakkers, and L. P. Kouwenhoven, *Signatures of Majorana fermions in hybrid superconductor-semiconductor nanowire devices,* Science **336**, 1003 (2012).

[3] W. Chang, S. M. Albrecht, T. S. Jespersen, F. Kuemmeth, P. Krogstrup, J. Nygård, and C. M. Marcus, *Hard gap in epitaxial semiconductor-superconductor nanowires,* Nat. Nanotech. **10**, 232 (2015).

[4] O. Gül, D. J. van Woerkom, I. van Weperen, D. Car, S. R. Plissard, E. P. A. M. Bakkers, and L. P. Kouwenhoven, *Towards high mobility InSb nanowire devices,* Nanotechnology **26**, 215202 (2015).

[5] S. M. Albrecht, A. P. Higginbotham, M. Madsen, F. Kuemmeth, T. S. Jespersen, J. Nygård, P. Krogstrup, and C. M. Marcus, *Exponential protection of zero modes in Majorana islands,* Nature **531**, 206 (2016).

[6] Ö. Gül, H. Zhang, J. D. S. Bommer, M. W. A. de Moor, D. Car, S. R. Plissard, E. Bakkers, A. Geresdi, K. Watanabe, T. Taniguchi, and L. P. Kouwenhoven, *Ballistic Majorana nanowire devices,* Nat. Nanotech. **13**, 192 (2018).

[7] F. Nichele, A. C. C. Drachmann, A. M. Whiticar, E. C. T. O'Farrell, H. J. Suominen, A. Fornieri, T. Wang, G. C. Gardner, C. Thomas, A. T. Hatke, P. Krogstrup, M. J. Manfra, K. Flensberg, and C. M. Marcus, *Scaling of Majorana zero-bias conductance peaks,* Phys. Rev. Lett. **119**, 136803 (2017).

[8] A. Grivnin, E. Bor, M. Heiblum, Y. Oreg, and H. Shtrikman, *Concomitant opening of a bulk-gap with an emerging possible Majorana zero mode,* Nat. Commun. **10**, 1940 (2019).

[9] S. Vaitiekėnas, G. W. Winkler, B. van Heck, T. Karzig, M.-T. Deng, K. Flensberg, L. I. Glazman, C. Nayak, P. Krogstrup, R. M. Lutchyn, and C. M. Marcus, *Flux-induced topological superconductivity in full-shell nanowires,* Science **367**, eaav3392 (2020).

[10] S. Vaitiekėnas, Y. Liu, P. Krogstrup, and C. M. Marcus, *Zero-field topological superconductivity in ferromagnetic hybrid nanowires,* Nat. Phys. (2020), 10.1038/s41567-020-1017-3.

[11] M. T. Deng, S. Vaitiekėnas, E. B. Hansen, J. Danon, M. Leijnse, K. Flensberg, J. Nygård, P. Krogstrup, and C. M. Marcus, *Majorana bound state in a coupled quantum-dot hybrid-nanowire system,* Science **354**, 1557 (2016).

[12] D. I. Pikulin, J. P. Dahlhaus, M. Wimmer, H. Schomerus, and C. W. J. Beenakker, *A zero-voltage conductance peak from weak antilocalization in a Majorana nanowire,* New J. of Phys. **14**, 125011 (2012).

[13] E. J. H. Lee, X. Jiang, R. Aguado, G. Katsaros, C. M. Lieber, and S. De Franceschi, *Zero-bias anomaly in a nanowire quantum dot coupled to superconductors,* Phys. Rev. Lett. **109**, 186802 (2012).

[14] E. J. Lee, X. Jiang, M. Houzet, R. Aguado, C. M. Lieber, and S. De Franceschi, *Spin-resolved Andreev levels and parity crossings in hybrid superconductor–semiconductor nanostructures,* Nat. Nanotech. **9**, 79 (2014).

[15] S. Das Sarma, J. D. Sau, and T. D. Stanescu, *Splitting of the zero-bias conductance peak as smoking gun evidence for the existence of the Majorana mode in a superconductor-semiconductor nanowire,* Phys. Rev. B **86**, 220506 (2012).

[16] T. O. Rosdahl, A. Vuik, M. Kjaergaard, and A. R. Akhmerov, *Andreev rectifier: A nonlocal conductance signature of topological phase transitions,* Phys. Rev. B **97**, 045421 (2018).

[17] G. L. R. Anselmetti, E. A. Martinez, G. C. Ménard, D. Puglia, F. K. Malinowski, J. S. Lee, S. Choi, M. Pendharkar, C. J. Palmstrøm, C. M. Marcus, L. Casparis, and A. P. Higginbotham, *End-to-end correlated subgap states in hybrid nanowires,* Phys. Rev. B **100**, 205412 (2019).

[18] G. C. Ménard, G. L. R. Anselmetti, E. A. Martinez, D. Puglia, F. K. Malinowski, J. S. Lee, S. Choi, M. Pendharkar, C. J. Palmstrøm, K. Flensberg, C. M. Marcus, L. Casparis, and A. P. Higginbotham, *Conductance-matrix symmetries of a three-terminal hybrid device,* Phys. Rev. Lett. **124**, 036802 (2020).

[19] D. Puglia, E. A. Martinez, G. C. Ménard, A. Pöschl, S. Gronin, G. C. Gardner, R. Kallaher, M. J. Manfra, C. M. Marcus, A. P. Higginbotham, and L. Casparis, *Closing of the induced gap in a hybrid superconductor-semiconductor nanowire,* arXiv preprint arXiv:2006.01275 (2020).

[20] H. Pan and S. Das Sarma, *Physical mechanisms for zero-bias conductance peaks in Majorana nanowires,* Phys. Rev. Research **2**, 013377 (2020).

[21] H. Pan, W. S. Cole, J. D. Sau, and S. Das Sarma, *Generic quantized zero-bias conductance peaks in superconductor-semiconductor hybrid structures,* Phys. Rev. B **101**, 024506 (2020).

[22] B. D. Woods, J. Chen, S. M. Frolov, and T. D. Stanescu, *Zero-energy pinning of topologically trivial bound states in multiband semiconductor-superconductor nanowires,* Phys. Rev. B **100**, 125407 (2019).

[23] M.-T. Deng, S. Vaitiekėnas, E. Prada, P. San-Jose, J. Nygård, P. Krogstrup, R. Aguado, and C. M. Marcus, *Nonlocality of Majorana modes in hybrid nanowires,* Phys. Rev. B **98**, 085125 (2018).

[24] C. Jünger, R. Delagrange, D. Chevallier, S. Lehmann, K. A. Dick, C. Thelander, J. Klinovaja, D. Loss, A. Baumgartner, and C. Schönenberger, *Magnetic-field-independent subgap states in hybrid Rashba nanowires,* Phys. Rev. Lett. **125**, 017701 (2020).

[25] E. Prada, P. San-Jose, and R. Aguado, *Transport spectroscopy of NS nanowire junctions with Majorana fermions,* Phys. Rev. B **86**, 180503 (2012).

[26] G. Kells, D. Meidan, and P. W. Brouwer, *Near-zero-energy end states in topologically trivial spin-orbit coupled superconducting nanowires with a smooth confinement,* Phys. Rev. B **86**, 100503 (2012).

[27] C.-X. Liu, J. D. Sau, T. D. Stanescu, and S. Das Sarma, *Andreev bound states versus Majorana bound states in quantum dot-nanowire-superconductor hybrid structures: Trivial versus topological zero-bias conductance peaks,* Phys. Rev. B **96**, 075161 (2017).

[28] A. Vuik, B. Nijholt, A. R. Akhmerov, and M. Wimmer, *Reproducing topological properties with quasi-Majorana states,* SciPost Phys. **7**, 061 (2019).

[29] C. Moore, C. Zeng, T. D. Stanescu, and S. Tewari, *Quantized zero-bias conductance plateau in semiconductor-superconductor heterostructures without topological Majorana zero modes,* Phys. Rev. B **98**, 155314 (2018).

[30] C. Moore, T. D. Stanescu, and S. Tewari, *Two-terminal charge tunneling: Disentangling Majorana zero modes from partially separated Andreev bound states in semiconductor-superconductor heterostructures,* Phys. Rev. B **97**, 165302 (2018).

[31] Y. Huang, H. Pan, C.-X. Liu, J. D. Sau, T. D. Stanescu, and S. Das Sarma, *Metamorphosis of Andreev bound states into Majorana bound states in pristine nanowires,* Phys. Rev. B **98**, 144511 (2018).

[32] M. T. Björk, C. Thelander, A. E. Hansen, L. E. Jensen, M. W. Larsson, L. R. Wallenberg, and L. Samuelson, *Few-electron quantum dots in nanowires,* Nano Lett. **4**, 1621 (2004).

[33] K. A. Dick, C. Thelander, L. Samuelson, and P. Caroff, *Crystal phase engineering in single InAs nanowires,* Nano Lett. **10**, 3494 (2010).

[34] D. Car, S. Conesa-Boj, H. Zhang, R. L. M. Op het Veld, M. W. A. de Moor, E. M. T. Fadaly, O. Gül, S. Kölling, S. R. Plissard, V. Toresen, M. T. Wimmer, K. Watanabe, T. Taniguchi, L. P. Kouwenhoven, and E. P. A. M. Bakkers, *InSb nanowires with built-in* $Ga_xIn_{1-x}Sb$ *tunnel barriers for Majorana devices,* Nano Lett. **17**, 721 (2017).

[35] S. Mi, D. I. Pikulin, M. Marciani, and C. W. J. Beenakker, *X-shaped and Y-shaped Andreev resonance profiles in a superconducting quantum dot,* J. Exp. Theor. Phys **119**, 1018 (2014).

[36] A. E. Antipov, A. Bargerbos, G. W. Winkler, B. Bauer, E. Rossi, and R. M. Lutchyn, *Effects of gate-induced electric fields on semiconductor Majorana nanowires,* Phys. Rev. X **8**, 031041 (2018).

[37] B. D. Woods, T. D. Stanescu, and S. Das Sarma, *Effective theory approach to the Schrödinger-Poisson problem in semiconductor Majorana devices,* Phys. Rev. B **98**, 035428 (2018).

[38] A. E. G. Mikkelsen, P. Kotetes, P. Krogstrup, and K. Flensberg, *Hybridization at superconductor-semiconductor interfaces,* Phys. Rev. X **8**, 031040 (2018).

[39] M. W. A. de Moor, J. D. S. Bommer, D. Xu, G. W. Winkler, A. E. Antipov, A. Bargerbos, G. Wang, N. van Loo, R. L. M. O. het Veld, S. Gazibegovic, D. Car, J. A. Logan, M. Pendharkar, J. Sue Lee, E. P. A. M. Bakkers, C. J. Palmstrøm, R. M. Lutchyn, L. P. Kouwenhoven, and H. Zhang, *Electric field tunable superconductor-semiconductor coupling in Majorana nanowires,* New J. of Phys. **20**, 103049 (2018).

[40] G. W. Winkler, A. E. Antipov, B. van Heck, A. A. Soluyanov, L. I. Glazman, M. Wimmer, and R. M. Lutchyn, *Unified numerical approach to topological semiconductor-superconductor heterostructures,* Phys. Rev. B **99**, 245408 (2019).

[41] I. van Weperen, S. R. Plissard, E. P. A. M. Bakkers, S. M. Frolov, and L. P. Kouwenhoven, *Quantized conductance in an InSb nanowire,* Nano Lett. **13**, 387 (2013).

[42] S. Heedt, W. Prost, J. Schubert, D. Grützmacher, and T. Schäpers, *Ballistic transport and exchange interaction in InAs nanowire quantum point contacts,* Nano Lett. **16**, 3116 (2016).

[43] J. Kammhuber, M. C. Cassidy, H. Zhang, O. Gül, F. Pei, M. W. A. de Moor, B. Nijholt, K. Watanabe, T. Taniguchi, D. Car, S. R. Plissard, E. P. A. M. Bakkers, and L. P. Kouwenhoven, *Conductance quantization at zero magnetic field in InSb nanowires,* Nano Lett. **16**, 3482 (2016).

[44] J. Gooth, M. Borg, H. Schmid, V. Schaller, S. Wirths, K. Moselund, M. Luisier, S. Karg, and H. Riel, *Ballistic one-dimensional InAs nanowire cross-junction interconnects,* Nano Lett. **17**, 2596 (2017).

[45] G. Badawy, S. Gazibegovic, F. Borsoi, S. Heedt, C.-A. Wang, S. Koelling, M. A. Verheijen, L. P. Kouwenhoven, and E. P. A. M. Bakkers, *High mobility stemless InSb nanowires,* Nano Lett. **19**, 3575 (2019).

[46] P. Aseev, G. Wang, L. Binci, A. Singh, S. Martí-Sánchez, M. Botifoll, L. J. Stek, A. Bordin, J. D. Watson, F. Boekhout, D. Abel, J. Gamble, K. van Hoogdalem, J. Arbiol, L. P. Kouwenhoven, G. de Lange, and P. Caroff, *Ballistic InSb nanowires and networks via metal-sown selective area growth,* Nano Lett. **19**, 9102 (2019).

[47] O. Gül, H. Zhang, F. K. de Vries, J. van Veen, K. Zuo, V. Mourik, S. Conesa-Boj, M. P. Nowak, D. J. van Woerkom, M. Quintero-Pérez, M. C. Cassidy, A. Geresdi, S. Koelling, D. Car, S. R. Plissard, E. P. A. M. Bakkers, and L. P. Kouwenhoven, *Hard superconducting gap in InSb nanowires,* Nano Lett. **17**, 2690 (2017).

[48] S. Gazibegovic, D. Car, H. Zhang, S. C. Balk, J. A. Logan, M. W. A. de Moor, M. C. Cassidy, R. Schmits, D. Xu, G. Wang, P. Krogstrup, R. L. M. Op het Veld, K. Zuo, Y. Vos, J. Shen, D. Bouman, B. Shojaei, D. Pennachio, J. S. Lee, P. J. van Veldhoven, S. Koelling, M. A. Verheijen, L. P. Kouwenhoven, C. J. Palmstrøm, and E. P. A. M. Bakkers, *Epitaxy of advanced nanowire quantum devices,* Nature **548**, 434 (2017).

[49] R. L. M. Op het Veld, D. Xu, V. Schaller, M. A. Verheijen, S. M. E. Peters, J. Jung, C. Tong, Q. Wang, M. W. A. de Moor, B. Hesselmann, K. Vermeulen, J. D. S. Bommer, J. Sue Lee, S. Andrey, M. Pendharkar, A. Marzegalli, S. Koelling, L. P. Kouwenhoven, L. Miglio, C. J. Palmstrøm, H. Zhang, and E. P. A. M. Bakkers, *In-plane selective area InSb–Al nanowire quantum networks,* Commun. Phys. **3**, 59 (2020).

[50] J. Danon, A. B. Hellenes, E. B. Hansen, L. Casparis, A. P. Higginbotham, and K. Flensberg, *Nonlocal conductance spectroscopy of Andreev bound states: Symmetry relations and BCS charges,* Phys. Rev. Lett. **124**, 036801 (2020).

[51] B. D. Woods, S. Das Sarma, and T. D. Stanescu, *Subband occupation in semiconductor-superconductor nanowires,* Phys. Rev. B **101**, 045405 (2020).

[52] C. Zeng, G. Sharma, T. D. Stanescu, and S. Tewari, *Feasibility of measurement-based braiding in the quasi-Majorana regime of semiconductor-superconductor heterostructures,* Phys. Rev. B **102**, 205101 (2020).

[53] S. Plugge, A. Rasmussen, R. Egger, and K. Flensberg, *Majorana box qubits,* New J. Phys. **19**, 012001 (2017).

[54] T. Karzig, C. Knapp, R. M. Lutchyn, P. Bonderson, M. B. Hastings, C. Nayak, J. Alicea, K. Flensberg, S. Plugge, Y. Oreg, C. M. Marcus, and M. H. Freedman, *Scalable designs for quasiparticle-poisoning-protected topological quantum computation with Majorana zero modes,* Phys. Rev. B **95**, 235305 (2017).

[55] R. M. Lutchyn, J. D. Sau, and S. Das Sarma, *Majorana fermions and a topological phase transition in semiconductor-superconductor heterostructures,* Phys. Rev. Lett. **105**, 077001 (2010).

[56] Y. Oreg, G. Refael, and F. von Oppen, *Helical liquids and Majorana bound states in quantum wires,* Phys. Rev. Lett. **105**, 177002 (2010).

[57] G. E. Blonder, M. Tinkham, and T. M. Klapwijk, *Transition from metallic to tunneling regimes in superconducting microconstrictions: Excess current, charge imbalance, and supercurrent conversion,* Phys. Rev. B **25**, 4515 (1982).

ACKNOWLEDGEMENTS

From the moment that I first learned about Majoranas while exploring options for my bachelor's research project, I was immediately fascinated. At first, the exciting challenge to understand their abstract and peculiar behavior mostly drew me. Later, my motivation was only strengthened by the prospect of their technological advantages. I feel lucky to have had the opportunity to focus my PhD on exactly the topic I had set out to study. And then it turned out that the place that offered this opportunity was similarly special. QuTech proved to be a place with both a stimulating and very welcoming open culture. I don't think I could have wished for a better environment for the last couple of years.

First of all, I want to thank **Leo**. Because of your deep and broad understanding of the field, you always have on point questions and comments at hand. I have very much enjoyed the strong degree of freedom we are allowed in our group. Despite your hands-off approach and your many responsibilities, I keep being impressed by your ability always be on top of all important matters. **Hao**, thanks for welcoming me in your team. You gave me the direction I very much needed in the beginning and kickstarted my PhD. You were always available to share your extensive knowledge in a very clear way, and your ability to navigate the social aspects both within and outside of the team is inspiring to me. Without that, we also wouldn't have enjoyed many of the fruitful collaborations with growers and theorists. I'm sure many great things lie ahead of you. **Önder**, you were also there from the very beginning, always ready to share your insights. Even though we didn't overlap for very long, I hope it took over some of your highly systematical and critical approach. I have always enjoyed our intense discussions and your tendency to never be satisfied. Fortunately, it turned out that our shared interests don't end at physics, which certainly helped me feel at home quickly. I hope to welcome you back home soon. **Michiel**, thanks to your deep and broad understanding, you are always able to offer different, interesting perspectives, and impressively on so many different topics. Your reasoned approach has led to some of our best results. You played a vital role in the very enjoyable social culture within QuTech. With your wide interests, I'm sure you'll be successful in whatever next career path you choose. **Di**, working with you was a pleasure. Your hard work has laid essential foundations for many new results in our group. You also created a great environment for all new students in our team. It was nice to see your strong development on both the scientific and personal level over the last few years. **Nick** and **Guan**, with your eagerness to learn and strong work ethics, you have played crucial roles in a multitude of important developments in our lab and have now found yourselves very interesting projects I'm eager to keep hearing about. **Kiefer** and **Qing**, although I haven't worked with you very closely, you kept the team efforts alive when I started writing. Thanks for all the chats near the coffee machine, and of course the avocado trips. **Vukan**, it's too bad that there wasn't more time for us to work together, but I enjoyed your relentless stream of questions and to see your determination to understand all the ins and outs to a very detailed level. All the best in your new team! And to

the many people other people that played crucial roles on the theory and material sides, **Michael**, **Roy**, **Sasa**, **Bas**, **Andrey**, **Georg**, **Chun-Xiao**, and **Mihir**, thanks for the many discussions, I have learned immensely from you.

In the early days, before joining Hao's team, you **John** taught me the first in-and-outs of cleanroom work and basic characterization measurements. I was immediately impressed by your detailed knowledge of both all of the equipment and the physics. After that **Kun** guided me through my first project in collaboration with TNO, albeit for a short while. I very much enjoyed your friendliness, and optimism, and confidence of the good things to come in our lab. When the project seemed to have hit a dead end, **Arjan**, you helped out as best as possible. On the TNO side, a special word goes out to **Ruud**. Working in the TNO cleanroom with you was a pleasure, not in the least because of the relaxing jazz in the background. Finally, **Hans**, **Arnold**, and **Nick**, thanks your all your assistance and for sharing a slightly different perspective than the purely academic one.

After Hao left Delft and the spectroscopy measurements on the aluminium nanowires came to an end, **Angela**, you adopted me in your young group. Unfortunately, we never got around to collaborate on the exciting new RF experiments. Nevertheless, I highly appreciate your genuine interest in my progress and your critical questions. In turn, together with the rest of the team, **Willemijn**, **Arno**, **Marta**, **Lukas**, **Lukas**, and **Jaap** you taught me about RF experiments and also brightened up the final stage of my PhD. **Arno**, I hope one day we'll return to a snowy Veldhoven. **Bernard**, thanks for your always well-considered input. And, **Gijs**, I enjoyed late-night conversations at conferences and your honest advice. I'm glad we can keep that going in future!

The daily office life of course wouldn't have been the same without the fellow members of our 'Tropological Island'. **Fokko**, beside from your impressive determination at work, I will not forget the small things you did to brighten up my day, like covering my desk with balloons. **Nikolai**, my evening companion and always prepared with good fabrication advice. Your passionate convictions made for some very interesting conversations. I hope to visit Finland soon to cash in the promised beer! **Alex**, no one else in the lab was so genuinely interested in all the little steps forward in my experiments. Thanks for all your initiatives on group activities. See you next time at the Scheveningen beach? **Damaz**, I fondly remember our many coffee trips, the bonding that summer most of the group was away for conferences, and later of course our nice shared trip on the East Coast with your great stories on US history. Good luck with the last part of your thesis! Then, thanks the many others in QuTech that have made it both welcoming and stimulating place, **Udit**, **Florian**, **Francesco**, **Elham**, **David**, **Jie**, **Sebastian**, **Arjan**, **Jakob**, **Daniël**, **Dominique**, **Ting**, **Christian**, **Srijit**, **Yuki**, **Lin**, **Amrita**, **Kian**, **Luca**, **Vanessa**.

Working in an experimental lab would not have been easy without the great technical support. **Jason**, thanks for always making time to help out quickly urgent matter, to teach new skills, and for keeping the lab somewhat organized. Working with the fridges was made easy by **Olaf**. Thanks for your many patient explanations of all the fridge details, it was very fun and helpful. And **Mark**, thanks for keeping the evaporators filled with a seemingly never-ending supply of gold. **Raymond**, **Raymond**, and **Martijn**, thanks for your input on understanding the intricate details of our electronic measurements. To all of the cleanroom staff, with your strong efforts on training, often swift help and repairs, you have impressively managed to keep everything running smoothly. Finally, **Remco**,

Siebe, **Roy**, and **Jelle**, thanks for our supply of cryogenics, cooling water, and other supplies running smoothly. For the very quick and efficient handling on any administrative questions, I would particularly like to thank **Simone** and **Jenny**.

James, I'm very glad we ended up going to San Sebastian together. Ever since, we have shared unforgettable moments, you have been there for any kind of support, and through your open, inviting nature you also allowed me to meet countless more amazing people. **Nodar**, still my Delft companion, and always there to share a good time or to offer a listening ear. Your place has been like a second home to me. Keep being you! **Beatrice**, your endless enthusiasm, ideas, invitations, and critical points of view have helped to shape me to be the person I am today. I hope that very soon we can will have a sequel to our crazy Wednesday. **Willemijn**, although we never worked together, it feels as if we've spend this journey together. How you can make people feel so comfortable within your presence is incredible. I can't wait to see in what fascinating shape your next journey while take. **Vidak**, thanks for all you dark insults and companionship on sunny beaches. I'm sure you're trying, but all the macabre jokes still can't hide your other side. I'm looking forward to see what our next working from home destination will be. **Deniz**, fortunately through all those sunny Delft barbecues a few summers ago, I also got to know your kind-hearted nature better. And of course our shared tastes in music, good job on also infecting James now! **Amanda** & **Daniel**, you're such warm people. I have so many fond memories of your many invitations. It's always an adventure to meet the variety of intriguing people you surround yourselves with. **Helena**, never lose your amazing attitude. You certainly brightened up my time in Delft. I hope to see you again soon in Tel Aviv!

Niels en **Maikel**, ondanks dat we ons over het land verspreid hebben, blijf het met jullie altijd als thuis voelen. Het is top om te zien dat na al die jaren overlap, we nu allemaal ons eigen pad succesvol weten te vinden. **Kees**, bedankt voor al je oprechte interesse in mijn onderzoek, maar vooral ook alles daarbuiten. De gezellige weekenden in Enschede brengen gelukkig nog altijd weer die mooie tijd aan de Wethouder naar boven. Veel succes met jouw promotie. **Douwe**, **Erik**, **Natasha** en **Martijn**, bedankt voor alle mooie avondjes en partijtjes. De plantenspuit is dan misschien omgeruild voor eeb wolkenkrabber en Manhattan, maar er ligt ons vast nog veel meer voor de boeg.

Aan mijn **ouders**, dankzij jullie heb ik de kans gekregen om deze bijzondere weg te volgen. Al was het voor jullie soms misschien onbekend en ondoorgrondelijk, heb ik me altijd aangemoedigd en vrij gevoeld om mijn interesses en ambities te volgen. **Nino**, we hebben samen al veel mooie en gekke momenten gedeeld en samen de wereld ontdekt. Niet veel mensen geven zoveel om de mensen om ze heen zoals jij. Met jouw creativiteit staat je nog van alles te wachten. Blijf me verbazen! **Anouk**, ik vind het prachtig om te zien hoe ook jij helemaal je eigen weg hebt gevonden en je je daar in blijft ontwikkelen. Ik ben trots op al je mooie creaties. Voor de rest van de **familie**, bedankt voor jullie luisterend oor en steun gedurende al deze jaren. Ik blijf het bijzonder vinden hoe hecht we zijn gebleven, ook nu we met steeds meer zijn.

Anastasia, φως μου, your endless support gave me comfort, also during some the challenging times. You were there to listen and to motivate me patiently, and fortunately also to share all the fun times and little trips. Let's keep following our ambitions and discover what the future will hold.

CURRICULUM VITÆ

Jurriaan Daniël Siegfried **BOMMER**

16-Aug-1991 Born in Vinkeveen, The Netherlands.

EDUCATION

2003–2009 Secondary school (*cum laude*)
Veenlanden College, Mijdrecht, The Netherlands

2009–2013 Bachelor of Science, Applied Physics
University of Twente, Enschede, The Netherlands
Thesis: Adsorption of redox-active molecules on platinum and boron doped diamond electrodes in nanofluidic electrochemical sensors
Advisor: Prof. dr. S. G. Lemay

2014 Internship
Institute of Superconducting and Electronic Materials,
Wollongong, Australia
Thesis: Magnetoresistance of $LaAlO_3/SrTiO_3$ interfaces
Advisor: Dr. A. V. Pan

2013–2015 Master of Science, Applied Physics
University of Twente, Enschede, The Netherlands
Thesis: Conduction at the surface of oxides
Advisor: Prof. dr. ir. J. W. M. Hilgenkamp

2015–2020 PhD, Applied Physics
Delft University of Technology, Delft, The Netherlands
Thesis: Zero-energy states in Majorana nanowire devices
Promotor: Prof. dr. ir. L. P. Kouwenhoven

EMPLOYMENT

2014 Research Assistant
Industrial Focus Group XUV Optics
University of Twente, Enschede, The Netherlands
Advisor: Dr. I. A. Makhotkin

2020–Current Measurement Engineer
Microsoft Quantum Lab Delft

LIST OF PUBLICATIONS

6. R. L. M. Op het Veld*, D. Xu*, V. Schaller, M. A. Verheijen, S. M. E. Peters, J. Jung, C. Tong, Q. Wang, M. W. A. de Moor, B. Hesselmans, K. J. Vermeulen, **J. D. S. Bommer**, J. S. Lee, A. Sarikov, M. Pendharkar, A. Marzegalli, S. Koelling, L. P. Kouwenhoven, L. Miglio, C. J. Palmstrøm, H. Zhang, E. P. A. M. Bakkers,
   In-plane selective area InSb–Al nanowire quantum networks,
   Communication Physics **3**, 59 (2020).

5. **J. D. S. Bommer***, H. Zhang*, Ö. Gül*, B. Nijholt, M. Wimmer, F. N. Rybakov, J. Garaud, D. Rodic, E. Babaev, M. Troyer, D. Car, S. R. Plissard, E. P. A. M. Bakkers, K. Watanabe, T. Taniguchi, L. P. Kouwenhoven,
   Spin-orbit protection of induced superconductivity in Majorana nanowires,
   Physical Review Letters **122**, 187702 (2019).

4. M. W. A. de Moor*, **J. D. S. Bommer***, D. Xu*, G. W. Winkler, A. E. Antipov, A. Bargerbos, G. Wang, N. van Loo, R. L. M. Op het Veld, S. Gazibegovic, D. Car, J. A. Logan, M. Pendharkar, J. S. Lee, E. P. A. M. Bakkers, C. J. Palmstrøm, R. M. Lutchyn, L. P. Kouwenhoven, H. Zhang,
   Electric field tunable superconductor-semiconductor coupling in Majorana nanowires,
   New Journal of Physics **20**, 103049 (2018).

3. H. Atesci, F. Coneri, M. Leeuwenhoek, **J. D. S. Bommer**, J. R. T. Seddon, J. W. M. Hilgenkamp, J. M. van Ruitenbeek
   On the formation of a conducting surface channel by ionic-liquid gating of an insulator,
   Annalen der Physik **530**, 1700449 (2018).

2. Ö. Gül*, H. Zhang*, **J. D. S. Bommer***, M. W. A. de Moor, D. Car, S. R. Plissard, E. P. A. M. Bakkers, A. Geresdi, K. Watanabe, T. Taniguchi, L. P. Kouwenhoven,
   Ballistic Majorana nanowire devices,
   Nature Nanotechnology **13**, 192 (2018).

1. H. Zhang*, Ö. Gül*, S. Conesa-Boj, M. P. Nowak, M. Wimmer, K. Zuo, V. Mourik, F. K. de Vries, J. van Veen, M. W. A. de Moor, **J. D. S. Bommer**, D. J. van Woerkom, D. Car, S. R. Plissard, E. P. A. M. Bakkers, M. Quintero-Pérez, M. C. Cassidy, S. Koelling, S. Goswami, K. Watanabe, T. Taniguchi, L. P. Kouwenhoven,
   Ballistic superconductivity in semiconductor nanowires,
   Nature Communications **8**, 16025 (2017).

* These authors have contributed equally.